

# Towards Multimodal Nonlinear Microscopy in Clinics

## Dissertation

zur Erlangung des akademischen Grades doctor rerum naturalium

(Dr. rer. nat.)



VORGELEGT DEM RAT DER CHEMISCH-GEOWISSENSCHAFTLICHEN  
FAKULTÄT DER  
FRIEDRICH-SCHILLER-UNIVERSITÄT JENA

von Diplomphysiker Tobias Meyer  
geboren am 04.06.1980 in Weimar

**Gutachter:**

1. Prof. Dr. Jürgen Popp

**Institut für Physikalische Chemie, Friedrich-Schiller-Universität Jena**

2. Prof. Dr. Benjamin Dietzek

**Institut für Physikalische Chemie, Friedrich-Schiller-Universität Jena**

3. Prof. Dr. Marcus Motzkus

**Institut für Physikalische Chemie, Ruprecht-Karls-Universität Heidelberg**

**Tag der öffentlichen Verteidigung:**

20.11.2013

# Contents

<b>1</b>	<b>Zusammenfassung</b>	<b>5</b>
<b>2</b>	<b>Summary</b>	<b>11</b>
1	Motivation . . . . .	11
2	Multimodal Nonlinear Imaging . . . . .	17
2.1	Nonlinear Effects . . . . .	17
2.2	The Optimal Parameters for Multimodal Imaging of Tissue . . . . .	28
3	Applications . . . . .	32
3.1	Phototoxicity . . . . .	32
3.2	Comparison with the Golden Standard . . . . .	33
3.3	Head and Neck Squamous Cell Carcinoma (HNSCC) . . . . .	35
3.4	Brain Tumors . . . . .	41
3.5	Cardiovascular Diseases (CVD) . . . . .	46
4	Compact Multi-Contrast Imaging Platform . . . . .	52
4.1	Compact Multimodal Nonlinear Microscope . . . . .	54
4.2	Novel Laser Sources for Multi-Contrast Microscopy . . . . .	62
5	Interpretation of Multimodal Image Data . . . . .	70
5.1	The Origin of CARS Contrast for Cell Nuclei Detection . . . . .	71
5.2	Interpretation of Multispectral CARS Data . . . . .	72
6	Conclusion & Outlook . . . . .	81
<b>3</b>	<b>Bibliographie</b>	<b>85</b>
<b>4</b>	<b>Documentation of Authorship</b>	<b>95</b>

## Contents

---

5	Nonlinear Microscopy for Brain Tumor Analysis	105
6	Multimodal Nonlinear Microscopy on HNSCC	133
7	Interpreting CARS Images Within the C-H-Stretching Region	157
8	Fiber Laser for CARS Based on Parametric Frequency Conversion	169
9	All-Spliced Fiber Laser for CARS Microscopy Based on FWM	189
10	Widely Tuneable FOPA for CARS Microscopy	207
11	Compact Microscope for Multimodal Imaging in Clinics	231
12	High Spectral Resolution CARS Imaging for Disease Diagnostics	267
13	Peer Reviewed Publications	303
14	Conference Contributions	307
15	Selbständigkeitserklärung	313
16	Danksagung	315

# 1 | Zusammenfassung

Seit der Erfindung der Mikroskopie hat sich dieses optische Instrument eine Schlüsselstellung in der biomedizinischen Forschung erobert und ist als solches unverzichtbar, z.B. in der histopathologischen Diagnostik oder der biologischen Grundlagenforschung. So sind morphologische Veränderungen auf (sub)zellulärer Ebene oder auf der Ebene der Gewebe momentan der Goldstandard für die zuverlässige Diagnose von Krankheiten, seien es Infektionskrankheiten, bösartige Neubildungen oder degenerative Erkrankungen. Die Vielfalt optischer Verfahren erlaubt es heute, Strukturen im Bereich einiger 10 nm aufzulösen. Farbstoffe markieren selektiv Gewebestrukturen wie Fette, bestimmte Proteinfasern wie Kollagen und Elastin oder die DNS als Träger der Erbinformationen. Seit Antikörper als hochspezifische molekulare Label verwendet werden, können selbst Einzelmoleküle selektiv detektiert werden. Dennoch stößt die optische Mikroskopie immer wieder an ihre Grenzen, z.B. in der intraoperativen Bildgebung und bei der Früherkennung von Krankheiten.

Bei der intraoperativen Bildgebung verbietet sich der Einsatz der meisten Farbstoffe aufgrund ihrer Toxizität, so dass der Chirurg seinen eigenen Augen und Erfahrungen vertrauen muss. Besonders kritisch stellt sich das bei der operativen Tumorresektion dar, bei der ein Behandlungserfolg nur durch vollständige Entfernung des betroffenen Gewebes erzielt werden kann, da zurückbleibendes krankhaftes Gewebe unvermeidbar zum Wiederauftreten der Erkrankung führt. Wenn die großzügige Entfernung von umgebendem gesunden Gewebe nicht möglich ist, wie beispielsweise wenn funktionell wichtige Strukturen betroffen sind z.B. bei Hirnoperationen, muss das zu operierende Gewebe exakt dargestellt werden können.

Auch die Früherkennung von Krankheiten ist von herausragender medizinischer und

gesellschaftlicher Bedeutung, lassen sich doch viele der heute verbreiteten Krankheitsbilder wie Krebs und Herz-Kreislauf-Erkrankungen in einem frühen Stadium gut behandeln. Momentan sind diese Erkrankungen jedoch in den Industrienationen für 75 % der Todesfälle verantwortlich, v.a. durch die meist späte Diagnose in einem fortgeschrittenen Stadium. Die Ursache dafür liegt darin begründet, dass in einem frühen Stadium der Krankheitsverlauf noch Symptomatik ist, so dass die Erkrankung nur sehr selten diagnostiziert wird. In fortgeschrittenem Stadium hingegen sind die Behandlungsmöglichkeiten eingeschränkt. Daher werden bildgebende Methoden gesucht, die es erlauben, Patienten nichtinvasiv oder minimal-invasiv auf frühe Anzeichen einer Erkrankung zu untersuchen, z.B. mit einer optischen Biopsie. Angespornt durch die Nachfrage nach neuen bildgebenden Verfahren in der Medizin wurden in den vergangenen Jahren mehrere nichtlineare optische Verfahren entwickelt, die es gestatten, Gewebestrukturen ohne den Einsatz externer Label mit subzellulärer Auflösung bis in 1 mm Tiefe zu beobachten und mit histologischen Färbungen vergleichbare Informationen über die Morphologie und chemische Zusammensetzung des Gewebes zu erhalten. Die Verfahren zur Erzeugung frequenzverdoppelten Lichtes (SHG), der durch Zweiphotonenabsorption angeregten Fluoreszenz (TPEF) und der kohärenten anti-Stokes Raman Streuung (CARS), ergeben als kombinierte Multikontrast-Mikroskopie ein sehr leistungsfähiges Werkzeug für die Untersuchung nativen Gewebes, das es ermöglicht, eine Vielzahl molekularer Marker orts aufgelöst zu detektieren.

Im Rahmen der vorliegenden Arbeit wurde in Fallstudien an (i) bösartigen Neubildungen des Hals-Nasen-Ohren-Bereiches, (ii) Hirntumoren und an Proben von (iii) Arteriosklerose betroffener Blutgefäße das Potential einer Kombination der drei genannten bildgebenden Verfahren im Hinblick auf deren Fähigkeit zur Visualisierung der mit dem Fortschreiten der Krankheit einhergehenden Gewebeveränderungen untersucht und durch Vergleich mit dem Goldstandard, histologischen Färbungen, bewertet. (i) Bei bösartigen Neubildungen im Hals-Nasen-Ohren-Trakt konnte eine Vielzahl der den Prozess der Karzinogenese begleitenden charakteristischen Gewebeänderungen nachgewiesen werden. Diese werden klassifiziert als Änderungen in der Gewebearchitektur, z.B. Änderung der Zelldichte, Verlust der Polarität der

---

Basalzellschicht, Verlust der Integrität der Basalmembran und anomale Keratin-Expression und zytologische Änderungen, z.B. ein geändertes Kern-Zytoplasma-Verhältnis, atypische Zellkernform und -größe und atypische Zellform und -größe. Neben morphologischen Änderungen konnten auch systematische chemische Änderungen nachgewiesen werden, wie z.B. eine Zunahme der Autofluoreszenz in dysplastischem Epithelgewebe und eine Verringerung des Lipidgehalts, beides Indizien für einen erhöhten Zellstoffwechsel. (ii) Die Architektur von gesundem Hirngewebe konnte dargestellt werden, was die Voraussetzung ist, um krankheitsbedingte Abweichungen von dieser Norm nachweisen zu können. So konnte der Aufbau des Kleinhirns eines Hausschweins abgebildet werden. So können die weiße und graue Hirnsubstanz sowie die einhüllende Membran, die Arachnoidia, unterschieden werden. An humanen Hirnproben konnten Einzelzellen und Axone visualisiert werden. Die mit bösartigen Neubildungen des Gehirns einhergehenden Änderungen v.a. in der Zelldichte konnten für die Tumorentitäten Gliom und Lymphom visualisiert und nekrotisches Tumorgewebe erkannt werden. Die für Sekundärtumore wie z.B. Hirnmetastasen von Karzinomen charakteristischen und für das Gehirn selbst morphologisch atypischen Tumorinseln konnten ebenfalls visualisiert werden. Neben den strukturellen, rein morphologischen Auffälligkeiten wurden auch Änderungen in der chemischen Zusammensetzung nachgewiesen, so ein reduzierter Lipidgehalt in Metastasen von Karzinomen im Vergleich zum durchschnittlich lipidreichen Hirngewebe. (iii) Bei kardiovaskulären Erkrankungen, speziell Arteriosklerose, konnten einerseits Aufbau und Struktur der Arterienwand als auch der abgelagerten Plaques visualisiert werden. Speziell die Verteilung von Kollagen, Elastin, Fetten und Cholesterolkristallen sind diesen Methoden zugänglich, was es ermöglichen könnte, die Wahrscheinlichkeit einer Thrombose aus Struktur und Zusammensetzung der Ablagerung präziser abzuschätzen. Eine methodische Schlüsselrolle steht der kohärenten anti-Stokes Raman Streuung zu, da hiermit die größte Zahl molekularer Marker sichtbar gemacht werden kann, denn die Zahl endogener SHG- und TPEF-aktiven Moleküle in Gewebe ist sehr gering. Um dieses Potential jedoch voll ausschöpfen zu können, müssen multispektrale Daten aufgenommen werden. Exemplarische konnte gezeigt werden, dass aus Bilddaten an lediglich zwei Ramanresonanzen, die für Methyl- und

## Zusammenfassung

---

Methylengruppen charakteristisch sind, auf die Verteilung von Proteinen und Lipiden geschlossen werden kann. Weiterhin lassen sich mit diesen Informationen ebenfalls die TPEF- und SHG-Signale präziser interpretieren, z.B. konnten SHG-Signale in arteriosklerotischen Läsionen Cholesterin zugeordnet werden, TPEF-Signale oxidierten Lipiden, während SHG- und TPEF-Signale aus der Arterienwand eindeutig Proteinstrukturen zugeordnet werden konnten.

Noch nicht abzusehen ist bislang, inwieweit sich die Informationen über chemische Veränderungen im Krankheitsverlauf diagnostisch verwerten lassen. Dazu wäre es erforderlich, die Techniken nicht nur an kleinen Fallstudien zu testen. Studien in größerem Rahmen, daher idealerweise in klinischer Umgebung, steht insbesondere die Komplexität und Empfindlichkeit der verwendeten Geräte gegenüber äußeren Einflüssen im Wege. Daher sind bei der Translation der Techniken in die klinische Anwendung insbesondere auch technische Hürden zu überwinden.

Im Rahmen der vorliegenden Arbeit wurde ein kompaktes, einfach zu bedienendes Mikroskop entworfen, das auch in der Klinik betrieben werden kann und Daten von hoher Qualität generiert. Das Gerät wurde dahingehend optimiert, dass ein großes Bildfeld die schnelle Untersuchung großer Flächen ermöglicht. Durch die Auslegung für nahinfrarote Anregungslaser können bei der Untersuchung humaner Gewebeproben Photoschäden auf ein Minimum reduziert und gleichzeitig die Eindringtiefe maximiert werden. Weiterhin wurde die Transmission optimiert, so dass kleine kompakte und weniger leistungsstarke Anregungslasersystem eingesetzt werden können. Diese Laser sind aber im Gegenzug ausgesprochen robust und wartungsarm, was einen großen Vorteil für den Einsatz in der Klinik darstellt.

Die für den klinischen Einsatz konzipierte kompakte Multikontrast-Mikroskopie-Plattform erlaubt die Aufnahme qualitativ hochwertiger Datensätze vergleichbar mit einem konventionellen und größeren Laboraufbau. Aber durch die kompakten Maße und einfache Handhabung ist das Gerät für klinische Tests in naher Zukunft geeignet.

Neben der Aufnahme der Daten ist es erforderlich, die Bildinformationen korrekt zu interpretieren. Hier wurde nachgewiesen, dass der Bildkontrast, der die Detektion von Zellkernen erlaubt, tatsächlich auf einen geringeren Lipidgehalt innerhalb der



---

Zellkerne im Vergleich zum umgebenden Zytoplasma zurückgeführt werden kann. Weiterhin wurde ein neuer Ansatz zur Analyse multispektraler CARS-Daten entwickelt, der auf Kolokalisationsanalyse basiert und damit etablierten Verfahren in der Fluoreszenzmikroskopie angelehnt ist. Damit kann die räumliche Verteilung verschiedener Raman-aktiver Marker aus multispektralen Datensätzen bestimmt werden. Zusammenfassend wurden im Rahmen der vorliegenden Dissertation die Verfahren der kombinierten SHG-, TPEF- und CARS-Multikontrastmikroskopie in Fallstudien getestet und durch Vergleich mit histologischen Färbungen validiert. Es konnte gezeigt werden, dass eine Vielzahl charakteristischer morphologischer und chemischer Gewebeveränderungen, die im Zusammenhang mit einem Krankheitsverlauf stehen, sichtbar gemacht werden können. Das Verfahren kann somit die Morphochemie des Gewebes sichtbar machen. Dazu wurden einerseits kompakte Geräte, die für den klinischen Einsatz geeignet sind, entwickelt und getestet und es wurden Verfahren entwickelt, welche die Interpretation der Daten erleichtern. Zukünftige Entwicklungen auf diesem Gebiet werden einerseits die Miniaturisierung der Instrumente sowie klinische Tests in größerem Umfang einschließen.



## 2 | Summary

### 1 Motivation

Since the invention of the optical microscope by Leeuwenhoek and other opticians in the Netherlands in the 16<sup>th</sup> century, microscopic imaging has developed into a key technique for the investigation of morphology and physiological processes in living organisms. It has opened up a new world for visualizing microscale structures which have been due to their small size invisible before. This gave birth to biomedicine beyond anatomy, in particular histology and cytology, since it is impossible to understand tissue function without recognizing the smallest building blocks of living organisms, the cells, and their subcellular machineries. Optical microscopy has since then been one of the most important if not the key instrument in live sciences and as such the microscope has paved the way to the understanding of the organization and function of life on the size scale hidden to the naked eye.

Therefore, it is not surprising that the greatest success in medicine in the past centuries was driven by microscopy: the discovery from Robert Koch and Louis Pasteur, that infectious diseases are caused by micro-organisms [1, 2]. This is based on a characteristic feature of microscopy. The optical resolution on the order of the wavelength of light enables imaging pathogens, e.g., bacteria and other single cell organisms, as visualized in figure 1.

Since then a multitude of more and more sophisticated optical microscopic methods have been developed, especially based on staining of thin sliced tissue biopsies, in order to provide histopathologists the information necessary for determining the disease status. Staining increases significantly the contrast and as such enables to

## Summary

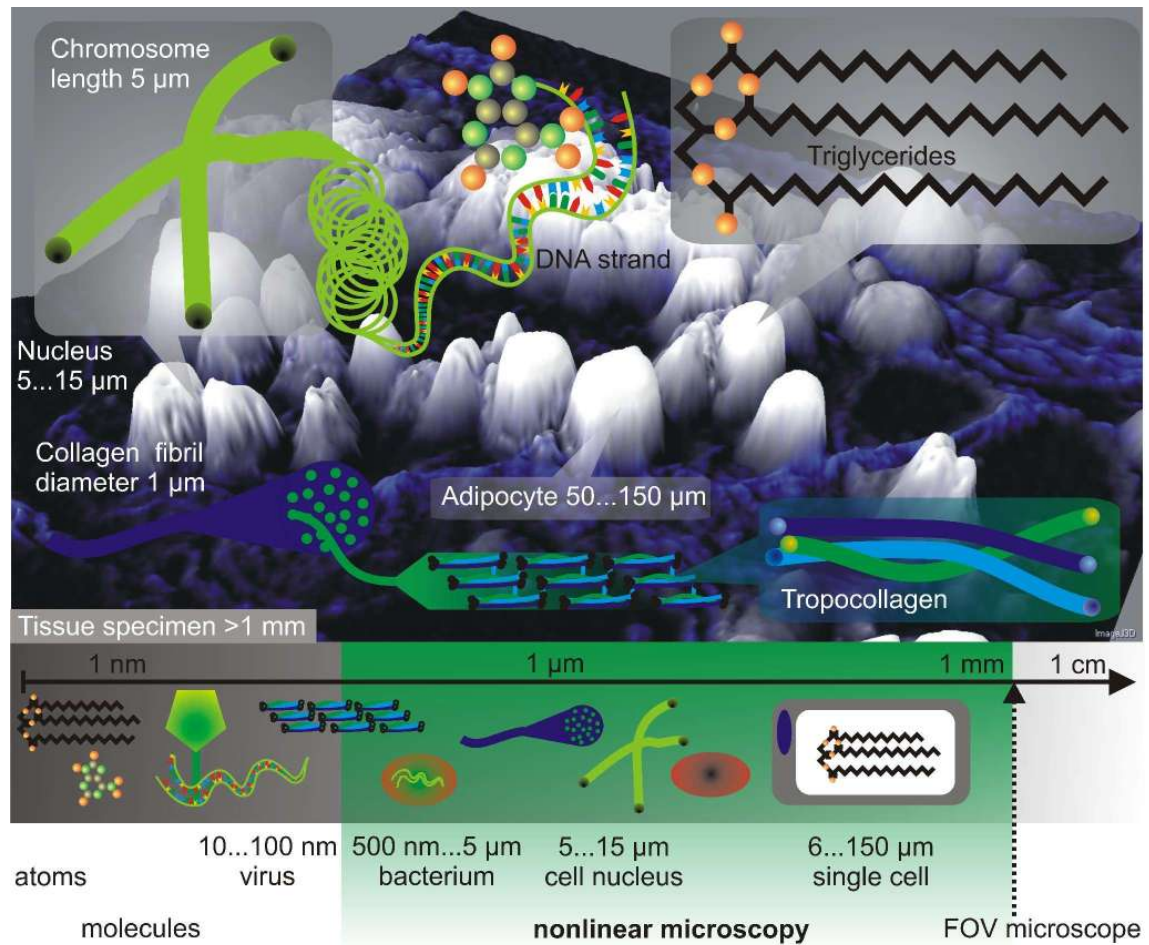


**Figure 1** – The size scales accessible to nonlinear imaging range from sub-cellular structures at the resolution limit of app. 300 nm, e.g., single bacterial cells and large collagen fibers, to few mm, the full field of view of an microscope objective covering a significant portion of a typical biopsy. Nonlinear imaging can also provide images in depths up to 1 mm. The sizes of some typical structures are indicated. FOV - field of view of an optical microscope

detect characteristic disease related structures with respect to the surrounding matrix. Both sub-cellular spatial resolution as well as molecular contrast are the basis of the success of staining histopathology for disease diagnostics. This is why staining histopathology is the current golden standard in medical diagnostics.

In order to illustrate the advantages of staining histopathology but also to identify limitations, the most widely used staining procedure is briefly explained in the following. This is the haematoxylin and eosin (H&E) stain. Here the basic colourant

haematoxylin tints acidic cellular structures blue, in particular the cell nucleus and ribosomes, while the acidic dye eosin stains alkaline tissue compounds like the cell's cytoplasm and collagen fibers bright red.

Consequently, visualization of structures neither basic nor acidic is cumbersome as is the case for fatty acids, which play a key role in a variety of pathologies as explained later. Furthermore, tissue preparation for histopathology is a very complex procedure, starting from taking a biopsy at a suspicious location followed by advanced tissue preparation and processing routines, i.e., tissue fixation and stabilization, paraffin embedding, microtome sectioning and preparation of microscopic slides, and finally finished by the staining process. The whole workflow of this world wide standard of formalin embedding paraffin fixation in combination with H&E staining takes approximately 1 to 2 days from biopsy to examination, but also a fast investigation in a couple of minutes is possible, e.g., during surgery. Hence, even though time is not a limitation, in order to obtain best results, careful processing at all preparation steps is required. Additionally, the number of routinely used dyes is limited as is the number of structures, which are discernible. This is due to the fact, that the method does not visualize a particular substance directly, but the affinity to bind a colourant.

To resolve this issue, since the 1940's immunohistochemistry has been developed providing high specificity by using antigens directly bound to fluorescence dyes or alternatively more recently by searching for characteristic DNA markers [3, 4].

This progress in histochemical methods mirrors directly the changes in the most prevalent life threatening diseases. During the last century, progress in medicine, in particular the discovery of antibiotics [5], and a general improvement in the living conditions has increased the average life span particularly in the developed countries and thus shifted the most common cause of death from infectious diseases to so-called lifestyle diseases. The challenges related to this shift of paradigm in medical science from fighting infectious diseases towards more difficult to cure chronic and lifestyle diseases are best illustrated by the two most prominent disease patterns in industrial countries: cardiovascular diseases (CVD) and cancer. Both account for almost 65% of deceases in Germany in 2011 [6].

## Summary

---

Despite tremendous efforts to develop potent therapeutics, success in fighting these disease patterns is still limited. This has several reasons: First, recent and ongoing progress in molecular biology, genetics and epigenetics indicates, that these diseases originate from subtle and diverse chemical alterations inside the body, which precede any detectable structural modifications [4, 7, 8, 9]. In particular genetic alterations which are assumed to be responsible for initiating the process of carcinogenesis are manifold, even though the aetiopathology may seem very similar. But as with any disease, early disease recognition is directly translated into a much better patient prognosis.

However, achieving early disease diagnosis is very ambitious, since tissue alterations in early stage cancer or CVD are subtle. Hence, treatment strategies focussing on this multifaceted problem will very likely include regular routine screening of many patients at risk. Therefore, novel analytical methods are required, which should ideally fulfil the following requirements:

- (1) The method is based on simple-to-use compact instruments such that the imaging tool is comprehensively available for diagnostics.
- (2) The technique should be fast and non- or only minimally invasive enabling usage for routine preventive medical examination ensuring patient safety and comfort during examination.
- (3) The imaging system is capable to precisely detect early molecular changes on cellular or subcellular level.

However, so far there are no established clinical imaging modalities allowing for visualizing the first subtle chemical changes on this size scale, i.e., on cellular or subcellular level. In terms of spatial resolution the most precise method and as such still under development is optical coherence tomography (OCT) providing a 1-2 mm of depth penetration and an optical resolution of few micrometers, which is at the limit for the detection of single cells and still insufficient for visualization of subcellular details [10, 11, 12]. Other imaging modalities offer either whole body imaging, e.g., X-ray tomography, magnetic resonance imaging (MRI) and positron emission tomography (PET), or provide depth penetrations of mm to cm, e.g., ultrasound, but at the cost of reduced spatial resolution [12]. In particular routine

clinical molecular imaging modalities like MRI, CT and PET require expensive and space consuming equipment in addition to specialists for instrument handling. Thus, these methods are not available in a comprehensive way, but only in large clinics and radiological praxis. This is why these methods are not suited for routine screening of patients for the purpose of prevention, which would require a much larger number of instruments at great expenses.

Hence, hand in hand with the perception, that early recognition is crucial for successful disease treatment, research has to focus on novel molecular imaging modalities that allow for the detection of subtle tissue alterations due to early stage lifestyle diseases, e.g., CVD and cancer. Such imaging modalities have to provide molecular contrast enabling to resolve subcellular disease related features as does the current golden standard of staining histopathology, but need to extract such information less invasive, ideally *in vivo*. Similarly important, the imaging method needs to rely on simple to use and low cost equipment, which allows installation in every doctor's practice.

Now the stage is set to introduce a selection of novel optical imaging methods that have been developed driven by research in both optics and biomedical research over the past years. Due to their nonlinear dependence on the excitation light intensity these methods are termed 'nonlinear' microscopy and are characterized by a unique set of properties, which make them particularly useful for imaging of native tissue: diffraction limited spatial resolution and intrinsic three-dimensional sectioning capabilities, label-free molecular contrast and a large penetration depth in tissue exceeding 1 mm by using near infrared lasers. Specifically the nonlinear imaging modalities coherent anti-Stokes Raman scattering (CARS), two photon excited fluorescence (TPEF) and second harmonic generation (SHG) microscopies, which will be introduced in more detail in the following section 2, provide tissue intrinsic molecular contrast based on endogenous markers.

In order to evaluate the potential of multimodal nonlinear microscopy for biomedical diagnostics, the following investigations need to be performed:

## Summary

---

- In case studies covering various disease patterns multimodal nonlinear imaging needs to be compared to the golden standard of staining histopathology, particularly in terms of spatial resolution and chemical image contrast, to evaluate the potential of this imaging approach for clinical diagnostics and to identify possible limitations. In particular the optimal imaging parameters, e.g., in terms of spectral resolution, excitation wavelength, power at the sample, need to be determined.
- Development and testing of prototype equipment, which is adapted to the optimal imaging parameters as derived from the case studies in order to prove that it is technologically feasible to transfer this technology into clinical settings. In addition, the instrument for multimodal nonlinear microscopy needs to be designed according to the demands for clinical application, e.g., in terms of small footprint, robustness and ease of handling.
- Research on image analysis and image interpretation, e.g., investigation the correlation of the observed image contrast with pathological tissue modifications and examination of efficient methods to extract information for the evaluation of the disease status.

Therefore, the prospects of these methods for biomedical applications, in particular for the visualization of tissue alterations for disease diagnostics is emphasized in the next section 3 focusing on head and neck cancers, brain tumors and on atherosclerosis. Based on these results, compact laser equipment has been tested and a microscopic platform has been developed to fit the demands for clinical applications. These technological improvements which are essential prerequisites for the translation of multimodal nonlinear microscopy from fundamental research into clinics are presented in section 4. Finally in section 5 results from research on image interpretation are presented.



## 2 Multimodal Nonlinear Imaging

In this section the concepts of nonlinear imaging will be introduced and specific properties summarized, which make this set of methods particularly useful for imaging human tissue. Furthermore, the optimal parameters for multimodal nonlinear imaging are discussed. Therefore, the optical properties of animal and human tissue in the visible to near infrared wavelength range are summarized as far as they restrict important imaging parameters, e.g., the excitation wavelength range.

### 2.1 Nonlinear Effects

The term 'nonlinear effects' summarizes in this contribution optical effects, which are proportional to higher orders of the excitation light intensity. In general, light matter interactions within materials and therefore also in tissue are in the frame of Maxwell's theory described by the polarization  $\vec{P}$  (see equation 1).

$$\vec{\nabla} \cdot \vec{D} = \vec{\nabla} \cdot (\epsilon_0 \vec{E} + \vec{P}) = \rho \quad (1)$$

In equation 1 the following symbols have been used:  $\vec{D}$ , displacement field,  $\epsilon_0$ -permittivity of the vacuum,  $\vec{E}$ , electric field,  $\vec{P}$ , polarization of the material,  $\rho$  charge density of the material. The polarization  $\vec{P}$  describes the response of matter to the incoming electric field  $\vec{E}$ . The origin of this response is due to the charges hidden in atoms and molecules, e.g., electrons and protons. There are two possible description: macroscopically using the susceptibility  $\chi$ , which describes the nonlinear response of a bulk medium. However, the origin of the polarizability  $\vec{P}$  is due to the molecular structure, hence the macroscopic susceptibility  $\chi$  is the sum of the molecular polarizabilities, e.g.,  $\alpha$  of the molecules within the macroscopic volume. When the macroscopic polarization  $\vec{P}$ , resulting from the interaction of matter and the incident electric field  $\vec{E}$ , is a function of the light intensity,  $\vec{P}$  can be written as a Taylor series in the electric field  $\vec{E}$  (equation 4).

$$\vec{P} = \epsilon_0 \cdot (\overleftarrow{\chi}^{(1)} \vec{E} + \overleftarrow{\chi}^{(2)} \vec{E} : \vec{E} + \overleftarrow{\chi}^{(3)} \vec{E} : \vec{E} : \vec{E} + \dots) \quad (2)$$

$$\equiv \epsilon_0 \cdot (\chi^{(1)} \vec{E} + \underbrace{\chi^{(2)} \vec{E}^2}_{SHG} + \underbrace{\chi^{(3)} \vec{E}^3}_{CARS, TPEF} + \dots) \quad (3)$$

$$= \epsilon_0 \cdot \sum_{n=1}^{\infty} \chi^{(n)} \vec{E}^n \iff |\chi^{(2n-1)}| \ll |\chi^{(2n+1)}| \quad (4)$$

Here the n-th order susceptibility is termed  $\chi^{(n)}$  are tensors of rank  $n + 1$ , hence equation 4 refers to a tensor product, as ascribed in the first row. To save space, the tensor product is simplified in the following notations. Similarly also the molecular response, the induced dipole moment  $\vec{p}$ , can be expressed as a Taylor series in the electric field.

$$\vec{p}_{ind} = \epsilon_0 \cdot \left( \alpha \vec{E} + \frac{1}{2} \beta \vec{E}_{SHG}^2 + \frac{1}{6} \gamma \vec{E}^3 + \dots \right) \quad (5)$$

In equation 5 the molecules polarizability is termed  $\alpha$ , the second order term  $\beta$  describes the lowest order hyperpolarizability and the next order hyperpolarizability is named  $\gamma$ . When using continuous wave illumination, the nonlinear terms are negligible, because the modulus of higher order susceptibilities  $\chi^n$  rapidly decreases with order n. However, when illuminating the sample by pulsed lasers instead of continuous wave (cw) sources, power levels sufficient for exciting second and third order nonlinear processes can be generated by maintaining average power and peak power levels below the damage threshold of tissue [13, 14, 15].

The available nonlinear processes possess unique properties very promising for *in vivo* tissue imaging:

- First, nonlinear imaging modalities allow for label-free molecular imaging by visualizing the distribution of endogenous markers. Since no labelling or staining is required, the methods are non toxic and therefore also applicable *in vivo*.
- Second, due to the nonlinear intensity dependence the signal is only generated within the focus and therefore also confined to the focus spot, which automatically results in three-dimensional resolved signal generation. In linear

## 2. Multimodal Nonlinear Imaging

microscopic techniques, e.g., fluorescence microscopy, a special optical layout, e.g., a confocal design, has to be used in order to provide high axial resolution.

- Third, due to the longer wavelength excitation, which reduces scattering, and the simple optical layout providing high signal collection efficiencies, the depth penetration in tissue can be as large as 1 mm in the case of TPEF autofluorescence [16, 17]. This is much higher than for single photon fluorescence with excitation wavelengths in the visible or UV.

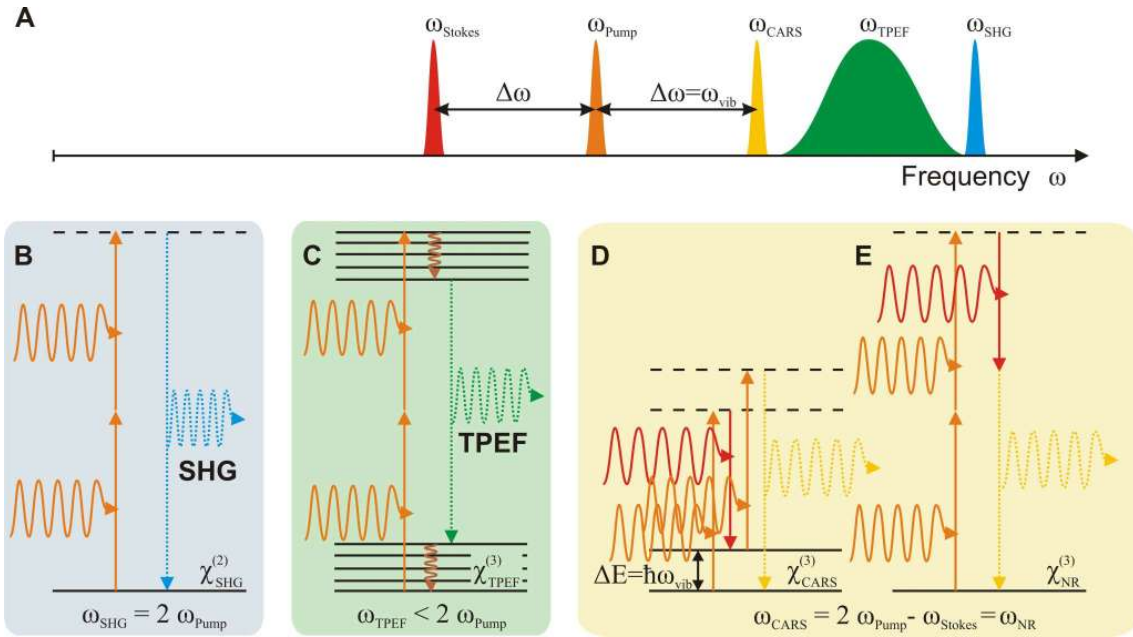


**Figure 2** – The nonlinear processes SHG, TPEF and CARS utilized for multimodal nonlinear imaging. In panel A the frequency ranges of the excitation lasers and of the emitted signals is displayed for the ideal case of no spectral overlap of TPEF and CARS signals. Panel B: SHG, scattering of two photons into a single photon of twice the energy and frequency, panel C: TPEF, a two photon absorption process is followed by relaxation and emissive de-excitation into the ground state, panel D: CARS, when the frequency difference of pump and Stokes laser matches a vibrational resonance, resonant scattering at the anti-Stokes frequency is emitted, but also non resonant processes depicted in panel E can contribute to the signal at the anti-Stokes frequency, limiting the contrast.

In the following focus will be put on the contrast mechanisms SHG, a  $\chi^{(2)}$ -process, and the  $\chi^{(3)}$ -processes TPEF and CARS. The three processes are schematically depicted in figure 2. In the ideal case depicted in figure 2 panel A, the SHG,

TPEF and CARS signals are spectrally separated emitted from the sample. Hence, SHG, TPEF and CARS can be simultaneously excited and detected by spectral filtering. The key advantage of multimodal nonlinear imaging by the combination of SHG, TPEF and CARS microscopy, is the direct visualization not only of tissue morphology but also of the molecular composition of the tissue, i.e., picturing the morphochemistry. The origin of the molecular contrast and the actual imaging properties are different for SHG, TPEF and CARS, therefore each method will be discussed individually in the following.

### Second Harmonic Generation (SHG)

SHG is a coherent scattering process as depicted in figure 2 panel B. Two photons are coherently scattered into a photon of twice the energy and frequency. For symmetry reasons, this process is forbidden in isotropic media and molecules. SHG can occur only in non isotropic systems, e.g., at interfaces or in highly ordered crystal-like structures.

The SHG signal intensity depends in detail on the peak intensity  $I_0$  and the magnitude of the second order nonlinear susceptibility  $\chi^{(2)}$ , which is the hyperpolarizability  $\beta$  multiplied by the number  $N$  of SHG active molecules within the focal volume (according to [18, 19]):

$$I_{SHG} \propto I_0^2 |\chi^{(2)}|^2 = I_0^2 \cdot N^2 \cdot |\beta|^2 \quad (6)$$

In tissue, specific proteins are organized in quasi crystalline structures. These proteins are collagen, the most frequent protein and a main constituent of the extracellular matrix, actin-myosin, the motor proteins of the muscle cells and tubulin, a protein of the cell cytoskeleton [20]. Recently also cholesterol crystals have been identified as sources of SHG signals [21]. However, there is no spectral difference in the SHG signal from the different markers, e.g., from collagen, tubulin or cholesterol. Therefore, by SHG alone discrimination of the distinct possible sources of SHG radiation is not possible. But since these proteins are usually not co-localized, they can be detected in combination with morphological information and knowledge about the abundance of the SHG active markers in specific tissues.

### Two Photon Excited Fluorescence (TPEF)

TPEF is neither a coherent nor a scattering process in contrast to SHG. TPEF is initiated by a two photon absorption in a chromophore followed by deactivation via autofluorescence as depicted in figure 2 panel B. The TPEF signal intensity dependence with respect to the number of chromophores  $N$ , the fluorescence quantum yield  $\Phi$ , the two-photon absorption cross section  $\sigma_{TPA}$  and the peak intensity of the excitation light  $I_0$  is shown in equation 7 according to [22, 23].

$$I_{TPEF} \propto N \cdot \Phi_F \cdot \sigma_{TPA} \cdot I_0^2 = N \cdot \sigma_{TPEF} \cdot I_0^2 \quad (7)$$

For simplicity, fluorescence quantum yield  $\Phi$  and the two-photon absorption cross section  $\sigma_{TPA}$  can be combined to the TPEF cross section  $\sigma_{TPEF}$ . TPEF depends - as SHG - on the square of the incident light intensity, but only linearly on the dye concentration  $N$ . However, fluorescing chromophores are rare in animal tissue [24], in contrast to plants. The most prominent autofluorophors include the proteins elastin and keratin, pigments like melanin and enzymes like NADH and flavines [25, 26]. But in comparison to the strong signals of exogenous dye labels, e.g., fluorescein or rhodamine, the two-photon cross section  $\sigma_{TPEF}$  of endogenous markers is orders of magnitude lower, e.g.,  $\sigma_{TPEF} = 0.1...0.04 GM$  for NADH at 700 nm [23, 24] in contrast to more than 100  $GM$  in case of rhodamine [27].  $1 GM = 10^{-50} cm^4 s$  is the unit for measuring the two photon absorption cross section, named after the Nobel laureate Maria Goeppert-Mayer.

### Vibrational Imaging - Spontaneous and Coherent Raman Effect

In contrast to SHG and fluorescence, which can be used to visualize only a limited number of endogenous markers in tissue, possessing very specific properties, e.g., an anisotropic quasi-crystalline structure in case of SHG and an absorbing chromophore, which is de-excited via fluorescence in case of TPEF, molecular vibrations are a general characteristic of molecules. The vibrational spectrum can be assessed by infra-red (IR) absorption and Raman scattering. While IR based techniques do not allow for sub- $\mu m$ -spatial resolution according to the fundamental resolution limit

## Summary

---

(see equation 13) and are not applicable in aqueous environment due to the strong IR absorption of water, only Raman based techniques come into consideration for *in vivo* vibrational imaging of tissue.

In order to appreciate the great wealth of information about molecular structure contained in the Raman spectrum, which firstly allows using all Raman-active molecules as markers and secondly provides much more structural information in comparison to TPEF and SHG, spontaneous Raman spectra of two biomolecules will be briefly explained in the following. In figure 3 Raman spectra of milk protein and triglyceride and the general molecular structures of peptides and triglycerides are exemplarily displayed. The Raman spectrum is characterized by spectral bands, resonances, at characteristic wavenumbers. The spectrum can be subdivided into the low wavenumber spectral region, i.e., in the range from 500 to 1000  $\text{cm}^{-1}$ , the so-called 'fingerprint' region, the adjacent group frequency region from 1000 to 1800  $\text{cm}^{-1}$  and the high wavenumber region, i.e., in the spectral range from 2700 to 3500  $\text{cm}^{-1}$ . In between there is a spectrally silent region devoid of Raman resonances with only few exceptions, e.g., C-D-stretching vibrations of deuterated molecules and triple bond stretch vibrations, e.g.,  $C\equiv C$  and  $C\equiv N$ . The so-called fingerprint spectral region is similarly molecule specific as a fingerprint is characteristic for a human, which is why this spectral region is mainly used for the identification of molecules.

Apart from identifying a specific molecule, Raman spectroscopy can be used to analyse the molecular structure. Raman based molecular structure determination is based on the fact, that many vibrational frequencies are only slightly influenced by the rest of the molecule but appear in a special spectral region, which is specific for the functional group. This is exemplarily illustrated for proteins and triglycerides in figure 3. In the protein spectrum figure 3 panel C the Raman band at 1000  $\text{cm}^{-1}$  corresponds to the ring breathing mode of benzene, hence is characteristic for aromatic amino acids, e.g., phenylalanine. The most prominent protein band at 1666  $\text{cm}^{-1}$ , the so-called amide I band, corresponds primarily to the C-O-stretching vibration of the peptide bond [28, 29].

The spectrum of triglycerides is dominated by bands assigned to the methyl and methylene groups and vibrations of the ester linkage between glycerol and the fatty

## 2. Multimodal Nonlinear Imaging

---

acids. The bands at 1400 to 1470  $\text{cm}^{-1}$  are due to C-H-deformation vibrations, e.g.,  $CH_3$ -bending as well as  $CH_2$ -scissoring, wagging and rocking modes, while the band at 1300  $\text{cm}^{-1}$  is assigned to the skeletal  $CH_2$ -in-phase-twist vibration. Two prominent bands originating in the ester functional group are at 1100  $\text{cm}^{-1}$ , which corresponds to a C-O-C-skeletal vibration and the C-O-stretch vibration of the carbonyl double bond of the ester group at 1750  $\text{cm}^{-1}$  [30].

In panel B of figure 3 the C-H-stretch vibrations of  $CH_2$ - and  $CH_3$ -functional groups are depicted. The corresponding spontaneous Raman spectra of proteins and triglycerides in the high wavenumber region are depicted in panel E of figure 3 and the symmetric and anti-symmetric C-H-stretching vibrations of methyl and methylene groups are indicated [31]. Even though proteins and triglycerides possess both  $CH_2$ - and  $CH_3$ -functional groups, the Raman spectrum of both groups of molecules is different, due to the different amount of the respective functional group per molecule and the different chemical environment. For example the ratio of  $CH_2$ - to  $CH_3$ -groups is approximately 2 in proteins according to the abundance of their building blocks, the amino acids [32], while it is significantly higher in triglycerides. This is mirrored in the much higher intensity of the symmetric  $CH_2$ -stretch vibration in triglycerides in comparison to proteins. Therefore, also the high wavenumber Raman spectrum is informative for differentiating biomolecules. However, application of spontaneous Raman in biomedical imaging is limited, since it is a very weak effect [33, 34, 35]: The strength of the Raman effect as described by the scattering cross section  $\sigma$  (see equation 8), is about  $\sigma_{Raman} \approx 10^{-30} \text{cm}^2$  [36] and therefore orders of magnitude smaller than the cross section for UV-VIS fluorescence  $\sigma_{Fluorescence} \approx 10^{-16} \text{cm}^2$  [37] and infra-red (IR) absorption  $\sigma_{IR} \approx 10^{-19} \text{cm}^2$  [38].

The Raman signal intensity expressed as a function of the frequency of the Stokes radiation  $\omega_S$ , the incident laser intensity  $I_0$ , the number density of molecules  $N$  and the derivative of the molecules polarizability  $\alpha$  with respect to the vibrational coordinate  $Q$  is given by equation 8 [39].

$$I(\omega_S) = N \cdot \frac{\omega_s^4}{12\pi\epsilon_0 c^3} Q_0^2 I_0 \left( \frac{d\alpha}{dQ} \right)_{Q=0}^2 \iff \sigma_{Raman} = \frac{\omega_s^4 Q_0^2}{12\pi\epsilon_0 c^3 z} \left( \frac{d\alpha}{dQ} \right)_{Q=0}^2 \quad (8)$$

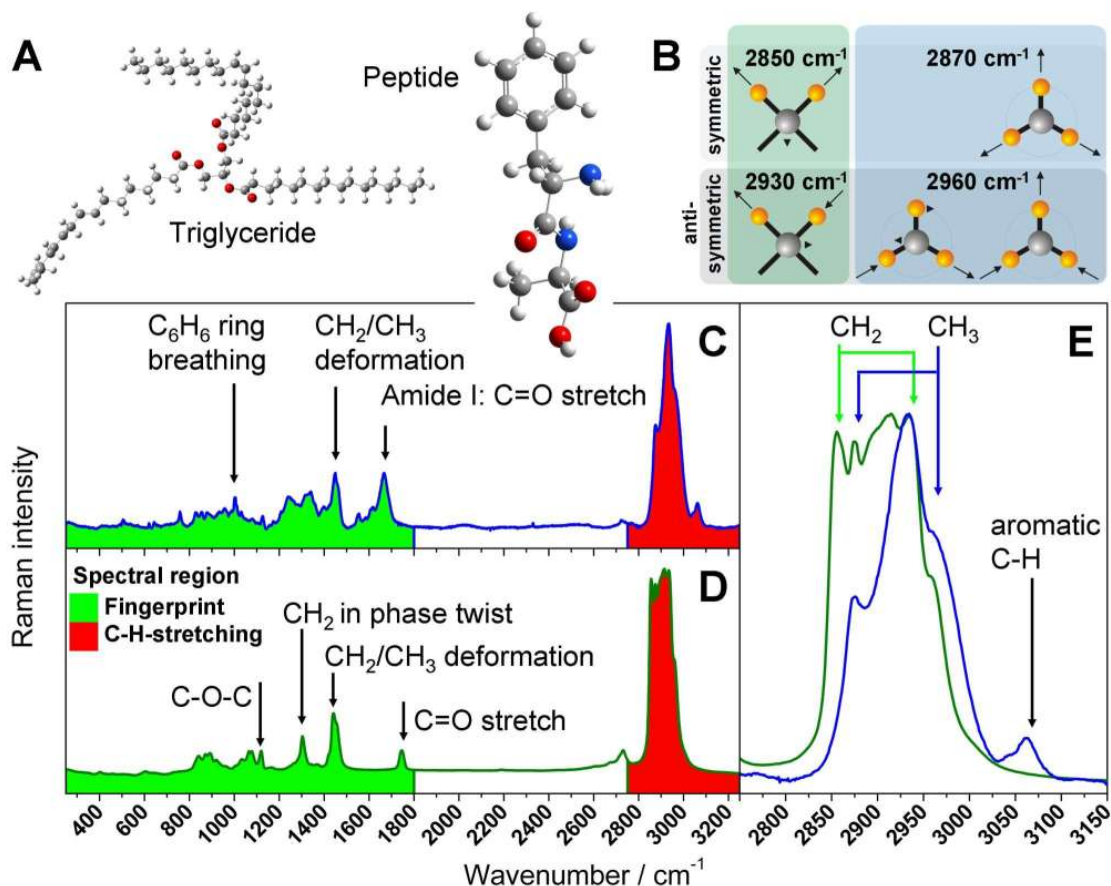


**Figure 3** – Structures (panel A) and Raman spectra of protein (panel C) and triglycerides (panel D), two highly abundant groups of biomolecules. The Raman spectrum is divided into the high wavenumber region marked in red, in which C-H, O-H and N-H stretching vibrations reside and the so called fingerprint region marked in green. The Raman spectrum in the fingerprint region is highly molecule specific, hence most useful for analysis. Intense vibrations are assigned to the respective functional group for both molecules, e.g., the C=O-stretch vibration of the peptide bond at  $1660\text{ cm}^{-1}$  or of the ester bond at  $1740\text{ cm}^{-1}$ . In CARS microscopy primarily the high wavenumber spectral region depicted in panel E is used for imaging due to the high signal levels. The characteristic CH-stretch vibrations of  $CH_3$ - and  $CH_2$ -functional groups are indicated in panel B.

One option to significantly enhance the Raman signal is to use the nonlinear analogue of the spontaneous Raman effect, one of the so-called 'coherent Raman' techniques. Several coherent Raman processes exist [39], e.g., stimulated Raman scattering (SRS), coherent Raman scattering and Raman induced Kerr effect (RIKE).



## 2. Multimodal Nonlinear Imaging

---

SRS [40], which can be either stimulated Raman gain (SRG) or simulated Raman loss (SRL), coherent anti-Stokes Raman scattering (CARS) [41] and Raman induced Kerr effect (RIKE) [42] have been employed for imaging. In this work focus will be on CARS only.

As TPEF, CARS is a third order nonlinear process, but requires illuminating the sample with two spatially and temporally overlapping laser pulses (see figure 2 panel D). When the frequency difference of both pulses matches the frequency of a Raman active molecular vibration, the molecules are coherently driven to vibrate in phase. This results in an intensity loss of the pump laser beam and gain of the Stokes laser beam. Further photons from the pump beam can be subsequently inelastically scattered from this coherent oscillations generating the CARS signal at the anti-Stokes frequency  $\omega_{CARS} = 2\omega_{pump} - \omega_{Stokes}$ .

The CARS signal intensity is both nonlinear in concentration as well as excitation intensity as displayed in equation 9, containing a term linear in number density  $N$  and a term quadratic in  $N$ .

$$I_{CARS} \propto \underbrace{|\chi_{CARS}^{(3)} + \chi_{nr}^{(3)}|^2}_{\propto N^2 + 2\chi_{nr}^{(3)}N} \cdot I_{pump}^2 \cdot I_{Stokes} \quad (9)$$

The nonlinear concentration dependence is detailed in chapter 12. Briefly, the nonlinear susceptibility  $\chi^{(3)}$  in the focal volume can be expressed using the number  $N_l$  of Raman active molecule of index  $l$  and their polarizability  $\alpha_a(\tilde{\omega})$  at the wavenumber position  $\tilde{\omega}$  :

$$I_{CARS}(\tilde{\omega}) \propto |\chi_{nr} + \sum_l N_l \alpha_l(\tilde{\omega})|^2 \quad (10)$$

This relationship is responsible for the term linear and quadratic in number density as indicated in equation 9. In order to compare spontaneous Raman and CARS, the CARS and Raman intensities can be rewritten according to [43] using the plane wave approximation as follows in terms of polarizability  $\alpha$  with respect to the vibrational

## Summary

---

coordinate  $Q$ , the wavevector  $k$  and the interaction length  $L$  in equation 11.

$$I_{CARS} \propto \omega_{CARS}^2 \cdot N^2 \cdot \left( \frac{d\alpha}{dQ} \right)_0^4 \cdot I_{Pump}^2 I_{Stokes} L^2 \text{sinc}^2 \left( \frac{\Delta k L}{2} \right) \quad (11)$$

$$\leftrightarrow I_{Raman} \propto \omega_S^4 \cdot N \cdot \left( \frac{d\alpha}{dQ} \right)_{Q=0}^2 \cdot I_0 \quad (12)$$

Due to the nonlinear concentration and intensity dependence as displayed in equation 9 and 11 the signal intensity is orders of magnitude enlarged in comparison to spontaneous Raman spectroscopy [44, 45], when the phase matching condition is fulfilled. Therefore, in case of high laser intensities the significant enhancement of the CARS signal in comparison to spontaneous Raman signal enables video rate image acquisition [46] and sub- $\mu\text{s}$  pixel dwell times in contrast to 25 ms per pixel in spontaneous Raman imaging [47].

However, this applies to high concentrations only. In this case, a coherent enhancement of 500 for CARS microscopy has been estimated [48], while for low concentrations, e.g., below concentrations in the mM range, this advantage is generally lost [49]. A further difference to spontaneous Raman scattering is due to the fact, that in case of CARS only a part of the spectrum is excited, which is spectrally covered by the spectral width of pump and Stokes laser pulses, while the full spectral information is automatically obtained in spontaneous Raman spectroscopy.

In principle CARS microscopy can be applied to visualize any vibration, e.g., the symmetric  $PO_2^-$  stretch vibration of the DNA backbone at  $1090 \text{ cm}^{-1}$  [50, 51], or protein vibrations in the fingerprint spectral window, e.g., the amide I vibration at  $1660 \text{ cm}^{-1}$  [51]. However, CARS imaging is usually performed to image the aliphatic C-H-stretching vibration of methylene groups at  $2850 \text{ cm}^{-1}$  for the visualization of lipids [52, 53, 54]. This is due to the fact, that the C-H-stretching resonances are the strongest within the CARS spectrum enabling highest imaging speeds up to video frame rate [46]. Also this spectral region is suited to detect compositional changes connected to disease progression, as demonstrated for Raman spectroscopy [55, 56]. In contrast to SHG and TPEF which are in principle background free methods, in parallel to CARS a so called unspecific nonresonant background is generated, which

## 2. Multimodal Nonlinear Imaging

---

limits the available image contrast as illustrated in figure 2 panel E. Non Raman resonant four wave mixing processes generate this background. Hence, the CARS image contrast is therefore dependent on the ratio of resonant signal to nonresonant background. Longer wavelength excitation light is advantageous, since the four wave mixing process becomes resonantly enhanced, when the virtual scattering state is energetically close to an electronic absorption (see figure 2 panel E). Furthermore, the background depends on the concentration of absorbing molecules. In order to reduce the nonlinear background in CARS microscopy, several methods have been proposed: polarization sensitive detection (P-CARS) [57], time delayed probing (T-CARS) [58, 59], interferometric detection (I-CARS) [60] and epi-detection (Epi-CARS) [61]. However, all of them come at the cost of either complicating the experimental setup (I-CARS, P-CARS) or significantly reducing the signal intensity (P-CARS, T-CARS, Epi-CARS).

In general, CARS as another nonlinear imaging method is suited to visualize the spatial distribution of abundant marker molecules in tissue and can therefore complement SHG and TPEF.

**Table 1** – Summary of characteristic properties of SHG, TPEF and CARS imaging

<b>SHG</b>	<b>TPEF</b>	<b>CARS</b>
$\propto N^2$	$\propto N$	$\propto N^2$
$\propto I_0^2$	$\propto I_0^2$	$\propto I_{pump}^2 \cdot I_{Stokes}$
$\tilde{\omega}_{SHG} = \sqrt{2}\Delta\tilde{\omega}_{Laser}$	$\Delta\lambda_{TPEF} \sim 50 \text{ nm}$	$\Delta\tilde{\omega}_{CARS} \sim 2 - 20 \text{ cm}^{-1}$
$\Delta\vec{k} = 0$	-	$\Delta\vec{k} = 0$
coherent	incoherent	coherent
directional	isotropic	directional
scattering	absorption	scattering
no bleaching	photobleaching	no bleaching

Table 1 summarizes characteristics of the beforehand described multimodal nonlinear microscopic imaging methods SHG, TPEF and CARS, which are relevant for

clinical diagnostics. In table 1, the following notation is used:  $N$ , number of marker molecules in the focal volume,  $I_0$  - intensity of the excitation laser,  $\tilde{\omega}_{Laser}$  - spectral width of the excitation laser,  $\Delta\lambda_{TPEF}$ -spectral width of TPEF emission,  $\Delta\vec{k}$  - phase mismatch.

Detailed examples of biomedical applications of multimodal imaging are introduced in the next section and described in depth in the respective articles [Meyer et al. 2011], [Meyer et al. 2013], and [Meyer et al. 2013 a].

## 2.2 The Optimal Parameters for Multimodal Imaging of Tissue

Even though the three imaging modalities TPEF, SHG and CARS are based on nonlinear effects, which can be excited by high intense ultrashort pulses, the requirements on characteristics of this pulsed laser are different for the three modalities. Therefore, in the following it is briefly discussed, which parameters, e.g., spectral resolution, are best suited in order to allow for simultaneous efficient excitation and detection of all three nonlinear signals. Furthermore, it will be briefly discussed, which optical properties of the sample, i.e., human or animal tissue, have to be taken into account in order to enable high quality tissue imaging in terms of spatial resolution and depth penetration.

The most important parameter for imaging is the excitation wavelength, which determines, e.g., the spatial resolution and depth penetration. According to Abbe's equation (equation 13) the spatial resolution is determined by the wavelength.

$$d_{min}^{xy} = \frac{\lambda}{2n \sin \alpha} \Leftrightarrow d_{min}^z = \frac{n\lambda}{NA^2} \quad (13)$$

In equation 13  $d_{min}^{xy}$  is the lateral resolution,  $d_{min}^z$  is the axial resolution,  $NA = n \cdot \sin \alpha$  is the numerical aperture of the microscope objective,  $n$  the refractive index. The depth penetration in tissue is limited at shorter wavelengths by scattering [62], which strongly increases with decreasing excitation wavelength [16], and in the near infrared (NIR) by onset of water absorption at roughly 1400 nm, which results in an optimal spectral window from 750 nm to 1400 nm for animal tissue

## 2. Multimodal Nonlinear Imaging

imaging depicted in figure 4. When using high NA objectives, sub- $\mu\text{m}$  spatial resolution is possible. The red and green curves in figure 4 represent the lateral, e.g.,  $d_{min}^{xy}$  and axial resolution, i.e.,  $d_{min}^z$  of a NA 0.4 microscopic objective. For TPEF

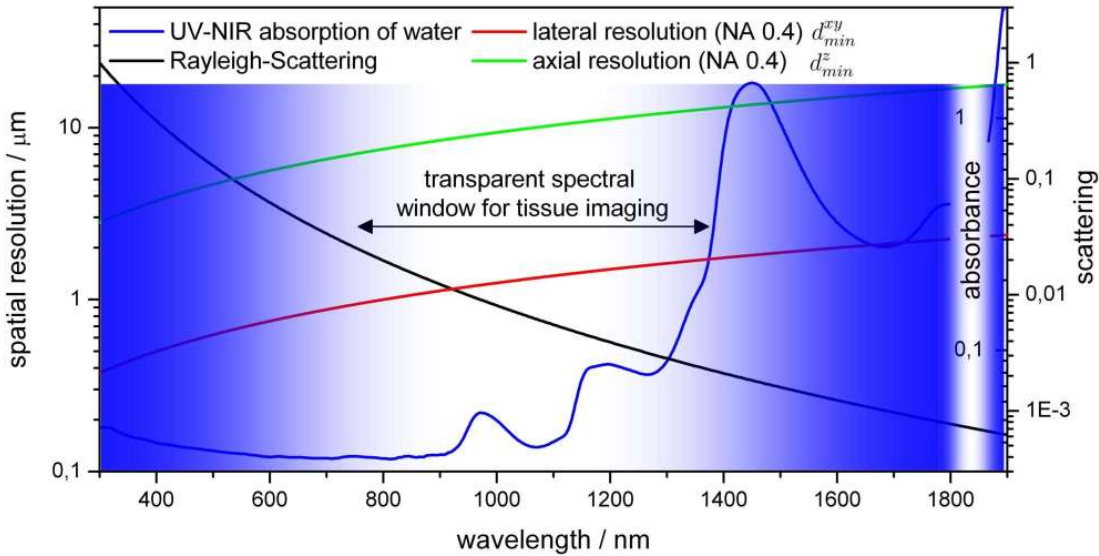


**Figure 4** – The absorption spectrum of water along with the wavelength dependence of Rayleigh scattering in the UV-NIR spectral range determine the most useful spectral window for imaging native tissue, which is in between 750 and 1400 nm as indicated. Furthermore, sub- $\mu\text{m}$  spatial resolution can be realized at high numerical aperture. The red and green curve describe the diffraction limited spatial resolution of an 0.4 NA objective.

excitation the wavelength of the illuminating laser needs to coincide with an electronic two-photon-absorption of endogenous fluorophores for efficient generation of autofluorescence signals. According to [24] approaching 1000 nm the TPEF cross sections of endogenous markers in tissue decrease rapidly. At 800 nm excitation of a selection of autofluorescing marker molecules, e.g., NADH, riboflavin and elastin, can be used, while excitation wavelengths below 800 nm significantly increase the fluorescence cross section of many marker molecules and allow detection of further fluorescing molecules [24]. Therefore, in order to use TPEF as contrast mechanism, the excitation wavelength needs to be below 1000 nm.

TPEF and SHG require a single excitation wavelength, while for CARS two wave-

## Summary

---

lengths have to be used. The following discussion of the effects of scattering and the optimal choice of excitation wavelength and intensity is restricted to CARS microscopy. In figure 5 panel A the CARS signal intensity is displayed as a function of the ratio of pump and Stokes intensity for different depths, e.g., at the surface, 100  $\mu\text{m}$  and 1000  $\mu\text{m}$  in the tissue and for three excitation wavelength sets taking into account the wavelength dependent scattering exemplarily for human skin [63, 64]. Even though the intensity at the surface is reduced for longer wavelength excitation due to the excitation frequency dependence, scattering reduces the excitation light intensity with depth exponentially. Hence while at the surface the pump and Stokes wavelengths of 670 and 830 nm produce twice the signal in comparison to 1000 and 1400 nm, 1 mm deep in the tissue the signal of the pump and Stokes at 1000 and 1400 nm produces a 70% stronger signal. However, the total amount of generated signal is reduced to 8.6% of the signal at the surface at 1 mm depth.

The optimal ratio of pump to Stokes intensity for thin samples is 2, corresponding to the peak of the plot shown in figure 5 panel A. For this intensity ratio at constant total intensity the maximal CARS signal is generated. However, since the shorter wavelength pump laser is stronger affected by scattering than the Stokes laser, the optimal intensity ratio increases with depth and decreases with wavelength as illustrated in figure 5 panel B for a depth of 1 mm. The optimal intensity ratio is 3.3 for pump and Stokes laser at 670 nm and 830 nm, while it is 2.7 for pump and Stokes laser at 1000 nm and 1400 nm.

A further difference when exciting TPEF and CARS signals results from the different spectral widths of vibrational and electronic resonances. According to [24], the two-photon absorption of autofluorescing markers are spectrally broad, i.e., in the range of 700 to 1000 nm exceeding 50 nm spectral width, which corresponds from 700-750 nm to 950  $\text{cm}^{-1}$ , while Raman resonances are spectrally narrow, e.g., few  $\text{cm}^{-1}$ . The desired spectral resolution restricts the minimum pulse duration according to the time-bandwidth product, equation 14. For a Gaussian laser pulse the time bandwidth product is given by:

$$0.44 \geq c_0 \cdot \Delta\tilde{\nu} \cdot \tau \quad (14)$$

## 2. Multimodal Nonlinear Imaging

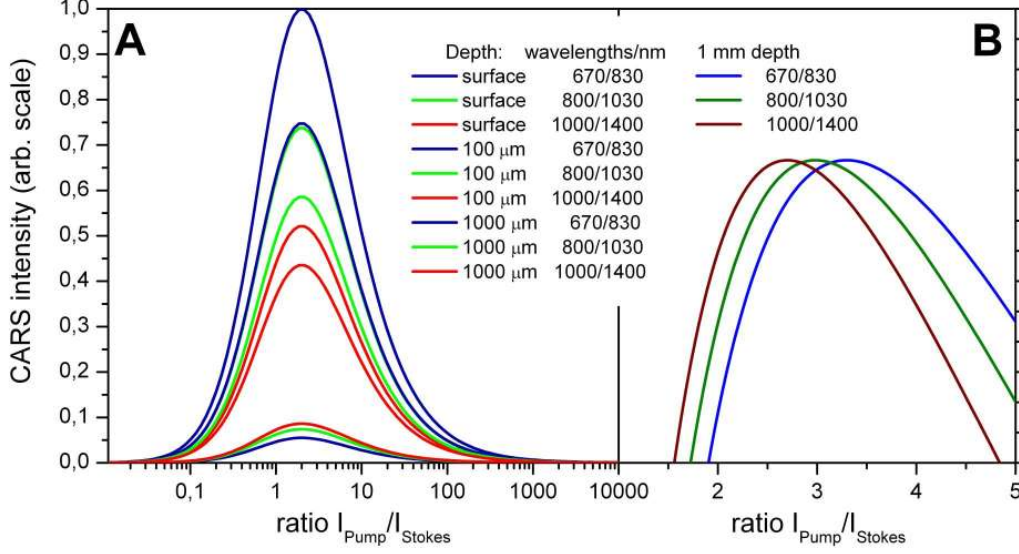


**Figure 5** – Graphical visualization of optimal parameters for CARS imaging of tissue. Panel A: Comparison of the CARS signal intensity at the surface, 100 and 1000  $\mu\text{m}$  deep in the tissue for three wavelengths sets for imaging the aliphatic C-H-stretching vibration of methylene groups at  $2850\text{ cm}^{-1}$ , i.e., pump/Stokes wavelengths 670 nm/830 nm (blue), 800 nm/1030 nm (green) and 1000 nm/1400 nm (red), as a function of the intensity ratio of pump/Stokes laser. Neglecting scattering, the optimal intensity ratio is 2, generating at constant power maximal CARS signal. Panel B: when scattering during penetration is considered, due to larger losses of the pump laser beam, a larger ratio of pump-to-Stokes laser is required, e.g., 2.7 for 1000 nm/1400 nm and 3.3 for 670 nm/830 nm for largest CARS signal at constant power 1000  $\mu\text{m}$  in the tissue.

Thus, in order to realize  $1\text{ cm}^{-1}$  spectral resolution for high contrast CARS microscopy, the pulse duration is  $\tau = 15\text{ps}$ . Further limits confine the maximum average power below the linear damage threshold, while the peak power needs to be on the order of several 100 W for efficient excitation of nonlinear processes. The average power  $P_{av}$  depends on laser repetition rate  $\nu_{\text{Laser}}$ , peak power  $P_{\text{peak}}$  and pulse duration  $\tau$  as follows:

$$P_{av} = P_{\text{peak}} \cdot \tau \cdot \nu_{\text{Laser}} \quad (15)$$

For imaging with a NA 0.4 objectives, average powers of 30 mW are safe, while peak powers of 500 W are required to excite the nonlinear processes. When a spectral resolution of  $1\text{ cm}^{-1}$  is required, the repetition rate is 4 MHz at a pulse duration of

15 ps, which is not usual for current laser sources.

In summary, the optimal parameters for multimodal nonlinear imaging of human tissue with high spectral resolution using simultaneously TPEF, SHG and CARS are wavelengths of 800 nm for the pump and 1030 nm for the Stokes laser, emitted at 4 MHz repetition rate with 15 ps pulse duration. The three nonlinear imaging methods SHG, TPEF and CARS use different molecular properties and therefore also complementary molecular markers. Thus the combination of SHG, TPEF and CARS termed "multimodal imaging" enables direct label-free visualization of the tissue structure and composition, i.e., the morphochemistry of the specimen.

## 3 Applications

This section summarizes applications of multimodal nonlinear imaging to the investigation of morphological as well as compositional changes connected to disease progression. The results presented have been partially published. The work on brain tumor imaging can be found in [Meyer et al. 2011], results from investigating tumors of the head and neck are integrated in [Meyer et al. 2013] and imaging of atherosclerosis is described in [Meyer et al. 2013 a].

In order to prove multimodal nonlinear microscopy a valuable clinical imaging tool, e.g., for routine screening, (1) the method needs to be safe and nontoxic, (2) multimodal nonlinear image data need to provide information on structural and compositional disease related changes for diagnostics.

### 3.1 Phototoxicity

Preceding widespread clinical application the phototoxic effects of this analytic method need to be assessed, as performed in detail for TPEF microscopy [13, 14]. These results indicate, that different effects contribute to sample damage. The most prominent damage process depends in detail on the laser parameters, e.g., wavelength, pulse duration, peak and average power. According to Hopt et al. [14], safe imaging conditions are peak intensities of  $750 \times 10^{12} \text{W/m}^2$ , which has been determined for a laser of 82 MHz repetition rate, 3 mW average power, 190 fs pulse



duration at 830 nm focused by a NA 0.9 objective. Therefore, in order to evaluate the potential of multimodal nonlinear microscopy as a clinical imaging tool, the photodamage of the specimen needs to be investigated for the laser parameters, which suit the envisioned biomedical application, e.g., surgical guidance. Specifically, it is necessary to determine if sample integrity during measurements is ensured at the average and peak intensities required for generating sufficient signal photons to support the desired image acquisition speed.

Lasers are already routinely used in surgery, e.g., head and neck surgery [65], but not yet applied to routine diagnostics. Thus, suitable imaging parameters for non-invasive routine imaging with no or minimal side effects have to be defined. In addition to phototoxicity studies performed for TPEF as the most commonly used nonlinear imaging modality, also for the CARS process phototoxicity studies have been performed [66, 15]. Scattering based methods such as CARS and SHG are less damaging than TPEF, since no electronic absorption process is involved. However, also in case of CARS the damage threshold is reduced by a factor of 2 when imaging in resonance with a Raman active molecular vibration [15]. Since CARS does not deposit any energy in the material as depicted in figure 2 panel D, other nonlinear processes contribute to the Raman resonant photothermal damage, e.g., SRS. SRG and SRL transfer up to 0.02% of the incident energy to the material [15]. However, at moderate power levels damage occurs only, if the laser is focused to a diffraction limited spot in the specimen for several seconds, while the typical exposition time in a CARS imaging experiment is only on the order of few  $\mu s$ . Therefore, it can be concluded, that at moderate power levels, e.g., few 10 mW at the specimen utilizing an excitation laser operating in the NIR spectral range and for pixel dwell times commonly used, i.e., on time scales of up to few ms, phototoxic effects are insignificant.

## 3.2 Comparison with the Golden Standard

In order to prove multimodal nonlinear imaging useful in biomedical applications, e.g., for surgical guidance and non invasive histopathologic examination of tissue, the methods capabilities for visualization of tissue morphology and composition need

## Summary

---

to be investigated and compared to the golden standard of staining histopathology for evaluation.

In this respect the capabilities of multi-contrast microscopy have to be characterized according to the following criteria:

- Comparison of visualization of tissue architecture with the golden standard of staining histopathology, i.e., morphological characteristics on the scale of tissue architecture, e.g., structure and shape of tissue layers, visualization of tissue boundaries, determination of cell density and ordering.
- Comparison of the methods visualization capabilities for cytologic characteristics, e.g., size and shape of single cells and cell compartments, e.g., cell nuclei.
- Evaluation of the basis of label-free contrast for the discrimination of diseased tissue with respect to benign tissue in order to understand the molecular origin of image contrast and evaluate, if such information provides additional insight in the process of disease progression.

Since the whole field of histopathology is beyond the scope of this short introduction, again focus will be on a few examples, namely head and neck squamous cell carcinoma (HNSCC), brain tumors and cardiovascular diseases (CDV) with emphasis on atherosclerosis.

The size scales relevant to histopathologic imaging ranges from sub- $\mu m$ , the size of bacterial cells and cell organelles like mitochondria, to the macroscopic extension of the specimen of some cm as schematically depicted in figure 1 in addition to relevant structures. Nonlinear microscopy perfectly fits histopathologic application, since it enables visualization of structures in the relevant size range from 300 nm up to few mm. Hence, the full range of sizes is accessible, apart from very tiny structures, e.g., viruses, single (macro)-molecules, e.g., DNA bases or collagen fibrils, which are not resolvable.

But in addition to optically resolving small sized structures, the contrast for visualizing these structures with respect to the surrounding matrix is even more important for clinical diagnostics. In this respect label-free multimodal nonlinear imaging provides high molecular contrast for a wide range of tissue structures.

## 3.3 Head and Neck Squamous Cell Carcinoma (HNSCC)

Visualization of the tissue morphology and structure is first illustrated for epithelial tissue of the head and neck with emphasis on the determination of structural changes related to the malignant transformation process, which is illustrated by H&E images of epithelium in different states of carcinogenesis in figure 6. The malignant transformation is manifested by characteristic morphological changes in tissue architecture and accumulation of cellular atypia, which increase with the grade of dysplasia or cancer.

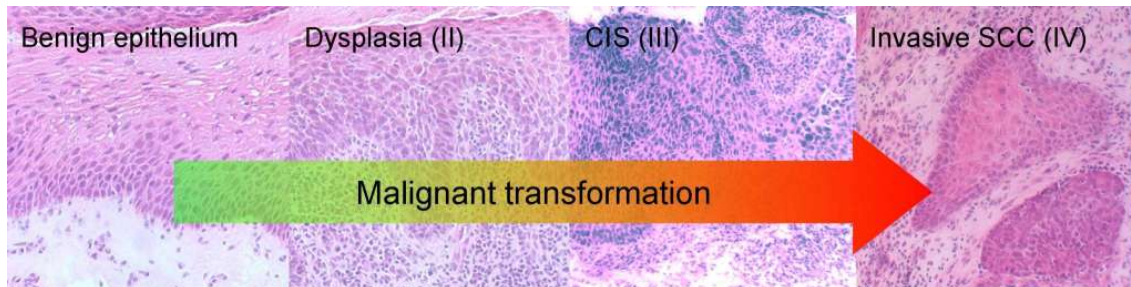


**Figure 6** – H&E stained tissue sections of normal epithelium, grade II epithelial dysplasia, carcinoma in situ (grade III) and squamous cell carcinoma (grade IV) representing the malignant transformation process. The carcinogenesis is accompanied by characteristic morphological changes driven by genetic modifications inducing changes in the chemical composition.

Benign epithelium is characterized by well differentiated epithelium starting from the bottom at the basal cell layer. Towards the top of the cell layer the cells orientation direction changes, the cells become thinner and lack nuclei. Cell division takes place in the basal cell layer only. Dysplastic epithelium is characterized by architectural changes, e.g., bulbous rete pegs, hypercellularity, altered maturation patterns of keratinocytes, keratin pearl formation, irregular epithelial stratification, loss of integrity of the basement membrane, lymphocyte infiltration, and cellular atypia, e.g., altered nucleus to cytoplasmic ratio, altered size and shape of cell nuclei, and multiple nuclei per cell [67]. If these changes are rare and affect the bottom third of the epithelium only, it is mild dysplasia (grade I), while if two thirds of the thickness are affected, the dysplastic grade is II. When the changes are frequent

## Summary

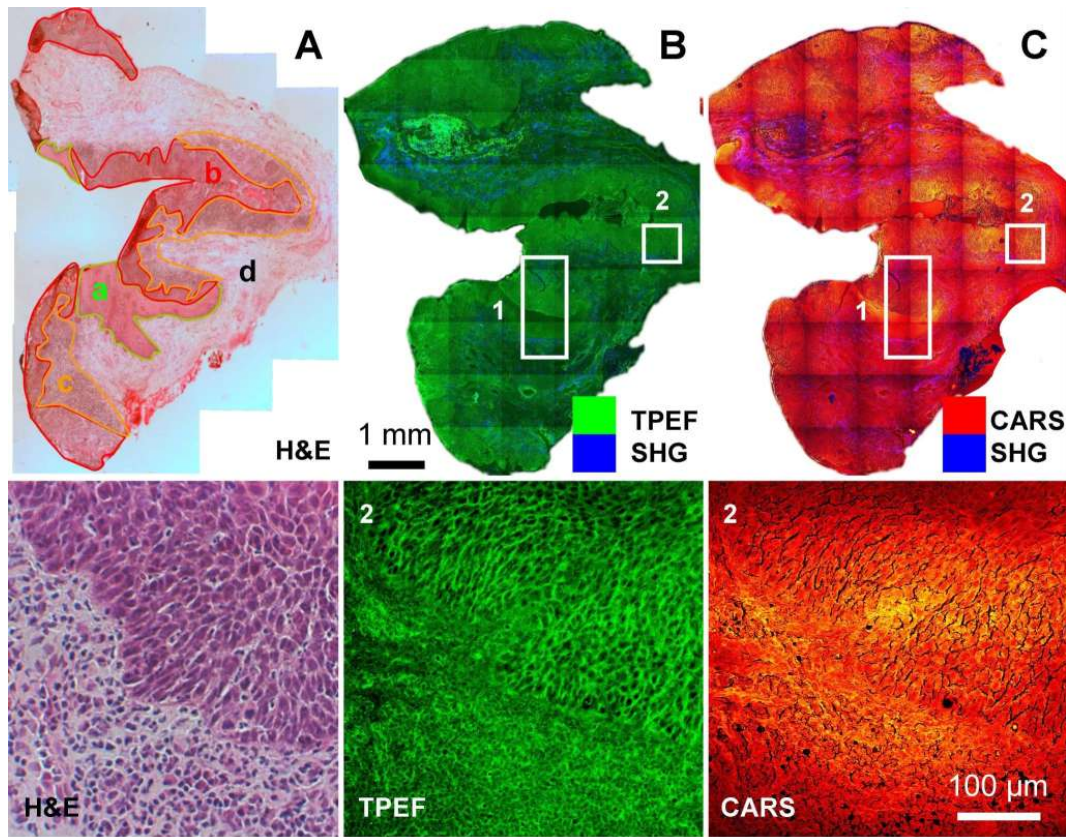
---

or affect more than two thirds of the thickness of the epithelium, the diagnosis is dysplasia grade III. Carcinoma in situ is the most severe form of dysplasia. Here tissue alterations are evident throughout the thickness of the epithelium, while the basement membrane towards the connective tissue is still intact. Breaking of cancer cells through the basement membrane is the hallmark for diagnosing squamous cell carcinoma.

In figure 7 H&E histologic images of a carcinoma of a laryngeal site (panel A) are contrasted to multimodal nonlinear images (panels B, C) of the parallel section. Since parallel sections are compared, the shape of the samples and the morphology differ in detail. However, in histopathology usually several parallel tissue sections are stained differently for diagnosis. Hence, the comparison of image data from parallel sections, as it is performed in this section, is a common procedure.

In the H&E stained image (figure 7 A) of a parallel section areas of different dysplastic grade are indicated: a - benign epithelium, b - dysplastic epithelium, c - inflammation of the connective tissue, d - connective tissue. The structures are also visible in the nonlinear images. The marked area 1 is depicted in detail in figure 8 displaying both normal and dysplastic epithelium, while region 2 is the transition region from dysplasia to inflammatory connective tissue. The lymphocytes have much smaller cell nuclei than epithelial cells, which is reproduced by TPEF imaging (figure 7 panel B 2) due to the NADH fluorescence, which provides negative nuclear contrast [68]. The cell and nuclei are visualized and the individual shapes are reproduced similar to the H&E image. The CARS image also shows the transition from connective tissue to epithelium, but single cells are only partially visible, e.g. in the healthy epithelium in figure 8 panel C.

In figure 8 benign and transformed, i.e. dysplastic, epithelium of a laryngeal site is displayed in detail. The upper image is the H&E histologic image of a parallel section (panel A), panel B and C are combinations of SHG and TPEF and SHG and CARS at  $2850\text{ cm}^{-1}$ . The differences in tissue architecture between benign and dysplastic epithelium are discernible in CARS-SHG and TPEF-SHG images, while differences in the size and shape of individual cells can be seen in the TPEF image. Single cells are only partially visualized by CARS in the healthy epithelium,



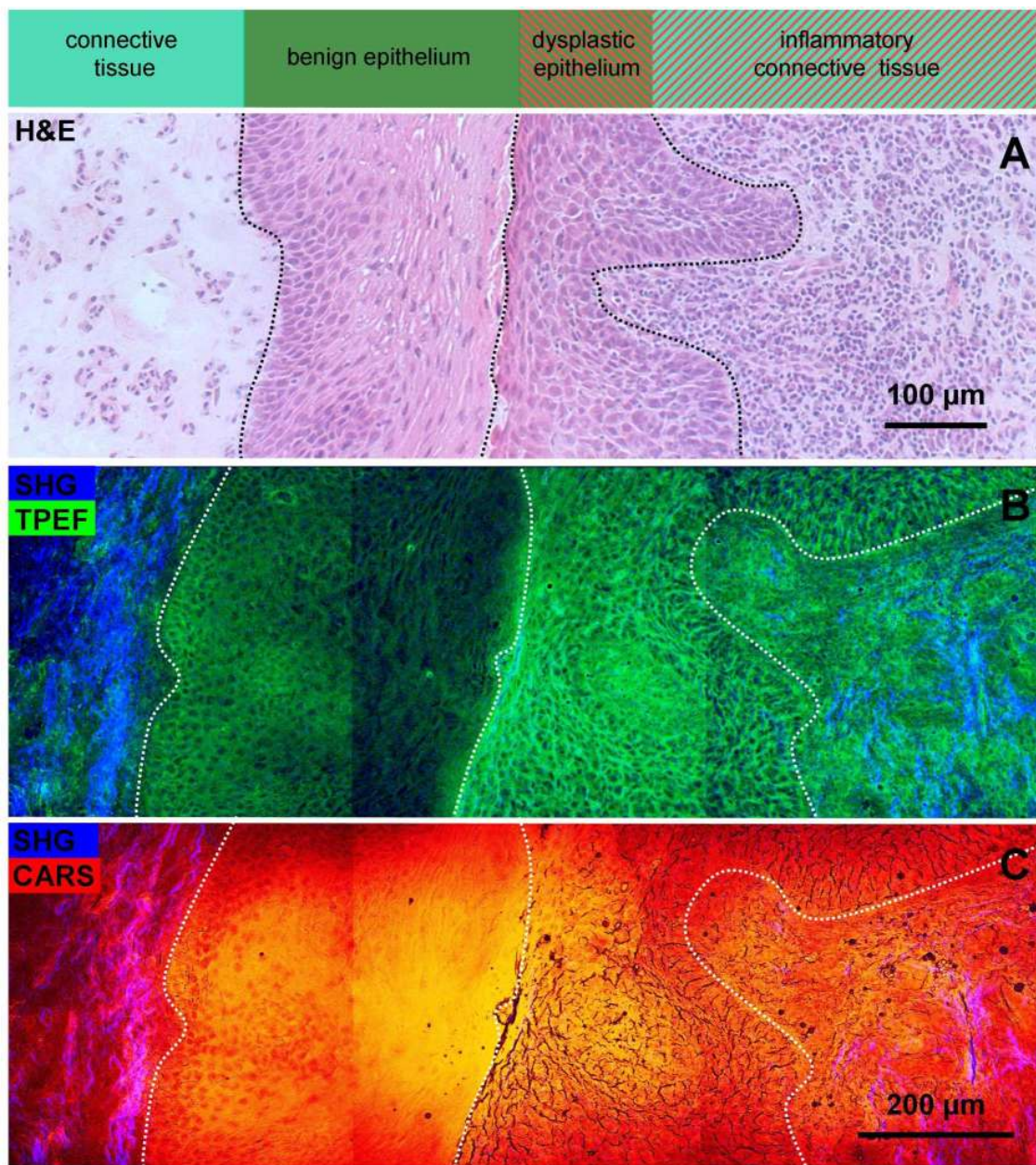
**Figure 7** – Histologic (A), and combined TPEF-SHG (B) and CARS-SHG (C) images of a HNSCC of a laryngeal site revealing the tissue architecture and characteristic morphological structures and disease related changes. In panel A areas of normal epithelium (a), dysplastic epithelium (b), inflammatory infiltrates (c) and connective tissue (d) are indicated. Area 1 is displayed in figure 8 in detail, while the transition region (2) from dysplastic epithelium to inflammation in the underlying connective tissue is displayed in the bottom row. The histologic images are taken from a parallel section.

figure 8 panel C. The shape of rete pegs as an architectural marker for dysplasia is reproduced by CARS and TPEF in figure 8 (panel B and C, right). Thus, the tissue boundaries are visualized by the nonlinear modalities. In particular SHG highlights the basement membrane (blue) and the ordering of collagen.

The connective tissue underlying dysplastic epithelium is characterized by high cell density due to inflammation, characterized by infiltration of lymphocytes (figure 8 panel B, right side). The layered structure of the dysplastic epithelium and the polarity of the basal cell layer is lost, and cytologic changes, e.g., altered nucleus to

## Summary

---



**Figure 8** – Comparison of the histologic H&E image of a parallel tissue section (panel A) and multimodal nonlinear images TPEF-SHG (B), CARS-SHG (C) demonstrating label-free visualization of characteristic morphological changes associated with the malignant transformation process, e.g., abnormal stratification, loss of polarity of basal cells, and altered nucleus-to-cytoplasmic ratio.

cytoplasm ratio as well as cell and nuclear size and shape are apparent. All these changes are invisible within the benign tissue on the left [69, 67]. Additional differences are evident from the nonlinear images: The autofluorescence of dysplastic epithelium and connective tissue is of higher intensity indicating higher NAD(P)H concentration and, therefore, higher metabolic activity in agreement with fluorescence measurements [70]. In addition, the collagen displayed in blue is less ordered within the connective tissue underlying dysplastic epithelium indicating weakening of the basement membrane in case of dysplasia preceding infiltrative growth of the cancer, which is not reproduced by H&E staining and necessitates additional staining for protein fibers. The CARS signal is also changed in dysplastic epithelium and characterized by a reduced overall intensity. The lower signal intensity indicating lower lipid content does also hint at an increased metabolic activity in dysplastic tissue in agreement with the autofluorescence image.

An example for a cancer growing invasively into the connective tissue at an oropharyngeal site is displayed in figure 9 panels A-C. The H&E image of a parallel section depicted in panel A displays a tumor nest surrounded by epithelial and connective tissue with lymphocyte infiltrates. The nonlinear TPEF (green, panel B) and CARS (red, panel C) images enable similarly the detection of the tumor nest, while the enclosing collagen fibers of the connective tissue are highlighted by SHG. The cell nuclei are visualized by TPEF only.

Another characteristic of HNSCC is overexpression of keratin. Such keratin pearl formation is correlated with the prognosis of the cancer and as such an important finding. In figure 9 panels D-F a keratinized carcinoma of a hypopharyngeal location is displayed. Keratin is detected by nonlinear imaging as a dense fluorescing protein structure by colocalized intense CARS and TPEF signals [71, 72, 73]. The in depth description of the application of multimodal nonlinear imaging towards the investigation of HNSCC is presented in chapter 6 [Meyer et al. 2013].

In summary in case of HNSCC multimodal nonlinear microscopy combining SHG, TPEF and CARS allows in agreement with histologic H&E staining visualization of cell density, size and shape of individual cells and cell nuclei. Nonlinear imaging allows determining the polarity of the basal cell layer, and evaluating the smooth-

## Summary

---

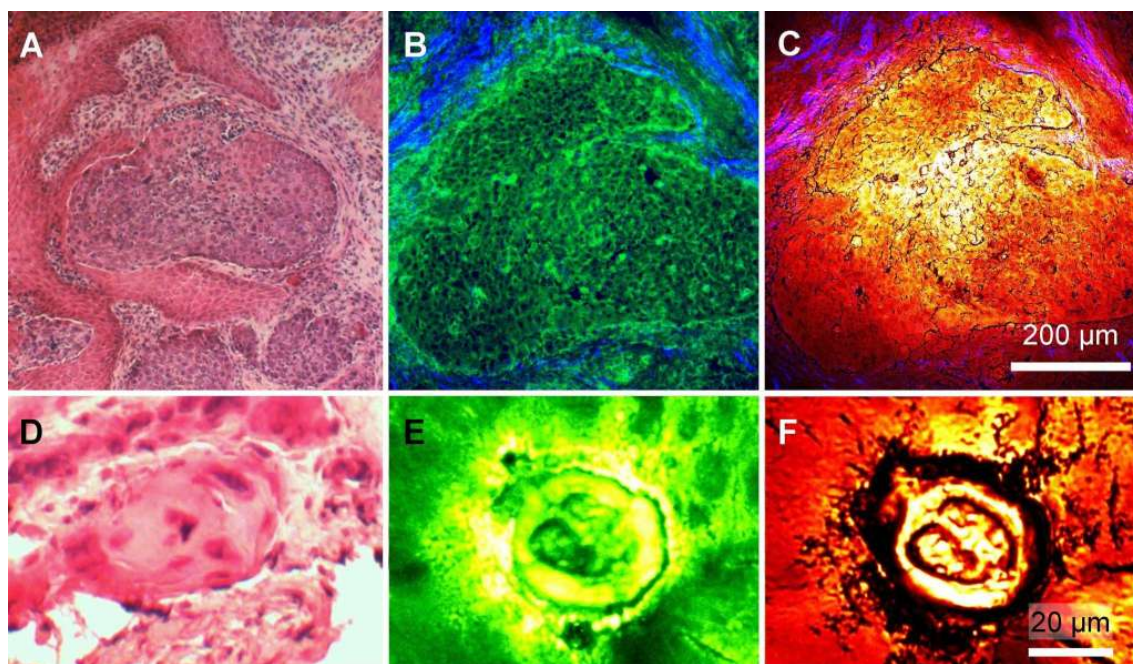


**Figure 9** – Comparison of H&E image of a parallel tissue section (A) and combined TPEF-SHG (B) and CARS-SHG (C) images of a tumor nest of an invasively growing HNSCC of an oropharyngeal site. TPEF visualizes the cell nuclei due to missing NADH autofluorescence, while SHG highlights collagen fibers of the connective tissue (blue). In panels D-E histologic H&E image (panel D) is compared to multimodal nonlinear images of a keratin pearl from a human keratinized carcinoma located in the hypopharynx. Keratin is visualized by TPEF fluorescence and high CARS intensity at  $2850\text{ cm}^{-1}$ .

ness of the basement membrane by visualizing the shape of rete pegs. Hence, the tissue architecture and many cytologic characteristics are reproduced. Some information retrieved by H&E staining is not accessible, e.g., mitotic figures and a greater affinity to haematoxylin called hyperchromasia due to the negative nuclei contrast. However, alternatively additional information on the molecular composition and metabolic activity is retrieved, which is not accessible by H&E staining, e.g., increased NADH fluorescence and decreased lipid content. Of particular importance is imaging the integrity of the basement membrane by SHG, which allows detection of cancer cells breaking through the membrane by SHG microscopy - the hallmark for diagnosing HNSCC.



#### 3.4 Brain Tumors

Even though the architecture and composition of the brain is significantly different from epithelium, also this organ can be imaged by multimodal nonlinear imaging as illustrated in figure 10 in case of the *cerebellum* of a domestic pig, *sus scrofa domestica*. The histologic image of the parallel H&E stained section is depicted in figure 10 panel A, while the label-free combined TPEF-SHG-CARS image is displayed in panel B. SHG (blue) particularly highlights the arachnoid membrane enclosing the brain due to the high collagen content, while CARS (red) highlights the axons wrapped in myelin sheath, which is composed of protein enriched with lipids. TPEF on the other hand can be used to locate the cells by their NAD(P)H fluorescence providing negative contrast for the detection of cell dense areas, e.g., the granule layer. The region marked by a white rectangle is enlarged in panels C and D showing the distinct layers of white and grey matter, which is subdivided into the cell dense granule layer, the layer of the larger Purkinje cells and the molecular layer containing only few cell bodies, as depicted and labelled in panel C. The nonlinear image in panel D visualizes the structure differently. CARS at  $2850\text{ cm}^{-1}$  enables detecting the white matter rich in lipids. The TPEF signal is lowest in the white matter and higher in the grey matter, providing negative contrast at the locations of cell nuclei for the detection of the granule cell layer. SHG finally highlights the arachnoid membrane, but also from the white matter and blood vessels signals are generated. This demonstrates, that the three imaging modalities TPEF, SHG and CARS add complementary information allowing analyzing the structure of brain tissue label-free.

This holds true also in case of human brain tissue, which was derived from the "normal" boundary of a brain tumor sample and therefore predominantly benign, as displayed in figure 11. By comparing the H&E image (panel A) with TPEF (B) and CARS image (C), several structures are detected: a small haemorrhage (1), cell nuclei (2), axons (3) and cholesterol crystals (4). Cholesterol crystals and axons are only detected by SHG and CARS, while the crystals are removed during the staining procedure. But also molecular and structural changes related to disease progression can be visualized as illustrated in figure 12. Brain tumors are categorized according

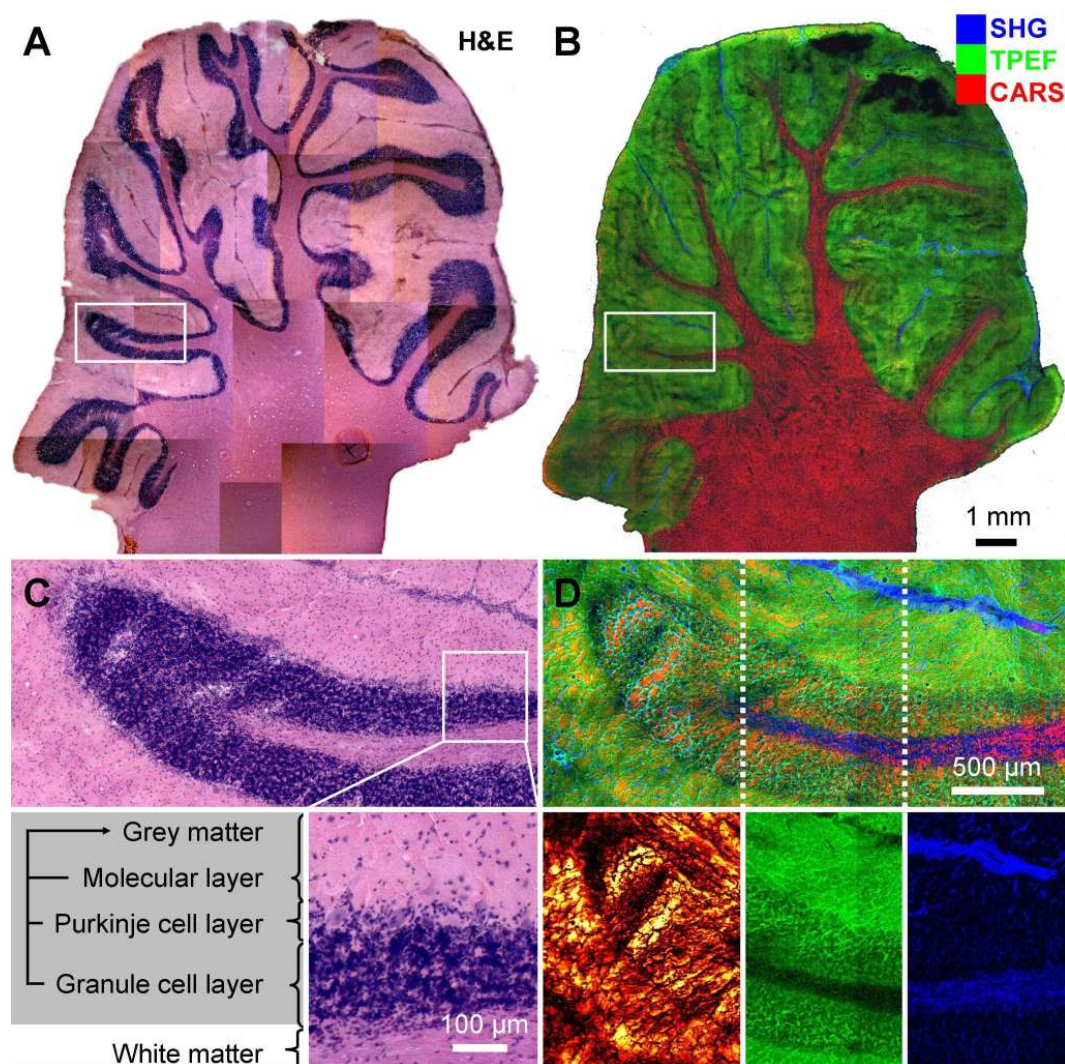


**Figure 10** – Comparison of an H&E stained (panel A) and a combined SHG-TPEF-CARS image at  $2850\text{ cm}^{-1}$  (panel B) of the *cerebellum* of a domestic pig (*sus scrofa domestica*) proving the capability of nonlinear microscopy to image large specimen label-free with high contrast comparable to staining histology. The marked region is enlarged in panels C and D proving discrimination of major morphological structures, e.g., white matter and granule cell, Purkinje cell and molecular layer of the grey matter, as indicated in the inset of panel C. The enclosing arachnoid membrane is bright blue (panel D). The complementary information of the three contrast mechanisms is visualized in panel D showing parts of the image for the single channels only, e.g., SHG highlights the membrane composed of collagen.

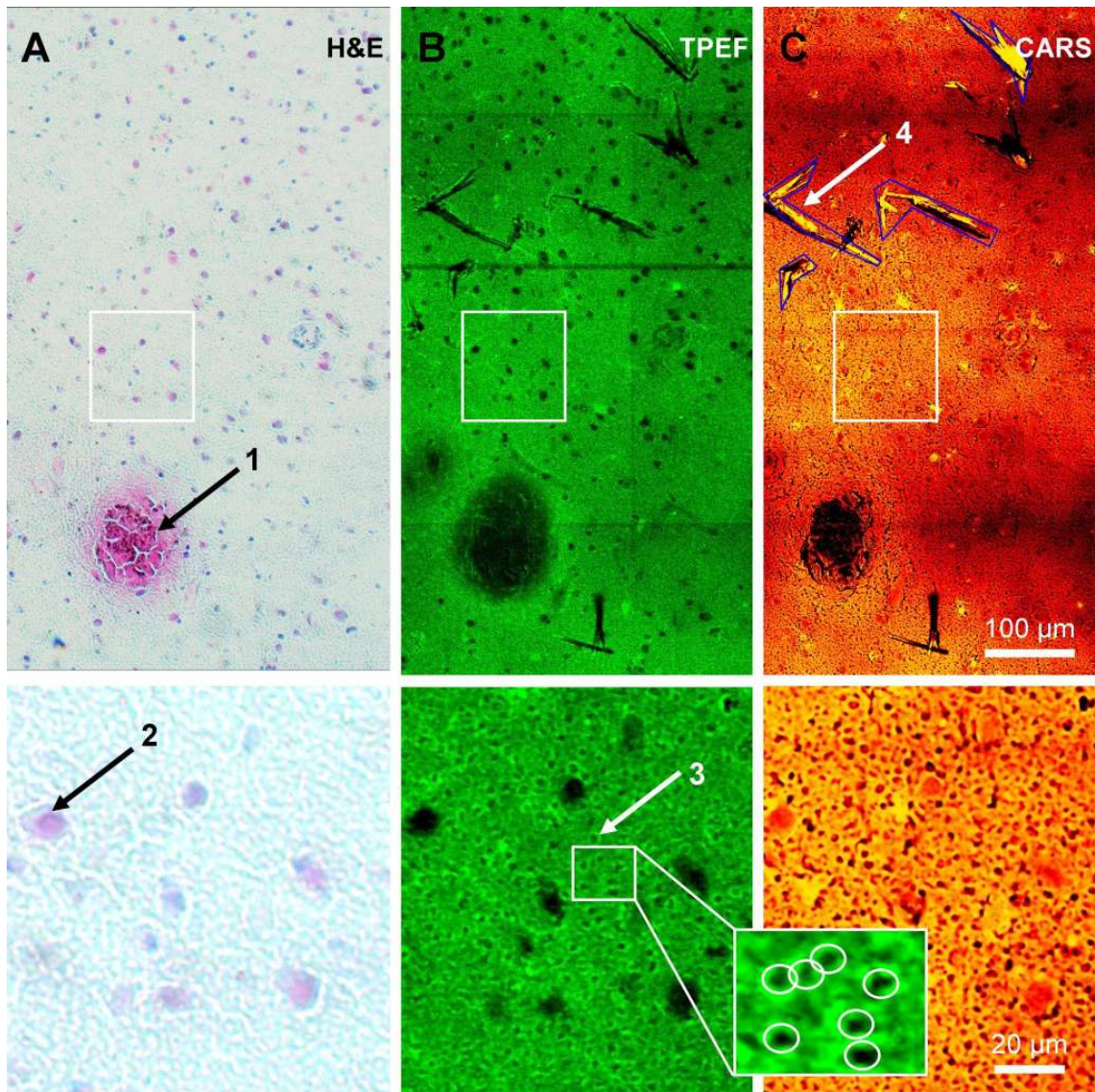


**Figure 11** – Comparison of histologic H&E images (panel A) with TPEF (panel B) and CARS images (panel C) at  $2850\text{ cm}^{-1}$  of human brain tissue demonstrating detection of haemorrhage (1), single cells and nuclei (2), and intersections of axons (3) and cholesterol crystals (marked blue) (4). The marked region in panels A-C is enlarged in the second row to improve the visibility of axons and cells, a part of the TPEF image is enlarged in the inset to display the small feature of intersecting axons.

to their origin in primary and secondary tumors. The most common tumor entity in the group of primary tumors are gliomas (displayed in panel A-C of figure 12) [74].

## Summary

---

The group of gliomas has a particularly bad prognosis due to its infiltrative growth, hence complete removal is virtually impossible resulting in tumor recurrence. Lymphomas (panel D-F) are derived from lymphoid tissue, displayed in the second row of figure 12. The most common tumors in the brain are metastases. In the third row of figure 12 in panels G-I a brain metastasis of a squamous cell carcinoma located in the lung is depicted.

Early detection and as complete resection of the tumor as possible are important therapeutic targets. This, however, requires detection of tumor tissue characterized by higher cell density, different size and shape of cells and nuclei, and grading by characteristic structures, e.g., vessel proliferates and necroses.

The most common tumors in the brain are secondary tumors, e.g., metastases of cancers as displayed in panels G-I of figure 12. They originate in other locations than the brain. Eventually the primary tumor is unknown, hence detecting the originating tumor location by morphological characteristics of the metastasis would be highly improving the diagnosis and influence further treatment strategies for this group of patients. In case of the metastasis of a lung cancer displayed in figure 12 panel G-I. The solid tumor and satellite tumor nests are visualized by differences in autofluorescence and CARS signal. In particular, the tumor tissue is characterized by a lower CARS intensity at  $2850\text{ cm}^{-1}$  than the surrounding necrotic tumor tissue. [75]

Thus, the nonlinear images of brain tissue and brain tumor specimen demonstrate visualizing the architecture and cytologic characteristics, e.g., cell density, by concentration gradients of NAD(P)H highlighted by TPEF as well as lipids visualized by CARS within the tissue.

Therefore, multimodal nonlinear microscopy enables the visualization of normal brain structures and the detection of tumors in the brain [75] & [Meyer et al. 2011] as described in more detail in chapter 5.

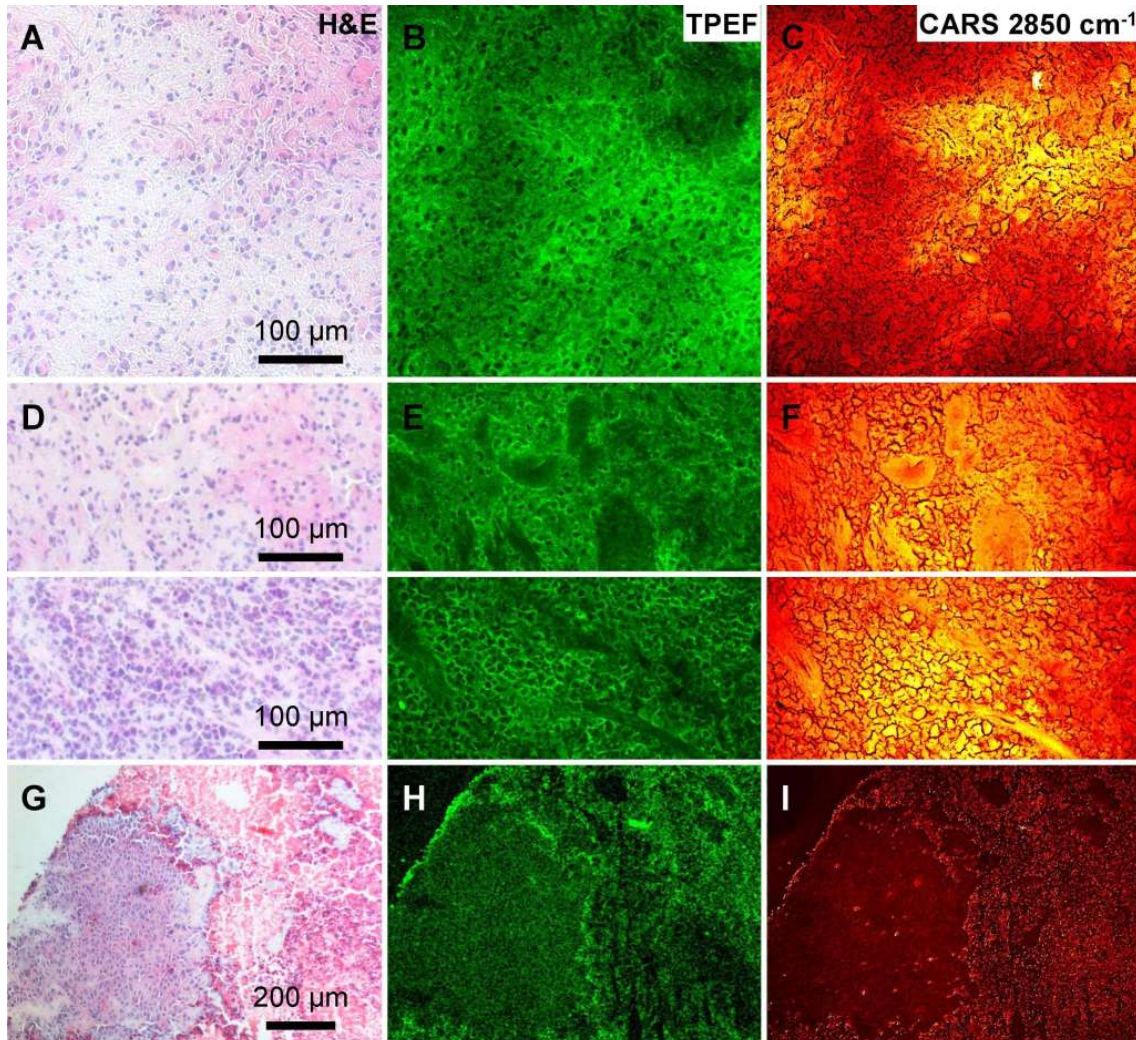


**Figure 12** – Comparison of histologic H&E with TPEF and CARS images at  $2850\text{ cm}^{-1}$  of malignant neoplasms in the brain demonstrating good correspondence of the label-free techniques with the golden standard H&E for visualizing the tissue morphology. In the first to third row the most common brain tumor entities are displayed, a glioma in the first row (A-C), areas of differing cell density of a lymphoma in the second row (D-F) and a cancer metastasis in the third row (G-I). Tumor nests of the lung carcinoma brain metastasis invade the surrounding brain tissue, panels G-I.

### 3.5 Cardiovascular Diseases (CVD)

While malignant tumors originate in modifications of the DNA, other prevalent diseases in the industrial nations are related to the metabolic syndrom, i.e., health risks associated with obesity and alterations in the lipid metabolism.

Multimodal nonlinear imaging and in particular CARS microscopy are powerful tools for lipid imaging [76, 53], not only as a clinical imaging tool, but also in fundamental research, e.g., to study the progression of macrophages to foam cells, which is involved in the process of atherosclerosis [77] and search for the genetic basis of the fat metabolism by investigating model organisms, e.g., *Caenorhabditis elegans* [78]. CARS enables label-free imaging of lipid droplets in macrophages depicted in figure 13 panels A-C with subcellular resolution. Autofluorescence and lipid droplets in the intestine of *Caenorhabditis elegans* are displayed in panel D. The worm's intestine is enlarged in panel E (white background) to display the lipid droplets more clearly.

In case of imaging cardiovascular diseases, different morphological structures and molecular markers are of interest as compared to cancer, hence the course of the disease is briefly summarized in the following to motivate, which structures are possible targets for imaging the disease progression. Cardiovascular diseases, with more than 40% the most common cause of death in Germany 2011 [6], are initiated as early as in the second or third decade of live, even though severe symptoms evolve usually much later in older patients [79]. Since this disease is particularly affected by the life style, e.g., risk factors include smoking, alcohol drinking, hypertension and hypercholesterolemia, i.e., a cholesterol rich diet and high body weight, the course of the disease can be significantly improved if the disease is recognized early. However, the detection of early atherosclerotic lesions is not trivial to accomplish. Just recently it has been realized, that atherosclerosis is not a lipid storage disease, but more appropriately characterized as a chronic inflammatory disease of the blood vessel walls [80]. In an early stage, atherosclerosis starts as a inflammatory process of the vessel wall initiated by infiltration of macrophages and T lymphocytes. Subsequently characteristic morphological changes are induced, e.g., wall thickening due to deposition and accumulation of lipids within the vessel wall.

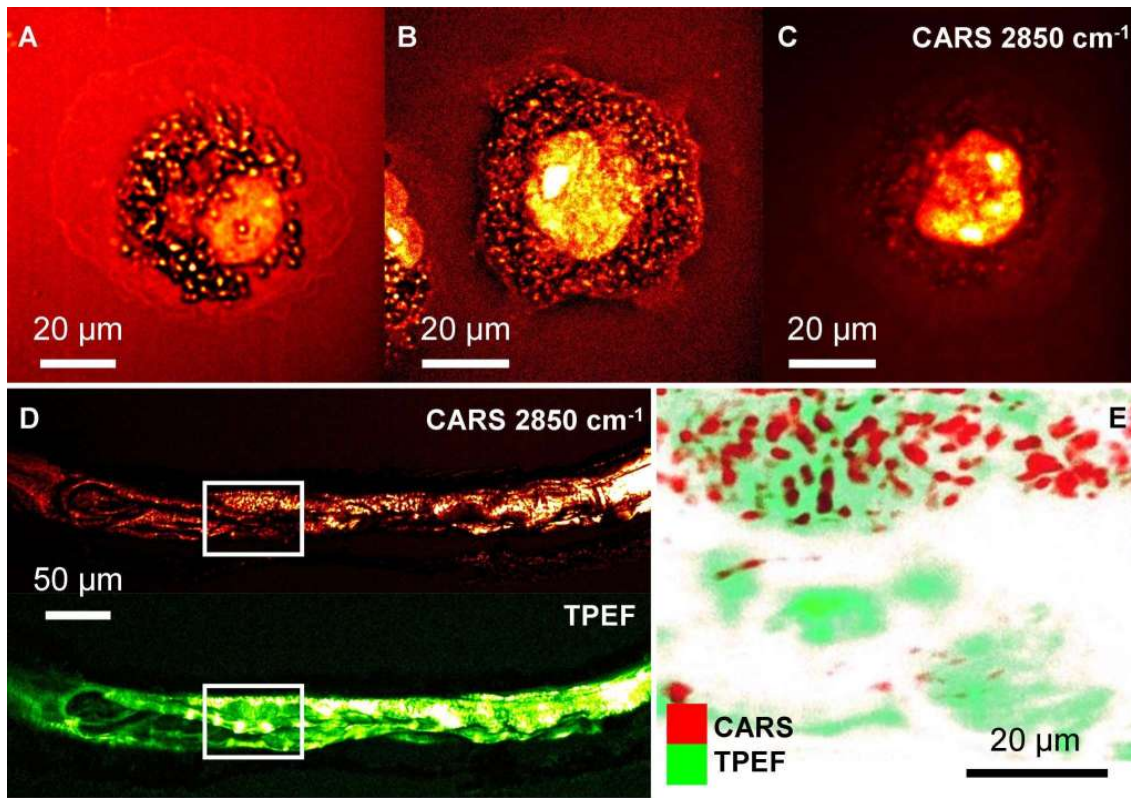


**Figure 13** – Imaging of model organisms for studying diseases related to the lipid metabolism. Panel A-C: Foam cell formation is implicated at an early stage of atherosclerosis. The lipid uptake of macrophages can be studied in detail by CARS microscopy at 2850 cm<sup>-1</sup> *in vivo*. Cell nuclei and lipid droplets are resolved. *Caenorhabditis elegans* is a model organism for studying the lipid metabolism, which can be investigated label-free by TPEF and CARS imaging, panel D. Single lipid droplets in the intestine are highlighted in red, panel E (white background) at larger magnification.

While in an advanced stage many vessels are affected by atherosclerotic deposits, only high risk plaques, so-called "vulnerable plaques" are surgically treated. Hence, the difficulty arises to detect the plaques, which are most likely to rupture causing acute events, e.g, thrombus formation. This risk of plaque rupture depends primarily on the plaque composition [79]. Characteristic structures of a high risk plaque, a thin-cap fibroatheroma (TCFA), include a fibrous cap thickness below 65 μm and a large necrotic or lipid core underneath the cap. Hence, in the following, multi-modal nonlinear imaging is applied to visualize characteristic structures, which de-

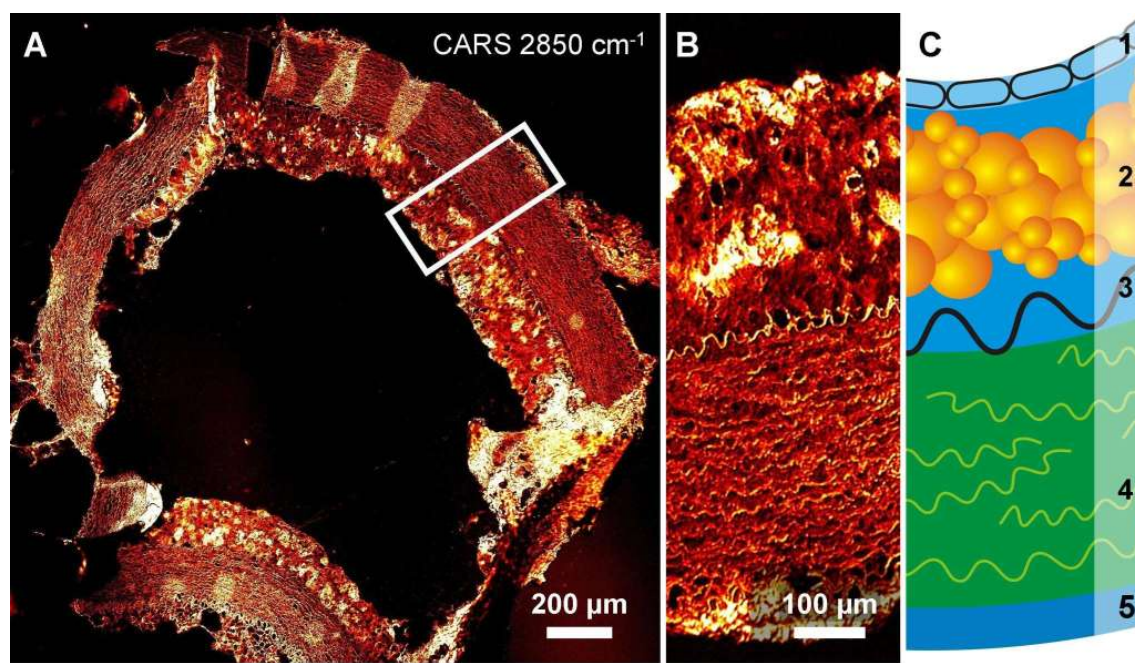


**Figure 14** – Panel A: CARS microscopic image of the cross section of a rabbits artery fed with a high cholesterol diet. Panel B: magnified area marked in panel A shows the structure of the artery as sketched in panel C: 1: endothelium, 2: atherosclerotic lipid deposit, 3: *elastica interna*, 4: *tunica media* composed of elastic fibers and smooth muscle cells, 5: *elastica externa*. (Panel A Reproduced by permission of The Royal Society of Chemistry)

termine the risk of atherosclerotic lesions. To investigate the plaque formation and structure an animal model is used. Rabbits fed with high cholesterol diet develop atherosclerotic lesions similar to humans and therefore allow studying the process of inflammation of the vessel wall initiating atherosclerosis and the plaque composition in detail. The cross section of an artery with plaque deposits is displayed in figure 14 panel A. The area marked by a white rectangle is enlarged in panel B of figure 14 and visualizes the morphology of the artery as illustrated in panel C. The innermost endothelium (1) separates the plaque (2) from the blood stream. Below the lipid deposition is a layer of elastic and collagen fibers, the *elastica interna* (3), followed by the *tunica media* consisting of smooth muscle cells and elastic protein fibers, which is enclosed by the *elastica externa*, rich in protein fibers.

While the artery architecture is visualized by CARS at  $2850\text{ cm}^{-1}$  only, SHG and TPEF add information on the molecular composition as illustrated in figure 15.



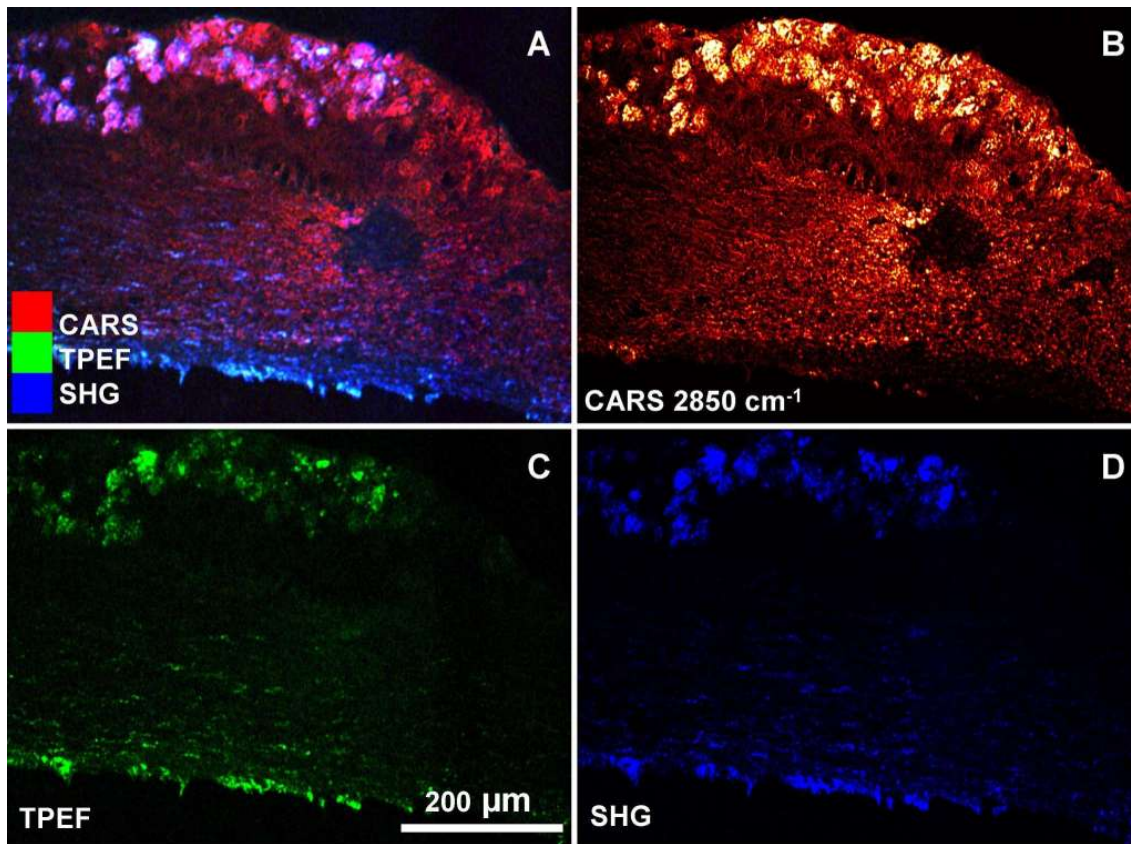


**Figure 15** – Multimodal microscopic image combining CARS at  $2850\text{ cm}^{-1}$ , SHG and TPEF for the visualization of a rabbit artery cross section to study the initiation of atherosclerosis (panel A). In panels B-D the separate channels are displayed. CARS allows visualizing the lipid component, while SHG highlights collagen and crystalline cholesterol. The TPEF emission is used to localize elastic protein fibers and oxidized fatty acids. Adapted with permission from the American Chemical Society, [dx.doi.org/10.1021/ac400570w](https://doi.org/10.1021/ac400570w).

The multimodal nonlinear image combining the SHG, TPEF and CARS displayed in panel A enables discrimination of the plaque, the *elastica interna* and *externa* and the *tunica media*. The single images are displayed in panels B-D. CARS at  $2850\text{ cm}^{-1}$  highlights the lipid deposits and visualizes the curly protein fibers in *elastica intima*, *externa* and *tunica media*. TPEF signals arise from the plaque and from the protein fibers. Fluorescence signals in lipid deposits have been assigned to oxidized lipids [81], while fluorescence in *tunica media* and *elastica interna* and *externa* is due to collagen and elastin [82]. The SHG signal from the protein fibers is due to colla-

## Summary

---

gen and actin-myosin of muscle cells [20], while signals in the plaque can also arise from crystalline cholesterol [21]. Thus, manifold information on plaque structure and composition, e.g., size, and shape of elastin, collagen and actin-myosin protein fibers, thickness and density of lipid deposits, the distribution of cholesterol crystals and oxidized lipids within plaque deposits are assessable by multimodal nonlinear microscopy.

However, discrimination of SHG and TPEF signals from different marker molecules emitted at the same signal wavelength is based on knowledge about the abundance of markers in specific tissue structures. By multispectral CARS imaging at multiple Raman resonances, however, precise assignment of the observed signals to the originating structure without additional knowledge is possible as illustrated in figure 16.

In figure 16 perivascular tissue is imaged by multispectral CARS- and SHG-microscopy. Periadventitial tissue surrounding the artery contains adipose tissue, nerves and smaller blood vessels as depicted in panel A. For comparison, the section has been subsequently stained with elastica van Giesons (EVG) staining for the visualization of elastic fibers and collagen. The histologic image is displayed in panel B of figure 16. The nonlinear and the histologic images display collagen fibers and a nerve bundle, which is magnified in panel C and lipid droplets and cytoplasm of adipocytes enlarged in panel D. Collagen fibers are highlighted by SHG and are better visualized in the nonlinear image than in the histologic image, as evident from panel D. Here partially strong SHG signal is observed, while there is no significant difference in the staining pattern discernible at the respective locations. The CARS image at two resonances,  $2844\text{ cm}^{-1}$  and  $2942\text{ cm}^{-1}$ , characteristic for  $CH_2$ - and  $CH_3$ -functional groups [83] allows for the discrimination of protein and lipid structures due to their different ratios of these functional groups. Thus, proteins appear bluish, while lipids, e.g., triglycerides in lipid droplets of adipocytes and the lipid rich myelin sheath, are depicted in green (panel C). Hence, CARS imaging at two spectral positions characteristic for  $CH_2$ - and  $CH_3$ -functional groups enables discrimination of lipids and proteins facilitating the assignment of fluorescence and SHG signals to protein and lipid structures.

Hence, also in case of imaging CVD requiring visualization of different morphologi-

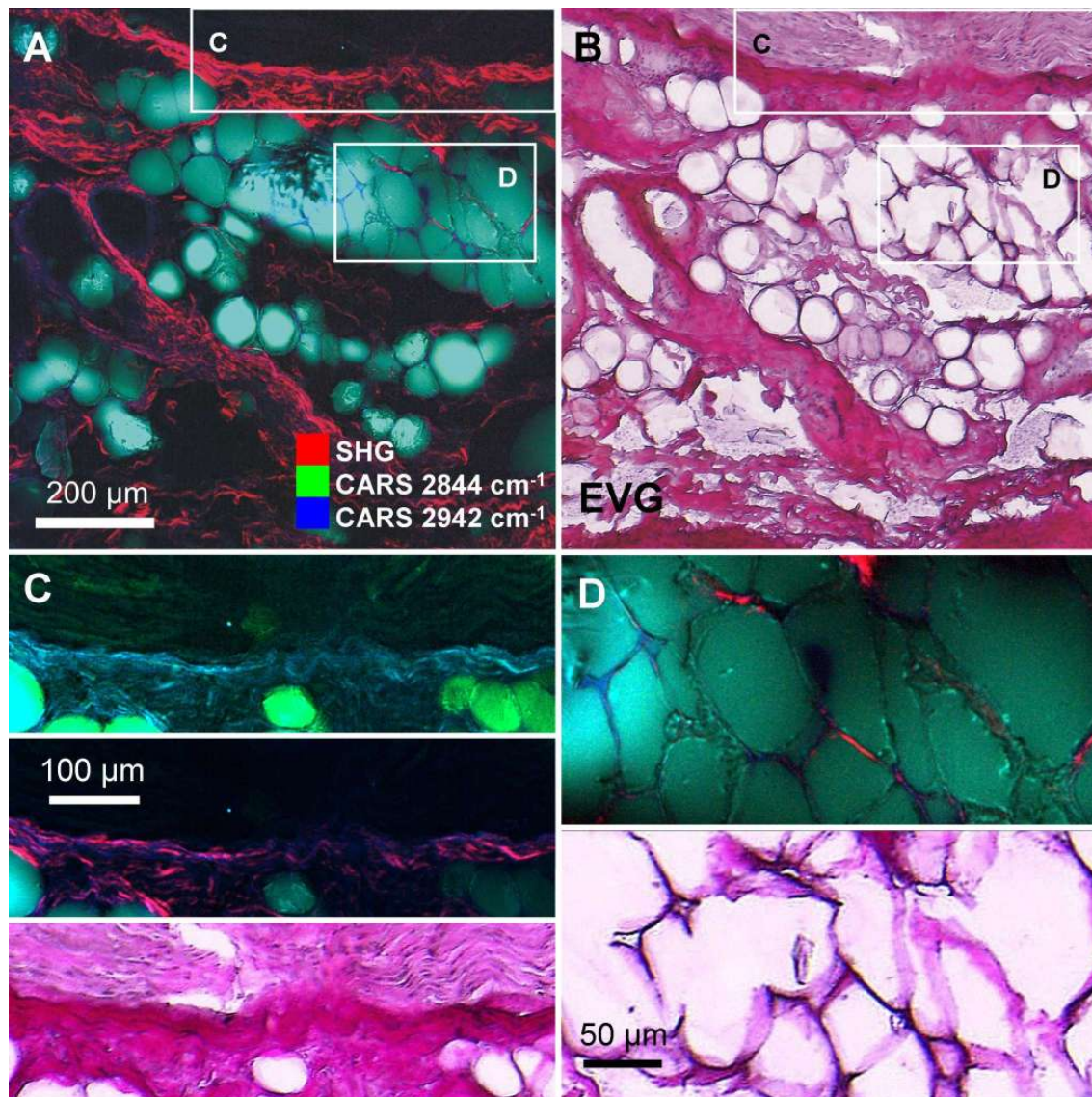


**Figure 16** – Multispectral CARS microscopy and SHG imaging of a human perivascular tissue specimen for a detailed insight in structure and composition of adipose tissue. To differentiate protein and lipid component, CARS images at two resonances characteristic for  $CH_2$ - and  $CH_3$ -functional groups at  $2844\text{ cm}^{-1}$  and at  $2942\text{ cm}^{-1}$  are superimposed in panel A (green and blue) together with SHG of collagen (red). The result agrees well with the EVG image in panel B. The marked areas are enlarged in panels C and D demonstrating visualization of myelin sheath (C), a lipid rich protein, lipid stores and the cytoplasm of adipocytes in the perivascular tissue (D).

## Summary

---

cal structures in comparison to cancer imaging, multi-contrast nonlinear microscopy visualizes the structure and composition of the arterial vessel wall and disease related lipid deposits.

In conclusion label-free multimodal nonlinear imaging provides molecular contrast based on the spatial distribution of endogenous markers as summarized in table 2 enabling visualization of structure and composition, i.e., the morphochemistry, of normal healthy tissue and disease related structural and chemical alterations in agreement with the golden standard of staining histopathology.

**Table 2** – Overview of marker molecules utilized for SHG, TPEF and CARS imaging.

SHG	TPEF	CARS
Collagen	NAD(P)H	Lipids, e.g.,
Actin-Myosin	Elastin, Collagen	Triglycerides, Cholesterol, Myelin
Crystalline	Keratin	Proteins, e.g.,
Cholesterol	Oxidized Lipids	Elastin, Collagen, Keratin

## 4 Compact Multi-Contrast Imaging Platform

Despite multiple studies have collected convincing data proving multimodal nonlinear imaging a powerful and versatile tool for biomedical diagnostics, application is still limited to fundamental research and has not yet arrived in clinics. This is due to the technical complexity of a state-of-the-art nonlinear imaging platform, which requires regular maintenance and is very sensitive to environmental changes, e.g., temperature fluctuations. Furthermore, the instrumentation is expensive, sophisticated to handle and space consuming, while an ideal biomedical imaging tool for routine diagnostics has to be facile to operate, compact, and rugged. Thus, translation of the methodology into clinical settings requires developing novel and more compact instruments. Thus, as illustrated in section 2, in order to optimize the signal generation efficiency and contrast for all three modalities, i.e., SHG, TPEF and CARS, for imaging of animal or human tissue, lasers of very specific characteristics, e.g., 15 ps pulse duration, 4 MHz repetition rate, 1 cm<sup>-1</sup> spectral resolution

## 4. Compact Multi-Contrast Imaging Platform

---

operating in the NIR spectral range of 800-1000 nm, are required.

Hence the following technical improvements need to be addressed:

- Development of a compact and robust microscope for biomedical imaging of native tissue enabling simultaneous detection of SHG, TPEF and CARS signals and optimized for use in combination with a low power pulsed NIR laser source. This requires specifically:
  - Reduced instrument complexity, e.g., minimal alignment
  - Optimized NIR transmission for using compact and low power lasers
  - Large field of view for fast imaging of mm-sized tissue samples at few seconds per frame and sub- $\mu\text{m}$  spatial resolution
  - Simple instrument control and acquisition of high quality image data
- Evaluation of compact tunable multicolour NIR-laser sources for optimized SHG-TPEF-CARS signal generation, depth penetration and spatial resolution at minimal sample damage for multimodal nonlinear microscopy according to the following requirements
  - Sufficient average and peak laser power at the specimen for efficient signal generation
  - Laser spectral tuning enabling multispectral CARS imaging
  - Optimal pump to Stokes power ratio 2:1
  - High spectral resolution for optimal CARS contrast
  - Minimal alignment, rugged, maintenance-free and compact instrument

Therefore, in this section a laboratory multimodal imaging platform is presented in order to highlight the modifications implemented into a compact imaging system adapted for application in clinics. Subsequently, results from testing compact fiber lasers for multi-contrast nonlinear microscopy are presented, which are in terms of the laser characteristics close to the before mentioned optimal parameter set. The presented results have been partially published in [Meyer et al. 2013 a], [Baumgartl et al. 2012], [Baumgartl et al. 2012 a], and [Chemnitz et al. 2012].

## 4.1 Compact Multimodal Nonlinear Microscope

In order to illustrate, that the equipment currently used for multimodal microscopy is not suited for use in clinical environment, a typical laboratory setup is depicted in figure 17. In panel A the setup is schematically sketched, while a photograph of the laser source is depicted in panel B. In particular high power ultrafast laser systems are sensitive to environmental changes, e.g., of temperature or vibrations and require additional equipment for cooling and power supply. Therefore, these lasers need to be installed on optical tables within climatised laboratories. In order

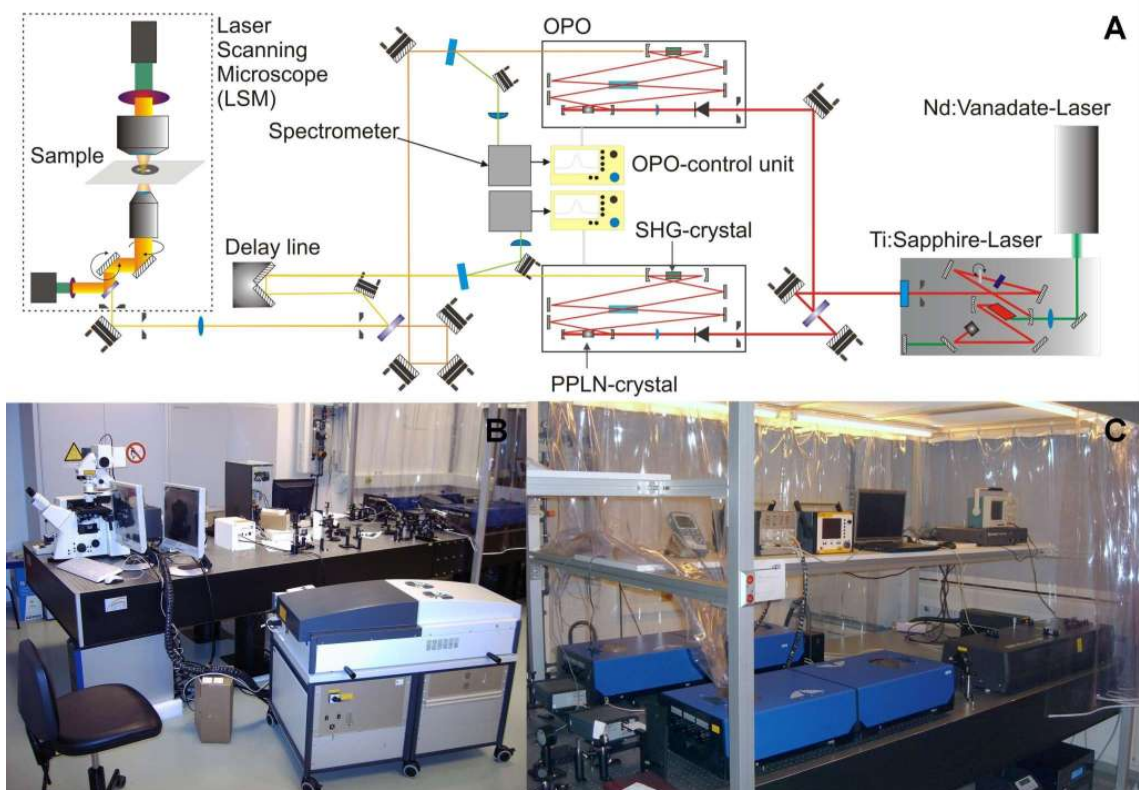


**Figure 17** – Sketch (panel A) of a laboratory setup for multimodal nonlinear imaging consuming significant space, e.g., 1.5 m x 6 m on an optical table, and power and requiring regular alignment due to long free space beam paths susceptible to temperature changes. Panel B: laser scanning microscope (left) including the electronic hardware and internal lasers in the large module (bottom right). In panel C a photograph of the laser system is depicted, showing the Ti:Sa-Laser on the right in grey and the OPOs in blue. For instrument control spectrometers and an oscilloscope are needed.

#### 4. Compact Multi-Contrast Imaging Platform

---

to illustrate the complexity of a laboratory nonlinear multimodal imaging platform, the system will be briefly described in the following. First, the whole setup requires a large laser table of  $1.5 \text{ m} \times 6 \text{ m}$  in a climate controlled laser lab for installation of laser scanning microscope and the three-stage laser system. The first stage of the laser consists of a water cooled 18 W Nd:Vanadate continuous wave laser (Coherent Verdi-V18) pumped by diode stacks, which is then used to pump a separately water cooled high power Titanium:Sapphire (Ti:Sa) laser (Coherent Mira HP) emitting up to 3 W of laser radiation in the range of 700 to 1000 nm with either 150 fs or 2 ps pulse duration. In order to force the laser to emit pulsed instead of continuous wave radiation, the Kerr lens mode locking effect of Sapphire is used. High peak intensities induce a change of the refractive index within the crystal, which focuses the high intensity part of the laser emission. In the plane of focus a slit is positioned. If the slit is narrowed, high losses are generated in the unfocused cw part of the laser emission, favouring pulsed operation. However, to stabilize the pulses, compensation of the group velocity dispersion is required. In the fs emission regime this is realized by a prism compressor, while in the ps-regime a Gires-Tournois-Interferometer is used. The emission is split to pump one or two optical parametric oscillators (APE), which generate by parametric conversion in a periodically poled Lithium niobate (PPLN) crystal NIR and IR radiation from 1000 nm to 1600 nm (signal-beam) and 1600 to 3200 nm (idler beam) of several 100 mW power. The pulse duration fits the length of the pumping laser pulse. By inserting a second crystal into the OPO cavity for temperature tuned phase matched second harmonic generation of the signal beam, visible radiation from 500 to 800 nm can be produced. Spectral tuning is realized by dispersion blocks in the OPO cavity, which induce temporal separation of the spectral components. Only the wavelength with the same round trip time in the OPO cavity as featured by the Ti:Sa laser is efficiently generated. The laser repetition rate is determined by the cavity length, hence a 76 MHz repetition rate corresponds to a 4 m laser cavity.

In order to perform CARS imaging, either the output of both OPOs or the output of one OPO and the Ti:Sa pump laser are recombined and spatially and temporally overlapped using a mechanical delay line and a dichroic mirror and are directed into

the entrance port of a laser scanning microscope (LSM510, Zeiss). Adjusting the mechanical delay is particularly demanding for fs pulses, since 200 fs pulses are only 60  $\mu\text{m}$  long, requiring very careful adjustment. Since the dispersion in glass is on the order of 10 ps/m [Chemnitz et al. 2012] in the NIR spectral range already 6 mm of additional glass in the beam path result in complete loss of the temporal overlap of 200 fs pulses, hence changing the microscope objective usually requires readjustment of the delay line. But also the spatial overlap is critical, since the focus position of both pump and Stokes laser beam have to coincide in order to generate the CARS signal, which is difficult for typical diffraction limited spot sizes down to sub- $\mu\text{m}$  in the specimen plane. All these facts underline, that adjustment of a multimodal nonlinear microscope is difficult. Even small changes in temperature induce shifting of the laser beam and vanishing of the CARS signal. Hence, after turning on the laser a waiting time on the order of 1 hour is needed until the thermal equilibrium within the laser system is established. The whole system furthermore consumes a significant amount of electrical power, e.g, typically 900 W for the Verdi-V18 pump laser and up to 5 kW for the laser scanning microscope.

Obviously such a system is anything but well suited to be operated in clinics. The same holds true for most of the laser platforms utilized for multimodal nonlinear microscopy or CARS microscopy, which are reviewed in the following. Special focus is paid on their potential clinical use, e.g., if instrumental miniaturization and reduction of maintenance is possible.

When using compact and robust laser sources, the average output power of such lasers is low compared to conventionally used solid state lasers, which easily provide several watts of power at 80 MHz repetition rate. Such high laser power can compensate for poor throughput of commercial laser scanning microscope optics, which are often not adapted to NIR excitation. Microscopes used for CARS imaging alone or in combination with other modalities for multimodal nonlinear microscopy are either based on modified laser scanning microscopes or home-built stage scanning microscopes [41]. The need for fast image acquisition in biomedical imaging is not met by slow stage scanning systems, even though they are advantageous when spectra are acquired [59], hence usually laser scanning microscopy is employed for



## 4. Compact Multi-Contrast Imaging Platform

---

investigating tissue [44] allowing for video rate image acquisition [46]. The overall NIR transmission of such poorly NIR-optimized instruments can be only 10% [84] or even less. Therefore, a home-built compact laser scanning microscope has been tailor made to meet both the requirements of low power NIR lasers as well as to fulfill the prerequisites for multimodal nonlinear imaging in clinical settings regarding small footprint and handling simplicity. The instrument is schematically depicted in figure 18 panel A, while a photograph of the instrument in the pathology department of the University Hospital Jena is displayed in panel B. It is anticipated, that apart from compact size, which allows for quick reinstallation on a moving platform, e.g., for bedside application, also an intuitive and easy instrument control has to be realized. In order to reach this goal, the system is reduced to the capabilities, which are required without affecting the quality of the image data, e.g., resolution, sensitivity, imaging speed and image contrast. The system is dedicated to multimodal nonlinear imaging utilizing the nonlinear processes of TPEF, SHG and CARS for signal generation. Therefore, the instrument does not support more than 4 detection channels.

The limited number of available options allow for a graphical user interface, which shows all relevant elements for system control on the screen without hidden menu items as depicted in figure 19. Since nonlinear imaging intrinsically confines the signal generation to the laser focus, a confocal instrument design is not required. This greatly simplifies the optical layout and improves the transmission. Furthermore, while confocal systems are limited to the detection of ballistic photons, which is a with tissue depth exponentially decreasing fraction of all generated signal photons, in nonlinear microscopy also scattered signal photons can be detected. These lower scattering losses result in the significantly improved penetration depth of multiphoton microscopy [17, 85, 86]. Further strategies to increase the fraction of detected scattered photons include to enlarge the detector size and to reduce the distance between specimen and detector. Since nonlinear signals are weak in comparison to the reflected laser intensity, which is removed by filtering, the detection system has been optimized to the detection of faint signals only. Due to these prerequisites photomultiplier modules (PMT) combining relatively high quantum efficiency and

## Summary

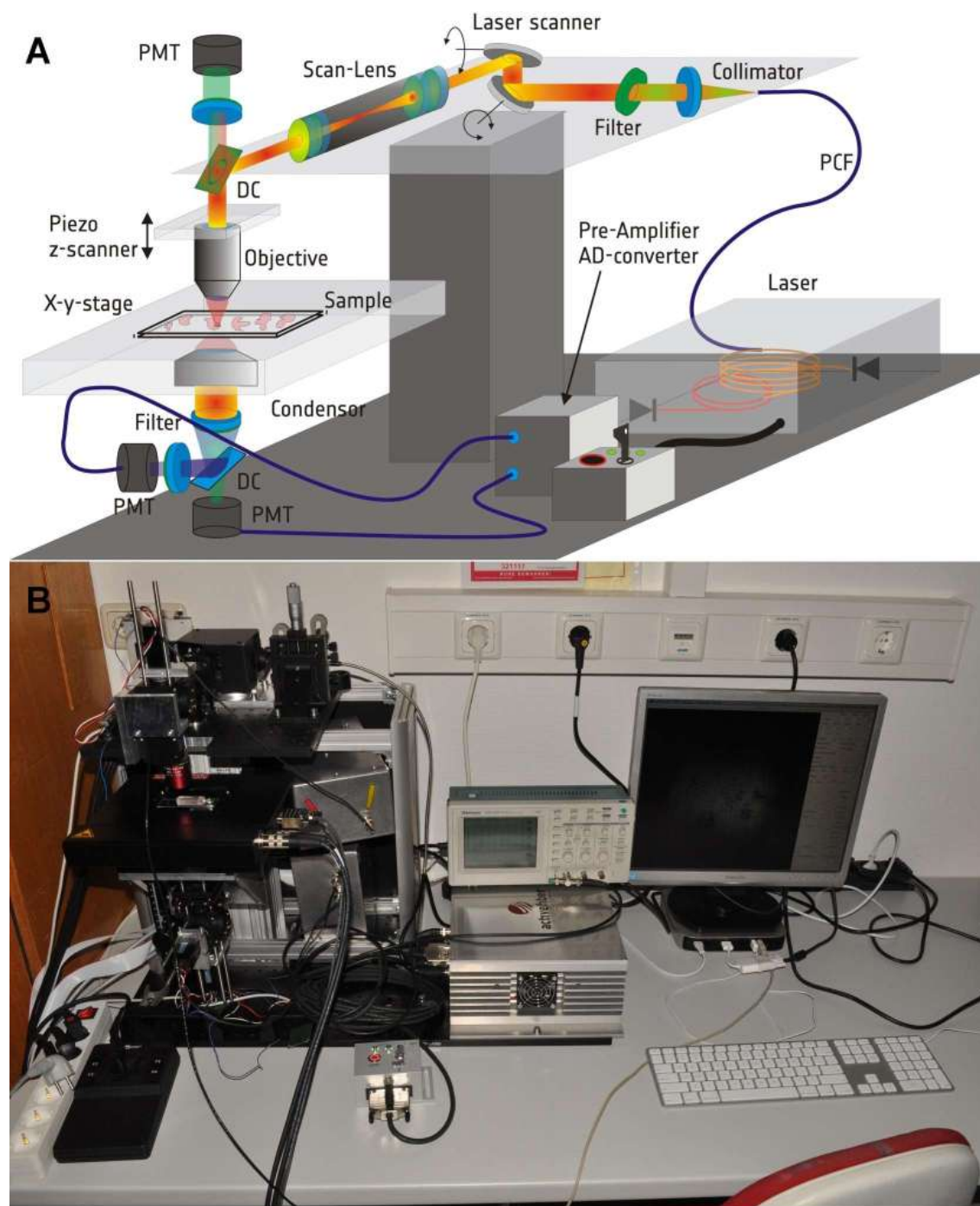


**Figure 18** – Panel A: Sketch of the compact laser scanning microscope and panel B: photograph of the instrument at the department of pathology, University Hospital Jena. Panel A reproduced by permission of The Royal Society of Chemistry, DOI: 10.1039/C3AN00354J.

## 4. Compact Multi-Contrast Imaging Platform

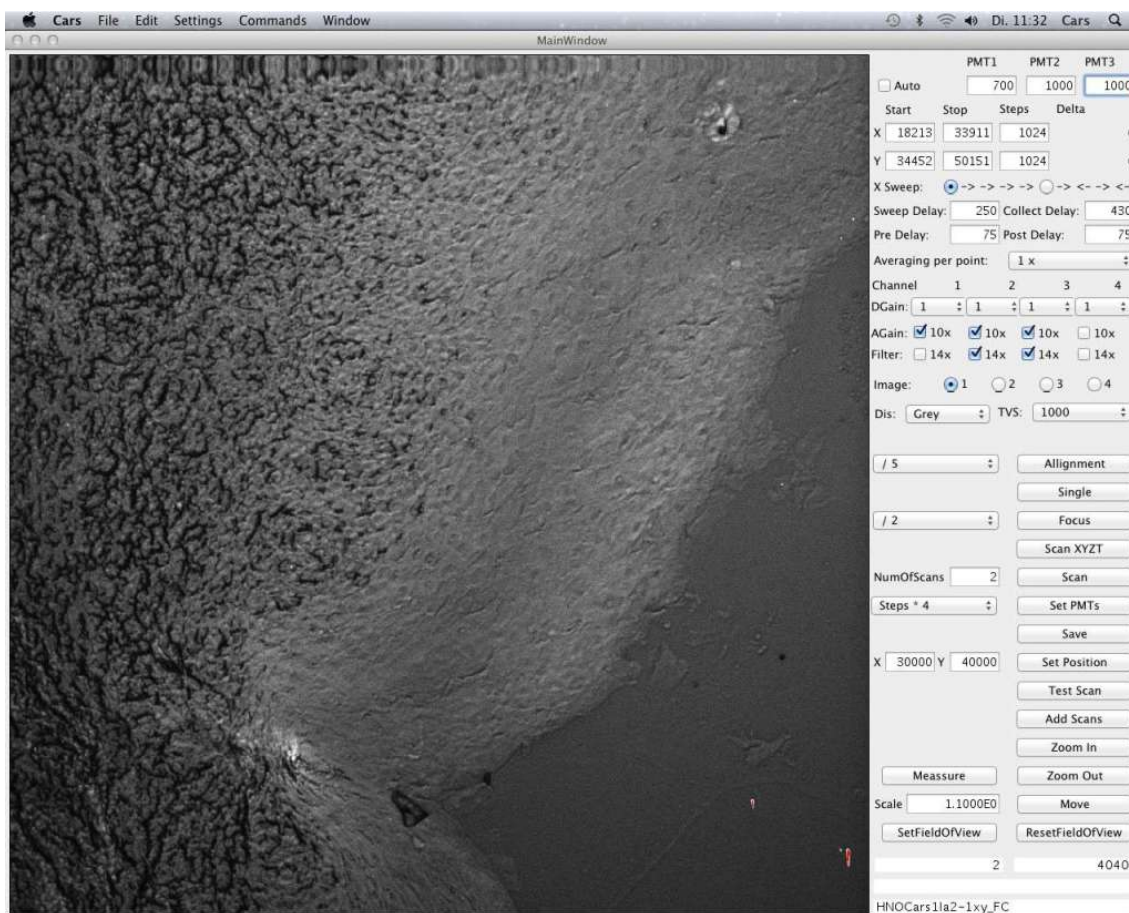


**Figure 19** – Screenshot of the graphical user interface for controlling the compact laser scanning microscope allowing for complete instrument control.

depending on the cathode material sufficient sensitivity in the NIR spectral range with high signal amplification of  $10^7$ , a high dynamic range of 1000 and a large active surface are used for detection. In order to electronically process the wide dynamic range of intensities provided by the PMT detector, the detection system has been designed for 16 bit data depth. This allows to use the full dynamic range of the detectors, hence enables simultaneous detection of weak and bright signals corresponding to a large range of concentrations. In addition it allows to simplify the instrument control, since adjustment of the PMT offset, which corrects for the voltage dependent dark current, is not required. In order to adapt for low power

## Summary

---

fiber lasers, only the galvanometric scanner, the NIR optimized scan lens and a dichroic mirror are included in the illumination beam path. Since spatial overlap of pump and Stokes laser at the focus is critical, the scan lens is based on NIR achromatic lenses (Edmund Optics), minimizing chromatic aberrations in the range from 750 to 1100 nm used in combination with a NIR apochromatic corrected microscope objective (Mitutoyo). Reflection losses of the scan lens are below 4 % by NIR antireflective coatings on the lenses in the spectral range from 750 to 1500 nm. The simple optical layout enabling highest excitation wavelength transmission and signal detection efficiency is illustrated in figure 20. The optical design of the illumination beam path results in an excellent overall NIR transmission of 60 % from the laser source onto the specimen, which is excellent, even when compared to an NIR optimized instrument [87], which provides 40 % transmission. The system is described in depth in chapter 11. Furthermore, the field of view is significantly enlarged to 1.4 mm in combination with a 20x objective, which allows for faster investigation of large specimens. An impression of the reduced size is given in figure 18, in particular when comparing it with figure 17. The footprint of the whole instrument including computers for instrument control is less than 1 m<sup>2</sup>. Important characteristics of the compact microscope are summarized in table 3.

**Table 3** – Summary of the characteristics of the compact nonlinear microscope

<b>Parameter</b>	<b>Compact Microscope</b>
Field of View (20×)	1.4 × 1.4 mm <sup>2</sup>
data depth	16 bit
max. number of detectors	4
pixel dwell time range	1-256 μs
image size / pixels	128 × 128 – 4096 × 4096
Footprint	45 × 45 cm <sup>2</sup>
image acquisition speed	up to 8 frames/s (128 × 128 pixels)
acquisition time (1024 × 1024)	1 s

#### 4. Compact Multi-Contrast Imaging Platform

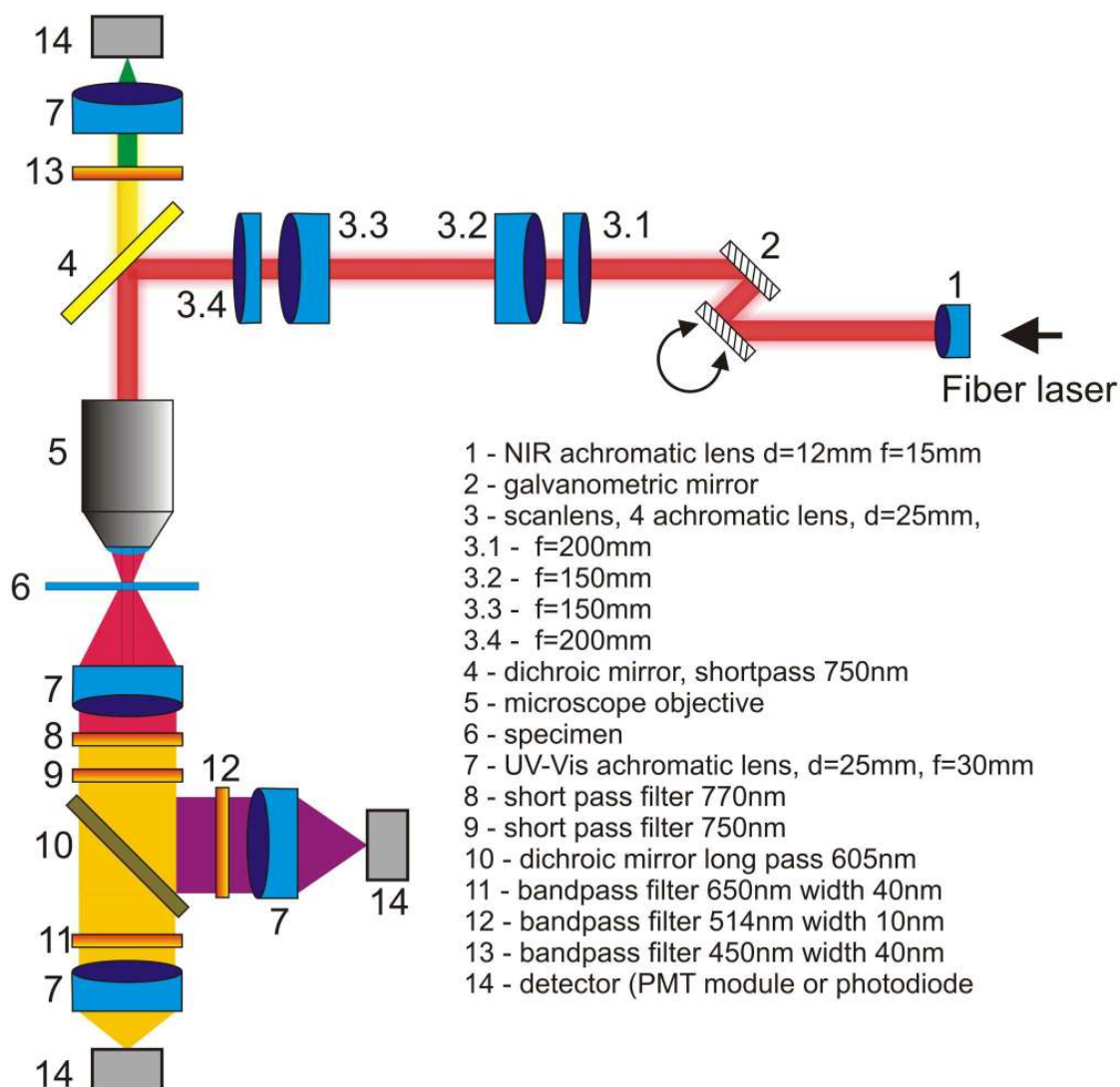


**Figure 20** – Optical layout of the compact microscope constructed for simultaneous TPEF, CARS and SHG imaging in a clinical setting, hence space and power consumption as well as alignment requirements are reduced. Reproduced by permission of The Royal Society of Chemistry, DOI: 10.1039/C3AN00354J.

A very important part of the microscope in order to reduce size and power requirements is a compact laser source. Subsequent to introducing laser sources for both CARS and multimodal nonlinear imaging, a novel fiber laser concept is presented in the following, which ideally suits the desired biomedical imaging application.

### 4.2 Novel Laser Sources for Multi-Contrast Microscopy

Before presenting a novel approach for a fiber based compact laser suitable for multimodal microscopy, the laser sources applied to CARS microscopy in general and multimodal imaging are reviewed in the following part.

Historically, the first implementation of CARS microscopy relied on synchronized dye lasers in 1984 [88, 89, 90]. Since introducing the concept of tight focusing in combination with a collinear beam arrangement in 1999 only solid state lasers have been employed. In this collinear CARS microscopy experiment realized by Zumbusch et al. in 1999 [41], a 250 kHz repetition rate has been used, which did not allow for high frame rates. Therefore, subsequent sources were based on 80 MHz laser systems. Especially in the early years the pulse repetition rate was often lowered by pulse picking to few MHz. Most widely used laser sources for CARS microscopy are based on (1) two synchronized Ti:Sa-Lasers [44] with homebuilt synchronization circuit [91, 92] or using the synchronization electronics provided by the main manufacturers Coherent [93, 94] and Spectra Physics [44], (2) a combination of an optical parametric oscillator (OPO) pumped either by an ultrafast Ti:Sapphire [41, 95] or Nd:Vanadate laser [46, 96, 97]. In the second approach the OPO generates the tunable wavelength by parametric conversion, hence the repetition rate is automatically synchronized with the pumping oscillator, which reduces experimental complexity and adjustment requirements considerably.

It was already 2002 recognized, that the complex instrumentation is a major limiting factor for the methods applicability. To resolve this problem, a single but spectrally broadband laser source in combination with a pulse shaper has been used instead [98]. However, in order to realize full spectral coverage of  $3000\text{ cm}^{-1}$  bandwidth and access the important CH-stretching region, which provides in biological tissue the highest CARS signal intensity, ultrashort pulses of 5 fs pulse durations have to be used. These are few cycle lasers, which are extremely sensitive to environmental changes, e.g., vibrations or temperature fluctuations. In addition, all optical elements in the beam path cause reduced peak intensity and chirping of the pulse by dispersion, which has to be compensated for and needs to be adjusted, when optical elements as the microscope objective are changed. Since the pulse shaper required

#### 4. Compact Multi-Contrast Imaging Platform

---

is as complex as a second laser source or OPO, this approach has been found few applications [99] and is limited to multiplex CARS and CARS spectroscopy allowing acquisition of the full CARS spectrum [100].

Now it will be discussed, which laser parameters are particularly suited for multi-modal nonlinear imaging. Solid state lasers typically emit pulses of few hundred fs to several ps pulse duration at 80 MHz repetition rate. Recombining both lasers on the sample by careful alignment in space and time enables simultaneous excitation of nonlinear signals [101]. However, in case of 80 MHz oscillators the three processes, i.e., CARS, SHG, and TPEF, are either not simultaneously efficiently excited or the molecular contrast is reduced. For SHG and TPEF short fs pulses of high peak power are most efficient, while for CARS longer pulses fitting the small spectral linewidth of Raman bands are preferable to optimize the ratio of resonant signal to nonlinear background. Hence, ps pulses provide higher contrast, but come at the cost of reduced total signal intensity [102] due to the low peak intensity compared to a fs-laser of the same average power. To overcome this limitation various laser sources have been proposed, e.g., performing successively CARS- and TPEF-SHG-imaging using synchronized ps-lasers for CARS and a fs laser for TPEF and SHG [82]. Obviously, this approach is technically challenging and does not allow for simultaneous acquisition of SHG, TPEF and CARS signals, which is not desirable for *in vivo* diagnostics in order to avoid motion artefacts. Alternatively either spectral resolution by using fs-lasers [97] or SHG and TPEF signal generation efficiency have been sacrificed [103] when using 80 MHz ps lasers. However, if the C-H-stretching resonance is used for CARS imaging, fs-spectral resolution is sufficient [102] due to the large spectral width of this band, which is in detail composed of several closely spaced vibrational resonances [31]. However, the disadvantageous size, complexity and sensitivity of solid state lasers prevent their widespread application.

The key demand on a laser for coherent Raman imaging is to provide a multicolour tunable output. Generating different frequencies from a single laser source in an OPO is based on nonlinear effects in low symmetric crystals like LBO or BBO. However, also optical fibers with crystal like micro-structure named "photonic crystal fibers" (PCF) provide high conversion efficiencies for nonlinear effects and are

## Summary

---

therefore likewise suited for wavelength conversion. Already in a first approach in 2003 the pump laser beam at 643 nm was generated in a PCF [104] and recombined with another fraction of the Ti:Sa-pump laser at 795 nm to probe the aromatic CH-stretching vibration of polystyrene beads, however requiring long integration times due to the low peak powers available from the PCF. More efficient is to use the supercontinuum of a PCF as Stokes beam for multiplex CARS imaging or spectroscopy [105, 106, 107, 108, 109, 110].

However, optical fibers do not only provide an efficient way for wavelength conversion. When the fibers are specially doped, they can be used as a gain medium allowing for ultracompact and environmentally stable fiber laser sources. These fiber lasers are due to their small size and long gain medium, which allows for high amplifications and beam quality, promising sources to succeed current solid state lasers. Therefore, fiber lasers have been employed to substitute current solid state lasers for pumping conventional OPOs [111]. However, as mentioned above, PCFs provide also an efficient way of fiber based wavelength conversion, hence research has focused on fiber integration of the CARS pump laser as well as using a nonlinear fiber for frequency conversion and wavelength tuning. Different nonlinear processes in fibers can be utilized to generate a synchronized output at a different wavelength. These processes are supercontinuum generation [112], which is a combination of several nonlinear effects like self phase modulation, soliton generation, soliton fission and dispersive wave generation, soliton generation alone [113, 114] or four wave mixing (FWM) [115, 116]. The laser sources developed by Krauss et al.[113] and Pegoraro et al.[114], both published in 2009, provide fiber integrated tunable lasers. However, both laser concepts rely on free space optics to overlap pump and Stokes pulses spatially and temporally, and suffer from relatively low spectral resolution and power for the tunable Stokes beam. The source presented by Zhai et al. [115] represents a fiber OPO system, utilizing a PCF in an resonator to generate signal and idler beams by FWM. Hence, except for replacing the nonlinear crystal by a PCF, the concept is similar to the one of Kieu et al. [111]. Also in this case the power output of the OPO is limited to few mW at 50 MHz repetition rate, the spectral resolution is poor due to 100 fs pulse duration and free space optics for beam



## 4. Compact Multi-Contrast Imaging Platform

---

recombination are still required.

By seeding the FWM process Lefrancois et al. realized a higher spectral resolution of  $15 \text{ cm}^{-1}$  in parallel to an output power of more than 150 mW at 54 MHz repetition rate, which suffices to be used as pump beam. Even spectral tuning across  $500 \text{ cm}^{-1}$  has been realized. However, the signal of the PCF is recombined in space and time with another fraction of the pump fiber laser, still requiring additional free space optics for alignment. Furthermore, due to the short pulse duration of 2 ps, adjustment of the temporal overlap when changing microscope objectives is required.

Another fiber based approach relaxes the requirement for aligning the temporal pulse overlap by using longer pulses of 35 ps duration at a reduced repetition rate of approximately 13 MHz to balance the loss of peak power due to the longer pulse duration [87]. Here, a fast electronically tunable ps Stokes laser is combined with a fiber laser at 1080 nm driven by the same electronics for synchronization. This approach allows for high speed spectrum acquisition of CARS spectra at  $0.5 \text{ cm}^{-1}$  spectral resolution. However, the tuning range is limited to the CH-stretching range from 2700 to 2950  $\text{cm}^{-1}$ . Due to the excitation in the NIR, i.e., the pump wavelength is around 800 nm, TPEF of autofluorescing molecules is less effectively excited in addition to the fact, that the Stokes wavelength at 1524-1608 nm is already affected by stronger water absorption in tissue as evident from figure 4.

Based on the known specifications deduced from multimodal nonlinear microscopy utilizing a conventional laser source [Meyer et al. 2011], [Meyer et al. 2013] and on the optimal parameters as introduced in section 2 a different fiber laser source has been developed at the Institute of Applied Physics in Jena as depicted in figure 21.

It differs from all beforehand mentioned concepts, since signal, idler and residual pump wavelength emitted from the PCF are used for CARS imaging directly, as depicted in panel A. This laser concept provides two important advantages: First, the low repetition rate of 1...2 MHz and the long ps pulse duration of 25...100 ps emitted from the same fiber results in perfect spatial overlap of pump and Stokes wavelength. Second, due to the long pulse duration, the temporal overlap of pump and Stokes pulses is almost not affected by dispersion, which is on the order of below

## Summary

10 ps/m [Chemnitz et al. 2012]. Hence, a delay line is dispensable. Therefore, this arrangement simplifies adjustment greatly and allows for the first time a fiber based setup without any free space optics [Baumgartl et al. 2012 a]. Additionally, due to precisely balancing repetition rate and pulse duration, at acceptable average powers of below 30 mW at the specimen similar peak power as compared to a few 100 fs 80 MHz laser can be realized. This is due to the fact, that lowering

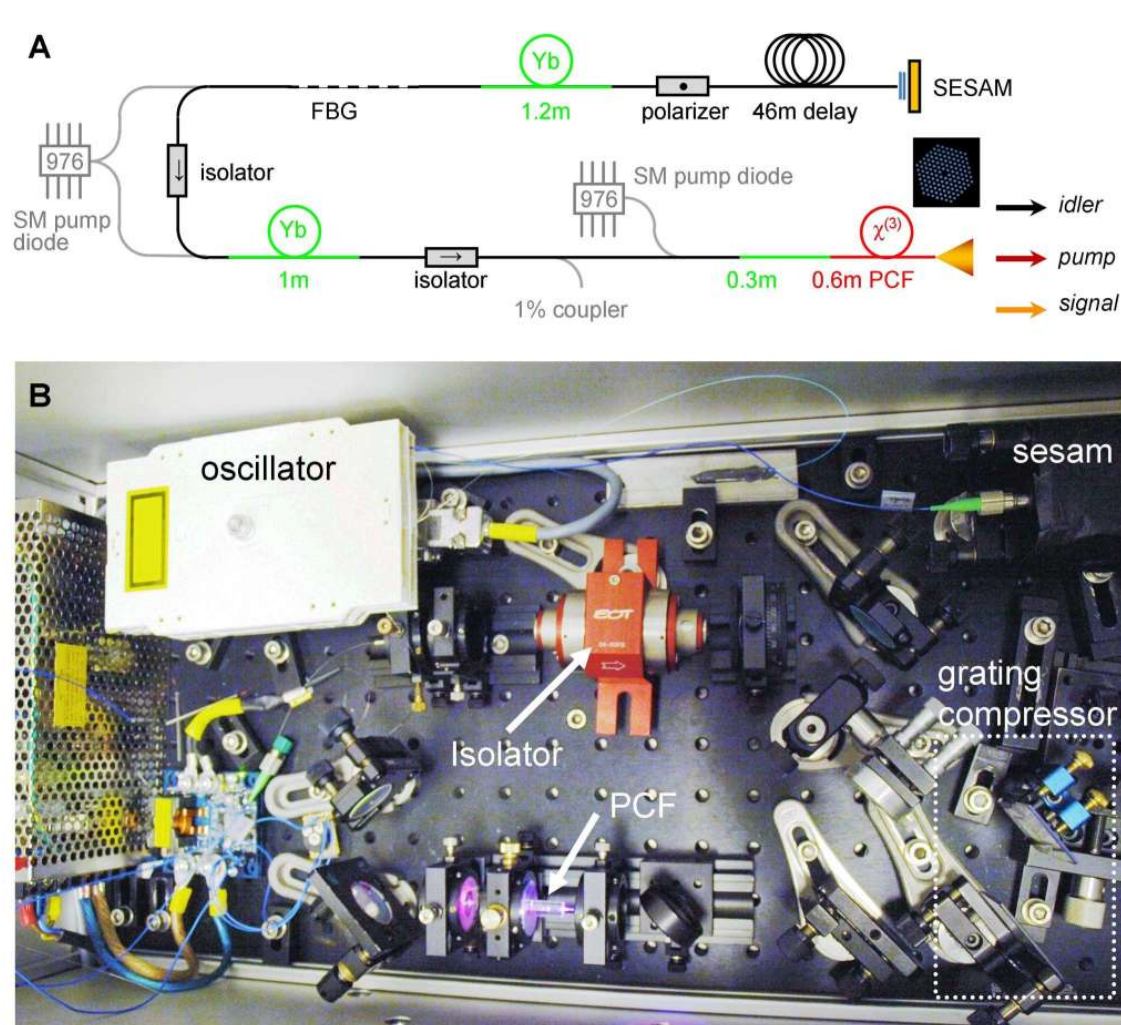


**Figure 21** – Panel A: Schematic layout of the all-fiber laser concept [Baumgartl et al. 2012 a]. Panel B: Photograph of a similar fiber laser used for CARS microscopy. The footprint is only 30 cm by 60 cm. Panel A is reproduced by permission of The Optical Society, Optics Express, 20(19) 21013 (2012).

## 4. Compact Multi-Contrast Imaging Platform

---

the repetition rate by a factor of 80 is compensated by the longer pulse duration of 25 ps, which directly corresponds to a 300 fs 80 MHz system of the same average power.

Hence, the beforehand mentioned discrepancy of either efficiently excite SHG and TPEF or provide high resonant contrast for CARS, which applies for 80 MHz laser sources, is resolved when using 25 ps lasers at 1-2 MHz repetition rate. Therefore, apart from their striking simplicity, this laser concept enables simultaneous high spectral resolution CARS- and high efficient TPEF- and SHG-signal generation. As demonstrated by [Chemnitz et al. 2012], by seeding the FWM process the spectral resolution can be increased to  $1 \text{ cm}^{-1}$  in combination with spectral tunability from 1200 to  $3800 \text{ cm}^{-1}$  except for a small spectral gap in the silent vibrational spectral region around  $2000 \text{ cm}^{-1}$ , which is not relevant for label-free imaging. Hence, this tuning range compares well with alternatively realized tunable fiber based sources for multimodal imaging, which provide tuning ranges of  $1050\text{-}2220 \text{ cm}^{-1}$  [115],  $2700\text{-}2950 \text{ cm}^{-1}$  [87],  $1100\text{-}3800 \text{ cm}^{-1}$  [113] or  $2400\text{-}3400 \text{ cm}^{-1}$  [114], respectively. The fiber lasers are in depth described in the chapters 8, 9, 10 and results from using these laser sources for biomedical imaging are presented therein.

In order to illustrate the performance of the microscope in comparison with a laboratory nonlinear imaging platform, the same thin tissue sections of human HNSCC specimen as described in detail in section 3 have been imaged utilizing different imaging setups, e.g., different lasers and microscopes. The tested laser sources include a 2 ps Ti:Sa-Laser in combination with an OPO as described at the beginning of this section, a pulsed Nd:Vanadate laser (HighQ lasers) of 7 ps pulse duration in combination with an OPO, a compact tunable fiber laser similar to the source described in [113] (Toptica) and finally the novel light source developed by at the Institute of Applied Physics, FSU Jena. The results are displayed in figure 22. The standard system consisting of a laser scanning microscope and Ti:Sa-OPO system operating in the VIS-spectral range has been used as a reference. The images obtained with this instrument are displayed in the first column, while the other columns present images acquired using the compact home-built instrument in combination with the different laser sources mentioned above.

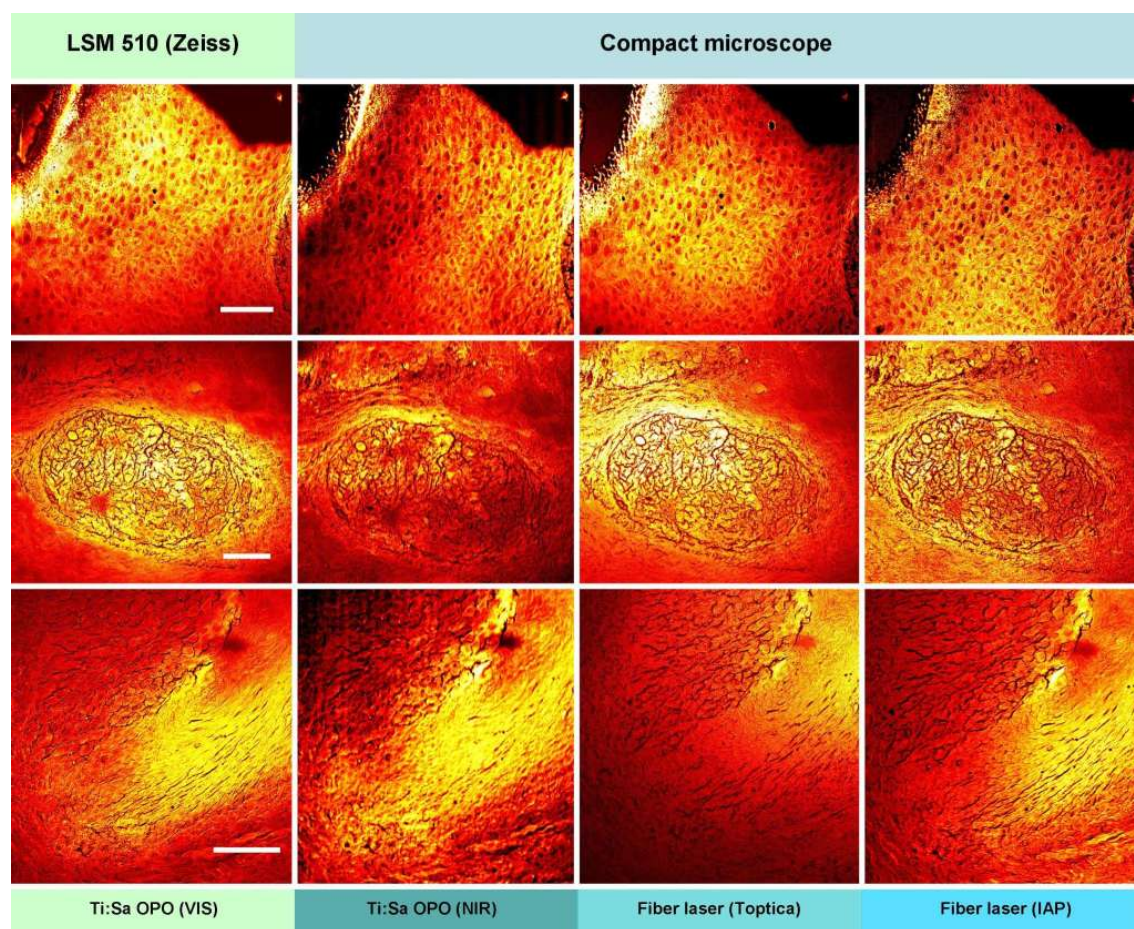


**Figure 22** – In order to illustrate the performance of the compact CARS microscope utilizing several laser sources, CARS microscopic images of HNSCC tissue samples at the aliphatic CH-stretching vibration of methylene groups at  $2850\text{ cm}^{-1}$  are compared to images from the same specimen acquired using the laboratory system. Further images of these samples are depicted in figures 7, 8 and 9. The microscope used to acquire the images is indicated on the top, while the laser source is stated below. First row: benign epithelium, individual cells and nuclei are discernible, sample of an oropharyngeal site. Second row: HNSCC tumor nest embedded in connective tissue, oropharyngeal site. Third row: boundary of dysplastic and benign epithelium, laryngeal site. Scale bar  $100\ \mu\text{m}$

In the first row benign epithelium and in the second row a tumor nest of a grade IV HNSCC both of an oropharyngeal site are displayed, while the transition region from benign epithelium to connective tissue and dysplastic epithelium at a laryngeal site is visualized in the third row. As evident, the compact laser scanning microscopes retrieves image data of similar quality as compared to the commercial LSM.

## 4. Compact Multi-Contrast Imaging Platform

---

In the first row of figure 22 single epithelial cells are clearly resolved. A tumor nest invasively growing into the connective tissue characterized by slightly higher lipid content is similarly discernible in the second row. The higher lipid content of benign epithelium in contrast to dysplasia and surrounding connective tissue is also reproduced in all configurations (third row). The image quality of different laser sources working at similar wavelengths and characterized by spectral widths of similar magnitude is comparable in combination with the same microscope, as evident by comparing the second to fourth column of figure 22, even though the ratio of pump and Stokes laser intensity, the spectral widths as well as repetition rate and average powers are slightly different as summarized in table 4. When precisely

**Table 4** – Overview of the lasers and their characteristics tested for CARS imaging.  $\Delta\tilde{\nu}$ -spectral width,  $\lambda_{Pump}$ -wavelength of pump laser,  $\lambda_{Stokes}$ -wavelength of Stokes laser, P(pump), P(Stokes) - output power of pump and Stokes laser, E/pump pulse - energy per pump laser pulse.

Parameter	Coherent VIS	Coherent NIR	Toptica	IAP
repetition rate	76 MHz	76 MHz	40 MHz	1 MHz
pulse duration	2 ps	2 ps	1 ps	30 - 100 ps
$\Delta\tilde{\nu}$	20 $\text{cm}^2$	20 $\text{cm}^2$	10 $\text{cm}^2$	40 $\text{cm}^2$
$\lambda_{Pump}$	670 nm	775 nm	775 nm	795 nm
$\lambda_{Stokes}$	830 nm	995 nm	995 nm	1032 nm
P(Pump) (output)	< 300 mW	> 1 W	130 mW	25 mW
P(Stokes) (output)	> 1 W	50 mW	3-5 mW	> 100 mW
E/pump pulse	4 nJ	13 nJ	3.25 nJ	25 nJ

comparing the images, some differences are apparent. Firstly, slightly greater pulse-to-pulse laser power fluctuation due to multiple fiber amplifier stages as sketched in figure 21 of the fiber laser translates into larger noise in comparison to solid state lasers. However, this noise is not large and therefore not apparent at first sight. Secondly, due to the low pulse repetition rate of 1 MHz, there is a weak periodic noise pattern, since the laser repetition rate is of similar magnitude as compared to the data acquisition rate of 1 MHz, which is 500 kHz low pass filtered preceding analogue to digital conversion. Therefore, the noise does not significantly deteriorate

the image quality, which is also demonstrated in figures 13 panels A-C, 14 panels A and B, 15, 16 and 27. However, the apparent advantages of the fiber laser concept, e.g., adjustment simplicity, signal generation efficiency, spectral resolution, clearly dominate.

Hence, the presented microscopic system in combination with the compact low repetition rate fiber laser is a promising instrument for clinical diagnostics.

## 5 Interpretation of Multimodal Image Data

Even though the information extracted from multimodal image data correlates with tissue characteristics routinely assessed by staining histopathology as illustrated in section 3, the origin of the observed image contrast is different, e.g., due to the distribution of endogenous markers. In order to provide the basis for disease recognition, the expression of molecular markers needs to be correlated with disease progression. Therefore, research is ongoing in order to understand the molecular basis of the observed endogenous image contrast, which potentially provides additional insight in biochemical mechanisms associated with disease status. In this chapter work on the interpretation of multimodal image data is presented, focusing on relating the endogenous image contrast to compositional changes. For the endogenous TPEF and SHG-active markers, correlations of marker signal with disease status have been analyzed, e.g., correlating the increased NADH autofluorescence in dysplasia with the altered metabolic activity [70] or evaluating disease induced modifications of collagen structure [117, 118, 119]. For CARS microscopy, however, systematic studies on the connection of disease induced molecular changes and the observed signal are at the beginning, hence, the presented work focuses primarily on approaches to interpret the observed CARS image contrast:

- Investigation of the origin of reduced CARS signal intensity within the C-H-stretching spectral region, which enables the detection of cell nuclei and can be employed to automatically extract quantitative information, e.g., the cell density, average size and shape of nuclei, the nucleus to cytoplasmic ratio.
- Development of methods to differentiate multiple CARS markers utilizing multispectral CARS imaging in the C-H-stretching spectral region and determi-

nation of the optimal imaging parameters, e.g., the optimal spectral resolution for discrimination of multiple marker molecules.

The data presented in this section has been published in [Meyer et al. 2012] & [Meyer et al. 2013 b].

### 5.1 The Origin of CARS Contrast for Cell Nuclei Detection

As demonstrated for epithelial and brain tissue, cell nuclei can be detected by lower CARS intensity at  $2850\text{ cm}^{-1}$  at the location of the cell nuclei in contrast to the surrounding cytoplasm. In order to analyze the origin of this contrast, a brain metastasis of a squamous cell carcinoma specimen has been investigated by CARS at  $2850\text{ cm}^{-1}$  and Raman imaging and the results are compared to H&E staining in figure 23. In the first row the image of the successively H&E-stained section is depicted in panel A, while the CARS image is visualized in panel B, which provides contrast suitable for the automated detection of cell nuclei and cell bodies [120]. The results from image analysis are presented in panels C and D for the detection of cell nuclei and cells, respectively.

For comparison, a parallel section was analyzed by Raman imaging and subsequently vertex component analysis has been performed within the C-H-stretching vibrational spectral region. Two components VC 1 and VC 2 have been retrieved. The corresponding spectra are plotted in panel E. While VC 1 is characterized by high Raman intensity at the aliphatic CH-stretching vibration of methylene groups at  $2850\text{ cm}^{-1}$  characteristic for lipids, spectral signatures at  $2930\text{ cm}^{-1}$ , which are characteristic for methyl groups, contribute primarily to VC 2. The corresponding abundance map of VC 1 is displayed in panel F, while the abundance map of VC 2 is depicted in panel G. As evident, the image in panel F agrees with the CARS image in panel B proving, that the Raman signals at  $2850\text{ cm}^{-1}$  are lower at the location of the cell nuclei. The contrast is inverted in the abundance map of VC 2, i.e., the Raman intensity at  $2930\text{ cm}^{-1}$  is higher at the location of nuclei than within the surrounding cytoplasm, as displayed in panel G. In panel H the subsequently H&E stained histologic image is displayed for comparison. Both VC 1 and VC 2 can be used for the detection of cell nuclei, but only the Raman signal at  $2850\text{ cm}^{-1}$  com-

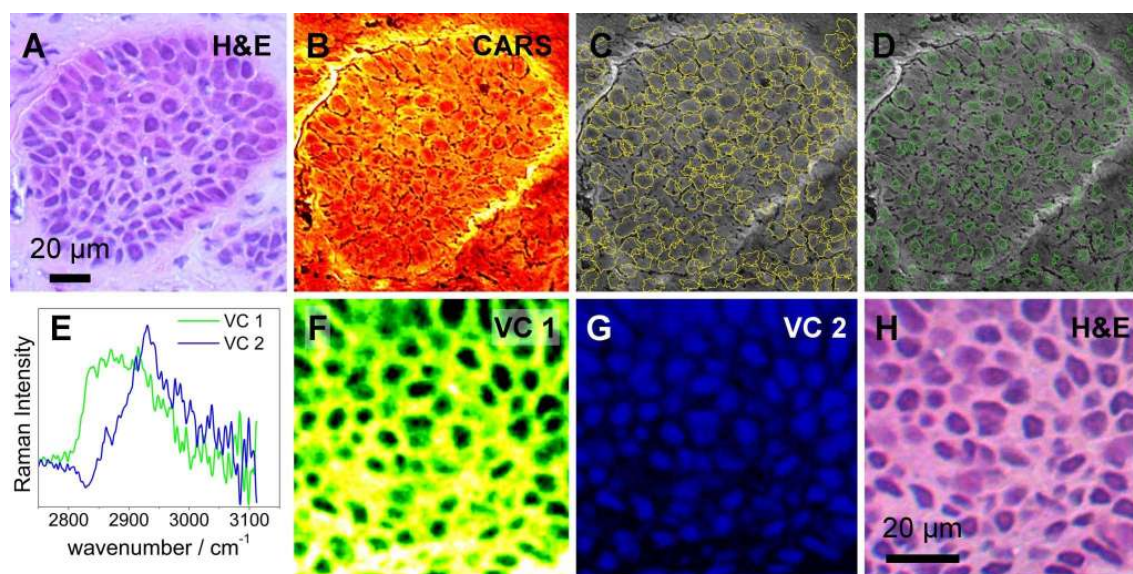


**Figure 23** – Comparison of a subsequently H&E stained section (panel A) with the CARS image (2850 cm<sup>-1</sup>) (B) of a human carcinoma brain metastasis enabling detection of individual cells and nuclei. The image contrast allows for the automated detection of cells and cell nuclei displayed in panels C and D. The molecular basis of the CARS image contrast allowing cell nuclei detection is analyzed by Raman imaging in the CH-stretching spectral region of a parallel section displayed in panels E-H. Panel E: vector component analysis (VCA) of the Raman data retrieves two spectral components VC 1 and 2. Panel F: The contrast of the abundance map of VC 1 is similar to the CARS image, above in panel B, substantiating that cell nuclei detection in CARS is due to the on average lower Raman intensity at 2850 cm<sup>-1</sup> in the nucleus with respect to the surrounding cytoplasm, which is associated with the lipid component. Panel G: VC 2 corresponding to CH-stretching vibrations of CH and CH<sub>3</sub> groups provides positive nuclei contrast. The H&E image (H) is depicted for comparison. Adapted with kind permission from Wiley-VCH Verlag GmbH & Co. KGaA, J. Biophotonics 5(10), 729–733 (2012).

plies with the CARS image. Hence, the observed CARS image contrast enabling the detection of cell nuclei is based on the lower abundance of CH<sub>2</sub>-functional groups in the nucleus in comparison to the cytoplasm, i.e., the lipid content in cell nuclei is lower than in the cytoplasm.

## 5.2 Interpretation of Multispectral CARS Data

In this section it is outlined, how the multiplexing capabilities of CARS microscopy can be employed to analyze the spatial distribution of multiple Raman active marker



## 5. Interpretation of Multimodal Image Data

---

molecules. This is important for disease diagnostics, since exogenous labelling is difficult to apply. Therefore, endogenous markers need to be used. In human and animal tissue there is only a limited set of endogenous SHG- or TPEF-active molecular markers available, since the molecular properties required for generation of SHG and TPEF signals, e.g., non-inversion symmetric structure in case of SHG and autofluorescence in case of TPEF, are rare in tissue. Therefore, the chemical composition can be only partially analyzed by SHG and TPEF microscopy alone. Coherent Raman imaging can be used to overcome this limitation allowing to use many molecular markers, i.e., all Raman active molecules. However, in order to exploit this advantage, multispectral CARS data needs to be collected, since determining the number  $N$  of marker molecules labelled from the CARS signal at a single wavenumber position is not possible (see equation 10).

In the following, a novel approach to analyze multispectral CARS image data is presented. Since the largest CARS signals are generated within the C-H-stretching spectral region, this spectral part is primarily employed for CARS imaging. However, the most frequent biomolecules, e.g., proteins, triglycerides, DNA, contain  $CH_2$ - and  $CH_3$ -functional groups. Therefore, their Raman and CARS spectra are spectrally overlapping in this wavenumber range as depicted in case of Raman spectra in figure 3 for triglycerides and proteins. Therefore, analytic methods are required to disentangle the spectral contributions of different markers in order to determine the composition. Recently spectral decomposition algorithms used for Raman imaging have been employed to CARS and SRS data [121, 122].

In the following an alternative powerful approach is presented, which is based on colocalization analysis, originally developed for the analysis of multichannel fluorescence data in order to separate multiple fluorescence labels with overlapping fluorescence emission spectra[123]. The basic idea is, that pixels of similar color are occupied by the same molecules and the brightness of the pixel is a measure of concentration. In order to explain the principle, CARS imaging at two resonances  $\omega_1$  and  $\omega_2$  is considered. The CARS images at two resonances  $\omega_1$  and  $\omega_2$  are assigned to the blue and green image channel. The frequency scatter plot is the two-dimensional histogram of this two-channel image, which is a three-dimensional plot, depicted in

## Summary

---

figure 24. Along the axes of the plot the intensity  $I^{CARS}(\omega_{1/2})$  in each channel is plotted, while the brightness of an individual pixel in the plot corresponds to the number of pixels in the originating two color CARS image characterized by the corresponding pair of intensity values at  $I^{CARS}(\omega_1)$  and  $I^{CARS}(\omega_2)$ . A pixel occupied by a single Raman active substance labelled 'a' is characterized by the CARS intensities  $I_a^{CARS}(\tilde{\omega}_1)$  and  $I_a^{CARS}(\tilde{\omega}_2)$  at the frequencies  $\tilde{\omega}_i$  can be interpreted as a vector in the frequency scatter plot according to equation 16, which depends on the susceptibility of the substance  $a$  (equation 9).

$$\begin{pmatrix} I_a^{CARS}(\tilde{\omega}_1) \\ I_a^{CARS}(\tilde{\omega}_2) \end{pmatrix} \propto \begin{pmatrix} |\chi^{nr} + \chi_a^r(\tilde{\omega}_1)|^2 \\ |\chi^{nr} + \chi_a^r(\tilde{\omega}_2)|^2 \end{pmatrix} \quad (16)$$

This CARS intensity pair is according to equation 10 related to number of molecules  $N_a$  weighted by the polarizability  $\alpha_a(\tilde{\omega})$  of the molecule  $a$  at the frequency  $\tilde{\omega}_i$  shown in equation 17:

$$\begin{pmatrix} I_a^{CARS}(\tilde{\omega}_1) \\ I_a^{CARS}(\tilde{\omega}_2) \end{pmatrix} \propto \underbrace{N_a^2 \cdot \begin{pmatrix} \alpha_a^2(\tilde{\omega}_1) \\ \alpha_a^2(\tilde{\omega}_2) \end{pmatrix}}_{(1)} + \underbrace{2N_a \cdot \chi_{nr} \cdot \begin{pmatrix} \alpha_a(\tilde{\omega}_1) \\ \alpha_a(\tilde{\omega}_2) \end{pmatrix}}_{(2)} + \underbrace{\chi_{nr}^2 \begin{pmatrix} 1 \\ 1 \end{pmatrix}}_{(3)} \quad (17)$$

Hence, the position in the frequency scatter is directly related to the number of marker molecules  $a$  weighted by the polarizability  $\alpha_a$  of the molecule  $a$  at the wavenumber positions  $\tilde{\omega}_1$  and  $\tilde{\omega}_2$ . There are three vectorial components:

- (1) the first component depends on the square of number of molecules and dominates for high concentrations and when the polarizability is large in comparison to the nonresonant background.
- (2) The second vectorial component is linear in the number of molecules  $N_a$  and dominates for low concentrations or large nonresonant background or small polarizability  $\alpha_a$ .
- (3) The third component is the lowest observable pixel intensity, which is determined by the nonresonant nonlinear background  $\chi_{nr}$  and does not contain any molecular information.

In case of a pure linear concentration dependence, the pixels occupied by a single

marker  $a$  would be arranged along a line, e.g., along component (2), but due to the nonlinear concentration dependence of CARS, the pixels in the frequency scatter plot occupied by the same marker  $a$  bend to the right for higher concentrations of this marker  $a$ , as displayed in figure 24. This is also observed experimentally in figures 26 panel B and 27 panel C.

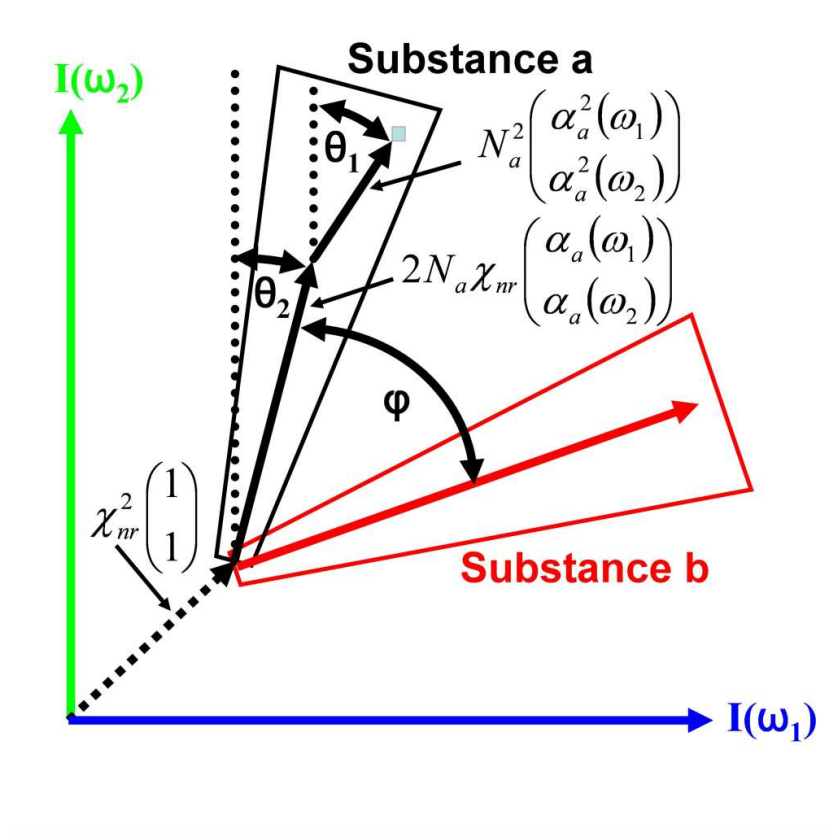


**Figure 24** – Correlation of the molecular structure and the scatter plot, a 2D-histogram of CARS images at two resonances  $\omega_1$  and  $\omega_2$ . The origin of the pixel cloud is determined by the nonresonant background  $\chi_{nr}$ , if noise from the detection electronics is neglected. Each pixel corresponds to a pair of intensities at both CARS resonances, which is related to the molecules polarizability  $\alpha$  at the resonance  $\tilde{\omega}_i$  and the number density  $N_a$ . Due to the interference of resonant and nonresonant signal, two vectorial contributions linear and quadratic in number density determine the position, which is why the scatter plot point cloud of a molecule is not linear, but slightly bend. When the spectral differences are large enough, two substances  $a$  and  $b$  cluster in separate regions of the scatter plot and allow locating both molecular markers in the original image. The separation angle  $\phi$  increases for high spectral resolution measurements.

## Summary

---

The relationship between pixel position in the two-dimensional histogram and the molecule specific parameters, i.e., number of molecules  $N_a$  and polarizability  $\alpha_a$  is displayed in figure 24.

Here two additional parameters are displayed, the angles  $\theta_1$ ,  $\theta_2$  and  $\phi$ . The angle  $\theta$ , the pointing direction of the vectorial component (2) is a measure of the polarizability ratio  $\alpha_a$  at the wavenumber positions  $\tilde{\omega}_1$  and  $\tilde{\omega}_2$ .

$$\sin \theta_1 = \frac{\alpha_a^2(\tilde{\omega}_1)}{\alpha_a^2(\tilde{\omega}_2)} \quad \sin \theta_2 = \frac{\alpha_a(\tilde{\omega}_1)}{\alpha_a(\tilde{\omega}_2)} \quad (18)$$

Component (2) points in direction  $2\theta$ , since it contains the square of the direction of component (2). The third component (3) is a displacement along the diagonal of the frequency scatter plot. Since the direction of the vectors in the frequency scatter plot is determined by the molecule specific polarization, the location in the plot is similarly a characteristic of the molecule  $a$ . This is depicted exemplarily for another molecule  $b$ , which is characterized by the polarizability  $\alpha_b(\omega_i)$ , thus pixels occupied by substance  $b$  cluster in another area of the two-dimensional histogram as depicted. Hence, the Raman active marker molecules  $a$  and  $b$  concentrate in different areas of the plot, as depicted in figure 24, which are separated by the angle  $\phi$ , which is determined by the molecules polarizability. In the region, in which the linear term (2) dominates, the angle  $\phi$  is given by:

$$\phi = \theta_b - \theta_a \quad (19)$$

Therefore, spectral separation in the frequency scatter plot is directly related to different polarizabilities, hence a molecular characteristic.

In the following, this image analysis approach is illustrated by separating protein from triglyceride contributions in multispectral CARS images. CARS images at two Raman resonances characteristic for methyl and methylene functional groups, i.e., at  $2850 \text{ cm}^{-1}$  and at  $2930 \text{ cm}^{-1}$ , are used. First the molecular basis of the discrimination of molecules by vibrational spectroscopy is illustrated in figure 25. The tissue specimen contains triglyceride depositions within adipocytes and protein fibers. Triglycerides and proteins are discernible by the abundance of  $CH_2$ - and  $CH_3$ -functional

## 5. Interpretation of Multimodal Image Data

groups, which is the basis of discriminating triglycerides from proteins within the C-H-stretching spectral region. In figure 26 panel A a two dimensional plot of the

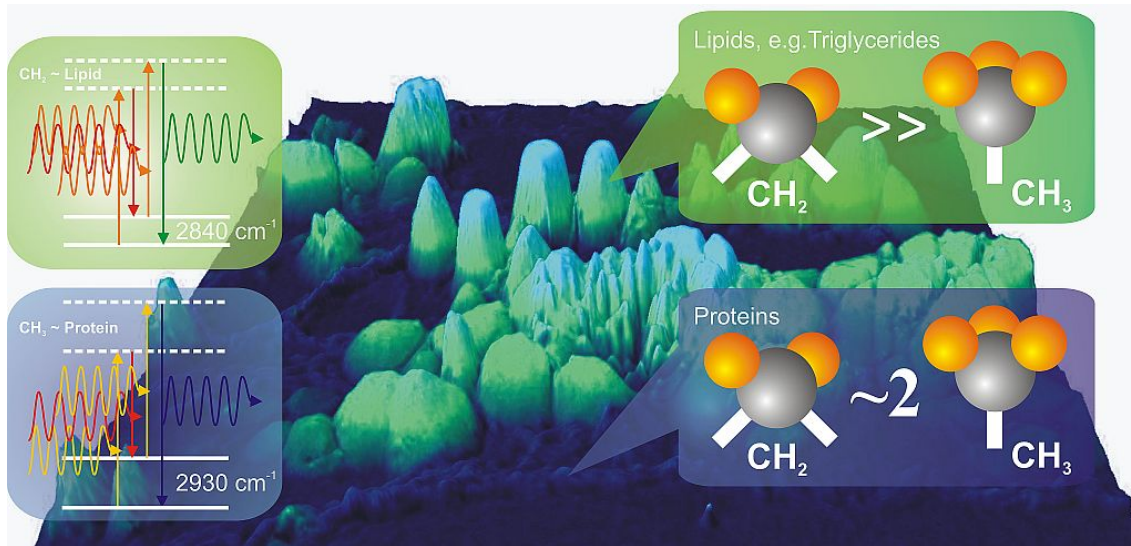


**Figure 25** – The structural basis of differentiating biomolecules within the C-H-stretching vibrational spectral region is depicted here in case of adipose tissue containing lipid deposits and protein fibers of the connective tissue. The structure of major biomolecules, e.g., triglycerides and proteins, incorporates different amounts of methylene and methyl groups, which allows for CARS spectroscopic discrimination, when two resonances characteristic for  $CH_2$ - and  $CH_3$ -functional groups are imaged.

number of methylene and methyl groups per molecule is displayed. Along the x-axis the number of  $CH_3$ -groups is plotted, while the number of  $CH_2$ -groups is displayed along the y-axis. Fatty acids as major building blocks of triglycerides are characterized by a high ratio of  $CH_2$ - $CH_3$  functional groups of ten to 16 for the most frequent fatty acids, e.g., stearic, palmitic and oleic acid. Proteins on the contrary are on average characterized by a  $CH_2$ - $CH_3$ -ratio of 2 when taking into account the abundance of all amino acids and their composition. Some amino acids, e.g., Alanin and Leucin, are plotted for comparison. As evident, both groups of biomolecules cluster in different areas of this plot of structural characteristics. This structural difference is used to discern triglycerides from proteins by multispectral CARS imaging.

Due to the higher  $CH_2$ - $CH_3$ -ratio, triglycerides are characterized by a larger CARS intensity ratio  $I_{CARS}(CH_2)$ - $I_{CARS}(CH_3)$ , than proteins, hence, lipids occupy the

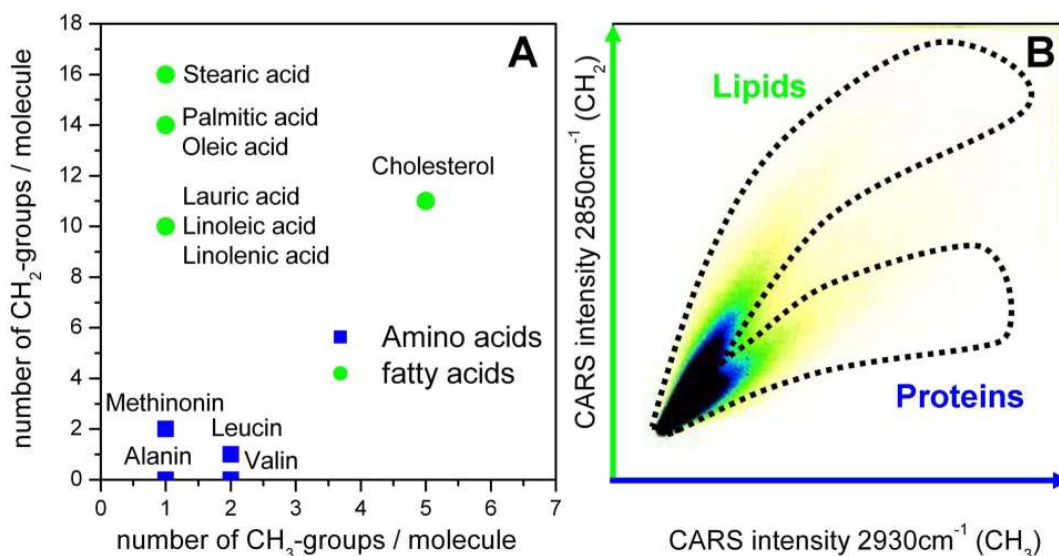


**Figure 26** – A: Number of methylene and methyl groups plotted for selected fatty acids and amino acids, the building blocks of proteins and triglycerides. On average the  $CH_2$ - $CH_3$ -ratio is 2 in proteins and larger than 10 in triglycerides, which is the basis for discerning proteins and triglycerides CARS microscopically. B: 2D-histogram, i.e., frequency scatter plot, of two CARS images at  $2850\text{ cm}^{-1}$  ( $CH_2$ ) and  $2930\text{ cm}^{-1}$  ( $CH_3$ ) of an artery section showing two separate pixel groups assigned to lipid and protein according to the  $CH_2$ - $CH_3$ -intensity ratios in agreement with the molecular structure depicted in panel A.

upper left region of the frequency scatter plot marked in figure 26 panel B, while proteins dominated image pixels cluster in the lower right part of the plot. The frequency scatter plot is calculated from CARS images of the cross section of an artery of a rabbit fed with a high cholesterol diet which were acquired at  $2850\text{ cm}^{-1}$  and  $2924\text{ cm}^{-1}$ , which are characteristic for  $CH_2$ - and  $CH_3$ -functional groups [83]. Dark pixels correspond to a high abundance of the respective intensity pair. Backprojecting of areas of the frequency scatter plot onto the original image allows localizing the protein and lipid pixels, which is exemplarily demonstrated in the following.

In order to demonstrate the application of this method for analyzing the composition of complex tissues, an artery section of a rabbit model for atherosclerosis has been investigated by multispectral CARS imaging at  $2850\text{ cm}^{-1}$  (green,  $CH_2$ ) and  $2924\text{ cm}^{-1}$  (blue,  $CH_2$ , see panel A) and SHG microscopy (panel B) displayed in figure 27. By multimodal imaging using CARS at one resonance only, one cannot

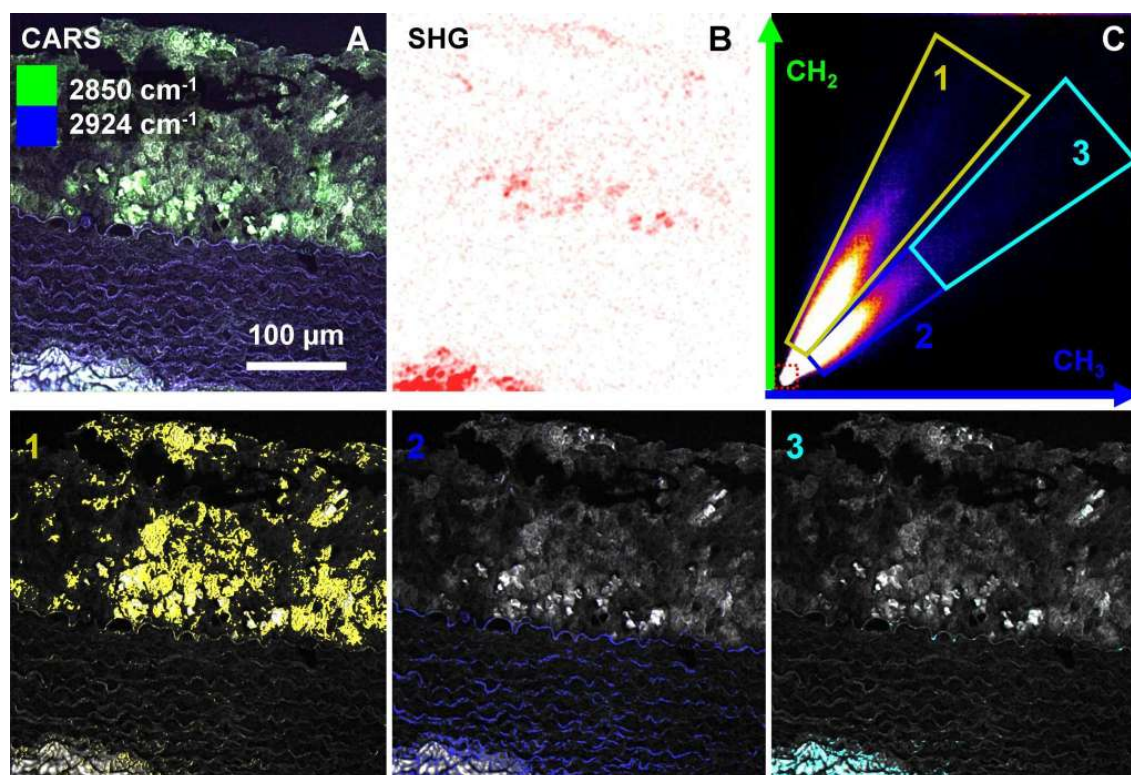


**Figure 27** – The principle of analyzing the tissue composition by multimodal microscopy incorporating multispectral CARS imaging is depicted in this figure. Here an artery section of an animal model for atherosclerosis (rabbit model) is imaged by CARS microscopy at two resonances, i.e.,  $2850\text{ cm}^{-1}$  (green,  $CH_2$ ) and  $2924\text{ cm}^{-1}$  (blue,  $CH_3$ ) in panel A, the SHG signal is depicted in red in panel B (white background). To determine the SHG active structure in the lipid deposits and in the *elastica externa* (bottom), the 2D-histogram of the CARS images (C) is analyzed, showing two distinct signal groups, i.e., proteins and lipids. By backprojecting the marked areas in the scatter plot onto the original CARS image, the plaque is identified as pure lipid structure, while the *tunica media* and the *elastica externa* are low and high intense protein structures. Hence, the SHG source in the plaque is an oxidized lipid, while it is collagen in the *elastica externa*. Adapted with permission from [dx.doi.org/10.1021/ac400570w](https://doi.org/10.1021/ac400570w) American Chemical Society.

discern between proteins and lipids spectroscopically (see figure 15). Similarly by SHG microscopy alone it is not possible to discriminate SHG signals from different molecules, since the emission wavelength is identical. However, this can be accomplished by CARS imaging at  $2850\text{ cm}^{-1}$  characteristic for  $CH_2$  and at  $2924\text{ cm}^{-1}$  characteristic for  $CH_3$ -functional groups. The composite CARS image showing  $CH_2$  in green and  $CH_3$  in blue is depicted in panel A, while the corresponding frequency

## Summary

---

scatter plot is displayed in panel C of figure 27 and the SHG signal is displayed in red in panel B. The frequency scatter plot enables discrimination of two clusters of pixels:

(1) is due to the larger  $CH_2-CH_3$ -CARS signal ratio assigned to lipids. (2, 3) are due to the smaller  $CH_2-CH_3$ -CARS intensity ratio assigned to proteins in agreement with the respective molecular structure (figure 26 panel A). By backprojecting the areas labelled 1-3 onto the original CARS image, the spatial distribution of this groups of pixels is retrieved as displayed in the second row of figure 27 panels 1-3:

(1) Lipid deposits are localized in the atherosclerotic lesion.

(2) Low intense protein contributions originate protein fibers of the *tunica media*, e.g, elastin of the elastic vessel wall, collagen fibers and actin-myosin of the smooth muscle cells. (3) High intense protein pixels originate in the *tunica externa* containing large amounts of collagen.

Hence, the multispectral CARS data enables to identify the source of SHG and TPEF signals, which is demonstrated for the SHG signal in the following. Within the plaque, no intense protein structures have been detected, therefore the source of SHG in this area is possibly a lipid, e.g., crystalline cholesterol [21]. The strong SHG signal in the *elastica externa*, however, is unambiguously assigned to a protein structure, i.e., collagen. Hence, multispectral CARS imaging enables assignment of TPEF, SHG signals to the originating molecule. However, as discussed in detail in [Meyer et al. 2013 b], in order to use co-localization analysis most effectively, high spectral resolution CARS measurements need to be performed, since the separation of the clusters in the frequency scatter plot decreases with increasing spectral width.

In summary, image analysis based on colocalization is a powerful tool for interpreting multispectral CARS data in the C-H-stretching region allowing analyzing the spatial distribution of multiple Raman active marker molecules in complex tissue.



## 6 Conclusion & Outlook

Driven by the demand for novel molecular imaging tools enabling label-free *in vivo* visualization of tissue structure and composition with subcellular spatial resolution in the biomedical sciences, multimodal nonlinear imaging has matured to a promising technique capable to fit these demands over the past years. This progress is directly related to the shift in medicine from fighting infectious diseases towards clinical patterns, which are not caused by pathogens, either so-called lifestyle induced diseases, e.g., atherosclerosis, or diseases originating from molecular changes within the body, e.g., malignant tumors. As illustrated, multimodal nonlinear imaging combining SHG, TPEF and CARS signals for tissue analysis constitutes a versatile imaging tool for a wide range of disease patterns. Moreover, nonlinear microscopy provides insight into the tissue structure beyond the pure visualization of morphology: Multicontrast microscopy allows determining the tissue composition, i.e., visualizing the distribution of molecular markers. As summarized in section 3, the structural information retrieved from multimodal images compares well with the current golden standard of staining histopathology, as illustrated for epithelial and connective tissue of the head and neck, benign and malignant brain tissue as well as tissue of the blood vessels.

In the course of the presented work, for three disease entities, i.e., (i) head and neck squamous cell carcinoma, (ii) brain tumors and (iii) cardiovascular diseases, systematic studies on a representative set of samples of unlabelled dried thin tissue sections have been performed to evaluate which parameters are accessible by combining SHG, TPEF and CARS imaging modalities.

(i) In case of HNSCC detection of a large set of morphological changes associated with the process of carcinogenesis and therefore required for grading of HNSCC has been demonstrated, e.g., architectural changes including loss of epithelial stratification, cell density, the integrity of the basement membrane and dyskeratosis as well as cytologic changes like the nucleus to cytoplasmic ratio, cell and nuclear size and shape and the polarity of basal cells.

(ii) In case of brain tissue the architecture of benign brain tissue has been visual-

## Summary

---

ized, e.g., white matter, the individual layers of the grey matter and the arachnoid membrane, in addition to the detection of single cells. Disease induced alterations have been determined as demonstrated for common brain tumors, i.e., glioma and lymphoma, as well as secondary tumors, i.e., cancer brain metastases.

(iii) For cardiovascular diseases, specifically atherosclerosis, beyond visualization of the morphology of the vessel wall and the plaque deposits, major molecular constituents have been identified, i.e., elastic protein fibers composed of elastin and collagen were detected in the vessel wall, whereas in addition to triglycerides, oxidized lipids and crystalline cholesterol were detected within the plaques.

While the number of TPEF and SHG markers is limited, multispectral CARS imaging enables a further extension of the available set of molecular markers. Imaging at two resonances characteristic for  $CH_2$ - and  $CH_3$ -functional groups allows discerning lipids and proteins and enables to assign the origin of SHG signals to crystalline cholesterol or collagen.

While the morphological information is in agreement with results from staining histopathology, label-free imaging provides furthermore direct access to disease related changes in the molecular composition. However, the diagnostic relevance of the additional information about chemical alterations associated with disease progression is not yet determined, since so far only proof-of-principle studies have been performed on a limited number of samples. This results primarily from the big technical challenges connected to clinical translation of these sophisticated imaging techniques.

Therefore, from a clinical perspective another important aspect is the successful implementation of the instrumentation into a compact and rugged platform without compromising the image quality. In order to bridge this gap, i.e., to translate the methodology into clinics, in the course of this work a compact microscope has been developed. The instrument provides an exceptionally large field of view and highest transmission of 70% for NIR radiation up to 1500 nm. The high optical throughput enables using novel ultra compact, adjustment-free fiber laser light sources of modest average power, which are insensitive to environmental changes, e.g., temperature variations and vibrations, and are, therefore, of high importance for the

demonstration of a working system in clinics. Furthermore, using NIR radiation for excitation is an indispensable prerequisite in order to minimize phototoxic effects and maximize the depth penetration in native tissue.

The presented microscope provides qualitatively similar image data as compared to a standard laboratory system but at greatly reduced instrument size, power consumption, adjustment requirements and instrumental complexity, readily suited for clinical testing in the near future.

According to the interpretation of CARS images, it has been shown, that the observed CARS image contrast, which enables the detection of cell nuclei, is based on the chemical composition of tissue. Furthermore, a novel image analysis approach has been presented, which allows to derive the spatial distribution of Raman active markers from multispectral CARS images.

In the course of this work, multimodal nonlinear microscopy combining SHG, TPEF and (multispectral) CARS imaging has been successfully applied to investigate structure along with the composition, e.g., the morphochemistry, of tissue and disease associated changes for three prevalent disease patterns. In parallel tools for image analysis and interpretation have been developed and ideal parameters for the efficient combination of the three imaging modalities have been derived. On this basis a compact microscopic platform has been developed suited for clinical application. Hence in future work extended testing of the methodology on larger sets of specimens need to be performed. To mature into a clinical imaging tool, miniaturization of the multimodal nonlinear microscopy equipment is required, ideally enabling integration into endoscopes in the near future.



## 3 | Bibliographie

### Publications contributing to this Thesis

- [Meyer et al. 2011] Meyer, Tobias, Bergner, Norbert, Bielecki, Christiane, Krafft, Christoph, Akimov, Denis, Romeike, Bernd F. M., Reichart, Rupert, Kalff, Rolf, Dietzek, Benjamin, & Popp, Jürgen. 2011. Nonlinear microscopy, infrared, and Raman microspectroscopy for brain tumor analysis. *Journal of Biomedical Optics*, **16**(2), 021113–021113.
- [Baumgartl et al. 2012] Baumgartl, Martin, Gottschall, Thomas, Abreu-Afonso, Javier, Díez, Antonio, Meyer, Tobias, Dietzek, Benjamin, Rothhardt, Manfred, Popp, Jürgen, Limpert, Jens, & Tünnermann, Andreas. 2012a. Alignment-free, all-spliced fiber laser source for CARS microscopy based on four-wave-mixing. *Optics Express*, **20**(19), 21010–21018.
- [Baumgartl et al. 2012 a] Baumgartl, Martin, Chemnitz, Mario, Jauregui, Cesar, Meyer, Tobias, Dietzek, Benjamin, Popp, Jürgen, Limpert, Jens, & Tünnermann, Andreas. 2012b. All-fiber laser source for CARS microscopy based on fiber optical parametric frequency conversion. *Optics Express*, **20**(4), 4484–4493.
- [Chemnitz et al. 2012] Chemnitz, Mario, Baumgartl, Martin, Meyer, Tobias, Jauregui, Cesar, Dietzek, Benjamin, Popp, Jürgen, Limpert, Jens, & Tünnermann, Andreas. 2012. Widely tuneable fiber optical parametric amplifier for coherent anti-Stokes Raman scattering microscopy. *Optics Express*, **20**(24), 26583–26595.
- [Meyer et al. 2012] Meyer, Tobias, Bergner, Norbert, Medyukhina, Anna, Dietzek, Benjamin, Krafft, Christoph, Romeike, Bernd F. M., Reichart, Rupert, Kalff,

## Publications contributing to this Thesis

---

- Rolf, & Popp, Jürgen. 2012a. Interpreting CARS images of tissue within the C–H-stretching region. *Journal of Biophotonics*, **5**(10),729–733.
- [Meyer et al. 2013] Meyer, Tobias, Guntinas-Lichius, Orlando, von Eggeling, Ferdinand, Ernst, Günther, Akimov, Denis, Schmitt, Michael, Dietzek, Benjamin, & Popp, Jürgen. Multimodal nonlinear microscopic investigations on head and neck squamous cell carcinoma: Toward intraoperative imaging. *Head & Neck*, **35**(9), E280–E287.
- [Meyer et al. 2013 a] Meyer, Tobias, Baumgartl, Martin, Gottschall, Thomas, Pascher, Torbjörn, Wuttig, Andreas, Matthäus, Christian, Romeike, Bernd F. M., Brehm, Bernhard R., Limpert, Jens, Tünnermann, Andreas, Guntinas-Lichius, Orlando, Dietzek, Benjamin, Schmitt, Michael, & Popp, Jürgen. A compact microscope setup for multimodal nonlinear imaging in clinics and its application to disease diagnostics. *Analyst*, **138**(14), 4048–4057.
- [Meyer et al. 2013 b] Meyer, Tobias, Chemnitz, Mario, Baumgartl, Martin, Gottschall, Thomas, Pascher, Torbjorn, Matthäus, Christian, Romeike, Bernd F. M., Brehm, Bernhard R., Limpert, Jens, Tünnermann, Andreas, Schmitt, Michael, Dietzek, Benjamin, & Popp, Jürgen. Expanding multimodal microscopy by high spectral resolution CARS imaging for clinical disease diagnostics. *Analytical Chemistry*, **85**(14), 703–6715.

---

## References

- [1] R. Koch, *Investigations into the etiology of traumatic infective diseases*. (Leipzig: F. C. W. Vogel, 1878).
- [2] L. Pasteur, *Scientific Papers. Vol. XXXVIII, Part 7. The Harvard Classics*. (New York: P.F. Collier & Son,, 1909–14).
- [3] I. B. Buchwalow and W. Böcker, *Immunohistochemistry: Basics and Methods* (Springer, 2010).
- [4] A. P. Feinberg and B. Tycko, “The history of cancer epigenetics,” *Nature Reviews Cancer* **4**, 143–153 (2004).
- [5] A. Fleming, “On the Antibacterial Action of Cultures of a Penicillium, with Special Reference to their Use in the Isolation of B. influenzæ,” *British journal of experimental pathology* **10**, 226–236 (1929).
- [6] *Todesursachen in Deutschland* (Statistisches Bundesamt Wiesbaden, 2011).
- [7] E. Gabrielson, K. Berg, and R. Anbazhagan, “Functional genomics, gene arrays, and the future of pathology,” *Modern Pathology* **14**, 1294–1299 (2001).
- [8] P. A. Futreal, L. Coin, M. Marshall, T. Down, T. Hubbard, R. Wooster, N. Rahman, and M. R. Stratton, “A census of human cancer genes,” *Nature Reviews Cancer* **4**, 177–183 (2004).
- [9] W. Timp and A. P. Feinberg, “Cancer as a dysregulated epigenome allowing cellular growth advantage at the expense of the host,” *Nature Reviews Cancer* **advance online publication** (2013).
- [10] A. F. Low, G. J. Tearney, B. E. Bouma, and I.-K. Jang, “Technology insight: optical coherence tomography—current status and future development,” *Nature Clinical Practice Cardiovascular Medicine* **3**, 154–162 (2006).
- [11] R. Puri, M. I. Worthley, and S. J. Nicholls, “Intravascular imaging of vulnerable coronary plaque: current and future concepts,” *Nature Reviews Cardiology* **8**, 131–139 (2011).
- [12] B. J. Vakoc, D. Fukumura, R. K. Jain, and B. E. Bouma, “Cancer imaging by optical coherence tomography: preclinical progress and clinical potential,” *Nature Reviews Cancer* **12**, 363–368 (2012).
- [13] K. König, T. W. Becker, P. Fischer, I. Riemann, and K.-J. Halbhuber, “Pulse-length dependence of cellular response to intense near-infrared laser pulses in multiphoton microscopes,” *Optics Letters* **24**, 113–115 (1999).
- [14] A. Hopt and E. Neher, “Highly nonlinear photodamage in two-photon fluorescence microscopy,” *Biophysical Journal* **80**, 2029–2036 (2001).
- [15] H. Wang, Y. Fu, and J.-X. Cheng, “Experimental observation and theoretical analysis of Raman resonance-enhanced photodamage in coherent anti-Stokes Raman scattering microscopy,” *Journal of the Optical Society of America B* **24**, 544–552 (2007).
- [16] F. Helmchen and W. Denk, “Deep tissue two-photon microscopy,” *Nature Methods* **2**, 932–940 (2005).
- [17] P. Theer, M. T. Hasan, and W. Denk, “Two-photon imaging to a depth of 1000µm in living brains by use of a Ti:Al2O3 regenerative amplifier,” *Optics Letters* **28**, 1022–1024 (2003).
- [18] P. J. Campagnola and L. M. Loew, “Second-harmonic imaging microscopy for visualizing biomolecular arrays in cells, tissues and organisms,” *Nat Biotech* **21**, 1356–1360 (2003).
- [19] L. Moreaux, O. Sandre, S. Charpak, M. Blanchard-Desce, and J. Mertz, “Coherent scattering in multi-harmonic light microscopy,” *Biophysical journal* **80**, 1568–1574 (2001).
- [20] W. Mohler, A. C. Millard, and P. J. Campagnola, “Second harmonic generation imaging of endogenous structural proteins,” *Methods* **29**, 97–109 (2003).

## References

---

- [21] J. L. Suhailim, C.-Y. Chung, M. B. Lilledahl, R. S. Lim, M. Levi, B. J. Tromberg, and E. O. Potma, "Characterization of Cholesterol Crystals in Atherosclerotic Plaques Using Stimulated Raman Scattering and Second-Harmonic Generation Microscopy," *Biophysical Journal* **102**, 1988–1995 (2012).
- [22] M. A. Albota, C. Xu, and W. W. Webb, "Two-photon fluorescence excitation cross sections of biomolecular probes from 690 to 960 nm," *Applied Optics* **37**, 7352–7356 (1998).
- [23] S. Huang, A. A. Heikal, and W. W. Webb, "Two-photon fluorescence spectroscopy and microscopy of NAD(P)H and flavoprotein," *Biophysical Journal* **82**, 2811–2825 (2002).
- [24] W. R. Zipfel, R. M. Williams, R. Christie, A. Y. Nikitin, B. T. Hyman, and W. W. Webb, "Live tissue intrinsic emission microscopy using multiphoton-excited native fluorescence and second harmonic generation," *Proceedings of the National Academy of Sciences of the United States of America* **100**, 7075–7080 (2003).
- [25] A. Diaspro, G. Chirico, and M. Collini, "Two-photon fluorescence excitation and related techniques in biological microscopy," *Quarterly Reviews of Biophysics* **38**, 97–166 (2005).
- [26] B.-G. Wang, K. König, and K.-J. Halhuber, "Two-photon microscopy of deep intravital tissues and its merits in clinical research," *Journal of Microscopy* **238**, 1–20 (2010).
- [27] C. Xu, W. Zipfel, J. B. Shear, R. M. Williams, and W. W. Webb, "Multiphoton fluorescence excitation: new spectral windows for biological nonlinear microscopy," *Proceedings of the National Academy of Sciences* **93**, 10763–10768 (1996).
- [28] R. Tuma, "Raman spectroscopy of proteins: from peptides to large assemblies," *Journal of Raman Spectroscopy* **36**, 307–319 (2005).
- [29] R. Schweitzer-Stenner, "Advances in vibrational spectroscopy as a sensitive probe of peptide and protein structure: A critical review," *Vibrational Spectroscopy* **42**, 98–117 (2006).
- [30] S. Bresson, M. E. Marssi, and B. Khelifa, "Raman spectroscopy investigation of various saturated monoacid triglycerides," *Chemistry and Physics of Lipids* **134**, 119–129 (2005).
- [31] N. B. Colthup, L. H. Daly, and S. E. Wiberley, *Introduction to infrared and Raman spectroscopy* (Academic Press, 1990).
- [32] P. Y. Bruice, ed., *Organic Chemistry* (Pearson Education Inc, 2004).
- [33] C. V. Raman and K. Krishnan, "A new type of secondary radiation," *Nature* **121**, 501–502 (1928).
- [34] C. V. Raman, "A change of wave-length in light scattering," *Nature* **121**, 619–619 (1928).
- [35] C. Raman and K. Krishnan, "The optical analogue of the Compton effect," *Nature* **121**, 711–711 (1928).
- [36] M. O. Trulson and R. A. Mathies, "Raman cross section measurements in the visible and ultraviolet using an integrating cavity: Application to benzene, cyclohexane, and cacodylate," *The Journal of Chemical Physics* **84**, 2068–2074 (1986).
- [37] L. Kastrop and S. W. Hell, "Absolute optical cross section of individual fluorescent molecules," *Angewandte Chemie International Edition* **43**, 6646–6649 (2004).
- [38] W. S. Barney, L. M. Wingen, M. J. Lakin, T. Brauers, J. Stutz, and B. J. Finlayson-Pitts, "Infrared absorption cross-section measurements for nitrous acid (hono) at room temperature," *The Journal of Physical Chemistry A* **104**, 1692–1699 (2000).
- [39] J.-X. Cheng and X. S. Xie, eds., *Coherent Raman Scattering Microscopy* (CRC Press, 2012).
- [40] C. W. Freudiger, W. Min, B. G. Saar, S. Lu, G. R. Holtom, C. He, J. C. Tsai, J. X. Kang, and X. S. Xie, "Label-Free Biomedical Imaging with High Sensitivity by Stimulated Raman Scattering Microscopy," *Science* **322**, 1857–1861 (2008).



- 
- [41] A. Zumbusch, G. R. Holtom, and X. S. Xie, "Three-Dimensional Vibrational Imaging by Coherent Anti-Stokes Raman Scattering," *Phys. Rev. Lett.* **82**, 4142–4145 (1999).
- [42] C. W. Freudiger, M. B. J. Roeffaers, X. Zhang, B. G. Saar, W. Min, and X. S. Xie, "Optical Heterodyne-Detected Raman-Induced Kerr Effect (OHD-RIKE) Microscopy," *J. Phys. Chem. B* **115**, 5574–5581 (2011).
- [43] W. M. Tolles, J. W. Nibler, J. R. McDonald, and A. B. Harvey, "A review of the theory and application of coherent anti-stokes raman spectroscopy (CARS)," *Applied Spectroscopy* **31**, 253–271 (1977).
- [44] J. X. Cheng, A. Volkmer, and X. S. Xie, "Theoretical and experimental characterization of coherent anti-stokes raman scattering microscopy," *Journal of the Optical Society of America B - Optical Physics* **19**, 1363–1375 (2002).
- [45] A. Volkmer, "Vibrational imaging and microspectroscopies based on coherent anti-Stokes Raman scattering microscopy," *Journal of Physics D: Applied Physics* **38**, R59–R81 (2005).
- [46] C. L. Evans, E. O. Potma, M. Puoris'haag, D. Cote, C. P. Lin, and X. S. Xie, "Chemical imaging of tissue in vivo with video-rate coherent anti-Stokes Raman scattering microscopy." *Proc Natl Acad Sci U S A* **102**, 16807–16812 (2005).
- [47] M. Okuno and H.-o. Hamaguchi, "Multifocus confocal raman microspectroscopy for fast multimode vibrational imaging of living cells," *Optics Letters* **35**, 4096–4098 (2010).
- [48] D. Pestov, G. O. Ariunbold, X. Wang, R. K. Murawski, V. A. Sautenkov, A. V. Sokolov, and M. O. Scully, "Coherent versus incoherent raman scattering: molecular coherence excitation and measurement," *Optics Letters* **32**, 1725–1727 (2007).
- [49] M. Cui, B. R. Bachler, and J. P. Ogilvie, "Comparing coherent and spontaneous raman scattering under biological imaging conditions," *Optics Letters* **34**, 773–775 (2009).
- [50] J. X. Cheng, Y. K. Jia, G. F. Zheng, and X. S. Xie, "Laser-scanning coherent anti-stokes Raman scattering microscopy and applications to cell biology," *Biophysical Journal* **83**, 502–509 (2002).
- [51] R. Mouras, G. Rischitor, A. Downes, D. Salter, and A. Elfick, "Nonlinear optical microscopy for drug delivery monitoring and cancer tissue imaging," *Journal of Raman Spectroscopy* **41**, 848–852 (2010).
- [52] C. L. Evans and X. S. Xie, "Coherent Anti-Stokes Raman Scattering Microscopy: Chemical Imaging for Biology and Medicine," *Annual Review of Analytical Chemistry* (2008) **1**, 883–909 (2008).
- [53] T. T. Le, S. Yue, and J.-X. Cheng, "Shedding new light on lipid biology with CARS microscopy," *Journal of Lipid Research* (2010).
- [54] J. P. Pezacki, J. A. Blake, D. C. Danielson, D. C. Kennedy, R. K. Lyn, and R. Singaravelu, "Chemical contrast for imaging living systems: molecular vibrations drive CARS microscopy," *Nat Chem Biol* **7**, 137–145 (2011).
- [55] S. Koljenovic', T. C. Bakker Schut, R. Wolthuis, B. de Jong, L. Santos, P. J. Caspers, J. M. Kros, and G. J. Puppels, "Tissue characterization using high wave number raman spectroscopy," *Journal of Biomedical Optics* **10**, 031116–031116 (2005).
- [56] J. Mo, W. Zheng, J. J. H. Low, J. Ng, A. Ilancheran, and Z. Huang, "High wavenumber raman spectroscopy for in vivo detection of cervical dysplasia," *Analytical Chemistry* **81**, 8908–8915 (2009).
- [57] J. X. Cheng, L. D. Book, and X. S. Xie, "Polarization coherent anti-Stokes Raman scattering microscopy," *Opt. Lett.* **26**, 1341–1343 (2001).
- [58] A. Volkmer, L. D. Book, and X. S. Xie, "Time-resolved coherent anti-Stokes Raman scattering microscopy: Imaging based on Raman free induction decay," *Applied Physics Letters* **80**, 1505–1507 (2002).
-

## References

---

- [59] R. Selm, M. Winterhalder, A. Zumbusch, G. Krauss, T. Hanke, A. Sell, and A. Leitenstorfer, "Ultrabroadband background-free coherent anti-Stokes Raman scattering microscopy based on a compact Er: fiber laser system," *Optics Letters* **35**, 3282–3284 (2010).
- [60] D. L. Marks, C. Vinegoni, J. S. Bredfeldt, and S. A. Boppart, "Interferometric differentiation between resonant coherent anti-Stokes Raman scattering and nonresonant four-wave-mixing processes," *Applied Physics Letters* **85**, 5787–5789 (2004).
- [61] J. X. Cheng, A. Volkmer, L. D. Book, and X. S. Xie, "An epi-detected coherent anti-stokes raman scattering (E-CARS) microscope with high spectral resolution and high sensitivity," *Journal of Physical Chemistry B* **105**, 1277–1280 (2001).
- [62] D. A. Boas, C. Pitris, and N. Ramanujam, eds., *Handbook of Biomedical Optics* (CRC Press, Taylor and Francis Group, Boca Raton, London, New York, 2011).
- [63] T. L. Troy and S. N. Thennadil, "Optical properties of human skin in the near infrared wavelength range of 1000 to 2200 nm," *Journal of Biomedical Optics* **6**, 167–176 (2001).
- [64] C. R. Simpson, M. Kohl, M. Essenpreis, and M. Cope, "Near-infrared optical properties of ex vivo human skin and subcutaneous tissues measured using the monte carlo inversion technique," *Physics in Medicine and Biology* **43**, 2465 (1998).
- [65] L. M. Akst and M. Strome, "Laser surgery for head and neck cancer," in "Squamous Cell Head and Neck Cancer," D. J. A. MD, ed. (Humana Press, 2005), *Current Clinical Oncology*, pp. 43–57.
- [66] Y. Fu, H. Wang, R. Shi, and J.-X. Cheng, "Characterization of photodamage in coherent anti-Stokes Raman scattering microscopy," *Optics Express* **14**, 3942–3951 (2006).
- [67] J. P. Sapp, L. Eversole, and G. Wysocki, *Contemporary Oral and Maxillofacial Pathology* (Elsevier, 2003).
- [68] D. Piston, "Imaging living cells and tissues by two-photon excitation microscopy," *Trends in Cell Biology* **9**, 66–69 (1999).
- [69] J. Reibel, "Prognosis of oral pre-malignant lesions: significance of clinical, histopathological, and molecular biological characteristics," *Critical Reviews in Oral Biology and Medicine: An Official Publication of the American Association of Oral Biologists* **14**, 47–62 (2003).
- [70] I. Pavlova, M. Williams, A. El-Naggar, R. Richards-Kortum, and A. Gillenwater, "Understanding the biological basis of autofluorescence imaging for oral cancer detection: High-resolution fluorescence microscopy in viable tissue," *Clinical cancer research : an official journal of the American Association for Cancer Research* **14**, 2396–2404 (2008).
- [71] Y. Wu, P. Xi, J. Qu, T.-H. Cheung, and M.-Y. Yu, "Depth-resolved fluorescence spectroscopy reveals layered structure of tissue," *Optics Express* **12**, 3218–3223 (2004).
- [72] Y. Wu, P. Xi, J. Qu, T.-H. Cheung, and M.-Y. Yu, "Depth-resolved fluorescence spectroscopy of normal and dysplastic cervical tissue," *Optics Express* **13**, 382–388 (2005).
- [73] M. C. Skala, J. M. Squirrell, K. M. Vrotsos, J. C. Eickhoff, A. Gendron-Fitzpatrick, K. W. Eliceiri, and N. Ramanujam, "Multiphoton microscopy of endogenous fluorescence differentiates normal, precancerous, and cancerous squamous epithelial tissues," *Cancer Research* **65**, 1180–1186 (2005).
- [74] A. Behin, K. Hoang-Xuan, A. F. Carpentier, and J.-Y. Delattre, "Primary brain tumours in adults," *The Lancet* **361**, 323–331 (2003).
- [75] C. L. Evans, X. Xu, S. Kesari, X. S. Xie, S. T. C. Wong, and G. S. Young, "Chemically-selective imaging of brain structures with CARS microscopy," *Optics Express* **15**, 12076–12087 (2007).

- 
- [76] T. T. Le and J.-X. Cheng, "Non-Linear Optical Imaging of Obesity-related Health Risks: Review," *Journal of Innovative Optical Health Sciences* **02**, 9–25 (2009).
- [77] C. Matthäus, G. Bergner, C. Krafft, B. Dietzek, S. Lorkowski, and J. Popp, "Monitoring intra-cellular lipid metabolism in macrophages by Raman- and CARS-microscopy," in "Biophotonics: Photonic Solutions for Better Health Care II," , vol. 7715, J. Popp, W. Drexler, V. V. Tuchin, and D. L. Matthews, eds. (SPIE, Brussels, Belgium, 2010), vol. 7715, pp. 771511–771518.
- [78] M. C. Wang, W. Min, C. W. Freudiger, G. Ruvkun, and X. S. Xie, "RNAi screening for fat regulatory genes with SRS microscopy," *Nature Methods* **8**, 135–138 (2011).
- [79] D. R. J. Owen, A. C. Lindsay, R. P. Choudhury, and Z. A. Fayad, "Imaging of Atherosclerosis," *Annual Review of Medicine* **62**, 25–40 (2011).
- [80] V. Z. Rocha and P. Libby, "Obesity, inflammation, and atherosclerosis," *Nature Reviews Cardiology* **6**, 399–409 (2009).
- [81] K. Arakawa, K. Isoda, T. Ito, K. Nakajima, T. Shibuya, and F. Ohsuzu, "Fluorescence Analysis of Biochemical Constituents Identifies Atherosclerotic Plaque With a Thin Fibrous Cap," *Arteriosclerosis, Thrombosis, and Vascular Biology* **22**, 1002–1007 (2002).
- [82] T. T. Le, I. M. Langohr, M. J. Locker, M. Sturek, and J.-X. Cheng, "Label-free molecular imaging of atherosclerotic lesions using multimodal nonlinear optical microscopy," *Journal of biomedical optics* **12**, 54007 (2007).
- [83] R. Lu, W. Gan, B.-h. Wu, Z. Zhang, Y. Guo, and H.-f. Wang, "C–H Stretching Vibrations of Methyl, Methylene and Methine Groups at the Vapor/Alcohol ( $n = 1-8$ ) Interfaces," *The Journal of Physical Chemistry B* **109**, 14118–14129 (2005).
- [84] X. L. Nan, E. O. Potma, and X. S. Xie, "Nonperturbative chemical imaging of organelle transport in living cells with coherent anti-stokes Raman scattering microscopy," *Biophysical Journal* **91**, 728–735 (2006).
- [85] D. Kobat, M. E. Durst, N. Nishimura, A. W. Wong, C. B. Schaffer, and C. Xu, "Deep tissue multiphoton microscopy using longer wavelength excitation," *Optics Express* **17**, 13354–13364 (2009).
- [86] N. G. Horton, K. Wang, D. Kobat, C. G. Clark, F. W. Wise, C. B. Schaffer, and C. Xu, "In vivo three-photon microscopy of subcortical structures within an intact mouse brain," *Nature Photonics* **7**, 205–209 (2013).
- [87] S. Bégin, B. Burgoyne, V. Mercier, A. Villeneuve, R. Vallée, and D. Côté, "Coherent anti-Stokes Raman scattering hyperspectral tissue imaging with a wavelength-swept system," *Biomedical Optics Express* **2**, 1296–1306 (2011).
- [88] M. D. Duncan, J. Reintjes, and T. J. Manuccia, "Scanning coherent anti-stokes raman microscope," *Optics Letters* **7**, 350–352 (1982).
- [89] M. D. Duncan, "Molecular discrimination and contrast enhancement using a scanning coherent anti-stokes raman microscope," *Optics Communications* **50**, 307–312 (1984).
- [90] M. D. Duncan, J. Reintjes, and T. J. Manuccia, "Imaging biological compounds using the coherent anti-stokes raman scattering microscope," *Optical Engineering* **24**, 352–355 (1985).
- [91] E. O. Potma, D. J. Jones, J. X. Cheng, X. S. Xie, and J. Ye, "High-sensitivity coherent anti-Stokes Raman scattering microscopy with two tightly synchronized picosecond lasers," *Optics Letters* **27**, 1168–1170 (2002).
- [92] D. J. Jones, E. O. Potma, J. X. Cheng, B. Burfeindt, Y. Pang, J. Ye, and X. S. Xie, "Synchronization of two passively mode-locked, picosecond lasers within 20 fs for coherent anti-Stokes Raman scattering microscopy," *Review of Scientific Instruments* **73**, 2843–2848 (2002).
-

## References

---

- [93] H. Wang, Y. Fu, P. Zickmund, R. Shi, and J.-X. Cheng, “Coherent anti-stokes Raman scattering imaging of axonal myelin in live spinal tissues.” *Biophys J* **89**, 581–591 (2005).
- [94] T. T. Le, C. W. Rehrer, T. B. Huff, M. B. Nichols, I. G. Camarillo, and J.-X. Cheng, “Nonlinear Optical Imaging to Evaluate the Impact of Obesity on Mammary Gland and Tumor Stroma,” *Molecular imaging : official journal of the Society for Molecular Imaging* **6**, 205–211 (2007).
- [95] V. V. Yakovlev, “Advanced instrumentation for non-linear Raman microscopy,” *Journal of Raman Spectroscopy* **34**, 957–964 (2003).
- [96] F. Ganikhanov, S. Carrasco, X. S. Xie, M. Katz, W. Seitz, and D. Kopf, “Broadly tunable dual-wavelength light source for coherent anti-Stokes Raman scattering microscopy,” *Optics Letters* **31**, 1292–1294 (2006).
- [97] H. Chen, H. Wang, M. N. Slipchenko, Y. Jung, Y. Shi, J. Zhu, K. K. Buhman, and J.-X. Cheng, “A multimodal platform for nonlinear optical microscopy and microspectroscopy,” *Optics Express* **17**, 1282–1290 (2009).
- [98] N. Dudovich, D. Oron, and Y. Silberberg, “Single-pulse coherently controlled nonlinear Raman spectroscopy and microscopy.” *Nature* **418**, 512–514 (2002).
- [99] B. von Vacano, T. Buckup, and M. Motzkus, “Highly sensitive single-beam heterodyne coherent anti-Stokes Raman scattering,” *Optics Letters* **31**, 2495–2497 (2006).
- [100] B. von Vacano and M. Motzkus, “Time-resolved two color single-beam CARS employing supercontinuum and femtosecond pulse shaping,” *Optics Communications* **264**, 488–493 (2006).
- [101] S. Yue, M. N. Slipchenko, and J.-X. Cheng, “Multimodal nonlinear optical microscopy,” *Laser & Photonics Reviews* **5**, 496–512 (2011).
- [102] A. F. Pegoraro, A. D. Slepov, A. Ridsdale, J. P. Pezacki, and A. Stolow, “Single laser source for multimodal coherent anti-Stokes Raman scattering microscopy,” *Applied Optics* **49**, F10–F17 (2010).
- [103] T. B. Huff, Y. Shi, Y. Fu, H. Wang, and J.-X. Cheng, “Multimodal nonlinear optical microscopy and applications to central nervous system imaging,” *Ieee Journal of Selected Topics In Quantum Electronics* **14**, 4–9 (2008).
- [104] H. N. Paulsen, K. M. Hilligsoe, J. Thogersen, S. R. Keiding, and J. J. Larsen, “Coherent anti-Stokes Raman scattering microscopy with a photonic crystal fiber based light source,” *Optics Letters* **28**, 1123–1125 (2003).
- [105] H. Kano and H. Hamaguchi, “Near-infrared coherent anti-Stokes Raman scattering microscopy using supercontinuum generated from a photonic crystal fiber,” *Applied Physics B: Lasers and Optics* **80**, 243–246 (2005).
- [106] H. Kano and H. Hamaguchi, “Ultrabroadband ( $> 2500 \text{ cm}^{-1}$ ) multiplex coherent anti-Stokes Raman scattering microspectroscopy using a supercontinuum generated from a photonic crystal fiber,” *Applied Physics Letters* **86**, 121113 (2005).
- [107] H. Kano and H. Hamaguchi, “Vibrationally resonant imaging of a single living cell by supercontinuum-based multiplex coherent anti-Stokes Raman scattering microspectroscopy,” *Optics Express* **13**, 1322–1327 (2005).
- [108] H. Kano and H. Hamaguchi, “In-vivo multi-nonlinear optical imaging of a living cell using a supercontinuum light source generated from a photonic crystal fiber,” *Optics Express* **14**, 2798–2804 (2006).
- [109] H. Kano and H. Hamaguchi, “Dispersion-compensated supercontinuum generation for ultrabroadband multiplex coherent anti-Stokes Raman scattering spectroscopy,” *Journal of Raman Spectroscopy* **37**, 411–415 (2006).
- [110] D. Li, W. Zheng, Y. Zeng, and J. Y. Qu, “In vivo and simultaneous multimodal imaging: Integrated multiplex coherent anti-Stokes Raman scattering and two-photon microscopy,” *Applied Physics Letters* **97**, 223702 (2010).

- [111] K. Kieu, B. G. Saar, G. R. Holtom, X. S. Xie, and F. W. Wise, "High-power picosecond fiber source for coherent Raman microscopy," *Optics Letters* **34**, 2051–2053 (2009).
- [112] A. C. T. Ko, A. Ridsdale, M. S. D. Smith, L. B. Mostaco-Guidolin, M. D. Hewko, A. F. Pegoraro, E. K. Kohlenberg, B. Schattka, M. Shiomi, A. Stolow, and M. G. Sowa, "Multimodal nonlinear optical imaging of atherosclerotic plaque development in myocardial infarction-prone rabbits." *Journal of biomedical optics* **15**, 20501 (2010).
- [113] G. Krauss, T. Hanke, A. Sell, D. Träutlein, A. Leitenstorfer, R. Selm, M. Winterhalder, and A. Zumbusch, "Compact coherent anti-Stokes Raman scattering microscope based on a picosecond two-color Er: fiber laser system," *Optics Letters* **34**, 2847–2849 (2009).
- [114] A. F. Pegoraro, A. Ridsdale, D. J. Moffatt, J. P. Pezacki, B. K. Thomas, L. Fu, L. Dong, M. E. Fermann, and A. Stolow, "All-fiber CARS microscopy of live cells," *Optics Express* **17**, 20700–20706 (2009).
- [115] Y.-H. Zhai, C. Goulart, J. E. Sharping, H. Wei, S. Chen, W. Tong, M. N. Slipchenko, D. Zhang, and J.-X. Cheng, "Multimodal coherent anti-stokes raman spectroscopic imaging with a fiber optical parametric oscillator," *Applied Physics Letters* **98**, 191106 (2011).
- [116] S. Lefrancois, D. Fu, G. R. Holtom, L. Kong, W. J. Wadsworth, P. Schneider, R. Herda, A. Zach, X. Sunney Xie, and F. W. Wise, "Fiber four-wave mixing source for coherent anti-Stokes Raman scattering microscopy," *Optics Letters* **37**, 1652–1654 (2012).
- [117] R. Cicchi, D. Kapsokalyvas, V. D. Giorgi, V. Maio, A. V. Wiechen, D. Massi, T. Lotti, and F. S. Pavone, "Scoring of collagen organization in healthy and diseased human dermis by multiphoton microscopy," *Journal of Biophotonics* **3**, 34–43 (2010).
- [118] A. Medyukhina, N. Vogler, I. Latka, S. Kemper, M. Böhm, B. Dietzek, and J. Popp, "Automated classification of healthy and keloidal collagen patterns based on processing of SHG images of human skin," *Journal of Biophotonics* **4**, 627–636 (2011).
- [119] R. Cicchi, N. Vogler, D. Kapsokalyvas, B. Dietzek, J. Popp, and F. S. Pavone, "From molecular structure to tissue architecture: collagen organization probed by SHG microscopy," *Journal of Biophotonics* **6**, 129–142 (2013).
- [120] A. Medyukhina, M. Tobias, M. Schmitt, B. F. M. Romeike, B. Dietzek, and J. Popp, "Towards automated segmentation of cells and cell nuclei in nonlinear optical microscopy," *Journal of Biophotonics* (2012).
- [121] R. S. Lim, J. L. Suhaim, S. Miyazaki-Anzai, M. Miyazaki, M. Levi, E. O. Potma, and B. J. Tromberg, "Identification of cholesterol crystals in plaques of atherosclerotic mice using hyperspectral CARS imaging," *The Journal of Lipid Research* **52**, 2177–2186 (2011).
- [122] C.-Y. Lin, J. L. Suhaim, C. L. Nien, M. D. Miljković, M. Diem, J. V. Jester, and E. O. Potma, "Picosecond spectral coherent anti-Stokes Raman scattering imaging with principal component analysis of meibomian glands," *Journal of Biomedical Optics* **16**, 21104 (2011).
- [123] Q. Li, A. Lau, T. J. Morris, L. Guo, C. B. Fordyce, and E. F. Stanley, "A Syntaxin 1, G $\alpha$ o, and N-Type Calcium Channel Complex at a Presynaptic Nerve Terminal: Analysis by Quantitative Immunocolocalization," *The Journal of Neuroscience* **24**, 4070–4081 (2004).



## 4 | Documentation of Authorship

### **Nonlinear microscopy, infrared, and Raman microspectroscopy for brain tumor analysis**

Tobias Meyer, Norbert Bergner, Christiane Bielecki, Christoph Krafft, Denis Akimov, Bernd F. M. Romeike, Rupert Reichart, Rolf Kalff, Benjamin Dietzek, and Jürgen Popp. *Journal of Biomedical Optics*, 16(2):021113–021113, 2011.

Tobias Meyer*	Acquisition and analysis of CARS data, preparation of the manuscript
Norbert Bergner*	Acquisition and analysis of Raman data
Christiane Bielecki	sample preparation, data analysis
Christoph Krafft	Interpretation of Raman data, preparation of the manuscript
Denis Akimov	Acquisition of CARS data, setting up CARS experiment
Bernd F. M. Romeike	Preparation of tissue specimen, staining histopathology, preparation of manuscript
Rupert Reichart	Procuration biopsy specimen
Rolf Kalff	Procuration biopsy specimen
Benjamin Dietzek	Project coordination and supervision, preparation of the manuscript
Jürgen Popp	Project coordination and supervision, discussion of results

\* both authors share first authorship of this manuscript.

All authors edited, revised and proof read the final manuscript.

### Interpreting CARS images of tissue within the C–H-stretching region

Tobias Meyer, Norbert Bergner, Anna Medyukhina, Benjamin Dietzek, Christoph Krafft, Bernd F. M. Romeike, Rupert Reichart, Rolf Kalff, and Jürgen Popp. *Journal of Biophotonics*, 5(10):729–733, 2012.

Tobias Meyer*	Acquisition and analysis of CARS data, preparation of the manuscript
Norbert Bergner*	Acquisition and analysis of Raman data
Anna Medyukhina	Development of automated image analysis for cell and cell nuclei detection, preparation of the manuscript
Benjamin Dietzek	Project supervision and coordination, preparation of the manuscript
Christoph Krafft	Interpretation of Raman data, preparation of the manuscript
Bernd F. M. Romeike	Preparation of the tissue specimen, staining histopathology, preparation of manuscript
Rupert Reichart	Procuration biopsy specimen
Rolf Kalff	Procuration biopsy specimen
Jürgen Popp	Project coordination and supervision, discussion of results

\* both authors share first authorship of this manuscript.

All authors edited, revised and proof read the final manuscript.

### Multimodal nonlinear microscopic investigations on head and neck squamous cell carcinoma: Toward intraoperative imaging

Tobias Meyer, Orlando Guntinas-Lichius, Ferdinand von Eggeling, Günther Ernst, Denis Akimov, Michael Schmitt, Benjamin Dietzek, and Jürgen Popp. *Head & Neck*, 35(9):E280–E287, 2013.

Tobias Meyer	Acquisition and analysis of CARS data, preparation of the manuscript
Orlando Guntinas-Lichius	Project coordination and supervision, procuration of biopsy specimen, preparation of manuscript
Ferdinand von Eggeling	Project coordination and supervision
Günther Ernst	Preparation of the tissue specimen, staining histopathology



Denis Akimov	Acquisition of CARS data, setting up CARS experiment
Michael Schmitt	Project supervision and coordination, discussion of results
Benjamin Dietzek	Project supervision and coordination, preparation of the manuscript, discussion of results
Jürgen Popp	Project coordination and supervision, discussion of results

All authors edited, revised and proof read the final manuscript.

### **All-fiber laser source for CARS microscopy based on fiber optical parametric frequency conversion**

Martin Baumgartl, Mario Chemnitz, Cesar Jauregui, Tobias Meyer, Benjamin Dietzek, Jürgen Popp, Jens Limpert, and Andreas Tünnermann. *Optics Express*, 20(4):4484–4493, 2012.

Martin Baumgartl	Development of laser source, data acquisition and analysis, preparation of the manuscript
Mario Chemnitz	Development of laser source
Cesar Jauregui	Project supervision and coordination, preparation of the manuscript
Tobias Meyer	Acquisition and analysis of CARS data
Benjamin Dietzek	Project coordination and supervision regarding CARS data acquisition and analysis
Jürgen Popp	Project coordination and supervision regarding CARS data acquisition and analysis, discussion of results
Jens Limpert	Project supervision and coordination, preparation of the manuscript
Andreas Tünnermann	Project supervision and coordination

All authors edited, revised and proof read the final manuscript.

### **Alignment-free, all-spliced fiber laser source for CARS microscopy based on four-wave-mixing**

Martin Baumgartl, Thomas Gottschall, Javier Abreu-Afonso, Antonio Díez, Tobias Meyer, Benjamin Dietzek, Manfred Rothhardt, Jürgen Popp, Jens Limpert, and Andreas Tünnermann. *Optics Express*, 20(19):21010–21018, 2012.

Martin Baumgartl	Construction of laser source, data acquisition and analysis, preparation of the manuscript
Thomas Gottschall	Setting up of laser source, data acquisition and analysis
Javier Abreu-Afonso	Setting up of laser source, data acquisition
Antonio Díez	Project coordination and supervision
Tobias Meyer	Acquisition and analysis of CARS data
Benjamin Dietzek	Project coordination and supervision regarding CARS data acquisition and analysis, discussion of results
Manfred Rothhardt	Development of parts of the fiber laser source
Jürgen Popp	Project coordination and supervision regarding CARS data acquisition and analysis, discussion of results
Jens Limpert	Project coordination and supervision
Andreas Tünnermann	Project coordination and supervision

All authors edited, revised and proof read the final manuscript.

**Widely tuneable ber optical parametric amplifier for coherent anti-Stokes Raman scattering microscopy**

Mario Chemnitz, Martin Baumgartl, Tobias Meyer, Cesar Jauregui, Benjamin Dietzek, Jürgen Popp, Jens Limpert, and Andreas Tünnermann. *Optics Express*, 20(24):26583–26595, 2012.

Mario Chemnitz	Construction of laser source, data acquisition and analysis, preparation of the manuscript
Martin Baumgartl	Construction of laser source, data acquisition and analysis, preparation of the manuscript
Tobias Meyer	Acquisition and analysis of CARS data, preparation of the manuscript
Cesar Jauregui	Project supervision and coordination, preparation of the manuscript
Benjamin Dietzek	Project coordination and supervision regarding CARS data acquisition and analysis, discussion of results
Jürgen Popp	Project coordination and supervision regarding CARS data acquisition and analysis, discussion of results
Jens Limpert	Project coordination and supervision
Andreas Tünnermann	Project coordination and supervision

All authors edited, revised and proof read the final manuscript.

### **A compact microscope setup for multimodal nonlinear imaging in clinics and its application to disease diagnostics**

Tobias Meyer, Martin Baumgartl, Thomas Gottschall, Torbjörn Pascher, Andreas Wuttig, Christian Matthäus, Bernd F. M. Romeike, Bernhard R. Brehm, Jens Limpert, Andreas Tünnermann, Orlando Guntinas-Lichius, Benjamin Dietzek, Michael Schmitt, and Jürgen Popp. *Analyst*, 138(14):4048-4057, 2013.

Tobias Meyer	Design and construction of microscope setup, data acquisition and analysis, preparation of the manuscript
Martin Baumgartl	Design and construction of the fiber laser, data acquisition
Thomas Gottschall	Design and construction of the fiber laser, data acquisition
Torbjörn Pascher	Electronic hardware and data acquisition software design and construction
Andreas Wuttig	Optimization and modelling of the scan lens system
Christian Matthäus	Tissue specimen preparation, data analysis and interpretation
Bernd F.M. Romeike	Preparation of human atherosclerotic tissue and rabbit model specimen, staining histopathology, data analysis and interpretation, preparation of manuscript
Bernhard R. Brehm	Supervision and coordination of animal model experiments, taking of tissue specimen
Jens Limpert	Project coordination and supervision of fiber laser development, discussion of results
Andreas Tünnermann	Project initiation, coordination and supervision regarding fiber laser development, discussion of results
Orlando Guntinas-Lichius	Collection of cancer tissue biopsies of the head and neck, interpretation of the image data
Benjamin Dietzek	Project coordination, preparation of the manuscript, discussion of results
Michael Schmitt	Project coordination, preparation of the manuscript, discussion of results
Jürgen Popp	Project initiation, coordination and supervision, discussion of results

All authors edited, revised and proof read the final manuscript.

**Expanding multimodal microscopy by high spectral resolution CARS imaging for clinical disease diagnostics**

Tobias Meyer, Mario Chemnitz, Martin Baumgartl, Thomas Gottschall, Torbjörn Pascher, Christian Matthäus, Bernd F. M. Romeike, Bernhard R. Brehm, Jens Limpert, Andreas Tünnemann, Michael Schmitt, Benjamin Dietzek, and Jürgen Popp. *Analytical Chemistry*, 85(14):6703-6715, 2013.

Tobias Meyer	Acquisition and analysis of CARS data, preparation of the manuscript
Mario Chemnitz	Construction of laser source and data acquisition
Martin Baumgartl	Construction of laser source and data acquisition
Thomas Gottschall	Setting up laser source and data acquisition
Torbjörn Pascher	Development, design and construction of electronic hardware and data acquisition software of the microscope
Christian Matthäus	Tissue specimen preparation, data interpretation
Bernd F.M. Romeike	Preparation of tissue specimen, staining histopathology, preparation of manuscript
Bernhard R. Brehm	Project coordination and supervision, procurement of biopsy specimen
Jens Limpert	Project coordination and supervision
Andreas Tünnemann	Project coordination and supervision
Michael Schmitt	Project coordination and supervision, discussion of results, preparation of the manuscript
Benjamin Dietzek	Project coordination and supervision, discussion of results, preparation of the manuscript
Jürgen Popp	Project coordination and supervision, discussion of results

All authors edited, revised and proof read the final manuscript.

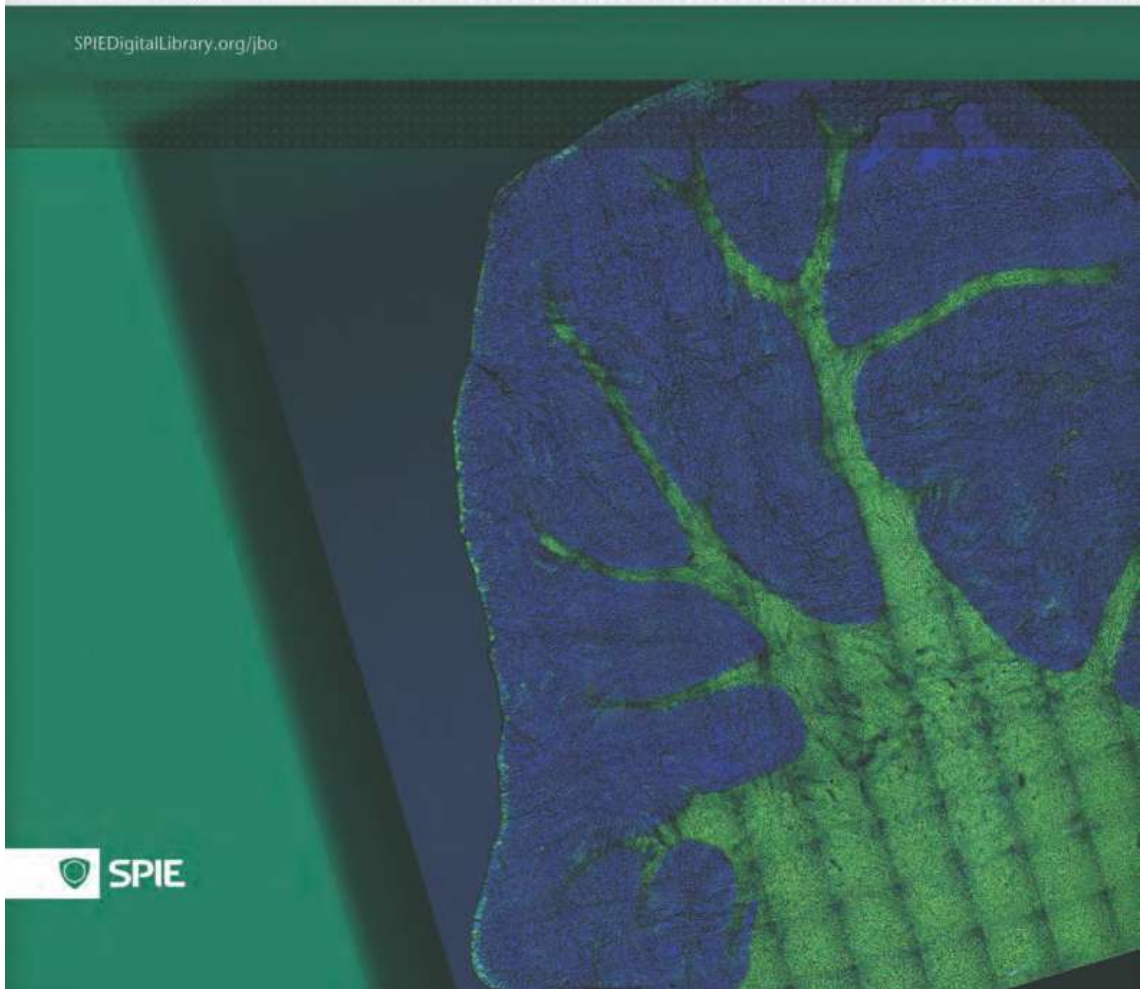
Herewith the accuracy of the Documentation of Authorship is approved.

Prof. Dr. Jürgen Popp

Vol. 16 · No. 2 | February 2011  
ISSN 1083-3668

# Journal of Biomedical Optics

[SPIEDigitalLibrary.org/jbo](http://SPIEDigitalLibrary.org/jbo)



 SPIE

**Adapted with kind permission from SPIE:**

**Authors:** Tobias Meyer, Norbert Bergner, Christiane Bielecki, Christoph Krafft, Denis Akimov, Bernd F. M. Romeike, Rupert Reichart, Rolf Kalff, Benjamin Dietzek, and Jürgen Popp.

**Titel:** "Nonlinear microscopy, infrared, and Raman microspectroscopy for brain tumor analysis."

**Journal:** *Journal of Biomedical Optics*, 16(2):021113–021113, **2011**.

©Copyright 2011 The International Society for Optics and Photonics (SPIE).

Reproduced with permission.





## 5 | Nonlinear Microscopy, IR and Raman Microspectroscopy for Brain Tumor Analysis

**Tobias Meyer,<sup>a\*</sup> Norbert Bergner,<sup>a\*</sup> Christiane Bielecki,<sup>b</sup> Christoph Krafft,<sup>a</sup> Denis Akimov,<sup>a</sup> Bernd F. M. Romeike,<sup>c</sup> Rupert Reichart,<sup>d</sup> Rolf Kalf,<sup>d</sup> Benjamin Dietzek,<sup>a,e</sup> and Jürgen Popp<sup>a,e</sup>**

\* both authors contributed equally to this work

<sup>a</sup> Institute of Photonic Technology e.V., Albert-Einstein-Straße 9, 07745 Jena, Germany

<sup>b</sup> University Medical Center Jena, Clinic for Internal Medicine II, Department of Gastroenterology, Erlanger Allee 101, 07747 Jena, Germany

<sup>c</sup> University Medical Center Jena, Department of Neuropathology, Erlanger Allee 101, 07747 Jena, Germany

<sup>d</sup> University Medical Center Jena, Clinic for Neurosurgery, Erlanger Allee 101, 07747 Jena, Germany

<sup>e</sup> Friedrich-Schiller-University Jena, Institute of Physical Chemistry, Helmholtzweg 4, 07743 Jena, Germany

## **Abstract**

Contemporary brain tumour research focuses on two challenges: First, tumour typing and grading by analyzing excised tissue is of utmost importance for choosing a therapy. Secondly for prognostication the tumour has to be removed as completely as possible. Nowadays, histopathology of excised tissue using haematoxylin-eosine staining is the golden standard for the definitive diagnosis of surgical pathology specimens. However, it is neither applicable *in vivo*, nor does it allow for precise tumour typing in those cases when only non-representative specimens are procured. IR and Raman spectroscopy, allow for very precise cancer analysis due to their molecular specificity, while nonlinear microscopy is a suitable tool for rapid imaging of large tissue sections. Here, unstained samples from the brain of a domestic pig have been investigated by a multimodal nonlinear imaging approach combining coherent anti-Stokes Raman scattering, second harmonic generation and two photon excited fluorescence microscopy. Furthermore, a brain tumour specimen was additionally analyzed by linear Raman and FTIR imaging for a detailed assessment of the tissue types that is required for classification and to validate the multimodal imaging approach. Hence label-free vibrational microspectroscopic imaging is a promising tool for fast and precise *in vivo* diagnostics of brain tumours.

**KEY WORDS:** Raman microspectroscopy; coherent anti-Stokes Raman scattering microscopy; infrared microspectroscopy; nonlinear imaging; multiphoton microscopy; brain tumor.

## Introduction

Even though brain cancers are not among the most common types of cancer accounting for approximately 3% of all tumors [1], the therapy of brain tumors is a very important issue. First, they are especially abundant in children and adolescents. Here 22.9% of all cancers diagnosed originate in the brain and only leukaemia is more prevalent than tumors of the central nervous system [1]. Second, since metastases are the most prevalent type of brain tumors, dealing with brain cancer will give valuable insight into the process of metastasizing, which is, to a large extent, responsible for the lethality of cancer.

For the successful treatment of brain cancers, a precise assignment of the tumor type and grade is of utmost importance as is the detection of the tumor in an early development stage. These prerequisites of successful therapy need to be met, because medical treatment differs substantially for individual forms of tumors. This is again due to the fact that metastases are far more common than primary tumors, and successful treatment requires removal of the primary tumor as well. Furthermore, during surgery it is crucial to remove the cancerous tissue as completely as possible to prolong the time without symptoms and the survival rate of the patient[2]. A particular challenge in neurosurgery is to preserve normal brain tissue and minimize deficits in brain functions.

Nowadays, the commonly used standard method in neuropathology is staining with haematoxylin and eosine (H&E). The dye eosine stains proteins and the cytoplasm bright pink, while haematoxylin stains basophilic structures like DNA blue-purple. However, this rather simple method is limited to *ex vivo* investigations.

According to the importance of cancer treatment not only in the brain tremendous efforts have been undertaken in order to improve and invent imaging techniques for an early detection of tumor tissue. Noninvasive approaches for brain imaging to be stated here are computer tomography, magnetic resonance tomography (MRI), and positron emission tomography (PET)[3]. Immunohistochemistry is used to complement histopathology [4], whereas elastic light scattering [5], autofluorescence, optical coherence tomography [6], and fluorescent labeling [2] are recent experimen-

tal methods that have been applied intraoperatively to identify cancerous tissue *in vivo*. In fluorescence imaging fluorescing molecules like fluorescein bound to human serum albumin (HSA) [2] or the porphyrine derivative 5-aminolevulinic acid [7] are injected. Due to the faster metabolic rate of tumor cells the fluorescing particles are enriched over time within the cancerous tissue. A few hours after application the tissue is illuminated by laser light during surgery and the fluorescing cancerous tissue is removed. This allows for a more thorough resection of the tumor compared with conventional methods [2]. But despite its advantages, this technique suffers from severe restrictions. First of all, brain cancers do not accumulate fluorophores if the blood-brain barrier is still intact. This is especially true in the early stages of the cancer. In later stages the barrier is often damaged and fluorophores can penetrate more easily from the blood into cancerous tissue. As shown in [2], only 84% of the cancer absorbed the fluorescing species. Second, fluorescent labelling does not allow for tumor typing, because the dyes are not specific labels. This is, in principle, also true for other beforehand mentioned brain imaging techniques as MRI and PET. The tumor detection is based on a different enrichment of a marker substance in cancerous and physiological tissue. Third, fluorescence-based techniques suffer from the limited stability of the fluorophores, which tend to photobleach upon laser irradiation. Other optical methods like optical coherence tomography (OCT) and elastic light scattering use differences in physical properties, e.g., refractive index, for differentiation of cancerous and normal tissue.

The work presented here aims at developing a fast, label-free, sensitive, and selective diagnostic tool for the investigation of cancerous tissue potentially even *in vivo*. To address these fundamental problems in current neuropathology and neurosurgery, vibrational spectroscopic methods have been used. Infrared (IR) and Raman spectroscopy – as longstanding and well-established methods for tissue typing and grading – have been applied to determine the chemical composition of tissue samples in order to validate the performance of the multiphoton microscopy approach. On this basis, nonlinear imaging techniques like coherent anti-Stokes Raman scattering (CARS), second harmonic generation (SHG), and two photon excited fluorescence (TPEF) have been employed for a rapid and label-free visualization of the morphol-

ogy and composition of brain tissue.

Raman and IR spectra provide molecule specific fingerprints. Since each cell or tissue has a distinct chemical composition, biological species or tissue types can be identified by their Raman and IR spectra [8, 9]. Consequently, these methods are increasingly used for disease recognition [10]. In the context of brain tissue, Fourier transform infrared (FTIR) and Raman microspectroscopic imaging have already been applied to classify malignant gliomas [11], to determine the primary tumor of brain metastases [12, 13, 14, 15] to detect meningioma [16] and to identify tumors in mice and rats [17, 18, 19]. However, even though IR and Raman spectroscopy are promising, they have some method-intrinsic limitations. IR spectroscopy suffers from the strong absorption of water, which is the reason why its application is hampered *in vivo* [20, 21, 22]. Furthermore, the wavelength of the IR light ( $\sim 2.5 - 10\mu\text{m}$ ) is larger than that of visible light; hence high optical resolution on a subcellular level cannot be achieved in IR microspectroscopy. Raman microspectroscopy on the other hand uses visible or near-IR light and is applicable in aqueous environment. However, the Raman scattering efficiency is very low. Therefore, integration times in the order of seconds per spectrum are needed and fast data acquisition cannot be realized for imaging. Furthermore weak Raman signals of tissue are often overwhelmed by the tissues' autofluorescence.

Both limitations can be overcome by using a nonlinear version of Raman scattering, i.e., coherent anti-Stokes Raman scattering (CARS) microscopy, has been applied. In CARS the sample is illuminated by two pulsed lasers whose frequencies differ by the frequency of the molecular vibration to be imaged [23, 24]. The lasers are temporally and spatially overlapped on the sample at the focus of the microscope. The vibrational level selected for imaging is then selectively populated, because the beating frequency of both pulses corresponds to the vibration of interest and forces the molecules to vibrate. The excitation scheme is depicted in 1 panel b. Due to the nonlinear enhancement the CARS signal is much stronger than the spontaneous Raman signal. Therefore, CARS allows for fast data acquisition while preserving the chemical specificity of vibrational spectroscopy. Using single-band CARS microscopy, i.e., imaging the spatial distribution of a single Raman band in a microscope, it

is possible to achieve image acquisition with video repetition rate [25]. This fast image acquisition rate of single-band CARS comes at the price of reduced chemical information compared to recording the full Raman and/or IR spectrum. However, the virtual freedom of the image from single photon fluorescence and the ability to follow biological processes on timescales of fractions of seconds with subcellular resolution combined with its relative simplicity in the experimental setup is unparalleled for all currently available optical imaging techniques. But two drawbacks have to be kept in mind. First, other nonlinear processes generate a method-intrinsic background at the CARS signal wavelength limiting the image contrast. Second, as the signal depends on the square of the concentration of scattering molecules spectral contributions of less abundant molecules are small. But despite these drawbacks it has been proven to be an extremely sensitive method for imaging lipids and other molecules rich in aliphatic C-H-stretching vibrations capable of investigating normal brain tissue and brain tumors [26, 27]. In addition a variety of skin disorders such as, e.g., human basal cell carcinoma [28] can be probed by CARS microscopy.

In the present work we have combined CARS microscopy with SHG and TPEF imaging to obtain multimodal nonlinear spectroscopic images [29]. SHG – as CARS – is a nonlinear scattering process. A diagram of the process is displayed in 1 panel c. In SHG, two photons are fused to a single photon of twice the energy. This effect is limited to structures lacking inversion symmetry and depends on the square of the concentration of scatterers. Since the SHG signal is the coherent superposition of the emissions of single molecules only highly ordered molecular structures give rise to an intense signal. In tissue, the most abundant molecule having a large SHG cross section is collagen. The collagen distribution and structure is an important indicator for tumor type and grade, since the metastatic potential of tumors correlates with the degradation of collagen [30]. Furthermore the structure of collagen governs the delivery of therapeutics in tumors [31]. Beside these tumor-specific applications SHG allow for imaging microtubules in nerve tissue and connective tissue and is thence a promising technique for visualizing the composition and morphology of brain tissue [32]. For the investigation of different diseases like liver fibrosis or chronic arthritis SHG has been successfully applied to visualize the collagen net-

work [33, 34]. The third applied nonlinear imaging method is TPEF. The scheme of TPEF is depicted in 1 panel d. Here, two NIR photons are simultaneously absorbed and hence, TPEF is only observed within the laser focal spot where the photon density is highest. Therefore, bleaching effects and out of focus fluorescence are greatly reduced. Another advantage is the use of NIR illumination. Here, the depth penetration in tissue is highest. For all these nonlinear techniques a pulsed laser source is required to supply a high photon density at low average powers to avoid photodamage.

Summarizing what has been laid out before the scope of this paper is to present a combination of spectroscopic techniques first for a precise and sensitive investigation of brain tissue and second for a rapid detection of cancerous tissue during surgery. Based on IR and Raman studies particular emphasize is put on CARS, SHG, and TPEF imaging as these nonlinear spectroscopic modalities contain the potential for fast bedside imaging applications in clinics [35]. The manuscript is structured as follows. First, the methods and the experimental setup are presented. Afterwards, results are presented from the application of nonlinear imaging to examine the morphology of brain tissue sections from a domestic pig. To verify our findings we have checked the results using conventional H&E staining microscopy and IR and Raman studies. Then, the application of CARS imaging to investigate human brain tumor sections is displayed and discussed.

## Methods

### Nonlinear Microscopic Imaging

In Fig. 1 the experimental setup for CARS, SHG, and TPEF imaging is depicted. This multimodal nonlinear imaging experimental setup is based on a previously reported setup for CARS microscopy [36]. The main laser source is a coherent Mira HP Ti:Sa-Laser pumped by a Verdi-V18 Nd-Vanadate laser. The laser can be operated in fs or ps-pulse mode. For superior spectral resolution in CARS microscopy the laser is operated in the ps-pulse mode at 830 nm. A typical Raman line has a bandwidth of 2 to 10  $\text{cm}^{-1}$ . This corresponds very well to the linewidth of a ps laser,



as a 1 s laser pulse at 800 nm has a bandwidth of  $15 \text{ cm}^{-1}$  assuming a Gaussian line profile. A fraction of the laser serves as the Stokes pulse, another fraction is used to pump an optical parametric oscillator (OPO, APE, Berlin, Germany) generating the pump wavelength. It is widely tunable from 500 to 800 nm, allowing for imaging in the wavenumber region between 500 and  $4000 \text{ cm}^{-1}$ . Both pulse trains are spatially and temporally overlapped, and subsequently fed into a commercial laser scanning microscope (LSM 510 Meta, Zeiss, Jena, Germany). To scan large sample areas a  $10 \times$  /NA 0.3 EC Plan-Neofluar (Zeiss) has been used. The field of view is  $1.2 \times 1.2 \text{ mm}^2$ . Typical parameters for image acquisition are  $1024 \times 1024$  pixels,  $2.5 \mu\text{s}$  integration time per pixel, averaging of eight single images, resolution  $1.2 \mu\text{m}$ . For larger areas of interest, a mosaic of several single images is acquired. For SHG and TPEF imaging only the Ti:Sa-laser is used at 826 nm working in the ps-mode. In the microscope several stacked filters (Thorlabs, Newton, New Jersey; Omega Optical, Brattleboro, Vermont; LOT, Darmstadt, Germany) are used to separate the signal from the lasers used for excitation. For CARS imaging a set of short pass filters from Thorlabs and Omega optics has been used. The typical laser power at the sample is in the order of 50 mW for CARS microscopy. For SHG imaging a very narrow laser line bandpass filter centred at 413 nm has been employed (LOT) in combination with a stack of short pass filters from Omega optics and Thorlabs. For TPEF the internal filters of the microscope have been used. For image analysis and image processing LSM image examiner (Zeiss), LSM image browser (Zeiss) and ImageJ (Wayne Rasband, NIH) have been applied.

## **Raman Spectroscopic Imaging and Data Analysis**

Raman images were collected in backscattering mode using a commercial microscopic Raman system (RXN1 Microprobe, Kaiser Optical Systems, Ann Arbor, MI, USA). The system consists of a multi-mode diode laser at 785 nm emission (Invictus-Laser from Kaiser optical system), an f/1.8 spectrograph with a holographic transmissive grating (Kaiser) and a Peltier-cooled, back-illuminated, deep-depletion CCD detector (Andor Technology, Belfast, UK). The microscope is coupled to the Raman system by fiber optics. Raman images were recorded in the serial mapping mode

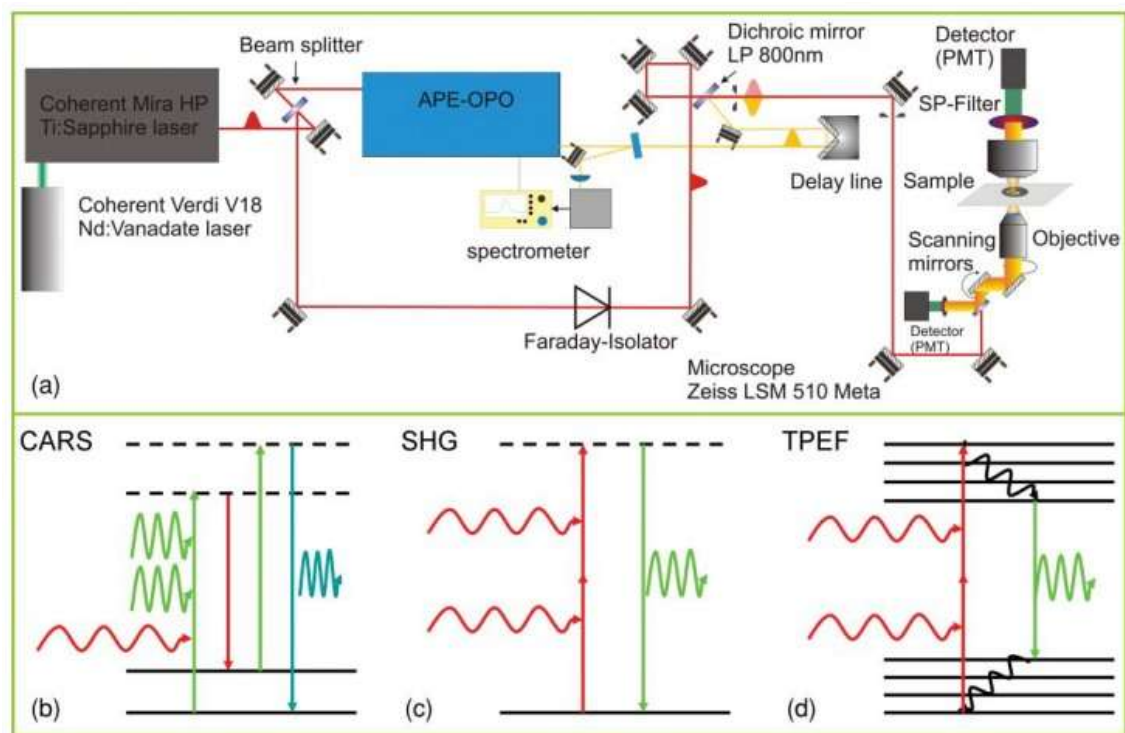


**Figure 1** – (a) Setup for CARS, SHG, and TPEF imaging. A Ti:Sa ultrafast laser oscillator is operated in the ps-pulsing mode for high spectral resolution in CARS microscopy ( $\sim 10 \text{ cm}^{-1}$ ). One fraction of the laser serves as Stokes beam or as excitation laser for SHG and TPEF imaging. The second fraction pumps an optical parametric oscillator (OPO) from APE generating the tunable pump laser for CARS imaging in the range from  $500\text{--}4000 \text{ cm}^{-1}$ . Pump and Stokes laser are recombined in space and time and fed into a commercial laser scanning microscope (Zeiss LSM 510 Meta). The signal is separated from the exciting lasers by a set of filters (Thorlabs, LOT, Omega Optical, Zeiss) and detected using a photomultiplier tube. CARS and SHG as shown in (b) and (c) are non-absorptive processes. The CARS process requires simultaneous illumination by two lasers whose difference in frequency matches a vibrational resonance (b). The emitted light is shorter in wavelength than the wavelengths of the illuminating lasers. But this process is not background free. Other nonlinear processes also generate photons at the CARS signal wavelength, reducing the image contrast. In SHG two photons of longer wavelength are fused to form an elastically scattered photon of twice the energy. This process is only allowed in non-centrosymmetric media. Therefore this method allows for selective imaging of non-symmetric structural proteins like collagen. In (d) the principle of TPEF imaging is depicted. By simultaneous absorption of two near infrared photons the molecules are excited to a higher electronic state and emit light of shorter wavelength when relaxing to the electronic ground state.

at 10  $\mu\text{m}$  m step size with 10 s exposure time per spectrum using a  $100 \times \text{NA } 0.9$  objective. Each Raman spectrum covers the range of 200 to  $3450 \text{ cm}^{-1}$  at a spectral resolution of  $4 \text{ cm}^{-1}$ . The acquisition software Holograms (Kaiser) automatically performs cosmic spike removal, wavelength calibration and intensity calibration.

The Raman images were imported into Matlab (The Mathworks, Natick, MA, USA) for pre-processing. In-house written scripts were applied for background subtraction, baseline correction and vertex component analysis (VCA). The application of VCA to reconstruct Raman images has recently been described in detail [37]. Briefly, given a set of mixed hyperspectral vectors and considering that each vector is a linear combination of spectral signatures, linear unmixing aims at estimating the number of reference substances, also called endmembers, their spectral signatures and their abundance fractions. If the number of substances and their signatures are not known, hyperspectral unmixing falls into the class of blind source separation problems. VCA offers an unsupervised solution to the blind source separation problem which was first described in 2005 [38]. VCA represents the image raw data in a space of smaller dimensionality aiming to retain all relevant information. Scope of VCA is that endmembers represent spectra of pure chemical constituents. Then, scores denote the concentration of the endmember spectra. The VCA algorithm iteratively projects data onto a direction orthogonal to the subspace spanned by the endmembers already determined. The new endmember signature corresponds to the extreme of the projection. The algorithm iterates until all endmembers are exhausted. Finally, the dimensionality of the procedure is reduced to a few endmembers, and all other spectra are expressed as linear combinations of these endmembers.

## **Fourier Transform Infrared Imaging**

FTIR images were collected in transmission mode using a commercial FTIR spectrometer (model 670, Varian, Agilent Technologies, Santa Clara, California) and an FTIR microscope with a  $64 \times 64$  focal plane array detector (model 620, Varian). The microscope was equipped with a Cassegrain  $15 \times \text{NA } 0.4$  objective. The microscope chamber was enclosed in a home-build box and purged by dry air to reduced spectral contributions from water vapor. Each image covers an area of  $350 \times 350$

$\mu\text{m}^2$  with each pixel corresponding to an area of  $5.5 \times 5.5 \mu\text{m}^2$ . The mosaic data acquisition mode enables to assess larger sample areas by acquiring a series of FTIR images and composing them to one image. For the current work a  $3 \times 2$  mosaic was collected covering areas of  $1050 \times 700 \mu\text{m}^2$ . Each IR spectrum was acquired in the interval 900 to  $4000 \text{ cm}^{-1}$  at a spectral resolution of  $4 \text{ cm}^{-1}$  with a zero filling factor 1 and Blackman Harris term 3 apodization. The data sets were processed using the program Cytospec ([www.cytospec.com](http://www.cytospec.com)) and Matlab. After baseline correction and removal of low intensity spectra, K-means cluster analysis was used to partition the data set into K clusters so that the differences between the data within each cluster are minimized and the differences between clusters are maximized according to some defined distance measure. Here, the K-means cluster algorithm used multiplicative signal correction for intensity normalization, squared Euclidean distances, five clusters and the spectral regions from 900 to  $1800 \text{ cm}^{-1}$ .

## Tissue Specimens

For CARS, SHG, and TPEF imaging of domestic pig brain tissue, unprocessed fresh cerebral tissue from a local slaughter-house has been shock frozen in liquid nitrogen. Tissue sections of 20 to  $50 \mu\text{m}$  thickness have been prepared using a Leica microtome model CM 3050 S. Parallel sections were stained with hematoxylin and eosine (H&E) using a standard protocol. The stained sections were investigated by brightfield and laser scanning fluorescence microscopy. The unstained sections have been analyzed by CARS, SHG, and TPEF microscopy. Tumor tissue specimens from human brain neoplasms were procured during surgery at the university hospital in Jena. Tissue was shock frozen and cryostat sections of  $10 \mu\text{m}$  thickness were cut. Slides were H&E stained and examined with brightfield microscopy by the neuropathologist Dr. Romeike. Parallel unlabelled sections were investigated by FTIR, Raman and CARS microscopy.

## Results

To illustrate the potential of the nonlinear imaging methods in the field of neurosurgery with respect to conventional H&E staining the cerebellum of a domestic pig has been investigated. At H&E stained sections different brain cell types like Purkinje cells and granule cells as well as the cell nuclei, which are especially abundant in the granule cell layer, were identified by the neuropathologist Dr. Romeike. White and grey matter consisting of granule cell layer, Purkinje cell layer and the molecular layer are discernible. Furthermore, the white matter containing the myelin fibres for signal transmission, the arachnoid membrane, which envelopes the brain, and smaller and larger blood vessels penetrating the brain transporting oxygen and nutrients were discriminated in the H&E image as shown in Figs. 2(a) – 4(a) [see Fig. 2(a) for an overview and Figs. 3(a) and 4(a) for more detailed H&E images as indicated by the boxes in Fig. 2]. On the other hand, the CARS, SHG, and TPEF images 2(b) and (c) of the parallel section show at similar accuracy the basic morphology of the sample. As the field of view using a  $10 \times$  objective was smaller than the tissue section, the H&E, CARS, SHG, and TPEF images were composed of  $15 \times 15$  single images. CARS at the CH-stretching vibration of  $2850 \text{ cm}^{-1}$  shows a very pronounced signal in the white matter, since the nerve fibers are rich in fatty acids, which give rise to an intense CARS signal [27]. Even the orientation of the fibres can be visualized, which is a particularly interesting capability of this method. In this respect, it seems very likely that polarization sensitive detection schemes [26, 32, 39] will highlight the orientation of the nerve fibres in the brain with higher contrast. The gray matter appears darker in the CARS image.

In Fig. 2(c) the spatial distributions of autofluorophores (TPEF, blue) and collagen (SHG, green) is displayed. For excitation the NIR laser was tuned to 826 nm. The TPEF signal has been detected in the range between 435-485 nm, hence the SHG signal, which appears at 413 nm is spectrally filtered and excluded. The image faintly shows the granule cell layer with its large amount of nuclei. The white matter appears darker than the uniformly illuminated gray matter. This is due to the fact, that several fluorophores are excited simultaneously, i.e., two-photon transitions in

elastin, collagen, and NAD(P)H are excited within the bandwidth of the laser pulse [40]. They all add to the signal in the spectral detection window and, consequently, their individual contributions are difficult to separate by the time-integrated measurements performed here. Since these molecules are distributed along the cellular structures, the TPEF image shows very well the morphology of the sample. SHG on the other hand selectively displays the arachnoid membrane which is composed of collagen.

To visualize fine morphological details of the sample CARS, TPEF, and SHG

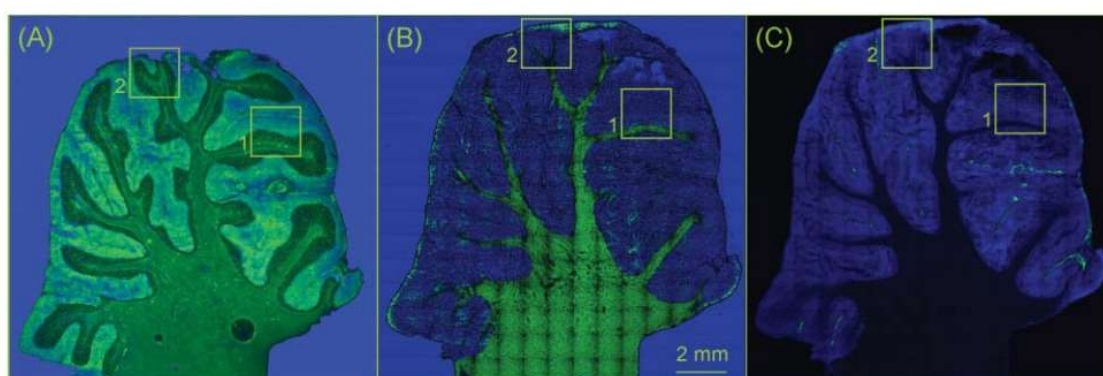


**Figure 2** – Comparison of (a) H&E, (b) CARS at  $2850\text{ cm}^{-1}$ , and (c) TPEF/SHG images of a cerebellum tissue section of a domestic pig. Similar information can be extracted using either H&E staining or nonlinear imaging methods. H&E staining visualizes the morphology of the cerebellum (a); the boxed region 1 and 2 are depicted in Figs. 3 and 4 for more detailed views. CARS allows us to differentiate white (green) and gray matter (blue) (b). In (c) a combined SHG and TPEF image shows the SHG emission (green) of the arachnoid membrane. In the TPEF channel (blue) (excitation 835 nm, emission 435–485 nm) the white matter appears darker than the grey matter and the granule layer is faintly accentuated.

imaging has been performed and a composite image is displayed in Fig. 3(b). CARS allows to differentiate white (bright green) and gray matter. The arachnoid membrane, which is to a large extent composed of ordered collagen, is exclusively visualized by SHG (red), while TPEF allows to faintly discern the granule layer of the gray matter (blue). However, fine structural details on single cell level like single cell nuclei could not be visualized, which can be seen in the H&E image in Fig. 3(a) showing nuclei of the granule cell layer and single Purkinje cells.

In Fig. 4 the boxed area 2 of Fig. 2 is magnified. The CARS image (B) allows vi-

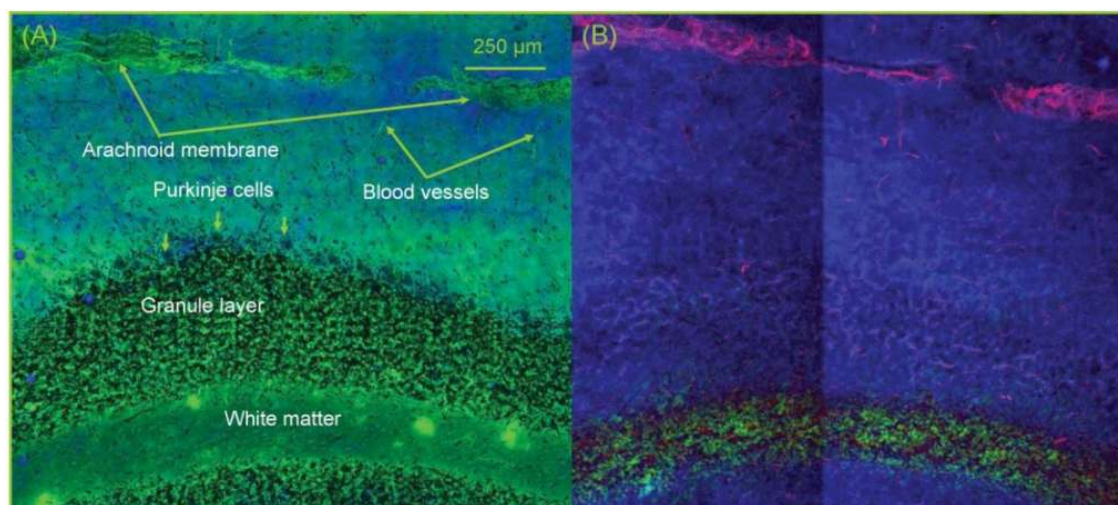


**Figure 3** – Comparison of a H&E stained section (a) and a composite CARS (green channel), SHG (red) and TPEF (blue) image of an unstained parallel section (b) of cerebellum of a domestic pig as indicated by the boxed area 1 of Fig. 2. This enlarged view (a) shows fine details on single cell level, the white matter with few nuclei, the granule cell layer with its extremely high density of small neurons, the larger Purkinje cells adjacent to the granule layer, blood vessels, and the arachnoid membrane. Except for the cell nuclei, single Purkinje cells and blood vessels, the basic structural components are also visible in the composite CARS (green), SHG (red), and TPEF (blue) image (b).

sualizing white and gray matter as well as the molecular layer, the outermost layer of the gray matter. To increase the CARS image contrast a nonresonant image at  $2700\text{ cm}^{-1}$  has been subtracted from a resonant CARS image following Refs. [41] and [42] [Fig. 4(c)] resulting in a contrast rich image, which clearly allows to separate white and gray matter. However, even though the contrast improved significantly, single cells and the granule layer are not discernible at this level of optical magnification.

Additional TPEF and SHG imaging reveals further details as shown in Fig. 4(d). Besides visualizing the arachnoid membrane the collagen structures of small blood vessels pervading the brain become visible by SHG imaging (green). Again the granule layer adjacent to the white matter is visible in the TPEF channel (blue). The nonlinear imaging modality pursued in this work has proven capable of resolving structural details of the sample comparable to H&E staining on a size scale larger than single cells. Hence, it can be concluded that such approach will be suited for

resolving the morphology and tumor margins of primary brain tumors and metastases potentially even during surgery.

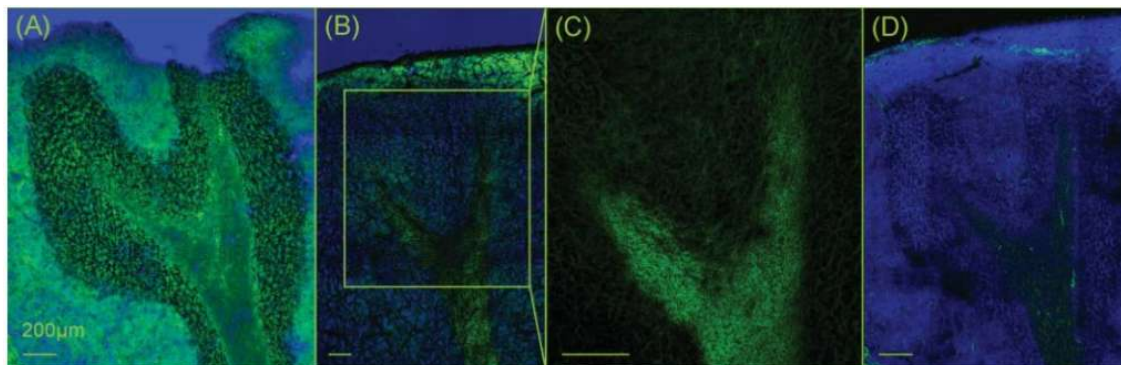


**Figure 4** – Comparison of a H&E stained image of the boxed area 2 of Fig. 2 with CARS, SHG, and TPEF images of a parallel unstained section. (a) Cellular details are visible in the H&E stained image as assigned in Fig. 3 (a). The corresponding CARS image (b) shows white and grey matter and highlights the outermost layer of the cerebellum, the molecular layer. To increase the image contrast, a nonresonant CARS image at  $2700\text{ cm}^{-1}$  has been subtracted resulting in a contrast rich image (c). The white matter appears bright, while the grey matter is much darker. Using TPEF and SHG however in (d), the granule cell layer is faintly visible (TPEF, blue), while SHG selectively highlights areas of densely packed and ordered collagen fibres (green), which are not exclusively within the arachnoid membrane but also in blood vessels. The size of each image is indicated by the scale bar of  $200\ \mu\text{m}$ .

Figure 5 compares the H&E stained tissue section of a brain metastasis [Fig. 5(a)], which originated from a lung carcinoma, with a CARS image recorded at  $2850\text{ cm}^{-1}$  [Fig. 5(b)], Raman images [Fig. 5(c) – 5(f)] and an FTIR image [Fig. 5(g)] of an unstained parallel tissue section. Raman and FTIR imaging of the same tumor sample have been applied to evaluate the results from CARS imaging. The H&E stained tissue section reveals a solid tumor mass with high cell density in the right portion, a region of lower tumor cell density in the central part and necrotic tissue particular in the lower left portion. As the brain metastasis of a lung carcinoma contains the molecular information of the primary tumor, the biochemical composition and morphology significantly differs compared with brain tissue and necrosis. Hence, the solid tumor is identified in the CARS image by a well delineated, homogeneous area of higher intensities. This corresponds to a distinct lipid content in comparison



with brain tissue, as confirmed by the Raman and FTIR spectra that are presented below (Fig. 6).

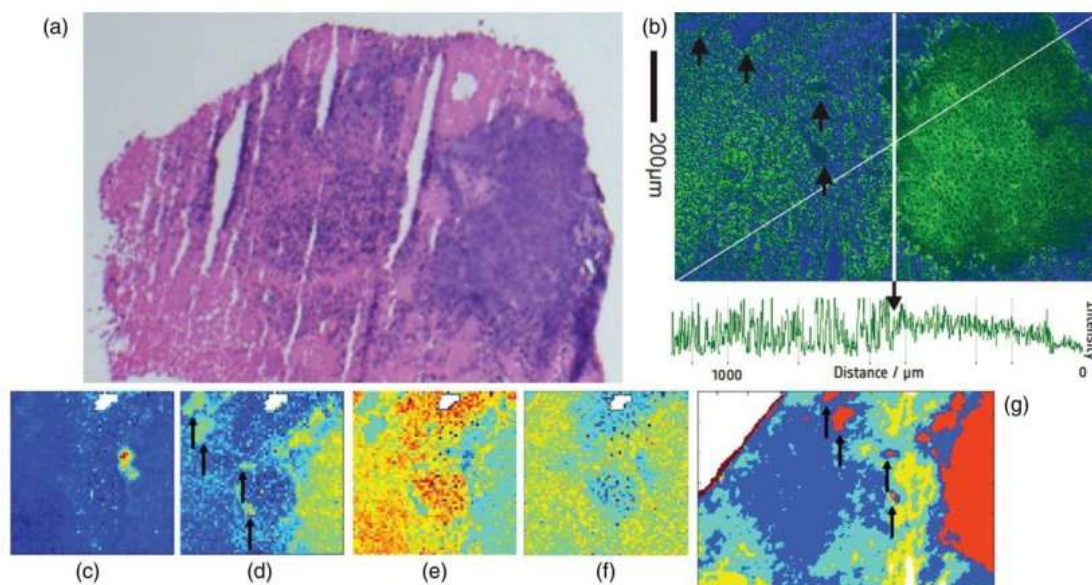


**Figure 5** – H&E stained tissue section (a), CARS image at  $2850\text{ cm}^{-1}$  in blue-green false colors with a spectral profile along the diagonal line (b), Raman image analyzed by VCA (c)–(f) and FTIR image (g) analyzed by k-means clustering from brain metastasis of lung carcinoma. Even though only one resonance is used for CARS imaging, the tumor margin is clearly visible in (b). The transition of necrotic brain tissue to tumor is resolved within an accuracy of  $10\ \mu\text{m}$  due to the different intensity profile in necrotic and cancerous tissue. Single cell nuclei within the tumor appear dark because of reduced lipid content. The component (c) of the Raman image is assigned to blood vessels, (d) to tumor tissue, (e) to necrosis and (f) to cell nuclei. The cluster membership map of the FTIR image (g) separates tumor (orange), necrosis (yellow, cyan) and scattered tumor cells with necrosis (blue). Small islets of cancerous tissue outside the solid tumor are indicated by arrows. Comparing the images (b) with (c)–(g) the superior spatial resolution of CARS is apparent. The image acquisition time of CARS is also greatly reduced compared to FTIR and Raman imaging. Scale bar valid for all images.

The area of lower tumor cell density appears more heterogeneously. The intensity profile along the diagonal is shown below allowing for tumor margin detection with a spatial resolution of approximately  $10\ \mu\text{m}$ . Within this CARS image single cell nuclei are visible. They appear darker, since the density of CH-stretching vibration is lower within the nuclei [27]. Tumor islets identified by Raman and FTIR imaging

are indicated by arrows. Such structures are also discernible in the CARS image. Since the full vibrational spectrum is available for each position in the FTIR and Raman image, the analysis of these images reveals further insight in the composition of this tissue section. The VCA analysis of the Raman image resolves a component of high haemoglobin content between the solid tumor and the scattered tumor cells [Fig. 5(c)]. The assignment is confirmed by the endmember spectrum (Fig. 6, trace 1) which shows prominent haeme bands at 666, 739, 1250, and 1585  $\text{cm}^{-1}$ . The second component [Fig. 5(c)] corresponds to the solid tumor. In agreement with the higher CARS intensities the endmember spectrum (Fig. 6, trace 2) shows intense cholesterol (701  $\text{cm}^{-1}$ ) and phospholipid bands (719, 1085, 1299, 1440, and 1657  $\text{cm}^{-1}$ ). The area of lower tumor cell density corresponds to the third component

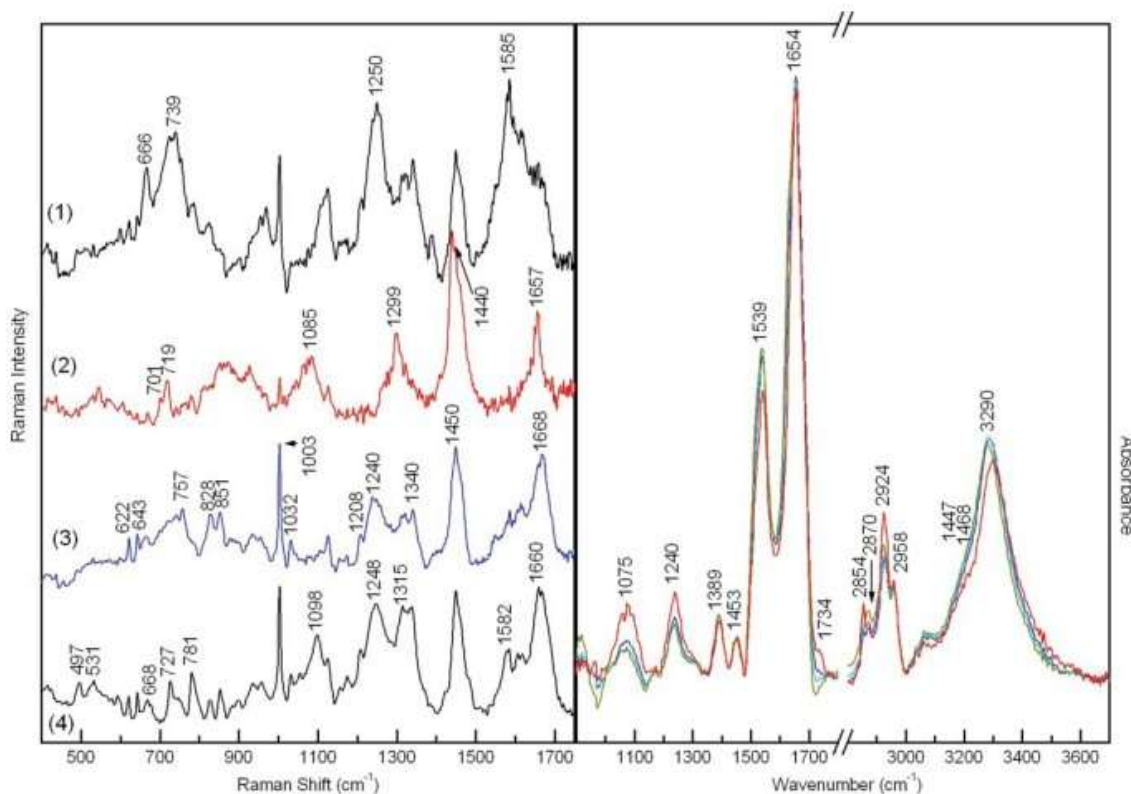


**Figure 6** – Left: Endmember spectra of the Raman images Fig. 5 panels (c)–(f) and right: mean cluster spectra of FTIR image from brain metastasis of lung carcinoma in Fig. 5 panel(g). See the results section for a detailed description and band assignment.

[Fig. 5(e)]. The endmember spectrum (Fig. 6, trace 3) is dominated by spectral contributions of proteins. Bands of aromatic amino acids (Phe: 622, 1003, 1032, 1208  $\text{cm}^{-1}$ ; Tyr: 643, 828, 851, 1208  $\text{cm}^{-1}$ ; Trp: 757, 1340  $\text{cm}^{-1}$ ) are identified. The positions of the protein amide III band (1240  $\text{cm}^{-1}$ ) and amide I band (1668  $\text{cm}^{-1}$ ) point to  $\beta$ -sheet secondary structures. The fourth component [Fig. 5(f)] is unevenly distributed in the left and right portion of the Raman image. The concentration is decreased in the central portion which corresponds to necrosis by comparison with the H&E stained image. The endmember spectrum (Fig. 6, trace 4) contains more intense bands due to DNA (497, 668, 727, 781, 1098, 1315, 1680  $\text{cm}^{-1}$ ). This is consistent with a high cell density in tumor and a low cell density in necrotic tissue. Furthermore, the amide bands significantly shift to 1248 and 1660  $\text{cm}^{-1}$  compared to the third endmember spectrum. This observation points to a change of secondary structures from  $\beta$ -sheets to more  $\alpha$ -helical and unordered conformations. The band at 531  $\text{cm}^{-1}$  is tentatively assigned to disulfide bridges between cysteine amino acids. The cluster membership map of the FTIR image contains five clusters [Fig. 5(g)]. The clusters are assigned to the solid tumor (orange cluster), necrosis (yellow and cyan), the scattered tumor cells (blue), and the tissue margin (brown). The mean cluster spectra are overlaid in Fig. 6 (right). In agreement with the Raman signature the IR spectrum of the orange cluster contains more intense spectral contributions of phospholipids (1075, 1240, 1734, 2854, 2924  $\text{cm}^{-1}$ ). Further differences compared with the other IR spectra are observed in the amide II (1539  $\text{cm}^{-1}$ ) and amide A band (3290  $\text{cm}^{-1}$ ) whose intensities are reduced relative to the amide I band (1654  $\text{cm}^{-1}$ ). The variations of the blue, cyan, and yellow cluster are smaller. The cluster mean spectrum of the brown cluster at the tissue margin is not displayed because it is strongly affected by spectral contributions of OCT medium.

## Discussion

As the current neuropathologic investigation of brain tumor sections is based on H&E staining microscopy it is limited to fixed (*ex vivo*) tissue specimen. This

work aims at providing nonlinear microspectroscopic tools allowing for a label free analysis of brain tissue with similar accuracy than the established H&E staining microscopy, which are potentially also applicable *in vivo* as already demonstrated [25, 31, 32, 35, 40, 43]. Single-band CARS in resonance with the CH-stretching vibration combined with TPEF and SHG imaging can give similar insight into the composition and morphology of brain tissue as does H&E staining. This is at least true on a larger size scale. On single cell level the resolution of H&E microscopy has been superior. This is mainly due to the fact that in order to scan large sample areas a low magnification large field of view  $10 \times$  objective has been used. Since SHG and CARS require phasematching, a high NA objective will not only increase the spatial resolution but also the efficiency of the signal generation for these processes. Further more the sample preparation is limiting the resolution.

In this study dried sections from shock frozen tissue have been investigated. Due to the drying process the tissue shrinks. As a result the sample is not uniform in thickness and refractive index, which degrades the image contrast. This is because the laser beams cannot be focused to a diffraction limited spot deep in the tissue, which also affects the efficiency of the signal generation due to the nonlinear dependence on the intensity of the excitation lasers. To circumvent this problem the tissue will be cut at room temperature using a vibratome in forthcoming studies. Preparation based alterations of the tissue are thereby minimized. Therefore, it is expected, that even finer structural details will become generally visible in CARS images. This more elaborate sample preparation offers another advantage. Since sample modifications are small and the sections remain in a humid environment, the conditions are more similar to those *in vivo*. Although this *ex vivo* study revealed significant results *in vivo* assessment of tissue will form the core of future investigation.

Especially SHG imaging has revealed paramount details, which are difficult to see if not completely invisible in H&E images. Since only ordered collagen is visualized, SHG offers high chemical selectivity. The image contrast is extremely high, because SHG selectively highlights exclusively the arachnoid membrane, blood vessels and other structures as axons composed of collagen. TPEF on the other hand allows

for label free imaging the morphology of the sample. Even though the contrast is less pronounced than in H&E images, the main structural details of brain tissue can be visualized. These are white and grey matter. In the latter even the granule cell layer appears accentuated, which is invisible in the CARS images.

CARS as the third nonlinear microspectroscopic technique employed is very promising for imaging the chemical composition. So far only the aliphatic CH-stretching band has been used for visualizing the distribution of lipids and membranes. However, this method already allows to clearly differentiate white and grey matter. Even the orientation of the nervous fibres is faintly visible. Due to differences in their chemical composition cancerous tissue could also be identified by CARS microscopy. The margin of lung tumor metastasis and necrosis has been detected with high spatial resolution of approximately  $10 \mu m$ . FTIR and Raman imaging have identified four small tumor islets outside the solid tumor mass, which are also visible in the CARS image. In general the molecular specificity of single band CARS microscopy is lower than in Raman or FTIR imaging, because in contrast to FTIR and Raman imaging single band CARS utilizes only one Raman resonance for contrast generation. Furthermore the CARS signal is unevenly generated across the field of view decreasing to the edges. This is due to the phasematching condition, which is not equally satisfied across the full field of view. Hence, the tumor islets at the edge of the field of view are difficult to visualize. Nevertheless CARS is sufficiently sensitive to delineate the solid tumor and islets employing acquisition times, which are greatly reduced compared to Raman and FTIR microspectroscopy.

However, as only single-band CARS has been applied in this study, detailed chemical information as encoded in the whole vibrational spectra of a sample has not been obtained yet by this nonlinear technique. Hence, in order to validate the nonlinear imaging approach the underlying variations in chemical composition between cancerous and normal tissue were characterized with high accuracy in Raman and FTIR images that allow distinguishing different features within each tissue sections. It has already been demonstrated that these techniques enable tumor typing and grading [19, 11, 12, 13, 14]. Therefore, to realize tumor typing or grading the entire vibrational fingerprint of a sample has to be used. The Raman and IR spectra

indicate that the main spectral differences between cancer and normal tissue are assigned to proteins and lipids. But these spectral variations are usually small and distributed across a wide spectral range requiring the use of multivariate statistical analysis algorithms. But FTIR and Raman imaging are far too slow for being applicable *in vivo*. Furthermore, the use of FTIR is restricted to dry samples, thus, despite its great success in characterizing tissue sections its *in vivo* application will be hampered by the presence of water in biological samples.

For an online, i.e., intra-surgery all-optical analysis of brain tissue CARS microscopy will be the method of choice, which might be combined with Raman analytics as recently demonstrated by Potma and co-workers in a proof-of-concept device [44]. But since already single band CARS does provide sufficient information for the detection of tumor tissue, [27] it is probably also capable of tumor typing, when more than a single resonance is used for imaging and when the results are combined with other nonlinear imaging modalities like SHG and TPEF. Furthermore, statistic image analysis can be applied to interpret CARS images [45, 46].

These first results are very promising. A combination of nonlinear imaging techniques visualized the morphology of brain tissue and differentiated cancerous and necrotic brain tissue. These findings were verified by FTIR and Raman imaging. In the future further improvements of these nonlinear methods might allow for a rapid analysis of dissected brain tissue accompanying brain surgeries or biopsies.

## Summary and Outlook

In order to become a useful complement or even substitute for standard staining methods, i.e., H&E staining, in neuropathology the technologically more complex nonlinear imaging methods must be able to demonstrate clear advantages in comparison to the established techniques. Here, it has been shown that a combination of recently developed multiphoton imaging modalities can provide similar structural information as does conventional H&E staining in neuropathology. In the present study CARS revealed general tissue textures as H&E stained samples, nevertheless, due to the use of a low-magnifying objective the CARS images do not reveal

sub-cellular structures. On the other hand, CARS neither requires elaborate sample preparation, nor is its application limited to *ex vivo* studies as detection of the signals in backscattering direction is possible. However, the experimental setup is somewhat more complicated. Nonetheless, progress in laser technology may enable that these techniques will be implemented in a compact microscope comparable in size to the bright field microscopes nowadays widely used in hospitals. We believe that the implementation of fibre lasers [47, 48, 49, 50] with their small footprint and robustness will bring CARS and nonlinear microscopy from specialized laser labs into hospital.

By shifting the excitation laser wavelength further into the near-IR, lower photo induced damage and higher depth penetration is expected comparable to the situation established for two-photon fluorescence. Hence, investigations will not be limited to the surface of the sample, but contactless and hence non-invasive measurements of tissue a few hundred microns deep are realistic. By utilizing different resonances for CARS imaging especially within the fingerprint spectral region chemically selective imaging of more structural details inside the brain is expected. For instance the granule cell layer is extremely rich in DNA which could be used to selectively image this region. A rapid multispectral analysis of biopsies will allow for faster and more precise tumor typing. For the future we aim for a fast and reliable intraoperative diagnosis of the tumor type and grade by using solely nonlinear imaging modalities.

## **Acknowledgments**

Financial support from European Union via the Europäischer Fonds für Regionale Entwicklung (EFRE) and the Thüringer Ministerium für Bildung Wissenschaft und Kultur (TMBWK) (projects: B578-06001, 14.90 HWP, and B714-07037), via the German Science Foundation (Jena School of Microbial Communication) and the German Federal Ministry for Science and Education (BMBF) MediCARS (FKZ: 13N10774) is gratefully acknowledged. The authors thank Martin Hedegaard (University of Southern Denmark) for assistance with writing the Matlab scripts for VCA. B.D. thanks the Fonds der Chemischen Industrie for financial support.

## References

- [1] Husmann, G., Kaatsch, P., Katalinic, A., Bertz, J., Haberland, J., Kraywinkel, K., and Wolf, U. *Krebs in Deutschland*, volume 7. Robert Koch-Institut und die Gesellschaft der epidemiologischen Krebsregister in Deutschland e. V., (2010).
- [2] Kremer, P., Fardanesh, M., Ding, R., Pritsch, M., Zoubaa, S., and Frei, E. *Neurosurgery* **64**, ons53—ons61 (2009).
- [3] Chen, W. *J Nucl Med* **48**(9), 1468–1481 September (2007).
- [4] Takei, H., Bhattacharjee, M. B., Rivera, A., Dancer, Y., and Powell, S. Z. *Archives of Pathology & Laboratory Medicine* **131**(2), 234–241 (2007).
- [5] Gong, J., Yi, J., Turzhitsky, V. M., Muro, K., and Li, X. *Disease Markers* **25**(6), 303–312 (2008).
- [6] Böhringer, H., Lankenau, E., Stellmacher, F., Reusche, E., Hüttmann, G., and Giese, A. *Acta Neurochirurgica* **151**(5), 507–517 (2009).
- [7] Stummer, W., Pichlmeier, U., Meinel, T., Wiestler, O. D., Zanella, F., and Reulen, H.-J. *The Lancet Oncology* **7**(5), 392–401 (2006).
- [8] Gaus, K., Rösch, P., Petry, R., Peschke, K.-D., Ronneberger, O., Burkhardt, H., Baumann, K., and Popp, J. *Biopolymers* **82**(4), 286–290 (2006).
- [9] Krafft, C., Dietzek, B., and Popp, J. *The Analyst* **134**(6), 1046–1057 (2009).
- [10] Krafft, C., Codrich, D., Pelizzo, G., and Sergio, V. *Journal of Biophotonics* **1**(2), 154–169 (2008).
- [11] Krafft, C., Thümmeler, K., Sobottka, S. B., Schackert, G., and Salzer, R. *Biopolymers* **82**(4), 301–305 (2006).
- [12] Krafft, C., Bergner, N., Matthaus, C., Romeike, B., Reichart, R., Kalf, R., Dietzek, B., and Popp, J. In *Biomedical Vibrational Spectroscopy IV: Advances in Research and Industry*, Mahadevan-Jansen, A. and Petrich, W., editors, volume 7560, 756007–756008 (SPIE, San Francisco, California, USA, 2010).
- [13] Krafft, C., Shapoval, L., Sobottka, S. B., Schackert, G., and Salzer, R. *Technology in Cancer Research & Treatment* **5**(3), 291–298 (2006).
- [14] Krafft, C., Shapoval, L., Sobottka, S. B., Geiger, K. D., Schackert, G., and Salzer, R. *Biochimica et Biophysica Acta (BBA) - Biomembranes* **1758**(7), 883–891 (2006).
- [15] Krafft, C., Sobottka, S. B., Schackert, G., and Salzer, R. *Journal of Raman Spectroscopy* **37**(1-3), 367–375 (2006).
- [16] Koljenović, S., Schut, T. B., Vincent, A., Kros, J. M., and Puppels, G. J. *Analytical Chemistry* **77**(24), 7958–7965 (2005).
- [17] Amharref, N., Beljebbar, A., Dukic, S., Venteo, L., Schneider, L., Pluot, M., Vistelle, R., and Manfait, M. *Biochimica Et Biophysica Acta* **1758**(7), 892–899 (2006).
- [18] Bamberg, K. R., Schültke, E., Wood, B. R., MacDonald, S. T. R., Ataelmannan, K., Griebel, R. W., Juurlink, B. H. J., and McNaughton, D. *Biochimica Et Biophysica Acta* **1758**(7), 900–907 (2006).
- [19] Krafft, C., Kirsch, M., Beleites, C., Schackert, G., and Salzer, R. *Analytical and Bioanalytical Chemistry* **389**(4), 1133–1142 (2007).
- [20] Li, G., Thomson, M., Dicarlo, E., Yang, X., Nestor, B., Bostrom, M. P. G., and Camacho, N. P. *Applied Spectroscopy* **59**(12), 1527–1533 (2005).



- [21] Greve, T. M., Andersen, K. B., and Nielsen, O. F. *Spectroscopy* **22**(6), 437–457 (2008).
- [22] Gloor, M., Hirsch, G., and Willebrandt, U. *Archives of Dermatological Research* **271**(3), 305–313 (1981).
- [23] Zumbusch, A., Holtom, G. R., and Xie, X. S. *Phys. Rev. Lett.* **82**(20), 4142–4145 (1999).
- [24] Volkmer, A. *Journal of Physics D: Applied Physics* **38**(5), R59–R81 (2005).
- [25] Evans, C. L., Potma, E. O., Puoris'haag, M., Côté, D., Lin, C. P., and Xie, X. S. *Proc Natl Acad Sci U S A* **102**(46), 16807–16812 November (2005).
- [26] Fu, Y., Huff, T. B., Wang, H.-W., Wang, H., and Cheng, J.-X. *Optics express* **16**(24), 19396–19409 November (2008).
- [27] Evans, C. L., Xu, X., Kesari, S., Xie, X. S., Wong, S. T. C., and Young, G. S. *Optics Express* **15**(19), 12076–12087 (2007).
- [28] Vogler, N., Meyer, T., Akimov, D., Latka, I., Krafft, C., Bendsoe, N., Svanberg, K., Dietzek, B., and Popp, J. *Journal of Biophotonics* **3**(10-11), 728–736 (2010).
- [29] Mertz, J. *Current Opinion in Neurobiology* **14**(5), 610–616 (2004).
- [30] Liotta, L. A., Tryggvason, K., Garbisa, S., Hart, I., Foltz, C. M., and Shafie, S. *Nature* **284**(5751), 67–68 (1980).
- [31] Brown, E., McKee, T., DiTomaso, E., Pluen, A., Seed, B., Boucher, Y., and Jain, R. K. *Nat Med* **9**(6), 796–800 (2003).
- [32] Huff, T. B. and Cheng, J.-X. *Journal of microscopy* **225**(Pt 2), 175–182 (2007).
- [33] Caetano-Lopes, J., Nery, A. M., Canhão, H., Duarte, J., Cascão, R., Rodrigues, A., Perpétuo, I. P., Abdulghani, S., Amaral, P. M., Sakaguchi, S., Kontinen, Y. T., Graça, L., Vaz, M. F., and Fonseca, J. a. E. *Arthritis Research & Therapy* **12**(1), R9 (2010).
- [34] Gailhouste, L., Grand, Y. L., Odin, C., Guyader, D., Turlin, B., Ezan, F., Désille, Y., Guilbert, T., Bessard, A., Frémin, C., Theret, N., and Baffet, G. *Journal of Hepatology* **52**(3), 398–406 (2010).
- [35] Konig, K. and Riemann, I. *Journal of Biomedical Optics* **8**(3), 432–439 (2003).
- [36] Meyer, T., Akimov, D., Tarcea, N., Chatzipapadopoulos, S., Muschiolik, G., Kobow, J., Schmitt, M., and Popp, J. *The Journal of Physical Chemistry. B* **112**(5), 1420–1426 (2008).
- [37] Miljkovic, M., Chernenko, T., Romeo, M., Bird, B., Matthäus, C., and Diem, M. *Analyst* (2010).
- [38] Nascimento, J. M. P. and Bioucasdias, J. M. B. *IEEE Transactions on Geoscience and Remote Sensing* **43**, 898–910 April (2005).
- [39] Wang, H. F., Fu, Y., Zickmund, P., Shi, R. Y., and Cheng, J. X. *BIOPHYSICAL JOURNAL* **89**(1), 581–591 (2005).
- [40] Schenke-Layland, K., Riemann, I., Damour, O., Stock, U. A., and König, K. *Advanced Drug Delivery Reviews* **58**(7), 878–896 (2006).
- [41] Akimov, D., Chatzipapadopoulos, S., Meyer, T., Tarcea, N., Dietzek, B., Schmitt, M., and Popp, J. *Journal of Raman Spectroscopy* **40**(8), 941–947 (2009).
- [42] Greve, M., Bodermann, B., Telle, H. R., Baum, P., and Riedle, E. *Applied Physics B: Lasers and Optics* **81**, 875–879 November (2005).
- [43] Bégin, S., Bélanger, E., Laffray, S., Vallée, R., and Côté, D. *Journal of Biophotonics* **2**(11), 632–642 November (2009).

- [44] Zimmerley, M., Younger, R., Valenton, T., Oertel, D. C., Ward, J. L., and Potma, E. O. *The Journal of Physical Chemistry B* **114**(31), 10200–10208 (2010).
- [45] Vogler, N., Bocklitz, T., Mariani, M., Deckert, V., Markova, A., Schelkens, P., Rösch, P., Akimov, D., Dietzek, B., and Popp, J. *Journal of the Optical Society of America A* **27**(6), 1361–1371 (2010).
- [46] Hagmar, J., Brackmann, C., Gustavsson, T., and Enejder, A. *Journal of the Optical Society of America A* **25**(9), 2195–2206 (2008).
- [47] Krauss, G., Hanke, T., Sell, A., Träutlein, D., Leitenstorfer, A., Selm, R., Winterhalder, M., and Zumbusch, A. *Optics Letters* **34**(18), 2847–2849 (2009).
- [48] Kieu, K., Saar, B. G., Holtom, G. R., Xie, X. S., and Wise, F. W. *Optics Letters* **34**(13), 2051–2053 (2009).
- [49] Marangoni, M., Gambetta, A., Manzoni, C., Kumar, V., Ramponi, R., and Cerullo, G. *Optics Letters* **34**(21), 3262–3264 November (2009).
- [50] Pegoraro, A. F., Slepkov, A. D., Ridsdale, A., Pezacki, J. P., and Stolow, A. *Applied Optics* **49**(25), F10–F17 (2010).

Adapted with kind permission from Wiley-VCH Verlag GmbH & Co. KGaA:

**Authors:** Tobias Meyer, Orlando Guntinas-Lichius, Ferdinand von Eggeling, Günther Ernst, Denis Akimov, Michael Schmitt, Benjamin Dietzek, and Jürgen Popp.

**Titel:** "Multimodal nonlinear microscopic investigations on head and neck squamous cell carcinoma - towards intra-operative imaging."

**Journal:** *Head & Neck*, 35(9):E280-E287 2012.

©Copyright 2013 Wiley-VCH Verlag GmbH & Co. KGaA.  
Reproduced with permission.



6 | Multimodal Nonlinear Microscopic Investigations on Head and Neck Squamous Cell Carcinoma - Towards Intra-Operative Imaging

**Tobias Meyer,<sup>1</sup> Orlando Guntinas-Lichius, MD,<sup>2</sup> Ferdinand von Eggeling, PhD,<sup>3</sup> Günther Ernst, MD,<sup>3</sup> Denis Akimov, PhD,<sup>1</sup> Michael Schmitt, PhD,<sup>1</sup> Benjamin Dietzek, PhD,<sup>1,4</sup> and Jürgen Popp, PhD,<sup>1,4,\*</sup>**

<sup>1</sup> Institute of Photonic Technology Jena, Albert-Einstein-Strasse 9, 07745 Jena, Germany

<sup>2</sup> Department of Otorhinolaryngology, Jena University Hospital, Lessingstrasse 2, 07740 Jena, Germany

<sup>3</sup> Institute of Human Genetics, Core Unit Chip Application, Jena University Hospital, 07740 Jena, Germany

<sup>4</sup> Institute of Physical Chemistry and Abbe center of Photonics, Friedrich-Schiller-University Jena, Helmholtzweg 4, 07743 Jena, Germany

\* Corresponding author: Prof. Dr. Jürgen Popp, Institute of Photonic Technology (IPHT) Jena e.V., Albert-Einstein-Straße 9, 07745 Jena, Phone: +493641206300, Fax: +493641206399, juergen.popp@uni-jena.de

## Abstract

**Background.** Prognosis and appropriate treatment of head and neck squamous cell carcinoma (HNSCC) depend on the tumor type routinely derived by invasive histopathology. A promising non-invasive alternative is nonlinear optical imaging, which is capable of *in vivo* tissue visualization for tumor typing and grading.

**Methods & Results.** Thin tissue sections from three cases aged 56 to 60 years presenting advanced carcinoma of the hypopharynx, larynx and left tonsil were investigated by coherent anti-Stokes Raman scattering (CARS), second harmonic generation (SHG) and two photon excited fluorescence (TPEF) to study the tissues morphochemistry. Morphologic alterations of prognostic significance, e.g. cell density, nuclear to cytoplasm ratio and keratinization as well as the underlying compositional changes during malignant transformation were determined, e.g. the distributions of lipids, collagen and autofluorophors.

**Conclusion.** Nonlinear imaging provides a non-invasive optical biopsy of the epithelial layer comparable to staining microscopy. By integration into an operational microscope routine screening of suspicious lesions and surgical guidance can be realized.

**KEY WORDS:** Nonlinear microscopy; head and neck cancer imaging; SHG; CARS; TPEF.

## Introduction

Despite enormous improvement of diagnostic and therapeutic possibilities, two thirds of patients with head and neck cancer are detected in advanced stage and even after curative treatment 30-50% sustain a locoregional recurrence with worse prognosis [1, 2]. Beside long periods without symptoms, the difficult access to some head and neck subsites and the field cancerization process are major reasons why it is so difficult to detect head and neck cancer in early stage as well as to guarantee clear tumor free margins (R0) when approaching a tumor with surgical therapy [3]. Tumor-free margins are a major prognostic factor for local tumor recurrence which occurs in 10-30% of patients with advanced disease [4]. The field cancerization process leads to the fact that the otorhinolaryngologist facing a suspicious lesion in the head and neck region typically is confronted with combination of inflammatory, dysplastic and cancerous areas. In early stage cases, it is difficult to differentiate chronic inflammation from early cancer and in advanced tumors it is difficult to define clinically, even when using endoscopic or microscopic assistance, the tumor borders. To date, the clinician only can rely on systematic biopsies and their histopathologic grading of the epithelial dysplasia. This is time consuming, must be performed *ex vivo*, and has methodological limitations. It is well known that there are other molecular factors indicating genetic altered cells beyond dysplasia that have major prognostic impact on tumor diagnosis and evaluation of tumor margins [3].

Fortunately, there are some promising new developments in optical diagnostics also discussed for future application in head and neck cancer [5]. The present case report is focused on nonlinear optical imaging techniques, based on fluorescence and Raman scattering [6, 7]. Raman spectroscopy is a laser-based technique that enables characterization of the chemical composition of complex samples. Raman spectroscopy based methods are being considered as techniques which could be complementary or even alternatively used to biopsy, pathology and clinical assays in many medical technologies. Two recent reviews on Raman spectroscopy in head and neck cancer have shown some exploratory results in classical squamous cell cancer [8, 9]. However, acquisition of spectra across a large area is time consuming, while single spectra



instead of images requires to measure at the appropriate location, which is difficult to choose. Therefore staining histopathology has been shown to be more precise. A recent review on the future of image-guided surgery in head and neck cancer even did not incorporate Raman scattering [10], since the Raman efficiency is low proving real time imaging impossible. However, coherent anti-Stokes Raman scattering (CARS) as a nonlinear Raman analogue can overcome these limitations and enables fast imaging [11, 12].

Therefore, the present case series focuses on the investigation of unstained thin tissue sections by means of multimodal nonlinear microscopy in order to give a proof-of-principle, that the progression of dysplasia to squamous cell carcinoma in head and neck cancer can be visualized by this combination of imaging methods. To validate the diagnostic potential of the combination of second harmonic generation (SHG), two photon excited fluorescence (TPEF) and CARS the results are compared to the current gold standard in histopathology, hematoxylin and eosin (H&E) staining. In this work tissue specimen from three cases containing representative material of benign epithelial tissue, dysplastic and malignant epithelium of laryngeal, hypopharyngeal, hypopharyngolaryngeal and oropharyngeal sites were investigated.

## Case Reports

The study protocol was approved by the ethics committee for human research at the Medical Faculty, Friedrich-Schiller-University Jena. Three patients with primary diagnosis of HNSCC were included into this pilot study. During diagnostic panendoscopy the primary tumors were first photographed. Biopsies were taken from the primary tumor site and its environment. Each biopsy was split into two parts. One part was forwarded for routine histopathological investigation. From the other part cryosections of 20  $\mu\text{m}$  thickness were used without further processing. For further alignment of standard diagnostics and multimodal imaging diagnostic parallel sections were used from each specimen. Parallel diagnostic pathological typing and grading was performed by a pathologist (G.E.) according to the current World He-

alth Organization (WHO) classification using H&E stained sections. In total, one unlabelled section and one parallel H&E stained section were analyzed per case.

To investigate the parallel thin tissue sections a combination of TPEF, SHG and

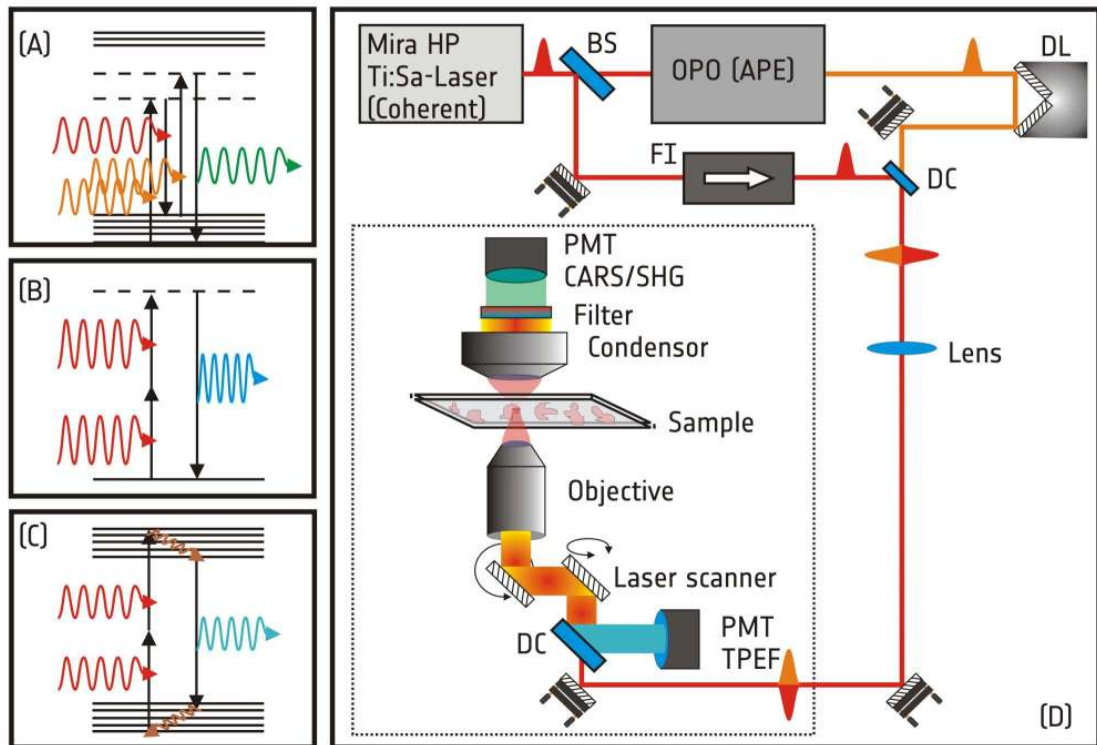


**Figure 1** – Sketch depicting the nonlinear processes for signal generation CARS (A), SHG (B) and TPEF (C), and the experimental setup used for nonlinear multimodal imaging (D). Here PMT denotes photo multiplier tube, FI Faraday isolator, DC dichroic mirror for beam combination or separation, DL mechanical delay line for temporal pulse synchronization, BS beam splitter.

CARS has been employed for multimodal nonlinear imaging utilizing NIR illumination from 670 to 1000 nm. The setup as depicted in Figure 1 has been described in detail elsewhere [12]. A Ti:Sa Laser (Coherent Mira HP) with an output power of 3 W at 76 MHz repetition rate emits pulses of either 200 fs or 2 ps duration. While 200 fs pulses due to their high peak intensities are ideal for SHG and TPEF imaging, their spectral resolution is insufficient for CARS imaging. Hence, CARS uses 2 ps pulses. The output of the Ti:Sa laser is split using a non-polarizing be-

am splitter. One fraction serves as excitation laser for SHG and TPEF imaging or further attenuated as Stokes beam for CARS imaging. The other fraction of the Ti:Sa-laser tuned to 830 nm is used to pump an optical parametric oscillator (OPO, APE, Germany) generating a continuously tunable laser output of up to 300 mW in the range of 500 to 800 nm and above 1000 nm. In the presented experiments the pump beam was tuned to 670 nm in order to perform CARS imaging using the aliphatic C-H-stretching vibration of lipids at  $2850\text{ cm}^{-1}$ . Both pump and Stokes laser pulse trains are temporally and spatially overlapped by a mechanical delay and a dichroic beam combiner and subsequently coupled into a laser scanning microscope (LSM 510 Meta, Zeiss). The signals are spectrally separated by dichroic beamsplitters, shortpass and bandpass filters (Zeiss, Omega Optics, Semrock, Thorlabs) and detected by photomultiplier tubes. In figure 1 the setup for subsequent CARS, SHG and TPEF imaging is schematically depicted. In the presented work CARS and SHG were recorded individually as for thin tissue sections both CARS and SHG are primarily emitted in forward direction and due to the available beamsplitter and filter combination, only one of both contributions could be recorded. Subsequent to CARS imaging 200 fs pulses at 830 nm were applied for TPEF and SHG imaging in order to maximize the signal generation efficiency for the latter two modalities. It was necessary to prove if multimodal nonlinear imaging is sufficiently precise to visualize the tissue morphology of HNSCC and is able to allow a grading of dysplasia and malignant tissue with similar precision as done by H&E staining histopathology. Therefore, it was analysed if it is possible to visualize a variety of standard architectural and cytological changes as given by actual WHO grading scheme (Table 1) also by multimodal nonlinear imaging. The completely label free multimodal images retrieve chemical images of the tissue. In the three cases presented the chemical composition changes in relation to normal tissue which is valuable for studying the process of cancerization. Additionally morphologic information of the multimodal nonlinear images was compared to the parallel H&E sections. Each individual imaging method highlights either a single or a group of chemical constituents of the tissue section, which is specifically lipids in case of coherent anti-Stokes Raman scattering (CARS), specifically collagen in case of second harmonic generation (SHG)

[13, 14] and various autofluorescing species like nicotinamide adenine dinucleotide (NADH), elastin and keratin in the case of two photon excited fluorescence (TPEF) [14, 15].

**Table 1** – Summary of morphologic alterations observable during malignant transformation on which the WHO grading scheme of epithelial dysplasia is based. The mentioned alterations can be visualized by nonlinear imaging. The loss of basement-membrane integrity presents the hallmark for diagnosing invasive carcinoma<sup>20</sup>

---

<b>Architectural changes</b>	<b>Cytological changes</b>
Irregular epithelial stratification	Abnormal variation in cell size and shape
Dyskeratosis	Abnorm. var. in nuclear size and shape
Hyperplasia	Increased nuclear/cytoplasmic ratio
Irregular shaped rete pegs	Enlarged nuclei and cells
Loss of integrity of basement membrane	Loss of polarity of basal cells

---

## Case 1

The first case was a 56-year old male patient with squamous cell carcinoma of hypopharynx and larynx (pT3pN2bM0; Figure 2). He was treated by partial resection of hypopharynx and larynx, neck dissection, transient tracheostomy, and postoperative radiochemotherapy.

In Figure 3 A a region of normal and dysplastic epithelium of the laryngeal side of the tumor is shown. The H&E stained parallel section (Figure 3 A) clearly showed morphologic alterations of the dysplastic epithelium, especially the irregular stratification, irregular shaped rete pegs, abnormal variation in nuclear as well as cell size and shape, increased nuclear to cytoplasm ratio and the predominantly loss of polarity of basal cells. In addition inflammation of the adjacent connective tissue was evident by high concentration of lymphocytes, partially also invading the epithelium.

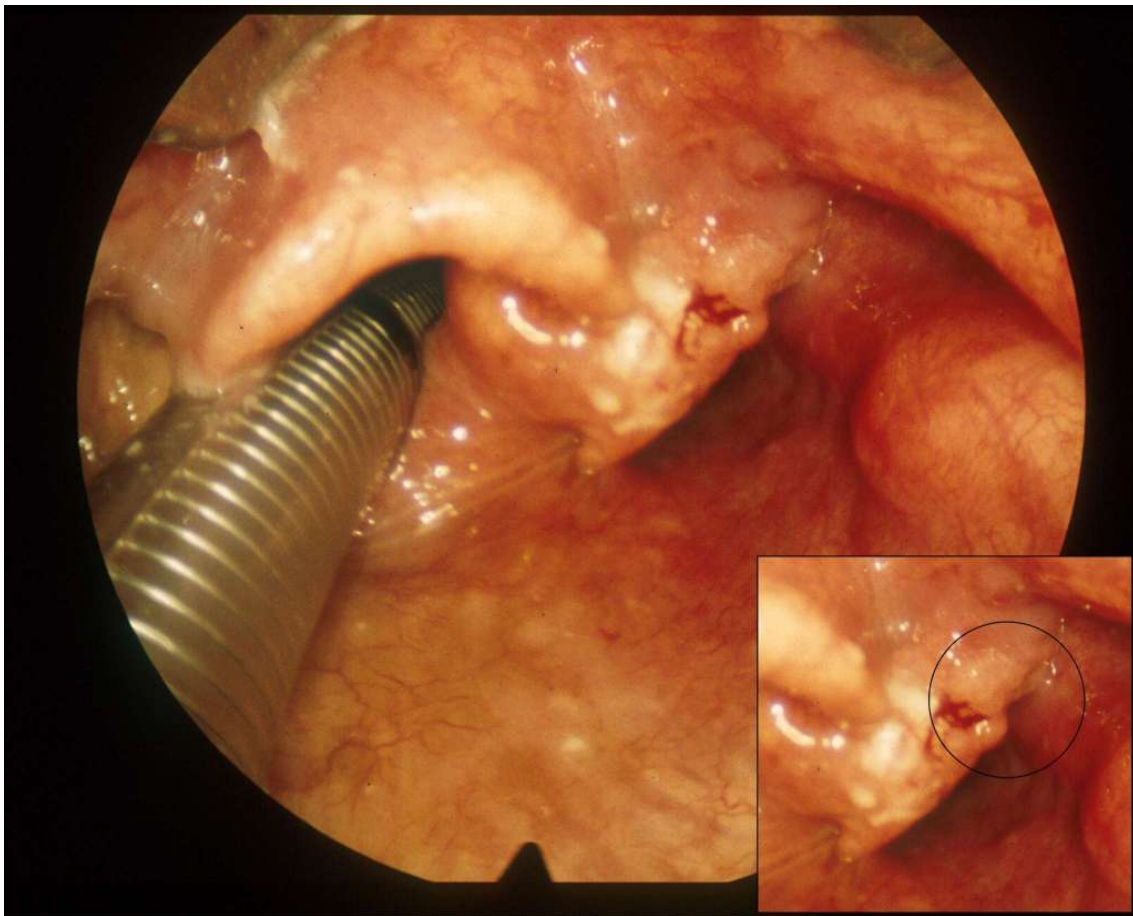


**Figure 2** – Endoscopic view on the carcinoma of hypopharynx-larynx of case 1. The magnification in the right lower corner is showing the area of the tumor border which was selected for the further investigation of the shift from normal to dysplastic and then to the malignant tumor (cf. Figures 3 and 4)

By direct comparison, all of these features were also discernible in the multimodal nonlinear images. For clarity only TPEF and SHG (Figure 3 B, TPEF green, SHG blue) and CARS and SHG (Figure 3 C, CARS grey scale, SHG blue) had been combined. The TPEF channel (detection window 435-485 nm) showed the cytoplasm in bright green, while the cell nuclei present as dark spots due to lacking fluorescence signal. The prominent signal within the cytoplasm was due to the presence of NADH/NADPH [16], a fluorescing metabolite.

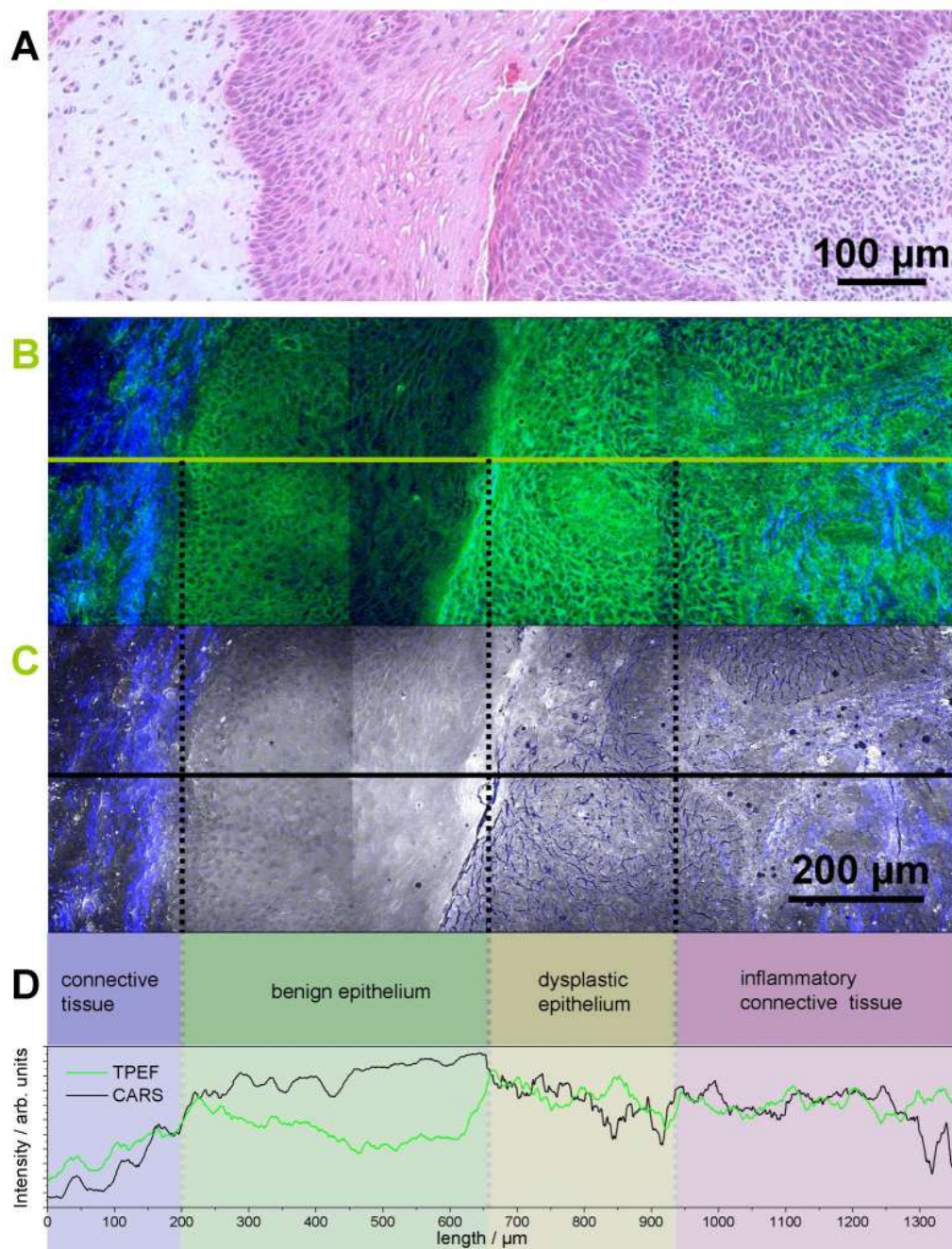


**Figure 3** – Comparison of a hematoxylin–eosin-stained (original magnification 20×) image (A) and nonlinear microscopic images of an unlabeled parallel tissue section showing normal (left) and dysplastic epithelium (right) of case 1 with hypopharyngeal–laryngeal carcinoma. Differences in the morphology as well as the chemical composition provide contrast for clear differentiation.

**continued caption Figure 3** composite image of SHG (blue) and TPEF 435–485 nm (green) is displayed in (B), whereas a combination of CARS (gray) and SHG (blue) is shown in (C). To generate these large images 3 single microscopic images are stitched together. Illumination artefacts at the boundary of these images are due to non-uniform illumination across the whole field of view. (D) Intensity cross sections of CARS and TPEF image along the marked lines demonstrate contrast between connective tissue, benign and dysplastic epithelium based on the concentration of autofluorescing species (TPEF), and lipids (CARS). The SHG signal is mainly due to collagen. The origin of residual SHG signal within dysplastic epithelium might be due to overexpression of collagen in the extracellular matrix of dysplastic epithelium with respect to benign tissue.

---

In addition, Figure 3 depicts intensity profiles along the marked lines, showing contrast in the fluorescence signal between normal and dysplastic tissue. Also the CARS channel provided contrast for differentiating normal from dysplastic epithelium as evident from 3 C and the corresponding intensity profile (black line, 3 D). The CARS intensity was - on average - higher within normal epithelium. It should be noted, that the intensity profile reflects relative changes of concentrations. Quantification is - however - due to the nonlinear concentration dependence of CARS, not possible. By SHG (3 panels B and C, blue) collagen containing structures within the connective tissue were visualized. This image modality was especially useful for visualizing the basement membrane, e.g. detect breaks through this membrane during invasive tumor growth and monitoring irregular shaped rete pegs. Comparing the SHG signal in the connective tissue below normal and dysplastic epithelium the structural differences were apparent. In particular for case 1 the smoothness of the basement membrane confining dysplastic epithelium decreased and the structure of collagen became more disordered in the connective tissue underlying dysplastic epithelium. This might be due to inflammation of the connective tissue. While the basement membrane is directly attached to the basal cell layer and parallel aligned in case of normal epithelium, the total collagen signal in the presented case of dysplastic epithelium was lower and not directly located at the basement. Much morphologic information on architectural and cytological changes usually obtained by H&E staining was also observed by nonlinear imaging. Especially the TPEF signal showed

---

the stratification of normal epithelium, which is disturbed in case of dysplasia. Since cell nuclei lack fluorescence signal and the cytoplasm produces a bright TPEF signal, also the change in nucleus to cytoplasm ratio, the irregular variation in cell and nuclear size and shape as well as the loss of polarity of basal cells is evident. To verify these results magnified images of areas of normal, dysplastic and malignant epithelial tissue of a larynx specimen of case 1 were analyzed and displayed in Figure 4. The first row displays H&E stained and multimodal nonlinear images of normal epithelium (4 A). The second and third rows show dysplastic epithelium and carcinoma in situ, respectively. In the first column, H&E stained brightfield images of comparable regions of the parallel section are shown, whereas the second and third column display combined TPEF (green) /SHG (blue) images and composite CARS (grey) /SHG (blue) images, respectively. The images reveal from panel Figure 4 A to C increasing morphologic alterations. The pronounced histological changes visible include the loss of stratification, the increasingly abnormal variation in cell and nuclear size and shape, loss of polarity of basal cell and the increasing inflammation within the connective tissue. The cell dense inflammatory infiltrate is particularly pronounced in the TPEF image of panel C (CIS) and accompanied by a marked loss in SHG signal of collagen.

## Case 2

The second case was a 59-year old male patient with a pT3N2bM0 carcinoma of the left tonsil. He was treated by partial pharyngectomy, neck dissection, radial-forearm flap, and postoperative radiochemotherapy. This case allowed examining by nonlinear microscopy how a more developed malignant grade resulted in breaking of cancer cells through the basement membrane and invasively growing into the connective tissue and the formation of tumor nests and cords (Figure 5). The borders of tumor islets infiltrating the connective tissue were visualized by SHG (blue), displaying dense collagen fibres compressed by invasive growth of malignant tissue. These dense collagen structures were also responsible for the strong CARS signal at  $2850\text{ cm}^{-1}$  due to the sensitivity of CARS with respect to densely packed organic structures as collagen fibers or keratin pearls. Thus collagen was visualized by colocalized CARS



and SHG signal as shown in Figure 5 F. TPEF allowed the visualization of the cell density, nucleus size and shape and nucleus to cytoplasm ratio of the malignant tissue (Figure 5 E). By comparing the images of classical histopathology with the findings from multimodal nonlinear imaging it became also in case 2 evident that multimodal imaging agreed well with the current golden standard of H&E staining histopathology.

### Case 3

The last case was a 60-year old male patient with a cT3cN2cM0 carcinoma of the hypopharynx. Due to severe comorbidity treatment consisted of tracheostomy and best supportive care. This case was an example for dyskeratosis, i.e. another possible change during malignant transformation, for instance the overexpression of keratin, a fluorescent protein, at unusual sites, e.g. within the epithelium. Such keratin pearls present valuable diagnostic markers for certain types of SCCs as abnormal keratinization and keratin pearls are a marker for negative human papillomavirus (HPV) status. This is especially important for SCC of the oropharynx, since 70% of tumors originating in this site are HPV associated. These tumors have a better prognosis than non HPV associated tumors and are usually non-keratinizing [17]. In Figure 6 A a section of the hypopharynx carcinoma is shown. The overview multimodal image in panel 6A shows keratinized regions employing CARS (grey scale) and TPEF (green). A single keratin pearl is magnified in panel 6 C. The strong CARS signal of the keratin pearl is due to the high density of the keratin structure and therefore a large amount of scattering functional  $CH_2$ -groups. For comparison a H&E stained image of a parallel section is displayed in panel 6 B. Arrows mark keratinized regions, which are intensely stained by eosin.

### Discussion

The multitude of morphologic and information on the chemical composition derived from multimodal imaging exceeded much the information content obtained from H&E stained images and might be of great value for a deeper understanding of the fundamental metabolic changes connected with disease progression.

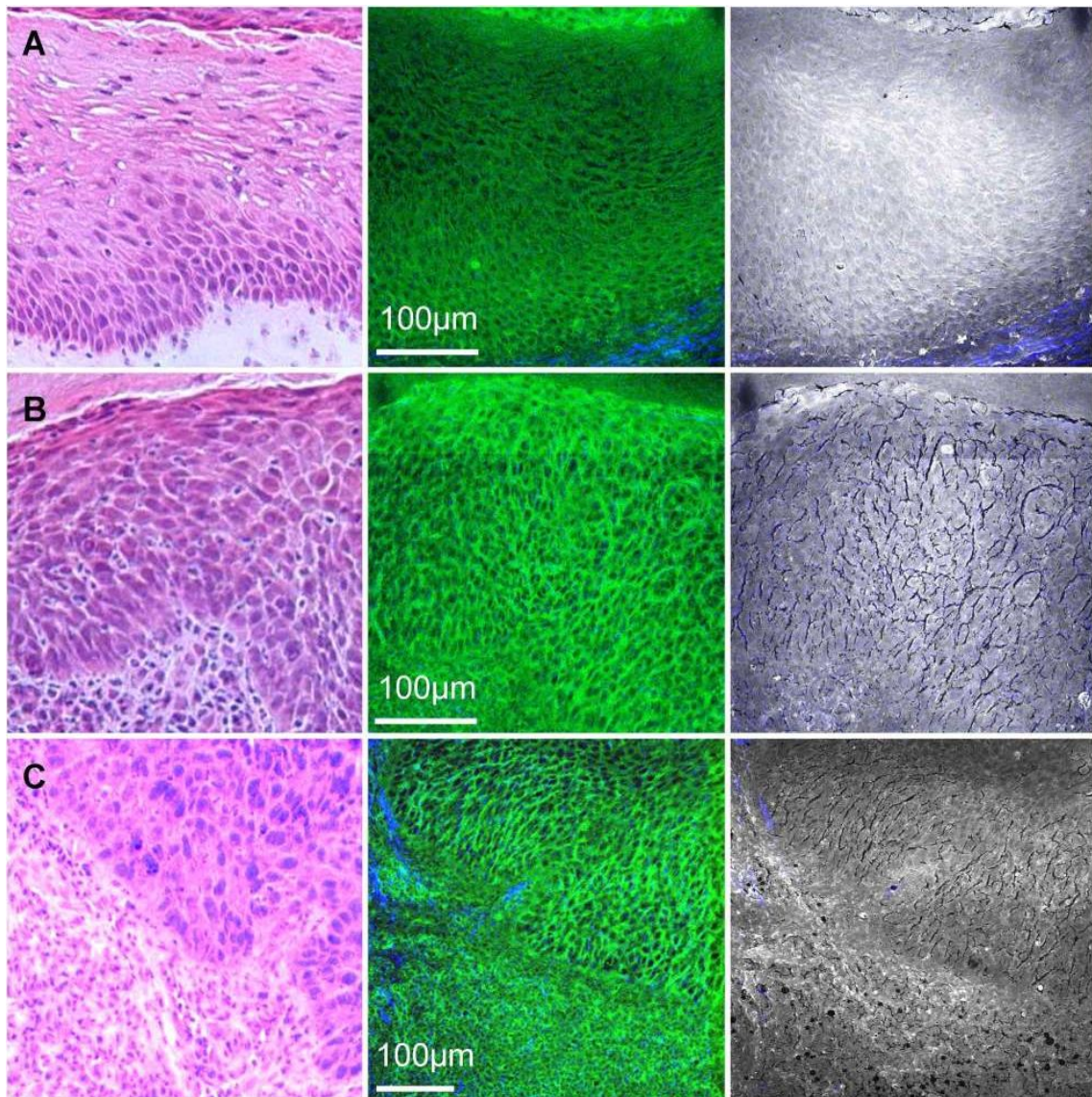


**Figure 4** – Morphological changes during malignant transformation of hypopharynx-larynx carcinoma in case 1. Compilation of H&E images (first column), merged TPEF (green, second column) and SHG images (blue, second and third column) and CARS images (grey scale, third row) images of normal epithelium (A), dysplastic tissue (B) and carcinoma in situ (C) of a larynx carcinoma specimen demonstrating label-free visualizing morphological changes during malignant transformation by nonlinear multimodal imaging. The most prominent are from top to bottom loss of stratification, inflammation of the connective tissue, abnormal variation in cell and nuclear size and shape. H&E images are obtained from a parallel tissue cut.

The presented three cases demonstrate the so far little employed prospects of multimodal nonlinear microscopy for head and neck cancer imaging: In the first case of a laryngeal cancer, an increased signal of NADH/NADPH within the cytoplasm of dysplastic epithelium in comparison to benign tissue was found. Its concentration in the cytoplasm is closely connected to the metabolic activity of the cell [16]. Hence, multimodal imaging allowed the detection of an overall increase in fluorescence signal in dysplastic epithelium that might be due to an increased metabolic activity. Since the CARS intensity was higher within normal epithelium, it can be concluded, that the lipid concentration was higher in benign tissue than in dysplastic or tumor tissue. Here, multimodal imaging enabled insight in chemical changes accompanying the malignant transformation process within the epithelium and extending into the adjacent connective tissue.

For this particular case the loss of smoothness of the basement membrane and the increased disorder of the structure of collagen in the connective tissue underlying dysplastic epithelium is most likely due to inflammation of the connective tissue [18, 19], a process closely related to carcinogenesis. The loss in SHG intensity can have in general two explanations: (i) The overall collagen concentration can be lower or (ii) the ordering of the collagen fibers is irregular, hence, reducing the generation of the second harmonic signal. It can be concluded that the boundary to the connective tissue is disturbed in dysplastic epithelium. Since the beforehand mentioned chemical alterations in lipid, NAD(P)H and collagen concentration cannot be derived from H&E staining, multimodal nonlinear imaging clearly adds information. Case 2 exemplified the high concordance of the morphologic findings in multimodal imaging and classic histomorphology. Of course, the accuracy of the method has now to be proven in a larger series of cases. Dyskeratosis was demonstrated in case 3 by the overexpression of keratin, a fluorescent protein, at unusual sites, e.g. within the epithelium [17, 20]. Such keratin pearls present valuable diagnostic markers for certain types of SCCs as abnormal keratinization and keratin pearls are regarded as a marker for HPV-negative oropharyngeal tumors [21]. Since a large amount of tumors originating in this site are HPV associated, this is an important finding for patient prognosis. In this regard, multimodal imaging might help in the future to reveal

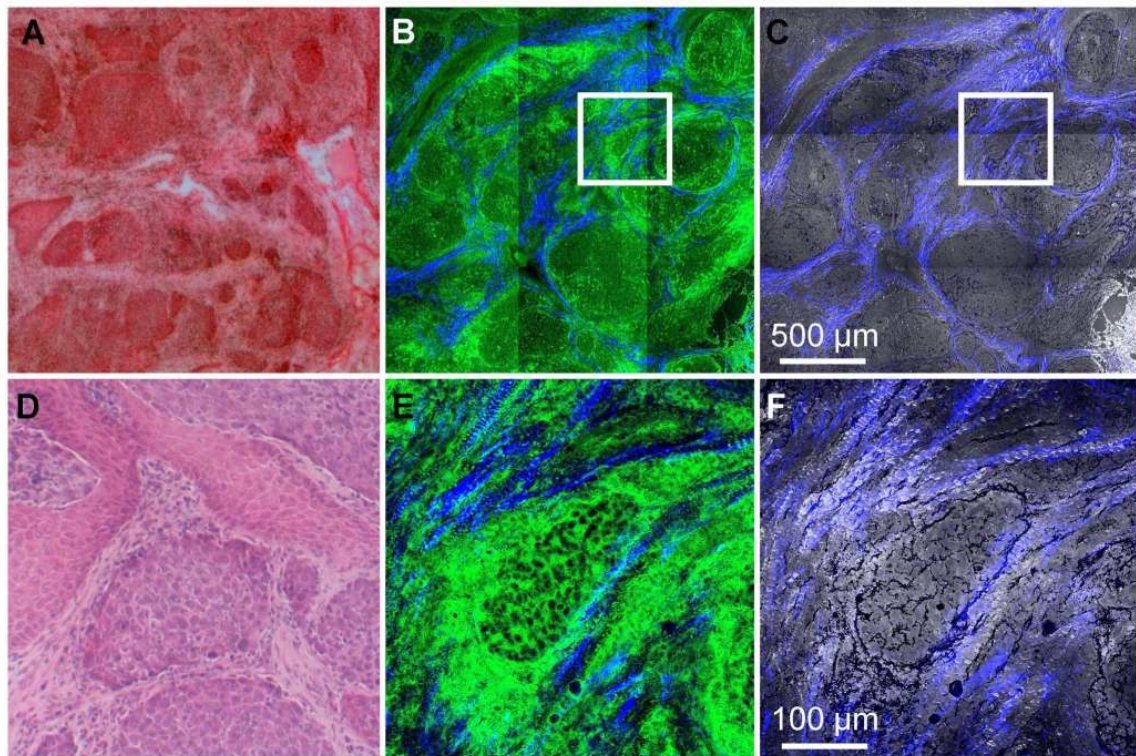


**Figure 5** – Invasively growing squamous cell carcinoma originating in the oropharynx of case 2. The upper row displays in panel A an H&E stained image of the parallel section, a combined TPEF (green) SHG (blue) image in panel B and a composite CARS (grey) and SHG (blue) image in C. Infiltrating tumor nests surrounded by collagen fibers within the connective tissue are visualized especially due to the pronounced SHG signal of collagen. The second row shows in panels E and F magnified images of a single nest as indicated in panels B and C. Here TPEF visualizes single cell nuclei, whereas CARS and SHG highlight the dense collagen structure. In panel D a H&E stained image of a tumor islet is shown for comparison. The H&E image is taken from a parallel tissue cut.

specific etiopathologic and molecular features of HPV-positive in differentiation to HPV-negative tumors. In the following the advantages but also current limitations of multimodal nonlinear imaging of HNSCC will be briefly discussed.

For routine clinical application novel methods have to significantly improve established diagnostics. For an imaging method especially contrast and resolution for visualizing relevant structures as well as speed are key features. In this respect nonlinear microscopy compares very well with alternative imaging modalities. These methods include vital staining with toluidine blue, autofluorescence at 400-460 nm

excitation, contact endoscopy, genetic analysis [17] ultrasound and optical-coherence tomography (OCT) [22]. However, all these approaches are associated with specific pitfalls. The dye toluidine blue used for vital staining has significant cardiac toxicity. Contact endoscopy and autofluorescence allow for determining the horizontal extension of a cancerous lesion, however, the thickness of the epithelial layer as additional grading factor is not assessable [23] due to the limited penetration depth of the excitation light. OCT and ultrasound on the other hand have high penetration

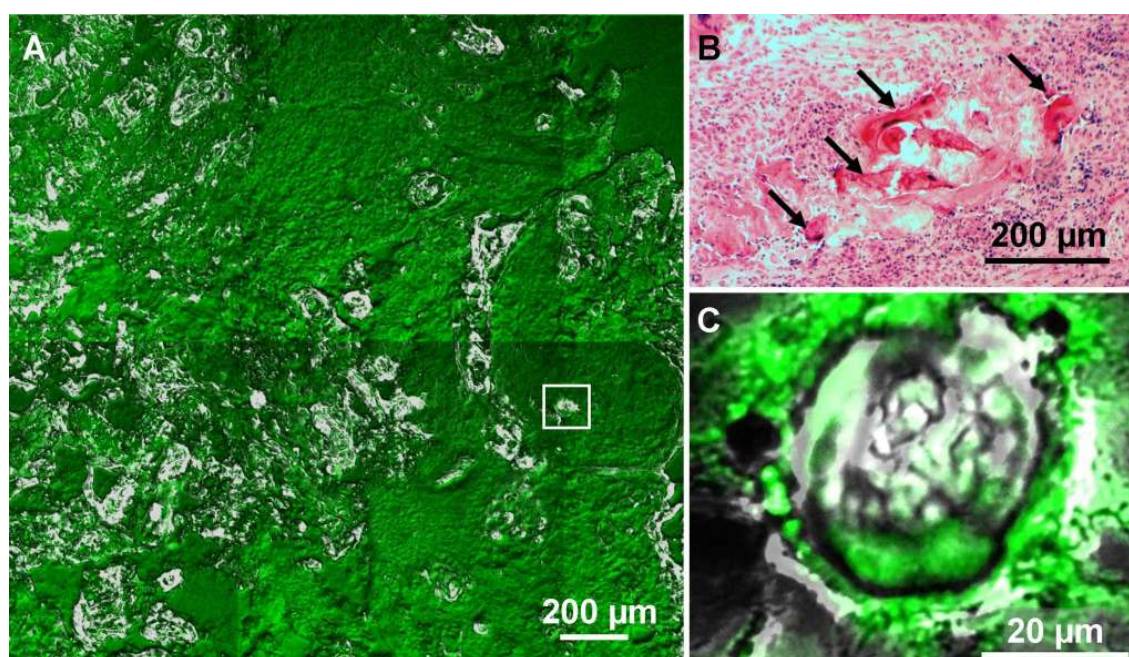


**Figure 6** – Imaging of dyskeratosis of a hypopharyngeal tumor in case 3. Dense keratin pearls give rise to intense fluorescence (green) colocalized with a pronounced CARS signal within the aliphatic C-H-stretching region at  $2850\text{ cm}^{-1}$  (white, grey scale). In panel A an overview image of TPEF (green) and CARS (grey scale) is displayed, panel C shows a magnified single pearl as indicated by the boxed area and in panel B a H&E stained image of a parallel section is displayed for comparison. The arrows mark keratin pearls in the H&E section. Keratin is eosinophilic and therefore intensely stained by eosin.

depth (typically more than 1 mm) but both techniques lack chemical contrast and spatial resolution, which e.g. is limited to typically  $15\ \mu\text{m}$  using OCT. Hence, OCT is not capable to detect cellular atypia relevant for histopathologic grading, e.g. size and shape of cell nuclei, nucleus to cytoplasm ratio [23]. Finally, genetic analysis on the other hand is too slow and cannot be applied intraoperatively.

As evident from the results presented, multimodal nonlinear imaging does not suffer from these limitations but offers unique advantages compared to the beforehand mentioned methods, which will be briefly summarized in the following. CARS, SHG and TPEF are label free and non-invasive and provide contrast based on the chemical composition of the tissue which compares well with H&E staining. Due to the use of NIR laser light the depth penetration is maximized to a few 100  $\mu m$  while maintaining diffraction limited optical resolution and 3D sectioning capability due to the confinement of the nonlinear excitation process to the laser focus allowing for visualizing cellular atypia inaccessible by OCT. Thus these techniques have been successfully employed in biomedical imaging. Second harmonic generation microscopy [13] specifically highlights the distribution of the structural protein collagen. The SHG signal is directional and depends quadratically on the density of the collagen fibrils in addition to their molecular order. Hence, it can be used as an indicator for ordering and density of collagen structures, both of which change in tumor environment [24, 25].

By TPEF the spatial distribution of autofluorescing molecular species can be visualized. In epithelial tissue of the head and neck abundant fluorophors include porphyrins, NAD(P)H, elastin [9] and keratin. Here especially the keratin composition changes during malignant transformation [26], and the NADPH concentration is a marker for increased metabolic activity in cancer [27]. TPEF can be applied to study the composition of epithelial tissue and detect dysplastic alterations by visualizing morphologic changes [28].

Similar to SHG the CARS signal is proportional to the square of the concentration of scatterers within the focal volume but depends on the cubed intensity of the illuminating lasers. CARS microscopy [11] is mainly utilized to visualize the lipid distribution of tissue, since lipids produce an exceptional large signal within the aliphatic C-H-stretching region at  $2850\text{ cm}^{-1}$  due to the high number of scatterers [29, 30]. Furthermore the lipid content has been shown to be sensitive to differentiate cancer from normal tissue in brain [12, 31] and colon tissue [32] since the lipid content in tumors is in general lower due to the fast metabolism of malignant tissue. The lipid metabolism and its connection to tumor growth has been the scope of a

few CARS microscopic investigations [33, 34]. Since all three methods have been shown to provide chemical contrast useful for cancer imaging, the synergistic combination of these modalities presents a promising approach to maximize the chemical contrast of nonlinear optical imaging. While a combination of OCT, SHG and TPEF was already applied to the visualization of squamous cell carcinoma [35], multimodal nonlinear imaging including CARS was not yet employed to investigate SCCs of the head and neck, but to visualize the chemical composition and spatial extent of basal cell carcinoma [36] beside various applications of TPEF and SHG to skin imaging [37, 38, 39].

In table 1 a comprehensive selection of morphologic parameters required for grading dysplasia of the head and neck is summarized, which can all be derived by multimodal nonlinear microscopy only. An overview of a complete list of morphologic alterations can be found here [20, 40]. Architectural changes like stratification, hyperplasia, and shape of rete pegs are accessible by either CARS or TPEF imaging, while keratin is detectable by colocalized CARS and TPEF signals. SHG provides an extremely sensitive imaging modality for monitoring the integrity of the basement membrane. Cytological changes on the other hand can be derived from TPEF and CARS images, where TPEF provides especially high contrast for the detection of nuclei. In addition to this pure morphologic data specific information on the chemical tissue composition, especially the collagen (SHG), lipid (CARS) and NADH (TPEF) distribution is obtained, which is helpful for studying the process of carcinogenesis.

Currently the application of nonlinear microscopy in clinics is limited due to the need for expensive, large laser equipment. These lasers require regularly maintenance and need to be operated by trained specialists. Therefore alignment and maintenance are time consuming. However, novel lasers sources [41] are being developed allowing for manufacturing small footprint and robust surgical microscopes for routine application in the future. Employing pulsed lasers inhibits also the use of established endoscopes, but development of novel fiber optic probes [42] is in progress. Here proof of principle experiments in clinical environment need to be performed in the near future. Also automated image analysis routines need to be developed for online

interpretation of the multimodal image data. Currently the time for acquiring raw images is on the order of fractions of a second to a few minutes depending on signal strength and image size, but videorate image acquisition is possible if sufficient signal is generated [43].

In conclusion multimodal nonlinear microscopy provides a variety of morphologic information required for grading of dysplastic and malignant epithelial tissue. In addition changes in the chemical composition during malignant transformation can be visualized. Especially a high depth penetration is a key feature for optical guidance and routine screening of suspicious lesions of the head and neck. This is due to the fact, that first tissue alterations in mild and moderate dysplasia manifest themselves in the lower part of the epithelial lining and are therefore not visible at the surface. By implementing these techniques into an endoscope or surgical microscope an on-line optical biopsy can be obtained. This has the potential of greatly improving speed and accuracy in diagnostics. Therefore the development of compact and robust light sources and optical probes as well as the development of automated image processing routines are prerequisites for translating these techniques to the clinics. Furthermore, the methodological spectrum could be used in future projects to analyse the tumor response during neoadjuvant or adjuvant chemotherapy or to describe chemical changes in the tumor environment during carcinogenesis.

## **Acknowledgments**

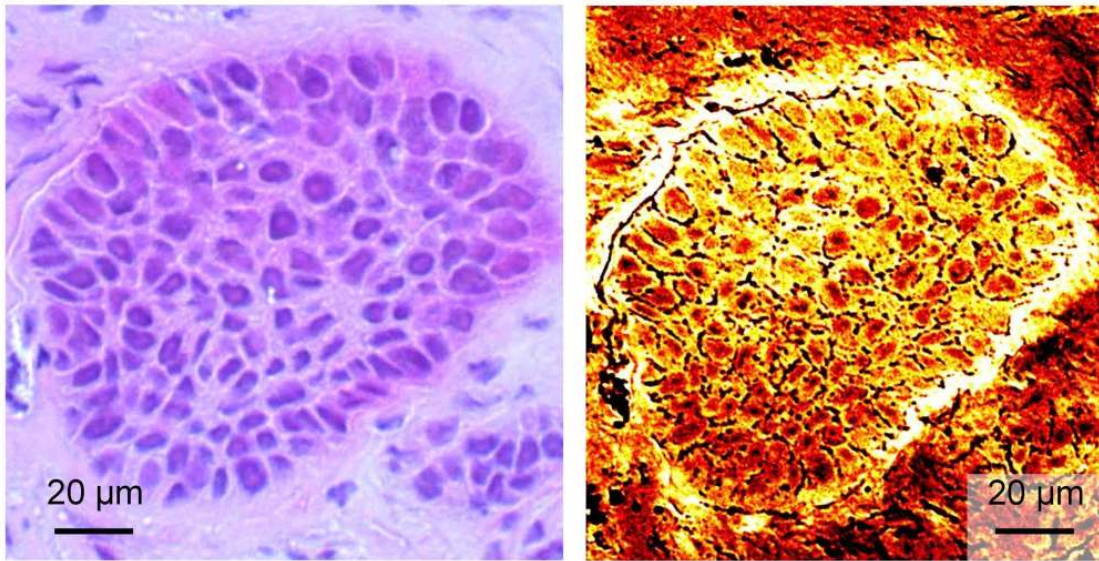
Financial support of the European Union via the Europäischer Fonds für Regionale Entwicklung (EFRE) and the "Thüringer Ministerium für Bildung Wissenschaft und Kultur (TMBWK)" (Projects: B714-07037, B578-06001, 14.90 HWP) and via the European network of excellence P4L (Photonics4Life) as well as financial support by the German Ministry for Science and Education (BMBF) *MediCARS* (FKZ: 13N10774) is highly acknowledged.



## References

- [1] Argiris, A., Karamouzis, M. V., Raben, D., and Ferris, R. L. *The Lancet* **371**(9625), 1695–1709 (2008).
- [2] Forastiere, A., Koch, W., Trotti, A., and Sidransky, D. *New England Journal of Medicine* **345**(26), 1890–1900 (2001).
- [3] Braakhuis, B. J. M., Brakenhoff, R. H., and Leemans, C. R. *The Oncologist* **10**(7), 493–500 August (2005).
- [4] Leemans, C. R., Tiwari, R., Nauta, J. J. P., Waal, I. V. D., and Snow, G. B. *Cancer* **73**(1), 187–190 (1994).
- [5] Upile, T., Jerjes, W., Sterenborg, H. J. C. M., El-Naggar, A. K., Sandison, A., Witjes, M. J. H., Biel, M. A., Bigio, I., Wong, B. J. F., Gillenwater, A., MacRobert, A. J., Robinson, D. J., Betz, C. S., Stepp, H., Bolotine, L., McKenzie, G., Mosse, C., Barr, H., Chen, Z., Berg, K., D’Cruz, A. K., Stone, N., Kendall, C., Fisher, S., Leunig, A., Olivo, M., Richards-Kortum, R., Soo, K., Bagnato, V., Choo-Smith, L.-P., Svanberg, K., Tan, I. B., Wilson, B. C., Wolfson, H., Yodh, A. G., and Hopper, C. *Head & Neck Oncology* **1**(1), 25 (2009).
- [6] Neugebauer, U., Clement, J. H., Bocklitz, T., Krafft, C., and Popp, J. *Journal of Biophotonics* **3**(8-9), 579–587 (2010).
- [7] Petry, R., Schmitt, M., and Popp, J. *ChemPhysChem* **4**(1), 14–30 (2003).
- [8] Harris, A. T., Rennie, A., Waqar-Uddin, H., Wheatley, S. R., Ghosh, S. K., Martin-Hirsch, D. P., Fisher, S. E., High, A. S., Kirkham, J., and Upile, T. *Head & Neck Oncology* **2**, 26 (2010).
- [9] Hughes, O. R., Stone, N., Kraft, M., Arens, C., and Birchall, M. A. *Head & Neck* **32**(11), 1544–1553 November (2010).
- [10] Keereweer, S., Sterenborg, H. J. C. M., Kerrebijn, J. D. F., Van Driel, P. B. A. A., de Jong, R. J. B., and Löwik, C. W. G. M. *Head & Neck* .
- [11] Zumbusch, A., Holtom, G. R., and Xie, X. S. *Phys. Rev. Lett.* **82**(20), 4142–4145 (1999).
- [12] Meyer, T., Bergner, N., Bielecki, C., Krafft, C., Akimov, D., Romeike, B. F. M., Reichart, R., Kalff, R., Dietzek, B., and Popp, J. *Journal of Biomedical Optics* **16**(2), 21113 (2011).
- [13] Campagnola, P. *Biophysical Journal* **82**(1), 493–508 (2002).
- [14] Cicchi, R., Crisci, A., Nesi, G., Cosci, A., Giancane, S., Carini, M., and Pavone, F. S. In *Advanced Microscopy Techniques*, Campagnola, P., editor, volume 7367 of *Proceedings of SPIE-OSA Biomedical Optics*, 7367. Optical Society of America, (2009).
- [15] Zipfel, W. R., Williams, R. M., Christie, R., Nikitin, A. Y., Hyman, B. T., and Webb, W. W. *Proceedings of the National Academy of Sciences of the United States of America* **100**(12), 7075–7080 (2003).
- [16] Huang, S., Heikal, A. A., and Webb, W. W. *Biophysical Journal* **82**(5), 2811–2825 (2002).
- [17] Pai, S. I. and Westra, W. H. *Annual Review of Pathology: Mechanisms of Disease* **4**(1), 49–70 (2009).
- [18] Coussens, L. M. and Werb, Z. *Nature* **420**(6917), 860–867 (2002).
- [19] Balkwill, F. and Mantovani, A. *The Lancet* **357**(9255), 539–545 (2001).
- [20] Sapp, J. P., Eversole, L., and Wysocki, G. *Contemporary Oral and Maxillofacial Pathology*. Elsevier, (2003).
- [21] Chernock, R. D., El-Mofty, S. K., Thorstad, W. L., Parvin, C. A., and Lewis, J. S. *Head and Neck Pathology* **3**(3), 186–194 (2009).
- [22] Kraft, M., Glanz, H., von Gerlach, S., Wisweh, H., Lubatschowski, H., and Arens, C. *Head & Neck* **30**(12), 1628–1635 (2008).

- [23] Arens, C., Glanz, H., Wönckhaus, J., Hersemeyer, K., and Kraft, M. *European Archives of Oto-Rhino-Laryngology: Official Journal of the European Federation of Oto-Rhino-Laryngological Societies (EUFOS): Affiliated with the German Society for Oto-Rhino-Laryngology - Head and Neck Surgery* **264**(6), 645–649 (2007).
- [24] Campagnola, P. *Anal. Chem.* **83**(9), 3224–3231 (2011).
- [25] Cicchi, R., Kapsokalyvas, D., Giorgi, V. D., Maio, V., Wiechen, A. V., Massi, D., Lotti, T., and Pavone, F. S. *Journal of Biophotonics* **3**(1-2), 34–43 (2010).
- [26] Ogden, G. R., Lane, E. B., Hopwood, D. V., and Chisholm, D. M. *British Journal of Cancer* **67**(6), 1324–1330 (1993).
- [27] DeBerardinis, R. J., Lum, J. J., Hatzivassiliou, G., and Thompson, C. B. *Cell Metabolism* **7**(1), 11–20 (2008).
- [28] Wilder-Smith, P., Osann, K., Hanna, N., Abbadi, N. E., Brenner, M., Messadi, D., and Krasieva, T. *Lasers in Surgery and Medicine* **35**(2), 96–103 August (2004).
- [29] Evans, C. L. and Xie, X. S. *Annual Review of Analytical Chemistry (2008)* **1**(1), 883–909 (2008).
- [30] Krafft, C., Ramoji, A. A., Bielecki, C., Vogler, N., Meyer, T., Akimov, D., Rösch, P., Schmitt, M., Dietzek, B., Petersen, I., Stallmach, A., and Popp, J. *Journal of Biophotonics* **2**(5), 303–312 (2009).
- [31] Evans, C. L., Xu, X., Kesari, S., Xie, X. S., Wong, S. T. C., and Young, G. S. *Optics Express* **15**(19), 12076–12087 (2007).
- [32] Krafft, C., Dietzek, B., and Popp, J. *The Analyst* **134**(6), 1046–1057 (2009).
- [33] Le, T. T., Rehrer, C. W., Huff, T. B., Nichols, M. B., Camarillo, I. G., and Cheng, J.-X. *Molecular imaging: official journal of the Society for Molecular Imaging* **6**(3), 205–211 (2007).
- [34] Le, T. T., Huff, T. B., and Cheng, J.-X. *BMC Cancer* **9**, 42 (2009).
- [35] Wilder-Smith, P., Krasieva, T., Jung, W.-G., Zhang, J., Chen, Z., Osann, K., and Tromberg, B. *Journal of Biomedical Optics* **10**, 51601 (2005).
- [36] Vogler, N., Meyer, T., Akimov, D., Latka, I., Krafft, C., Bendsoe, N., Svanberg, K., Dietzek, B., and Popp, J. *Journal of Biophotonics* **3**(10-11), 728–736 (2010).
- [37] Medyukhina, A., Vogler, N., Latka, I., Kemper, S., Böhm, M., Dietzek, B., and Popp, J. *Journal of Biophotonics* **4**(9), 627–636 September (2011).
- [38] Cicchi, R., Sestini, S., De Giorgi, V., Massi, D., Lotti, T., and Pavone, F. S. *Journal of Biophotonics* **1**(1), 62–73 (2008).
- [39] Laiho, L. H., Pelet, S., Hancewicz, T. M., Kaplan, P. D., and So, P. T. C. *Journal of Biomedical Optics* **10**, 24016 (2005).
- [40] Reibel, J. *Critical Reviews in Oral Biology and Medicine: An Official Publication of the American Association of Oral Biologists* **14**(1), 47–62 (2003).
- [41] Baumgartl, M., Chemnitz, M., Jauregui, C., Meyer, T., Dietzek, B., Popp, J., Limpert, J., and Tünnermann, A. *Optics Express* **20**(4), 4484–4493 (2012).
- [42] Balu, M., Liu, G., Chen, Z., Tromberg, B. J., and Potma, E. O. *Optics Express* **18**(3), 2380–2388 (2010).
- [43] Evans, C. L., Potma, E. O., Puoris'haag, M., Cote, D., Lin, C. P., and Xie, X. S. *Proc Natl Acad Sci U S A* **102**(46), 16807–16812 November (2005).



This chapter is based on the pre-peer reviewed version of the original article and adapted with kind permission from Wiley-VCH Verlag GmbH & Co. KGaA:

**Authors:** Tobias Meyer, Norbert Bergner, Anna Medyukhina, Benjamin Dietzek, Christoph Krafft, Bernd F. M. Romeike, Rupert Reichart, Rolf Kalff, and Jürgen Popp.

**Titel:** "Interpreting CARS images of tissue within the C-H-stretching region."

**Journal:** *Journal of Biophotonics*, 5(10):729—733, 2012.

©Copyright 2012 Wiley-VCH Verlag GmbH & Co. KGaA.  
Reproduced with permission.

The article has been published in final form at:  
[onlinelibrary.wiley.com/doi/10.1002/jbio.201200104](http://onlinelibrary.wiley.com/doi/10.1002/jbio.201200104).



## 7 | Interpreting CARS Images of Tissue Within the C-H-Stretching Region

**Tobias Meyer,<sup>1#</sup> Norbert Bergner,<sup>1#</sup> Anna Medyukhina,<sup>1</sup> Benjamin Dietzek,<sup>1,2</sup> Christoph Krafft,<sup>1</sup> Bernd F. M. Romeike,<sup>3</sup> Rupert Reichart,<sup>4</sup> Rolf Kalff,<sup>4</sup> and Jürgen Popp<sup>1,2\*</sup>**

<sup>1</sup>Institute of Photonic Technology e.V., Albert-Einstein-Strasze 9, 07745 Jena, Germany

<sup>2</sup> Institute of Physical Chemistry and Abbe Center of Photonics, Friedrich-Schiller-University Jena, Helmholtzweg 4, 07743 Jena, Germany

<sup>3</sup>Institute of Pathology, Neuropathology, Jena University Hospital, Erlanger Allee 101, 07747 Jena, Germany

<sup>4</sup> Clinic for Neurosurgery, Jena University Hospital, Erlanger Allee 101, 07747 Jena, Germany

# contributed equally to this work

\* corresponding author: juergen.popp@ipht-jena.de

## Abstract

Single band coherent anti-Stokes Raman scattering (CARS) microscopy is the fastest implementation of nonlinear vibrational imaging allowing for video-rate image acquisition of tissue. This is due to the large Raman signal in the C-H-stretching region. However, the chemical specificity of such images is conventionally assumed to be low. Nonetheless, CARS imaging within the C-H-stretching region enables detection of single cells and nuclei, which allows for histopathologic grading of tissue. Relevant information such as nucleus to cytoplasm ratio, cell density, nucleus size shape is extracted from CARS images by innovative image processing procedures. In this contribution CARS image contrast within the C-H-stretching region is interpreted by direct comparison with Raman mapping and correlated to the tissue composition justifying the use of CARS imaging in this wavenumber region for biomedical applications.

**KEY WORDS:** CARS microscopy, Raman micro spectroscopy, C-H-stretching vibration, vibrational imaging.

## Introduction

Since its revival in 1999 CARS microscopy [1] has become a powerful label-free imaging modality in life sciences [2, 3]. During the past years further vibrational imaging methods have been introduced [4, 5], but single band CARS is still the most simple and most widely used of all implementations.

In principle, all vibrational bands known from Raman microspectroscopy may be used for single-band CARS imaging. However, most signal photons and hence image contrast is generated in the C-H-stretching region, allowing for video-rate image acquisition [6] and capable of visualizing the spatial distribution of lipids and proteins [7]. CARS imaging in the fingerprint region offers higher molecular specificity but suffers from low signal levels, weak contrast and the necessity of spectrally narrow excitation. On the contrary to its widespread use in CARS microscopy the C-H-stretching spectral region is only marginally used for Raman imaging since the in-

formation content is supposed to be much lower compared to the fingerprint region. Therefore, the origin of the observed image contrast in CARS has not been correlated with Raman microspectroscopy. In this contribution CARS imaging of a human squamous cell carcinoma brain metastasis within the C-H-stretching spectral region reveals exemplarily the location of single cell nuclei and is therefore a promising imaging modality for label-free and non-invasive biomedical imaging. The origin of the observed CARS contrast for recognizing cell nuclei is interpreted with the help of Raman imaging. The results are compared to the golden standard of H&E staining histopathology. By non-invasive imaging of cell nuclei histopathologically relevant information like nucleus to cytoplasm ratio, cell density, nucleus size and shape can be extracted. This presents an essential prerequisite for *in vivo* grading of tissue by CARS microscopy in the future.

## Methods

CARS microscopic imaging and Raman microspectroscopy have been performed as described previously [8]. Biopsy specimens of patients at the Clinic for Neurosurgery, Jena University Hospital, were used with the permission of the ethics committee. 20  $\mu\text{m}$  thick frozen tissue sections of human brain tumor biopsies were used without further processing. Subsequent to vibrational imaging the samples were H&E stained for comparative analysis by the histopathological golden standard. For diagnostics pathological typing and grading of H&E stained parallel sections of the specimens were performed according to the current World Health Organization (WHO) Classification (BFMR).

In order to extract histopathologically relevant information from the CARS images, an image processing procedure for the segmentation of cell nuclei was performed, which is described in detail elsewhere [9]. The algorithm represents an alternative approach to image processing routines for extracting size, shape and other disease related cellular features of cancer tissue from CARS microscopic images [10, 11, 12]. In contrast to [11, 12] the manual selection of a point within a cell nucleus is not required; hence the algorithm allows fully automated extraction of histological fea-



tures by using, however, an approach different from [10]. The pre-processing of the images included smoothing with the edge preserving anisotropic diffusion filter and a subsequent edge detection procedure. The edge-picture served as an input for the compact Hough transformation, which was used to detect the location of the cells within the image. Each location point was then used for the radial search of the nuclear boundary in the gradient- (edge-) image, where high-amplitude positive gradient indicated nuclear boundaries. The detected boundaries were then employed to calculate nucleus size and cell density.

## Results and Discussion

In the following the relation of the CARS and Raman image contrast within the C-H-stretching region to the concentration of main tissue constituents, in particular lipids and protein, is illustrated. Furthermore, it is shown that this contrast allows for the detection of single cells and nuclei, which is required for histopathologic tissue grading. To do so a human brain tumor specimen was investigated within the C-H-stretching region by means of CARS imaging and Raman mapping. In figure 1 results from both nonlinear and linear Raman images as well as H&E staining of a human squamous cell carcinoma brain metastasis are presented. In panel A a brightfield microscopic image of the consecutively H&E stained section is directly contrasted to the CARS image of the same section before staining (B) acquired at  $2850\text{ cm}^{-1}$ . By Raman spectroscopy of the same tissue sections the CARS image contrast can be directly related to the abundance of major tissue components as displayed in figure 1 C-E. Vertex component analysis (VCA) of the Raman microscopic information results in clear differentiation of cell nuclei from the cytoplasm as evident from the abundance plots of the first two vertex components (VC) 1 and 2 in panels D and E. Panel C displays the corresponding spectra of the first two endmembers VC 1 and 2. Both abundance plots allow for differentiating cell nuclei and cytoplasm. The corresponding spectrum of VC 1 is the sum of the symmetric and antisymmetric  $\text{CH}_2$ -stretching vibration at  $2850\text{ cm}^{-1}$  and  $2930\text{ cm}^{-1}$  and the symmetric  $\text{CH}_3$  stretching vibration at  $2870\text{ cm}^{-1}$  [13]. These Raman re-

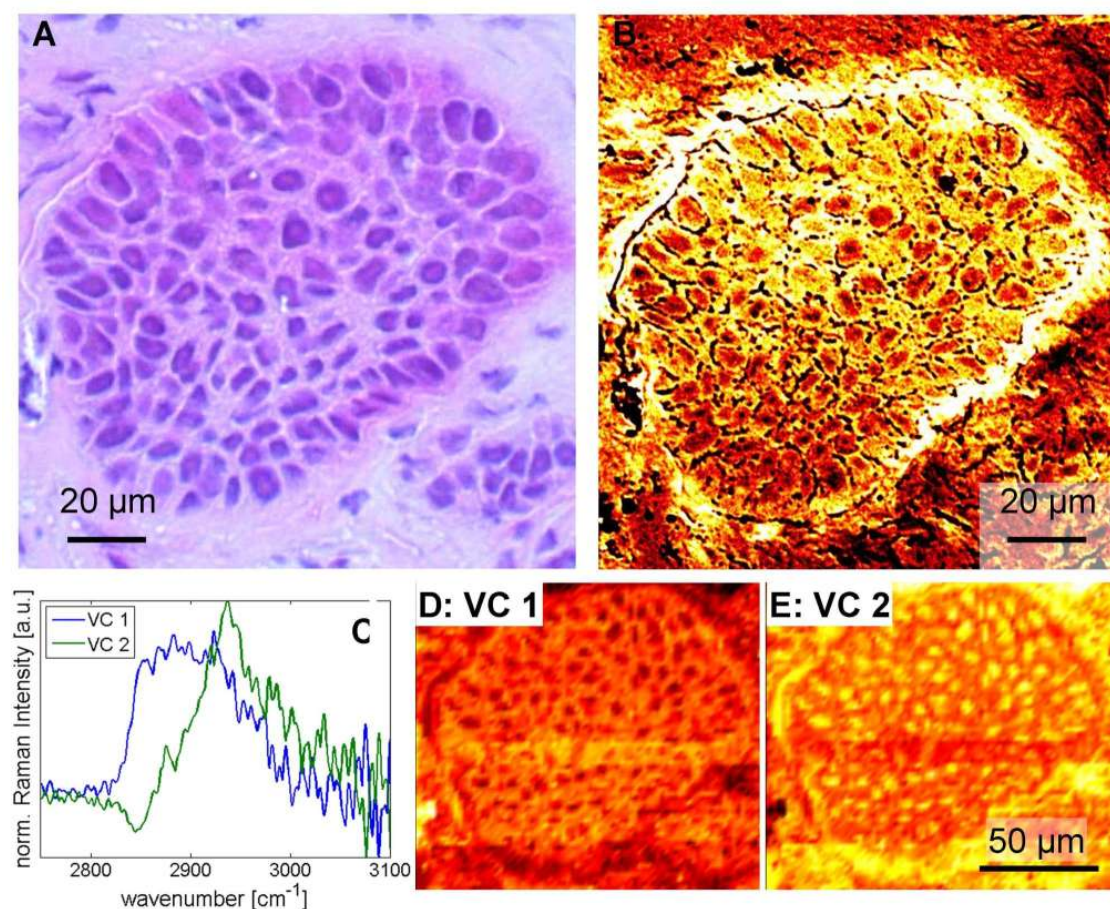
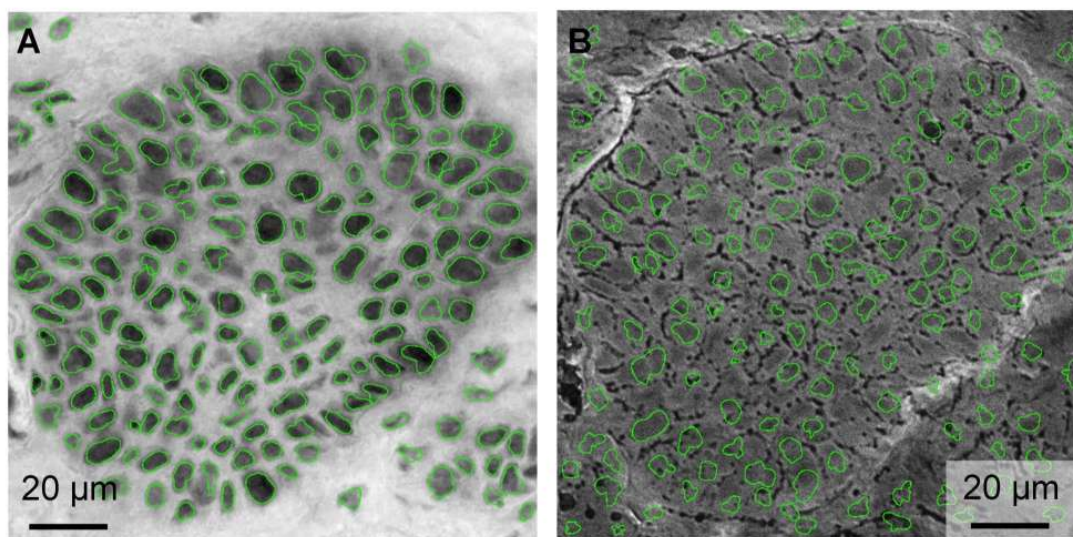


**Figure 1** – Direct comparison of the H&E stained (A) tissue section with CARS (2850 cm<sup>-1</sup>, B) as well as Raman microscopic images (D,E) of the unstained tissue within the C-H-stretching region of a human squamous cell carcinoma metastasis in the brain. The CARS and the Raman image accentuate the positions of single cell nuclei due to a spatially distinct lipid and protein distribution. Thus, cell nuclei and cell boundaries can be precisely determined allowing for extraction of morphologic parameters for tissue grading, e.g. nuclei size and shape, nucleus to cytoplasm ratio, cell density. The origin of vibrational image contrast is derived from the vertex component analysis of the C-H-stretching Raman data (see panel C), displaying endmembers of the first 2 vertex components. The corresponding abundance plots are shown in panels D and E. Both vertex components allow for differentiating cell nuclei from the surrounding tissue. The contrast is based on the symmetric and antisymmetric CH<sub>2</sub> and CH<sub>3</sub>-stretching vibration in the range from 2850 to 2955 cm<sup>-1</sup> in case of VC 1 and missing symmetric aliphatic CH<sub>2</sub>-stretching vibration of lipids at 2850 cm<sup>-1</sup> in combination with an intense symmetric CH<sub>3</sub>-stretching vibration of mainly proteins at 2930 cm<sup>-1</sup> in case of VC 2. Thus the contrast in VC 2 can be assigned to relative differences in the lipid/protein ratio between nuclei and cytoplasm. Since VC 1 is similar to the CARS signal, the origin of the CARS image contrast is due to the lipid content.

sonances originate from the most abundant molecules in tissue apart from water which are proteins, lipids and DNA. When comparing Raman and CARS image D and B the intensity distribution is very similar, proving that the negative contrast of the cell nuclei in CARS is related to a relative deficiency of these molecules with respect to the cytoplasm. Since DNA should be most abundant within the nuclei it can be concluded that the signal contribution of DNA is negligible. Thus taking into account the respective molecular structures VC 1 resembles the combined lipid and protein distribution, since lipids and protein contain significantly more methyl and methylene groups than DNA. The Raman spectrum of VC 2 is dominated by strong positive signals of the symmetric aliphatic C-H stretching vibration of methyl groups at  $2930\text{ cm}^{-1}$ . This vibration is a selective marker for proteins, which contain higher amounts of these functional groups than lipids or DNA. Thus, the image contrast in the abundance plot of VC 2 (figure 1 panel E) is related to a relative difference in the protein/lipid ratio and allows differentiating nuclei from the cytoplasm. Since the cell nuclei appear bright in the Raman image E in contrast to the CARS image, protein is not prominently contributing to the observed CARS signal at  $2850\text{ cm}^{-1}$ . In summary, CARS and Raman imaging allow differentiating cell nuclei and cytoplasm solely using the C-H-stretching vibrational spectral region. The CARS contrast at  $2850\text{ cm}^{-1}$  is based on the differences in the concentration of  $\text{CH}_2$ -functional groups in the nuclei and in the cytoplasm. Thus, in CARS imaging at  $2850\text{ cm}^{-1}$  (figure 1 panel B) image contrast for discerning cell nuclei and cytoplasm is mainly based on the lipid content, since the relative concentration of these functional groups is highest in lipids. Protein and especially DNA as major compounds in tissue contains significantly less methylene groups in addition to relatively large amounts of other hydrogen containing functional groups, namely  $\text{CH}_3$  in case of proteins and  $\text{CH}$ ,  $\text{OH}$  and  $\text{NH}$  groups in case of DNA.

The CARS image allows for discerning cell nuclei as evident by comparing panels A and B providing similar results as known from staining histopathology. Since single cell nuclei are resolved, histomorphological parameters required for grading of tissue are readily extractable using image processing routines, e.g. cell density, nucleus to cytoplasm ratio, nucleus size and shape. Therefore an image processing procedure

has been performed in order to extract histopathologically relevant parameters from the CARS image. For evaluation of this method the algorithm has been applied to the corresponding H&E image. In figure 2 H&E and CARS image are shown in grey scale in addition to the detected cell nuclei marked in green. The table below summarizes the results and confirms good correspondence with the consecutively H&E stained section in locating cell nuclei. The algorithm underestimates the number of cell nuclei by 20% and the area fraction by 33%, but still these results are very promising.



H&E image		CARS image
24%	Area fraction of cell nuclei	16%
112	Number of nuclei / 100 x 100 μm <sup>2</sup>	89

**Figure 2** – Comparison of the results of image analysis of an H&E stained image (A) and a CARS microscopic image (B) of a squamous cell carcinoma brain metastasis. The image contrast of the CARS image is sufficient for automated detection of cell nuclei, which corresponds well with the H&E stained image, as shown in the table below. The number of cell nuclei is 20% lower and the area fraction 33% lower than estimated from the H&E image.

## Conclusion

In summary CARS and Raman microscopy of the aliphatic C-H-stretching region at  $2850\text{ cm}^{-1}$  are capable of detecting single cell nuclei. However, since cell nuclei are identified by negative contrast in the CARS and VC 1 of the Raman data, e.g. a reduced lipid and protein signal, the DNA content cannot be determined and erroneous detection of nuclei can occur. A positive contrast of nucleic acid Raman bands can be detected in VC 2 and Raman images of brain tissue sections immersed in aqueous buffer[14]. An image processing procedure was applied to delineate cell nuclei. These findings have been interpreted with the help of experimentally slow Raman imaging. Indeed the lipid content within the cell nuclei has been shown to be lower explaining the molecular origin of the observed CARS image contrast. The results of vibrational imaging agree very well with histopathologic staining. It can be concluded, that single band CARS microscopy using ps pulses as the most rapid vibrational imaging technique is capable of providing information on the tissue morphology and composition similar to histopathologic staining. Since CARS imaging within the C-H-stretching spectral region reveals the position and extent of single cell nuclei this label free imaging technique holds great potential for non-invasive imaging and surgical guidance in future applications.

## Acknowledgments

Financial support of the European Union via the Europäischer Fonds für Regionale Entwicklung (EFRE) and the "Thüringer Ministerium für Bildung Wissenschaft und Kultur (TMBWK)" (Projects: B714-07037, B578-06001, 14.90 HWP) and via the European network of excellence P4L (Photonics4Life) as well as financial support by the German Ministry for Science and Education (BMBF) *MediCARS* (FKZ: 13N10774) is highly acknowledged.

## References

- [1] Zumbusch, A., Holtom, G. R., and Xie, X. S. *Phys. Rev. Lett.* **82**(20), 4142–4145 (1999).
- [2] Evans, C. L. and Xie, X. S. *Annual Review of Analytical Chemistry (2008)* **1**(1), 883–909 (2008).
- [3] Krafft, C., Dietzek, B., and Popp, J. *The Analyst* **134**(6), 1046–1057 (2009).
- [4] Freudiger, C. W., Min, W., Saar, B. G., Lu, S., Holtom, G. R., He, C., Tsai, J. C., Kang, J. X., and Xie, X. S. *Science* **322**(5909), 1857–1861 (2008).
- [5] Freudiger, C. W., Roeffaers, M. B. J., Zhang, X., Saar, B. G., Min, W., and Xie, X. S. *J. Phys. Chem. B* **115**(18), 5574–5581 (2011).
- [6] Evans, C. L., Potma, E. O., Puoris'haag, M., Coté, D., Lin, C. P., and Xie, X. S. *Proc Natl Acad Sci U S A* **102**(46), 16807–16812 November (2005).
- [7] Pliss, A., Kuzmin, A. N., Kachynski, A. V., and Prasad, P. N. *Biophysical Journal* **99**(10), 3483–3491 November (2010).
- [8] Meyer, T., Bergner, N., Bielecki, C., Krafft, C., Akimov, D., Romeike, B. F. M., Reichart, R., Kalff, R., Dietzek, B., and Popp, J. *Journal of Biomedical Optics* **16**(2), 21113 (2011).
- [9] Medyukhina, A., Tobias, M., Schmitt, M., Romeike, B. F. M., Dietzek, B., and Popp, J. *Journal of Biophotonics* (2012).
- [10] Gao, L., Hammoudi, A. A., Li, F., Thrall, M. J., Cagle, P. T., Chen, Y., Yang, J., Xia, X., Fan, Y., Massoud, Y., Wang, Z., and Wong, S. T. C. *Journal of Biomedical Optics* **17**(6), 66011–66017 (2012).
- [11] Gao, L., Zhou, H., Thrall, M. J., Li, F., Yang, Y., Wang, Z., Luo, P., Wong, K. K., Palapattu, G. S., and Wong, S. T. C. *Biomedical Optics Express* **2**(4), 915–926 April (2011).
- [12] Yang, Y., Li, F., Gao, L., Wang, Z., Thrall, M. J., Shen, S. S., Wong, K. K., and Wong, S. T. C. *Biomedical Optics Express* **2**(8), 2160–2174 (2011).
- [13] Colthup, N. B., Daly, L. H., and Wiberley, S. E. *Introduction to infrared and Raman spectroscopy*. Academic Press, (1990).
- [14] Bergner, N., Krafft, C., Geiger, K., Kirsch, M., Schackert, G., and Popp, J. *Analytical and Bioanalytical Chemistry* **403**, 719 (2012).

Adapted with kind permission from The Optical Society of America (OSA):

**Authors:** Martin Baumgartl, Mario Chemnitz, Cesar Jauregui, Tobias Meyer, Benjamin Dietzek, Jürgen Popp, Jens Limpert, and Andreas Tünnermann.

**Titel:** "All-fiber laser source for CARS microscopy based on fiber optical parametric frequency conversion."

**Journal:** *Optics Express*, 20(4):4484–4493, **2012**.

©Copyright 2012 The Optical Society of America (OSA).

Reproduced with permission.





## 8 | All-Fiber Laser Source for CARS Microscopy Based on Fiber Op- tical Parametric Frequency Con- version

**Martin Baumgartl,<sup>1,2\*</sup> Mario Chemnitz,<sup>1</sup> Cesar Jauregui,<sup>1</sup> Tobias Meyer,<sup>3,4</sup> Benjamin Dietzek,<sup>3,4</sup> Jürgen Popp,<sup>3,4</sup> Jens Limpert,<sup>1,2</sup> and Andreas Tünnermann<sup>1,2,5</sup>**

<sup>1</sup> Institute of Applied Physics, Abbe Center of Photonics, Friedrich-Schiller-Universität Jena, Albert-Einstein-Str. 15, 07745 Jena, Germany

<sup>2</sup> Helmholtz Institute Jena, Fröbelstieg 3, 07743 Jena, Germany

<sup>3</sup> Institute of Physical Chemistry and Abbe Center of Photonics, Friedrich-Schiller-University Jena, Helmholtzweg 4, 07743 Jena, Germany

<sup>4</sup> Institute of Photonic Technology e.V., Albert-Einstein-Straße 9, 07745 Jena, Germany

<sup>5</sup> Fraunhofer Institute for Applied Optics and Precision Engineering, Albert-Einstein-Str. 7, 07745 Jena, Germany

\* corresponding author: martin.baumgartl@uni-jena.de

## **Abstract**

A novel approach for an all-fiber mono-laser source for CARS microscopy is presented. An Yb-fiber laser generates 100 ps pulses, which later undergo narrowband in-fiber frequency conversion based on degenerate four-wave-mixing. The frequency conversion is optimized to access frequency shifts between 900 and 3200  $\text{cm}^{-1}$ , relevant for vibrational imaging. Inherently synchronized pump and Stokes pulses are available at one fiber end, readily overlapped in space and time. The source is applied to CARS spectroscopy and microscopy experiments in the CH-stretching region around 3000  $\text{cm}^{-1}$ . Due to its simplicity and maintenance-free operation, the laser scheme holds great potential for bio-medical applications outside laser laboratories.

**Keywords:** CARS microscopy, Raman micro spectroscopy, C-H-stretching vibration, vibrational imaging.

## Introduction

Coherent anti-Stokes Raman scattering (CARS) microscopy has proven to be a powerful tool in biomedical sciences [1]. By probing intrinsic vibrational molecule resonances of the specimen, chemical selective image contrast is obtained without the use of extrinsic labels [2]. Paired with its high sensitivity, CARS thus allows for microscopy of living cells and is a promising technique for real time in-vivo imaging, e.g. during brain cancer surgery.

As CARS is a four-wave-mixing (FWM) process, the signal generation requires synchronized laser pulses at different wavelengths. This imposes stringent requirements on the light source. At the same time, the frequency difference between the two synchronized pulse trains needs to match the molecular resonance of interest to obtain the desired chemical-selective contrast through the generation of a resonant anti-Stokes signal. Since the signal intensity is proportional to the pump/probe and Stokes intensities  $I_{CARS} \propto I_p^2 I_s$ , signal photons are primarily generated in a small focal volume, thus CARS additionally provides 3-dimensional sectioning capabilities.

The common approach to generate the pump and Stokes pulses is to use two synchronized mode-locked solid state lasers or one mode-locked laser in combination with an optical parametric oscillator (OPO), the latter approach thereby obviating the need for electronic synchronization. These systems are very versatile and deliver nearly ideal parameters. On the other hand, they are very expensive, large and require technical staff devoted to their constant alignment and maintenance. For this reason the application of CARS microscopy is still limited to a few specialized laboratories world-wide. A wider use in life sciences and especially in clinical environments critically depends on the development of suitable, easy-to-use, compact and, at the same time, inexpensive and reliable laser sources.

Fiber lasers are ideally suited to fulfill all these requirements, as they can be completely fiber integrated and, therefore, they can be extremely compact and robust. Hence, several sources intended for CARS microscopy have been developed using a fiber based driving laser in combination with some sort of frequency conversion

process for the intrinsically synchronized generation of the frequency shifted pulse train. Different approaches for frequency conversion relying either on bulk crystal based OPO [3] or fiber based processes such as soliton self-frequency shift (SSFS) [4, 5] or supercontinuum generation (SC) [6] have been pursued. Whereas a bulk OPO is clearly not compatible with fiber integration, also the fiber based approaches rely on free-space optics to some extent. One problem is that the frequency shifted solitons tend to be spectrally broad and, hence, they must be adapted to obtain high spectral resolution and a high contrast between the resonance and the nonresonant background in the CARS signal [1]. Furthermore, it is beneficial for the frequency conversion process (SSFS, SC) if the driving laser pulse is in the fs time scale [7], whereas for CARS mostly ps pulses are preferable. One strategy to solve this issue is to start with a narrowband ps driving laser and convert part of its output to fs durations before it is sent to the frequency conversion stage [4]. This is done by exploiting nonlinear spectral broadening in a fiber and by carrying out a subsequent temporal compression in a grating setup. Other approaches directly start with fs pulses and use second harmonic generation in long crystals to achieve spectral pulse compression at the end [6], or alternatively, they apply a spectrally focused CARS scheme by chirping the broadband pulses [5]. Also more sophisticated techniques like delayed multiplex CARS with ultrabroadband few cycle pulses have been demonstrated [8]. However, despite considerable progress, none of the presented concepts offers true turn-key and alignment-free operation as they depend on free-space optics and need adjustment of the pulse delay.

In this paper, we present a novel approach for all-fiber CARS laser sources which allows for complete fiber integration. Our system comprises a spectrally filtered fiber oscillator and a fiber optical parametric frequency conversion stage using degenerate four-wave-mixing (FWM) in an endlessly single-mode fiber. The frequency shift that can be obtained is determined by the fiber dispersion, which in turn influences the phase-matching condition of the parametric process. Moreover this frequency shift can be changed by tuning the wavelength of the driving fiber laser. Furthermore the FWM process inherently ensures that the pump laser pulse and the shifted component are both temporally and spatially overlapped at the fiber output. Thus they

are readily available for injection into a CARS microscope without the need of any combining optics or delay lines. This reduces overall system complexity significantly and makes it particularly easy to use. Besides, the single-fiber-end output is directly compatible with fiber-delivered probes [9] for in-vivo imaging. This holds true, since long ps pulses have been used, for which the additional dispersion within the microscopic objective and the tissue sample and even within another short piece of delivery fiber is negligible.

Our experimental scheme is based on an alignment-free ytterbium fiber laser delivering 118 ps pulses at an average power of up to 2 W and with variable repetition rates in the lower MHz range. The FWM fiber was chosen to attain frequency shifts from more than  $3500\text{ cm}^{-1}$  to below  $1000\text{ cm}^{-1}$  by tuning the driving laser by  $\pm 20\text{ nm}$  within the Yb-gain bandwidth. In the following sections the pump laser (section 2) and the frequency conversion stage (section 3) will be described. Afterwards experimental results from CARS spectroscopy of the aromatic CH-stretching vibration of toluene and CARS microscopic images are presented in section 4.

## The all-fiber pump laser system

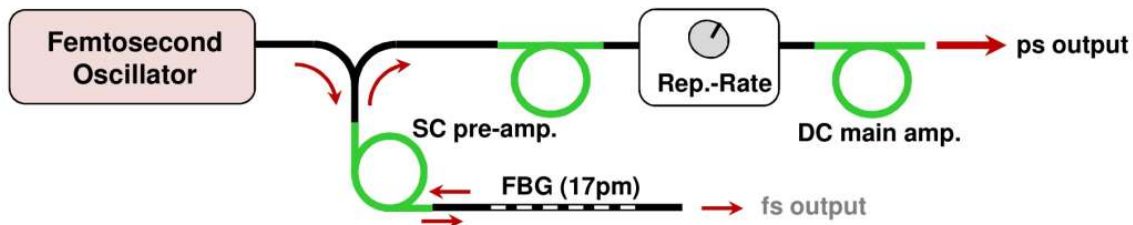


**Figure 1** – Schematic setup of the environmentally stable, alignment-free fiber laser system employed to drive the four-wave-mixing process. SC-single clad fiber, DC-double clad fiber, FBG-fiber Bragg grating.

To drive the nonlinear frequency conversion process, a reliable high-power pump laser is required. Hence, a fiber master oscillator power amplifier (MOPA) system, completely based on commercially available single-mode fiber components was developed. The exclusive use of polarization maintaining fibers results in an environmentally stable system. Furthermore, all components in the setup are fusion spliced

to obtain alignment-free operation.

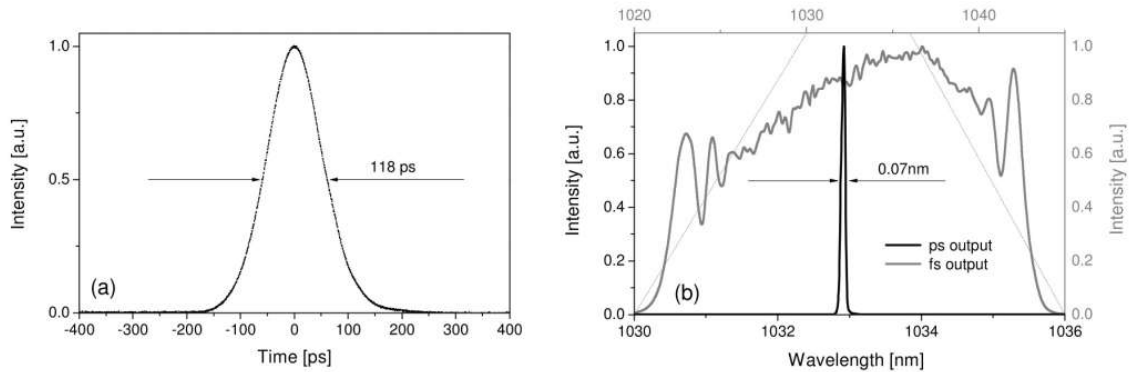


**Figure 2** – Output characteristics of the ps pump laser system. (a) Temporal pulse shape measured with a fast photo diode (18.5 ps) and a sampling oscilloscope (70 GHz). (b) Optical spectrum (black) (resolution 0.02 nm); additionally the spectrum of the fs output is shown (gray).

The fiber MOPA system is schematically depicted in Fig. 1. We begin with a self-starting, fully fiber-integrated femtosecond oscillator, passively mode-locked by a semi-conductor saturable-absorber. The oscillator setup and performance is analog to the one presented in [10]. Using a circulator and a narrowband (17 pm) fiber Bragg grating (FBG), a small part of the broad oscillator spectrum is carved out, and amplified in two core pumped pre-amplifiers (Nufern PM-YSF-HI). A fiberized acousto-optical modulator then reduces the repetition rate to 1 MHz just before the cladding pumped main amplifier (Liekki Yb1200-10/125DC-PM), which can provide up to 2 W of output power. Due to the narrow spectral bandwidth, the pulses reflected by the grating possess a long duration in the temporal domain. At the output of the main amplifier we measure a 0.07 nm spectral width (Fig. 2(b)) and a corresponding pulse duration of 118 ps (Fig. 2(a)), using an optical spectrum analyzer with 0.02 nm resolution and a 19 ps response time photodiode. These pulses, possessing  $\mu$ J-level energies and peak powers in the several-kW range, are used for frequency conversion in the next section. They can, moreover, be wavelength-tuned by variation of the filter element, e.g. by stretching the FBG. In addition, simultaneous multiple wavelength operation or selectable discrete wavelengths using a fiber

switch could be realized by application of several FBGs. Furthermore, we obtain chirped fs pulses at the transmission port of the FBG, which are not used further in this contribution, but which could be compressed as demonstrated in [10] and used for different nonlinear microscopy techniques such as two-photon fluorescence or second harmonic generation as additional methods providing image contrast.

## In-fiber frequency conversion by degenerate four-wave-mixing

The wavelength range from 780 to 980 nm for pumping the CARS process is beneficial for microscopy applications as it provides a good trade-off in terms of spatial resolution, penetration depth, non-resonant background and photodamage [1]. This wavelength range is therefore, the most widely used. The corresponding Stokes wavelength is, consequently, above 1000 nm. In our case, in order to exploit the advantages of Yb-fiber laser technology, the Stokes wavelength is designed to fall within the Yb-gain bandwidth between 1020 and 1080 nm. The all-fiber single-laser approach pursued here requires then, the frequency conversion of this Stokes wavelength to shorter wavelengths. The frequency-converted signal should be strong enough to pump the CARS process. It has been shown that degenerate FWM in photonic-crystal fibers can generate distinct new frequencies with high spectral densities [11, 12, 13]. Endlessly single-mode PCF designs allow for high conversion efficiencies as they ensure a good mode overlap even for widely separated wavelengths. The use of long picosecond pulses minimizes spectral broadening of the driving pulses induced by self-phase modulation (SPM) and thus allows for narrowband signal generation.

In degenerate FWM two pump photons are annihilated and one signal and one idler photon are generated at shorter and longer wavelengths, respectively. To avoid confusion, the terms pump and signal are written in *italic* in the following, wherever they refer to the FWM process. This should distinguish them from the pump and signal of the CARS process. (Note that the signal generated by FWM will be used as the pump for the CARS process. Moreover, the residual FWM pump pulse

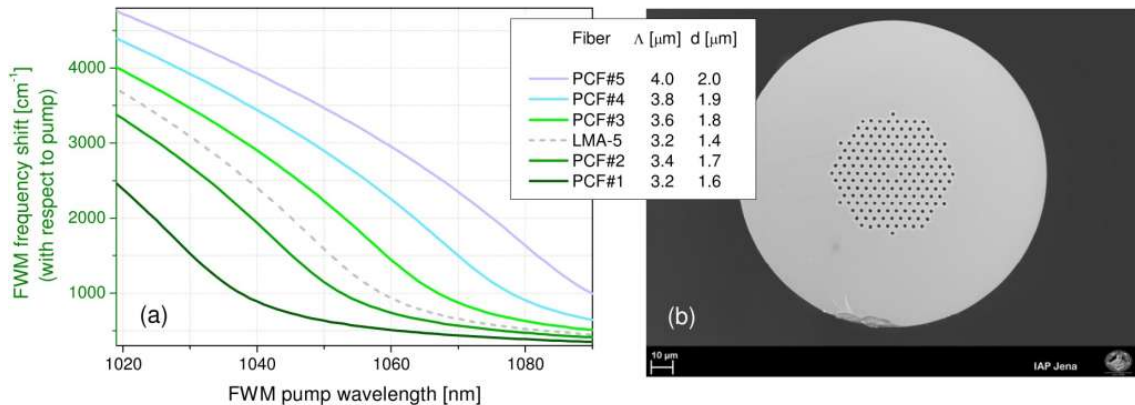


**Figure 3** – (a) DFWM frequency shift with respect to pump calculated for different PCF designs. The legend contains the geometrical parameters (hole-to-hole distance) and  $d$  (hole diameter). (b) Microscope image of PCF#5. The legend provides the geometrical parameters of the different fibers. All fibers are standard one-hole-missing designs with hexagonal hole arrangement. Note, that the relative dimensions are the same for PCF#1-5, hence, suppressing the scale bar, the microscope image would be identical for PCF#1-5.

will serve as the CARS Stokes (see upper inset Fig. 4). The parametric process of FWM can only take place if both energy  $2\omega_{pump} = \omega_{signal} + \omega_{idler}$  and momentum conservation  $2k_{pump} = k_{signal} + k_{idler} + 2\gamma P_{pump}$  are fulfilled [14]. The simultaneous fulfillment of these two conditions is known as phase-matching. Besides the product of nonlinearity parameter  $\gamma$  and pump power, the phase matching is only dependent on the dispersion of the fiber. Hence, the signal wavelength for a given pump can be conveniently selected by adjusting the structure parameters of the fiber. To select a suitable fiber we calculated the dispersion of the effective refractive index for different available PCFs (see legend in Fig. 3) using a numerical mode solver. Together with the equations above, the phase matched wavelength sets are easily determined for each fiber. Figure 4 displays the calculated mode profile for PCF# 2 and the corresponding signal (orange) and idler (black) wavelength pairs for pump wavelengths between 1 and 1.1  $\mu\text{m}$ . Additionally, the frequency difference (green) between signal and pump is plotted. This shows whether the generated signal could be used together with the pump laser to drive any CARS resonance of interest. In fact, for PCF# 2 tuning the pump between 1022 and 1055 nm generates the desired signal wavelengths between 770 and 964 nm. This corresponds to frequency shifts



between 3200 and 900  $\text{cm}^{-1}$ . Thus tuning the pump by only 33 nm gives access to the whole frequency range important for CARS microscopy. Of course, the same frequency difference is obtained with the idler, which could alternatively be used whenever longer wavelengths are of interest.

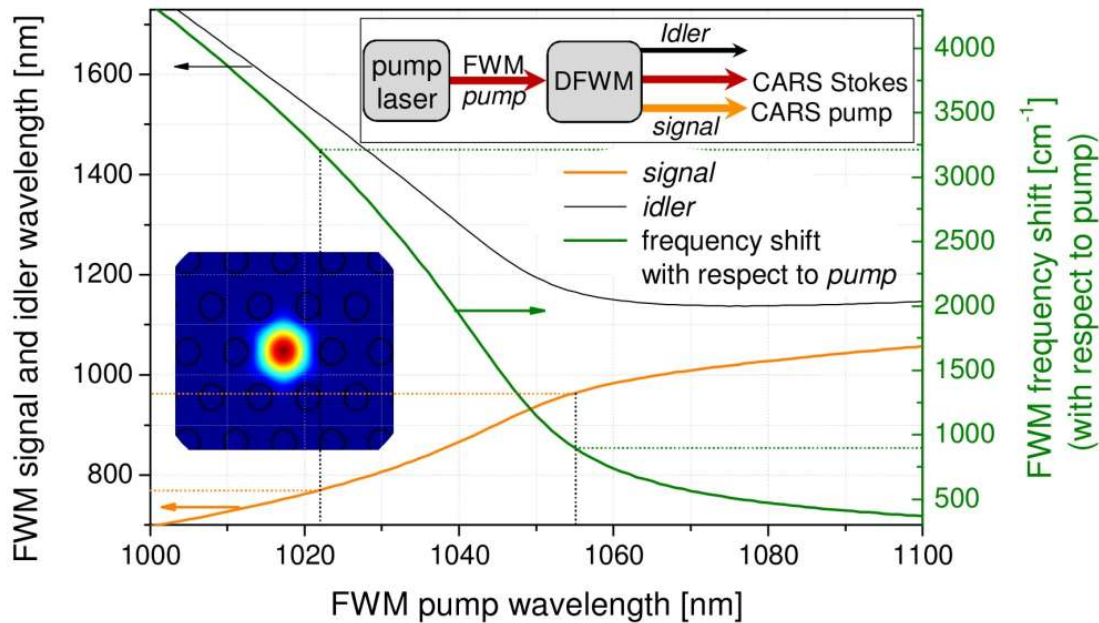


**Figure 4** – Signal and idler wavelengths that fulfill both energy and momentum conservation as a function of the pump wavelength, calculated for a peak power of 2 kW for PCF# 2. The green curve shows the corresponding frequency shift with respect to the pump that is obtained for different pump wavelengths. The inset on the left shows the simulated mode profile at 1030 nm, the upper inset illustrates the use of the different frequencies for CARS.

The investigated PCFs are one-hole-missing designs consisting of 7 rings of air holes. A microscope image of the fiber cross section is shown in Fig. 3(b), the design parameters (hole-to-hole distance and size) are given in the legend. The simulated frequency shifts obtained for the different fibers assuming an Yb-doped pump laser are shown in Fig. 3(a). At fixed pump wavelength of 1030 nm, the frequency shifts span from 1528 to 4340  $\text{cm}^{-1}$  with the presented fiber set, demonstrating the flexibility of the DFWM approach. We decided to use PCF#2 for our CARS experiments as it shifts across the important CH-stretching bands around 3000  $\text{cm}^{-1}$  when

using the pump laser around 1030 nm. Furthermore, as discussed above, this fiber perfectly maps the CARS relevant frequency range into a tuning range easily accessible with Yb-fiber lasers. The fiber's mode-field area is around  $14 \mu\text{m}^2$ , which gives rise to sufficiently high intensities already at moderate peak powers of some kW. For comparison, the corresponding curve for a commercially available fiber (LMA-5 NKT Photonics) is plotted (gray). It shows nearly the same characteristic and, thus, it could readily be used for the development of a low cost commercial CARS laser source.

As the phase matching is strongly related to the fiber parameters, any geometrical variations along the fiber length will reduce the efficiency and spectral signal purity. It is therefore beneficial to use short fibers to favor the FWM process over other competing nonlinear effects such as spontaneous Raman scattering [13]. A very short fiber on the other hand, would require high pump powers to obtain moderate conversion efficiencies. We determined that the optimum fiber length was 0.7 m for our purposes. This length allows for a clean signal and idler generation as shown in Fig. 5(a) for a pump power of 0.37 W. The fiber is pumped at 1033 nm generating a signal at 785 nm, which corresponds to a frequency shift of  $\sim 3050 \text{ cm}^{-1}$ , matching the aromatic CH-stretching vibrational resonance.

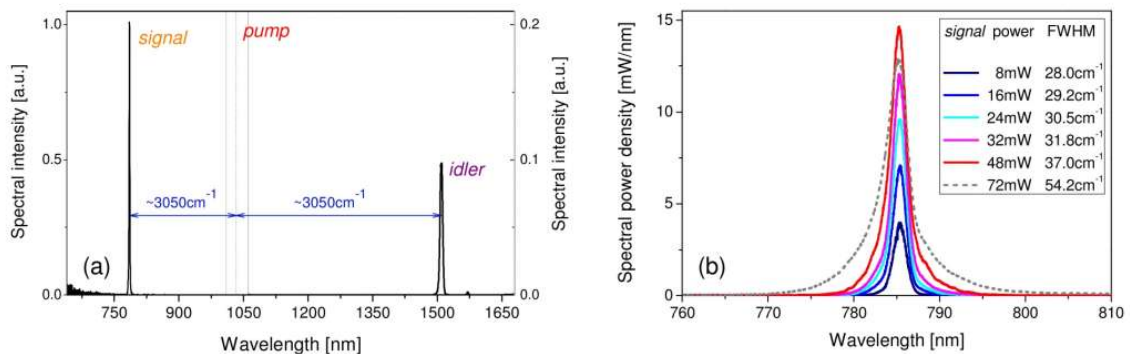


**Figure 5** – (a) Spectra of the clean signal and idler generation via DFWM in PCF#2, pumped with 0.37 W at 1033 nm. (b) DFWM signal spectra for increasing pump power, showing the evolution of maximum spectral power density and spectral width of the signal.

In reference [12] it has been shown that the temporal pulse shape gets increasingly

complex due to the occurrence of successive back-conversion processes in longer fiber sections. On the other hand, using a short conversion fiber, clean signal pulses can be generated, at the price of sacrificing some conversion efficiency. These signal pulses can be significantly shorter than the pump pulses, as conversion starts only around the pulse peak. As we are interested in clean signal generation, we chose such a working point. The temporal trace of the signal recorded with a photodiode (18.5 ps) and a sampling oscilloscope (70 GHz) is shown in Fig. 6(b). It has a full width at half maximum of 43 ps, which is about 3 times shorter than that of the pump pulse. More important, however, is the spectral width of the generated signal, as it influences the signal to noise ratio of the CARS signal due to the nonresonant background [1]. Figure 5(b) shows the signal spectrum for different signal powers (obtained by increasing the pump power). With increasing power the spectral power density increases up to 15 mW/nm for 48 mW total signal power. However, as the signal width gets broader, the power density does not increase further when going to higher power. For our CARS experiments we worked with 20 to 35 mW frequency converted power. If higher power would be required, one would have to use higher repetition rates or shorter conversion fiber lengths to remain in the narrow linewidth operation point.

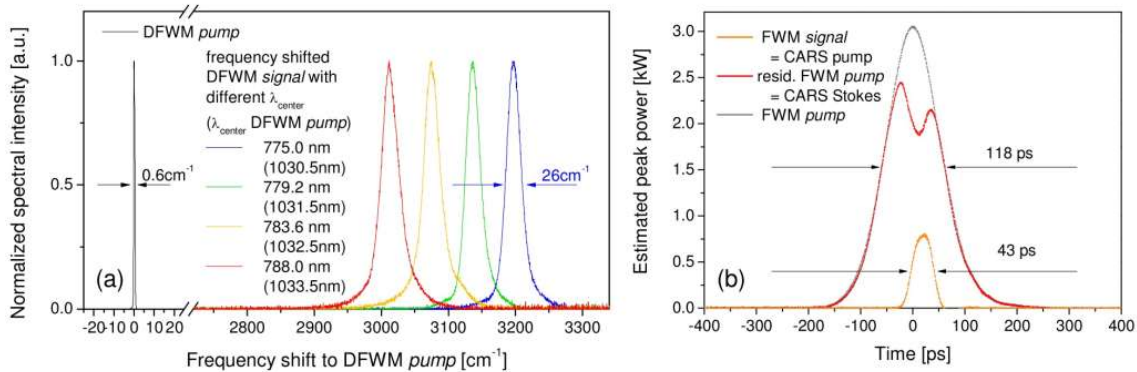


**Figure 6** – (a) Variation of the frequency shift by tuning the pump laser. (b) Temporal pulse shapes measured with a fast photo diode (18.5 ps) and a sampling oscilloscope (70 GHz). The FWM pump (gray), the FWM signal which is used as CARS pump (orange), and the residual, partially depleted FWM pump which is used as CARS Stokes (red) are shown. The area is normalized to the pulse energy to estimate the peak power.

As mentioned above, by tuning the wavelength of the pump laser the frequency shift can be varied over a large range, whereby both pump and signal wavelengths change. A continuous tunability over a few nanometers can be obtained from our pump laser by stretching the FBG. The resulting FWM signal spectra in terms of frequency shift are shown in Fig. 6(a) for PCF#2. The signal wavelength changes from 775 to 788 nm when the pump is tuned from 1030.5 to 1033.5 nm. So the frequency shift changes by  $200\text{ cm}^{-1}$  with this 3 nm pump tuning.

## Application of the two-color fiber source to CARS spectroscopy and microscopy

To demonstrate the suitability of the above concept for CARS applications, we performed a measurement of the aromatic CH-stretching vibrational resonance of toluene, using the simple scheme depicted in Fig. 7. After the pump laser being frequency shifted by DFWM in PCF#2, the output of the PCF is simply collimated and focused into the sample. No additional delay line is required as the pulses already overlap in space and time at the output of the fiber, which simplifies both the setup and the experimental effort, something of particular interest for the user. Behind the sample, the light is collected by a lens and coupled into a multimode fiber, which is connected to the detector. A 770 nm short pass filter is inserted behind the sample to block any residual pump light. Another long pass filter (650 nm) is used in front of the sample to block any small amount of light that might be present at the CARS signal wavelength, generated by non-phase-matched FWM in the PCF [9].

About 26 mW of CARS pump is sent to a  $10\times$  microscope objective (Olympus) to be focused into the sample. The signal is detected with a CCD spectrometer, but it could of course be obtained by any non-spectrally sensitive detector as well. As the signal is strong, no special care had to be taken regarding efficient photon collection or stray light. Figure 8(a) shows the CARS signal spectra for different frequency shifts between pump and Stokes. The width of each single spectrum is about

50  $\text{cm}^{-1}$ . Integration yields the total signal power, which is plotted in Fig. 8(b) together with a fit of the resonance line. The resulting linewidth is 60  $\text{cm}^{-1}$  as a result of the convolution of the laser linewidth with the resonance.

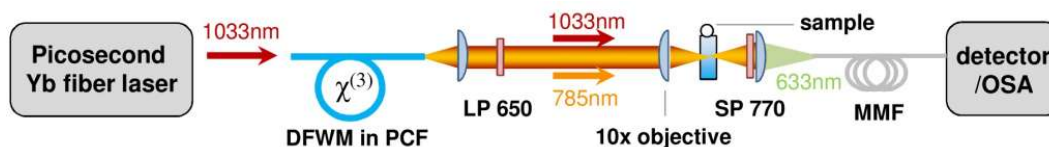


**Figure 7** – Simple CARS setup. The PCF output is simply collimated and focused into the sample. No additional delay line is required as the pulses are already overlapped. LP 650 - long pass 650 nm, SP 770 - short pass 770 nm, MMF - multi-mode fiber.

In order to test the imaging capabilities of the laser source, we attached it to a home-built laser scanning microscope. Using a 20  $\times$  objective (Mitutoyo Plan Apo NIR), images of glass spheres in toluene were taken (Fig. 9). Tuning to the resonance (left hand side of Fig. 9) the surrounding toluene generates a strong resonant CARS signal and hence appears bright, whereas the glass spheres remain dark creating a strong contrast in the picture. The raw images in Fig. 9 contain  $970 \times 970$  pixels and were acquired in less than 2 seconds without averaging. The series in Fig. 9 shows how the signal vanishes when the laser is tuned out of resonance. The nonresonant background is in comparison to the resonant CARS signal almost negligible (compare Fig. 9 left-right).

Against the common notion that pulses in the short ps range are optimal for CARS, longer pulses in the range of tens of picoseconds have many practical advantages. Obviously the temporal overlap between pulses becomes much less critical and, thus, passing several optical elements or even a certain fiber segment does not require for any readjustments. Moreover, very narrow bandwidths and high spectral resolution is obtained for transform limited pulses at durations of several tens of ps, which, at the same time results in higher signal to noise ratios as the nonresonant background coming from besides the excited vibrational line is suppressed. Finally, and even more important, when it comes to fiber delivered probes, the impact of undesired propagation effects is drastically reduced. This relates to both dispersion and self-

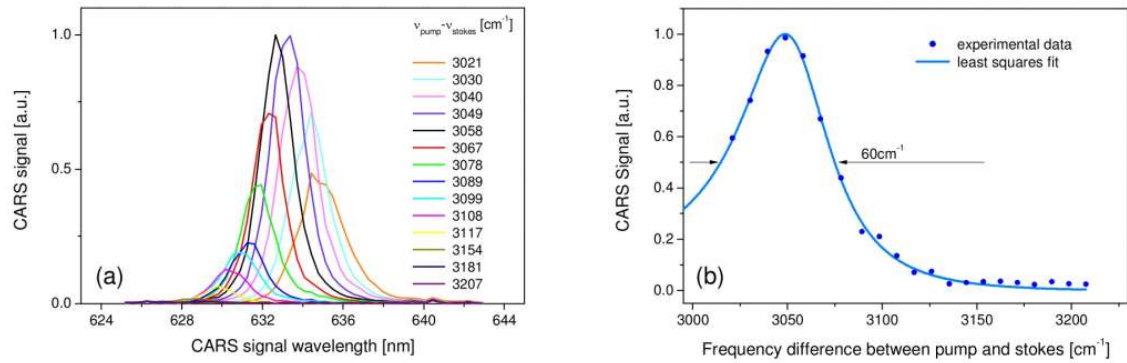


**Figure 8** – (a) CARS signal spectra and (b) CARS signal power, obtained by tuning the pump-Stokes frequency shift across the resonance of toluene

phase-modulation, when comparing pulses with equal peak power. At the same time longer pulses generate the same amount of CARS signal compared to shorter ones, as long as the peak and average power are kept constant. This implies that the

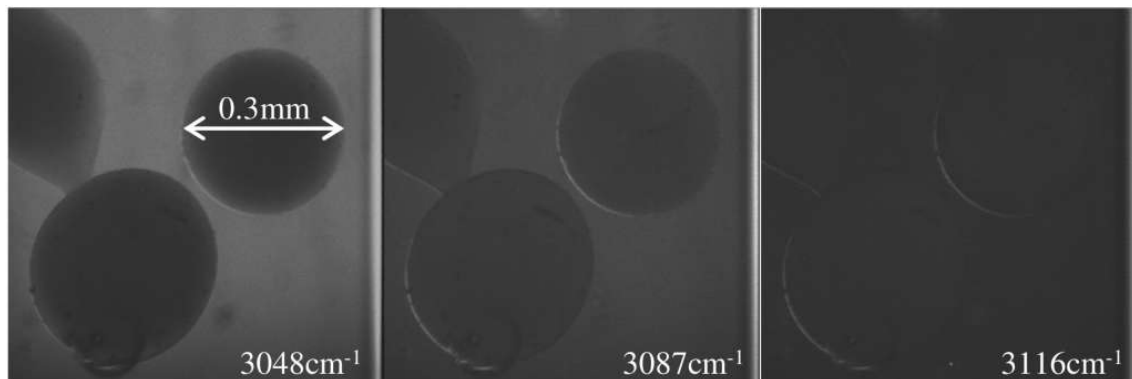


**Figure 9** – CARS microscopic images of glass spheres in toluene,  $970 \times 970$  pixels, no averaging. Detuning from resonance demonstrates high signal to noise ratios.

product of the repetition rate and the pulse duration remains constant as illustrated in Fig. 10. Thus, when the pulse duration is increased, the pulse energy needs to be increased by the same factor to keep the peak power constant. In order to remain at the same average power, consequently, the repetition rate has to be decreased by that factor. This increase in pulse energy is inherently happening in the amplifier if the repetition rate is decreased. Under this prerequisite, each long pulse generates more CARS signal even though the total CARS average power remains constant. Hence,

integration over several pulses for each pixel is not required anymore. On the other hand, fast acquisition times and real-time imaging require high repetition rates, thus repetition rates around few MHz represent a good trade-off. For example, a 1-MHz system would allow for an image of  $300 \times 300$  pixels at 11 frames per second.

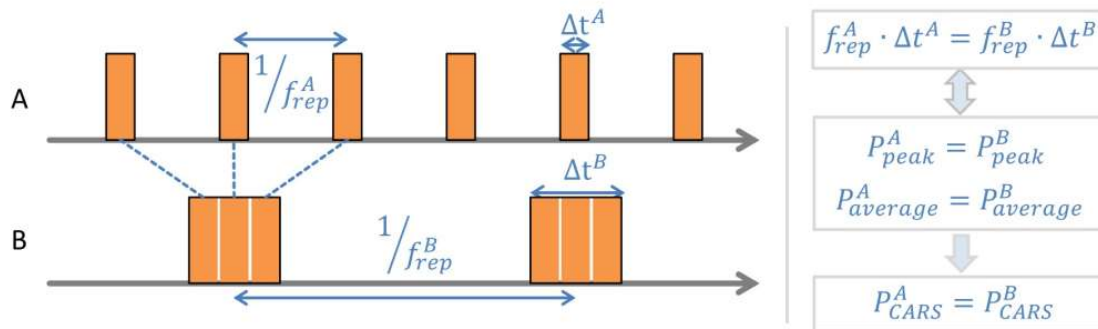


**Figure 10** – Illustration showing that long pulses (case B) yield the same CARS signal power as shorter ones (case A), as long as the repetition rate is lowered accordingly, keeping both average and peak power constant.

## Conclusion

We have demonstrated a novel all-fiber laser source approach for CARS microscopy based on degenerate FWM. An environmentally stable Yb-fiber laser generates 118 ps pulses around 1030 nm, which are then frequency converted in a PCF to obtain high-power, inherently synchronized CARS pump pulses with a duration of 43 ps. The generated wavelength pair around 780 nm and 1030 nm was used to probe the aromatic CH-stretch vibrational resonance of toluene at  $3050 \text{ cm}^{-1}$ . Reproduction of the CARS resonance bandshape by spectral tuning as well as microscopic imaging within the aromatic CH-stretching region demonstrates the CARS capabilities of the laser.

In contrast to other fiber based frequency conversion arrangements on the basis of supercontinuum generation or Raman scattering based soliton shifts, FWM gives the opportunity for narrowband frequency conversion directly to shorter wavelengths.

Using the emission of an Yb-fiber laser as CARS Stokes and as the field driving the FWM process, high-power CARS pump pulses can be generated in the preferred wavelength region around 800 nm. Alternatively the FWM idler around 1500 nm could be used as Stokes, whenever longer wavelengths would be required. Furthermore the FWM process is driven by long ps pulses and is consequently directly compatible with CARS, without the need for pulse post-processing like in other fs-based frequency conversion schemes.

The laser operates in the near infrared wavelength range offering several advantages as a maximized depth penetration and minimal sample absorption and photo damage in biological tissue. The long ps pulses minimize the influence of dispersion and do not lose temporal overlap. Furthermore the spectral resolution of the source with an excitation bandwidth of  $26\text{ cm}^{-1}$  as demonstrated corresponds to the linewidth of a vibrational resonance in the CH-stretching region ( $20\text{ cm}^{-1}$ ) for imaging lipids, thus, yielding a high ratio of resonant signal to nonresonant background. The resolution could be further improved by cw-seeding of the FWM process [15], which would condense the bandwidth closer to the transform limit. This would reduce the bandwidth to few  $\text{cm}^{-1}$ .

The main advantage of the proposed approach, however, is its simplicity of operation due to its full fiber integration. It provides pump and Stokes pulses temporally and spatially overlapped from one fiber end in combination with a compact and maintenance-free overall system. Hence, it paves the way to fiber-delivered in situ imaging systems.

By replacing the fs- by a ps-oscillator with low repetition rate the system could be simplified even further. Only one core pumped main amplifier would be required which could be directly spliced between the oscillator and the conversion PCF. Also a high repetition rate fiber coupled microchip laser [16] might be an alternative. With the whole system fitting into a small box, it could directly be attached to the microscope, thus becoming as easy to use as any halogen lamp. It could be made tunable by tuning the oscillator, but it could also be designed with a fixed frequency difference to serve one specific application as e.g. the imaging of lipids. As such, it could be a simple extension to existing fluorescence microscopes or a compact and



reliable device for in situ imaging, thus being a significant step towards establishing CARS microscopy in real-world and, in particular, in bio-medical applications.

## Acknowledgments

This work was partly supported by the German Federal Ministry of Education and Research (BMBF) under contract 13N10773 and 13N10774 as well as the Inter Carnot & Fraunhofer program under the project APUS. M. Baumgartl acknowledges support from the Carl-Zeiss-Stiftung. The authors thank T. V. Andersen from NKT Photonics for providing the photonic-crystal fibers.

## References

- [1] Evans, C. L. and Xie, X. S. *Annual Review of Analytical Chemistry (2008)* **1**(1), 883–909 (2008).
- [2] Zumbusch, A., Holtom, G. R., and Xie, X. S. *Phys. Rev. Lett.* **82**(20), 4142–4145 (1999).
- [3] Kieu, K., Saar, B. G., Holtom, G. R., Xie, X. S., and Wise, F. W. *Optics Letters* **34**(13), 2051–2053 (2009).
- [4] Andresen, E. R., Nielsen, C. K., Thøgersen, J., and Keiding, S. R. *Optics Express* **15**(8), 4848–4856 April (2007).
- [5] Pegoraro, A. F., Ridsdale, A., Moffatt, D. J., Pezacki, J. P., Thomas, B. K., Fu, L., Dong, L., Fermann, M. E., and Stolow, A. *Optics Express* **17**(23), 20700–20706 November (2009).
- [6] Marangoni, M., Gambetta, A., Manzoni, C., Kumar, V., Ramponi, R., and Cerullo, G. *Optics Letters* **34**(21), 3262–3264 November (2009).
- [7] Corwin, K. L., Newbury, N. R., Dudley, J. M., Coen, S., Diddams, S. A., Weber, K., and Windeler, R. S. *Physical Review Letters* **90**(11), 113904 (2003).
- [8] Selm, R., Winterhalder, M., Zumbusch, A., Krauss, G., Hanke, T., Sell, A., and Leitenstorfer, A. *Optics Letters* **35**(19), 3282–3284 (2010).
- [9] Balu, M., Liu, G., Chen, Z., Tromberg, B. J., and Potma, E. O. *Optics Express* **18**(3), 2380–2388 (2010).
- [10] Ortaç, B., Plötner, M., Schreiber, T., Limpert, J., and Tünnermann, A. *Optics Express* **15**(23), 15595 (2007).
- [11] Wadsworth, W. J., Joly, N., Knight, J. C., Birks, T. A., Biancalana, F., and Russell, P. S. J. *Optics Express* **12**(2), 299 (2004).
- [12] Nodop, D., Jauregui, C., Schimpf, D., Limpert, J., and Tünnermann, A. *Optics Letters* **34**(22), 3499 November (2009).
- [13] Lavoute, L., Knight, J. C., Dupriez, P., and Wadsworth, W. J. *Optics Express* **18**(15), 16193–16205 (2010).
- [14] Agrawal, G. P. In *Nonlinear Science at the Dawn of the 21st Century*, Christiansen, P. L., Sørensen, M. P., and Scott, A. C., editors, number 542 in Lecture Notes in Physics, 195–211. Springer Berlin Heidelberg (2000).

- [15] Mosley, P. J., Bateman, S. A., Lavoute, L., and Wadsworth, W. J. *Optics Express* **19**(25), 25337 November (2011).
- [16] Steinmetz, A., Nodop, D., Martin, A., Limpert, J., and Tünnermann, A. *Optics Letters* **35**(17), 2885–2887 September (2010).

Adapted with kind permission from The Optical Society of America (OSA):

**Authors:** Martin Baumgartl, Thomas Gottschall, Javier Abreu-Afonso, Antonio Díez, Tobias Meyer, Benjamin Dietzek, Manfred Rothhardt, Jürgen Popp, Jens Limpert, and Andreas Tünnermann.  
**Titel:** "Alignment-free, all-spliced fiber laser source for CARS microscopy based on four-wave-mixing"  
**Journal:** *Optics Express*, 20(19):21010–21018, **2012**.

©Copyright 2012 The Optical Society of America (OSA).  
Reproduced with permission.



## 9 | Alignment-Free, All-Spliced Fiber Laser Source for CARS Microscopy Based on Four-Wave-Mixing

**Martin Baumgartl,<sup>1\*</sup> Thomas Gottschall,<sup>1</sup> Javier Abreu-Afonso,<sup>2</sup>  
Antonio Díez,<sup>2</sup> Tobias Meyer,<sup>3,4</sup> Benjamin Dietzek,<sup>3,4</sup> Manfred  
Rothhardt,<sup>4</sup> Jürgen Popp,<sup>3,4</sup> Jens Limpert,<sup>1,2</sup> and Andreas  
Tünnermann<sup>1,2,5</sup>**

<sup>1</sup> Institute of Applied Physics, Abbe Center of Photonics,  
Friedrich-Schiller-Universität Jena, Albert-Einstein-Str. 15, 07745 Jena, Germany

<sup>2</sup> Departamento de Física Aplicada-ICMUV, Universidad de Valencia, Dr. Moliner  
50, 46100 Burjassot, Spain

<sup>3</sup> Institute of Physical Chemistry and Abbe Center of Photonics,  
Friedrich-Schiller-University Jena, Helmholtzweg 4, 07743 Jena, Germany

<sup>4</sup> Institute of Photonic Technology e.V., Albert-Einstein-Strasse 9, 07745 Jena,  
Germany

<sup>5</sup> Fraunhofer Institute for Applied Optics and Precision Engineering,  
Albert-Einstein-Str. 7, 07745 Jena, Germany

\* corresponding author: martin.baumgartl@uni-jena.de

## **Abstract**

An environmentally-stable low-repetition rate fiber oscillator is developed to produce narrow-bandwidth pulses with several tens of picoseconds duration. Based on this oscillator an alignment-free all-fiber laser for multi-photon microscopy is realized using in-fiber frequency conversion based on four-wave-mixing. Both pump and Stokes pulses for coherent anti-Stokes Raman scattering (CARS) microscopy are readily available from one fiber end, intrinsically overlapped in space and time, which drastically simplifies the experimental handling for the user. The complete laser setup is mounted on a home-built laser scanning microscope with small footprint. High-quality multimodal microscope images of biological tissue are presented probing the CH-stretching resonance of lipids at an anti-Stokes Raman-shift of  $2845\text{ cm}^{-1}$  and second-harmonic generation of collagen. Due to its simplicity, compactness, maintenance-free operation, and ease-of-use the presented low-cost laser is an ideal source for bio-medical applications outside laser laboratories and in particular inside clinics.

## Introduction

Coherent Anti-Stokes Raman scattering (CARS) microscopy is a potent technique for chemical selective tissue imaging [1]. By probing vibrational molecule resonances chemical information is obtained without the use of any labels. Hence, CARS allows for microscopy of living cells and is a promising technique for real time in vivo imaging, e.g. during brain cancer surgery [2]. However, CARS signal generation requires two synchronized picosecond pulse trains with their frequency difference matching the resonance frequency of interest. These are commonly generated using Ti:Sapphire or frequency doubled Nd-based bulk lasers in combination with a bulk optical parametric oscillator. Such systems are not only expensive and complex, but also require constant maintenance and alignment. A wider use of CARS in real-world applications, such as medical imaging in clinical environments, is crucially dependent on the development of compact, turn-key laser sources which are reliable and easy to use. Therefore, several attempts have been made to transfer the compactness and ruggedness of fiber laser technology to CARS laser sources. Nevertheless, while alignment-free fiber lasers are routinely operated in many industrial applications, the critical point for CARS still is the fiber based generation of a synchronized pulse train at a second wavelength. Besides electronic locking of two separate lasers [3] all-optical frequency conversion of a mono-laser source has been demonstrated [4, 5, 6, 7, 8], resulting in intrinsic passive synchronization of the two pulse trains. The fiber based frequency conversion is typically realized by soliton self-frequency shift [4, 5, 6]. However, in addition to the fiber sections all of these sources rely on free-space setups to adapt the generated pulses to suit the CARS process. Only recently optical parametric generation (OPG) by four-wave-mixing (FWM) in photonic-crystal fibers (PCF) [9, 10] has been demonstrated as new approach to generate passively synchronized pump and Stokes pulses for CARS [7]. The proposed scheme offers several advantages since the fiber-generated long-picosecond pulses can directly be used for CARS and complete fiber integration including fiber delivery becomes feasible. Also continuous-wave seeded FWM using short few ps pulses has been applied [8]. Using a cw-seed reduces the bandwidth of the FWM generated

pulses [11], which is advantageous for applications requiring high spectral resolution, e.g. probing narrow resonances in the fingerprint region. However, the use of 1-2 ps pulses as in [8] only results in moderate resolution; moreover, the short pulses hinder fiber integration both for the fiber amplifier due to increased nonlinear effects as for the CARS setup due to the extra delay lines needed to precisely control the temporal overlap.

In this contribution we present, to the best of our knowledge, the first alignment-free all-fiber laser source for CARS microscopy delivering synchronized pump and Stokes pulses from a single fiber end. Similar to the source proposed in [7] optical parametric frequency generation via in-fiber FWM is used to generate the CARS pump, while the residual fundamental laser pulses serve as CARS Stokes. The complete setup including the FWM stage is constructed of polarization maintaining (PM) fiber components, which are fusion spliced eliminating any free-space propagation. The ultra-compact setup is enabled by a novel ps master oscillator with low MHz repetition rate. This environmentally-stable, SESAM mode-locked all-fiber oscillator generates spectrally narrow pulses with 50 ps duration. It is therefore perfectly adapted to the requirements, reducing the number of components and, thus, the complexity and the footprint of the system. The turn-key CARS laser source has great benefit for the user as the fiber delivery eliminates alignment of the spatial and temporal pulse overlap. Microscopic multimodal nonlinear imaging is performed by probing the CARS CH-stretching vibration of lipids around  $2845\text{ cm}^{-1}$  and by probing second harmonic generation in the sample simultaneously. High quality images of atherosclerotic plaques at the inner human arterial wall are presented.

## The alignment-free all-fiber laser system

CARS microscopy of biological samples is limited to a certain window of laser parameters. Since CARS is a three-photon process the accumulated signal is increasing with the cubic of the peak power ( $P_{peak}$ ) multiplied by the duty-cycle ( $\eta_{duty}$ ) of the laser. The sensitivity of the detection system hence gives a minimum power requirement ( $P_{peak}^3 \cdot \eta_{duty} > \lim_{sens}$ ). At the same time, the onset of cell damage limits



the maximum power on the sample, while the damage mechanism is depending on tissue type, peak power and wavelength. Assuming, that cell damage is predominantly two-photon induced [12] the maximum condition is depending on the square of the peak power ( $P_{peak}^2 \cdot \eta_{duty} < \lim_{damage}$ ). Hence, a high peak power and a rather low duty cycle extend the useful operation window. Consequently, a short pulse duration ( $\tau$ ) and low repetition rate ( $f_{rep}$ ) is advantageous ( $\eta_{duty} = \tau \cdot f_{rep}$ ). In contrast, besides the decrease in spectral resolution, undesired NL effects and issues with temporal overlap and dispersion in optical elements, delivery fibers or in the case of deep tissue imaging become more and more critical for short pulses with few ps or sub-ps duration. A very low repetition rate, in turn, limits the scanning speed. Pulses with tens of ps duration represent a good compromise. They are ideally suited for practical CARS systems as they facilitate the experiment drastically. At the same time, they allow for very high spectral resolution and reach the required peak power of typically 0.1-1 kW in combination with MHz repetition rates (required for video rate imaging) at a moderate average power ( $P_{avg} = P_{peak} \cdot \eta_{duty}$ ). Indeed, for example a 20 ps system with its repetition rate lowered to 2 MHz has the same duty cycle as a system with 500 fs at 80 MHz, and, hence, under the above assumptions it is fully equivalent in terms of efficient CARS signal generation and the onset of cell damage.

Such pulse durations and peak power levels can be generated by FWM in PCFs [7, 9, 10, 11], where a launched pump pulse generates two new, equally separated frequency components at shorter (signal) and longer (idler) wavelengths. We decided on a target pulse duration of 20 ps as it is appropriate both for CARS imaging, due to the above mentioned reasons, as for pulse generation via FWM. Since the generated signal pulse is significantly shorter [7], this corresponds to a pump pulse between 50 and 60 ps, which is still long enough to keep spectral broadening via self-phase-modulation (SPM) reasonable and also long enough to generate a clean signal spectrum with suitable bandwidth, even without the use of a cw-seed keeping the system very simple.

To drive the FWM process a suitable all-fiber laser system was developed using only 6  $\mu\text{m}$ -core PM single-mode fiber (SMF). The following subsections describe the ps oscillator and the amplification and FWM stages.

### Environmentally-stable all-fiber oscillator with low repetition rate

As outlined above the target system requires a pulse source, which delivers around 50 ps pulses with narrow bandwidth and a low MHz repetition rate. Since pulse picking and spectral filtering as in [7] complicate the system it is highly desirable to generate such pulses directly from a simple oscillator.

The simplest Yb-fiber oscillator concept is the all-normal dispersion laser omit-

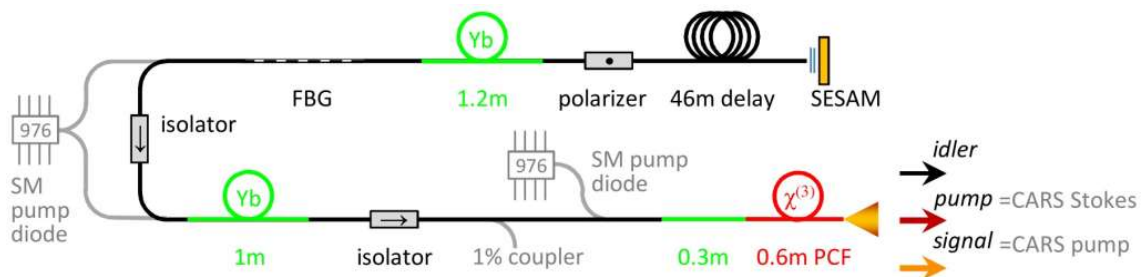


**Figure 1** – Schematic of the all-fiber CARS laser source, showing the ps oscillator (upper part) and the amplification and frequency conversion stages (lower part).

ting the dispersion compensation. Such lasers have been shown to operate at low repetition rate in a highly nonlinear regime with broad bandwidth stabilized by a several nm wide spectral filter [13]. On the other hand ps pulses with relatively narrow bandwidths have been obtained without spectral filter in linear regimes at high dispersion [14, 15]. However, in these cases the time-bandwidth product has still been relatively large. Here, a 10 mm long uniform fiber Bragg grating (FBG) with a width of 0.06 nm is used to spectrally narrow the pulses and stabilize the mode-locking. The FBG is, moreover, crucial to fix the wavelength to exactly match the requirements of the FWM and finally the CARS resonance. The laser is constructed in a simple linear configuration as shown in Fig. 1. The FBG represents one of the cavity end mirrors and with a peak reflectivity of 50% it also serves as output coupler. The other end mirror is formed by the semi-conductor saturable absorber mirror (SESAM) which is directly butt-coupled to the fiber. It has a modulation depth of 24%, a relaxation time of 9 ps and a saturation fluence of  $100 \mu\text{J}/\text{cm}^{-2}$ . The fiber section, realized with PM Panda fiber, consists of a delay section of about 50 m, a polarizer to select the oscillation axis and a 1.2 m active fiber section with a

pump absorption of 80 dB/m which is core-pumped through the FBG by a 976 nm single-mode diode.

With a low repetition rate of 1.9 MHz this simple oscillator generates a pulse train of 45 to 55 ps pulses depending on the pump level. At a launched pump power of 11 mW it produces 0.13 nJ pulses with a duration of 51 ps and a spectral width of 0.07 nm as shown in Fig. 2. The oscillator output is spliced to an optical isolator which is delivering the pulses to the amplification stages.

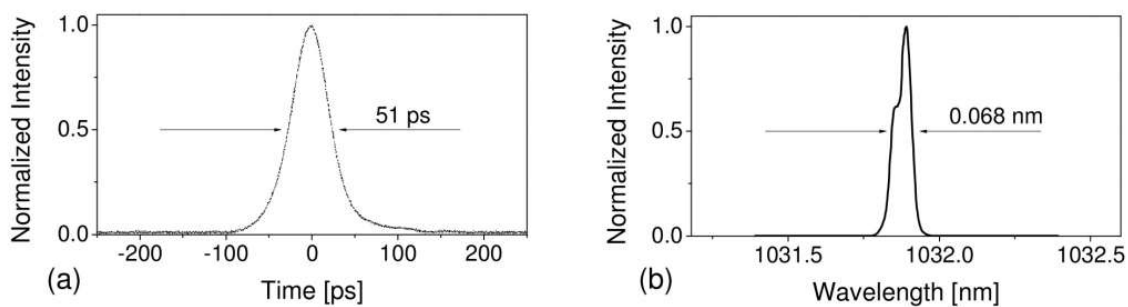


**Figure 2** – Oscillator pulse characterization: (a) Temporal characteristic measured with a fast photo diode (19 ps response time) and a 70 GHz sampling oscilloscope; (b) Spectrum measured with a resolution of 0.02 nm.

### Core-pumped SMF amplifier and all-fiber frequency conversion by FWM

The low repetition rate reduces the average power requirements for the whole laser system; hence, the amplifiers can be constructed only of SMF components, making the system very compact. A 1 m active fiber with a pump absorption of 250 dB/m is used to pre-amplify the pulses. This results in 7.5 mW seed launched into the 0.3 m long main amplification fiber (1200 dB/m pump absorption) which can deliver up to 0.5 W output power. With a resulting peak power of up to 5 kW the amplified pulses can easily drive the FWM process.

Efficient parametric signal and idler generation requires good overlap of the involved fiber modes and a suitable dispersion characteristic of the fiber to realize phase matching. Both can be fulfilled in endlessly single-mode PCFs which easily allow

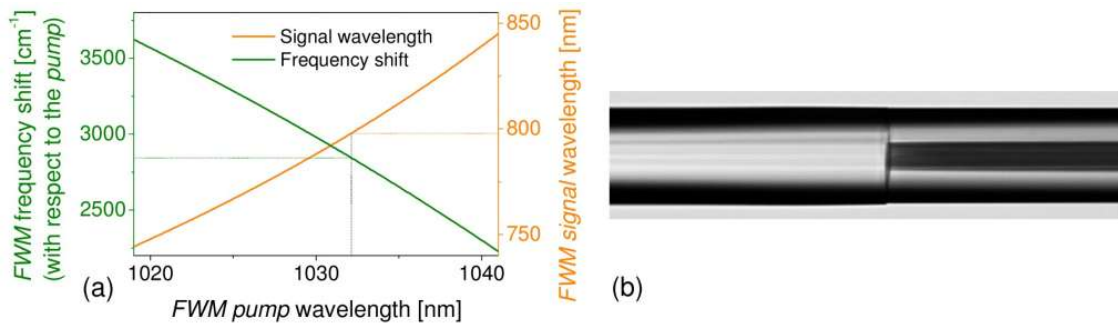


**Figure 3** – (a) FWM phase-matching diagram for the PCF showing the frequency shift and the corresponding signal wavelength over pump wavelength; (b) Microscope image of the splice between Yb-doped SIF (left) and PCF (right), the splice transmission is 74%.

one to tailor the dispersion by changing the air-hole structure [10]. As the majority of biomedical CARS imaging applications focuses on probing the resonances of lipids [16] we looked for a commercially available PCF with appropriate dispersion characteristic to generate the FWM signal at a frequency difference matching the C-H-stretching vibrational resonance of methylene groups around  $2845\text{ cm}^{-1}$  when being pumped around 1030 nm by an Yb-based fiber laser. For this purpose simulations analog to those in [7] were carried out and as a result a PCF offered by NKT Photonics named “LMA-5 PM” was identified to meet our requirements. The fiber has 4 rings of  $1.2\ \mu\text{m}$  air holes with a hole-to-hole separation of  $3.2\ \mu\text{m}$ . On the basis of the fiber’s phase-matching characteristic (see Fig. 3(a)) the central wavelength of the pump laser was chosen accordingly to generate the desired frequency shift of  $2845\text{ cm}^{-1}$ . As can be deduced from the slope in Fig. 3(a) the frequency shift changes by  $6.5\text{ cm}^{-1}$  per 0.1 nm pump wavelength variation. Due to manufacturing tolerances and uncertainties concerning the fiber parameters an experimental FWM measurement is required to test the frequency shift of the actual piece of PCF. With this measurement the simulation can be adapted to precisely design the target wavelength of the oscillator to finally meet the desired CARS excitation frequency.

The PCF was directly spliced to the main amplifier fiber using arc fusion splicing. Previous alignment of the Panda structure of both fibers was executed to ensure coupling into the slow axis of the PCF. The relatively similar mode-field diameters of nominal  $6.0\ \mu\text{m}$  (SIF) and  $4.4\ \mu\text{m}$  (PCF) allow for a high theoretical coupling

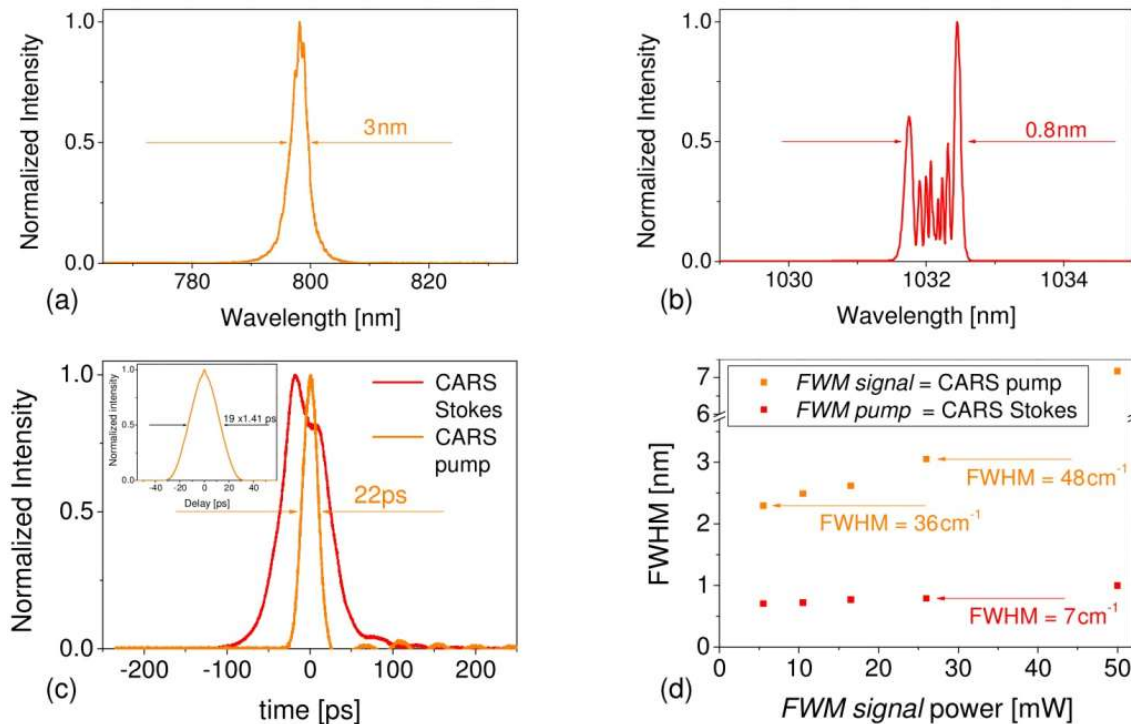


**Figure 4** – (a)-(c) Characterization of the generated pulses at 26 mW of signal power: Spectral shape of FWM signal (a) and corresponding residual pump (b), temporal shapes accordingly, measured with a fast photo diode (c) and signal pulse autocorrelation trace (c, inset). (d) Spectral width of FWM signal and residual pump for different signal power.

efficiency of 91% assuming Gaussian mode profiles. After optimization of the splice procedure parameters we obtain an excellent experimental value of 74% for the splice shown in Fig. 3(b). As can be seen the collapse length of the PCF air holes is kept very small. At the same time the splice is still strong enough to withstand pulling and bending during experimental handling. Finally, the PCF is cut to a length of 0.6 m and the fiber end is collapsed and angle polished.

At the end of this alignment-free configuration we measure 10.5 mW FWM signal at a pump power of 290 mW launched into the PCF. By turning up the pump this increases to 50 mW signal at 345 mW of pump. Due to the increasing parametric gain bandwidth, SPM-broadening of the pump spectrum and nonlinear broadening of the signal pulse itself, the bandwidth of the generated signal grows with increasing power. This dependency is shown in Fig. 4(d) where the spectral width of both signal

and residual pump is plotted for different signal levels. The graph demonstrates that power levels of several ten mW which are more than sufficient for CARS imaging applications can easily be generated with reasonable spectral widths of several ten wavenumbers.

The spectral shape of the FWM signal (serving as CARS pump) and the spectrum of the residual FWM pump (serving as CARS Stokes) are shown in Figs. 4(a), and 4(b) exemplarily for a signal power of 26 mW, which corresponds to the power level used in the subsequent CARS experiments. The spectra are centered around 797.9 nm and 1032.1 nm matching the desired frequency separation of  $2845\text{ cm}^{-1}$ . Due to the high peak power the pump spectrum shows significant SPM structures and it is broadened to 0.8 nm. The temporal pulse shapes were measured with a fast photo diode with a response time of 18.5 ps and a 70 GHz sampling oscilloscope. The recorded traces for the partially depleted pump pulse and the signal pulse are shown in Fig. 4(c). As the conversion starts only at the center of the pulse the generated signal is significantly shorter than the pump. It therefore reaches the detection limit of the equipment, hence, an additional autocorrelation measurement was performed (inset of Fig. 4(c)) measuring a pulse duration of 19 ps under the assumption of a Gaussian shape. From this we can estimate the peak power to 0.7 kW. The temporal walk-off between pump and signal in the PCF due to group-velocity mismatch is about 0.1 ps/cm and, hence, it is negligible regarding the pulse duration and fiber length. In consequence, a good temporal overlap of the pulses is automatically ensured for the CARS process.

## CARS imaging

To obtain a complete and compact CARS imaging system a scanning microscope was developed, which is simple to use and does not require an optical table. The optical layout has been simplified since a confocal microscope design is not required; instead the nonlinear processes provide intrinsic 3D sectioning capabilities. Due to the nonlinear nature of CARS the spatial overlap of the pump and Stokes pulses in

the focal spot is critical. Thus, conventional systems require careful adaptation and overlay of the separate pump and Stokes beams including control of the temporal pulse overlap, which make the alignment time consuming and difficult and increase space requirements and system complexity. For the experiment reported here, the fiber output of the laser is directly attached to the microscope as illustrated in Fig. 5. Pump and Stokes pulses are emitted simultaneously eliminating any need

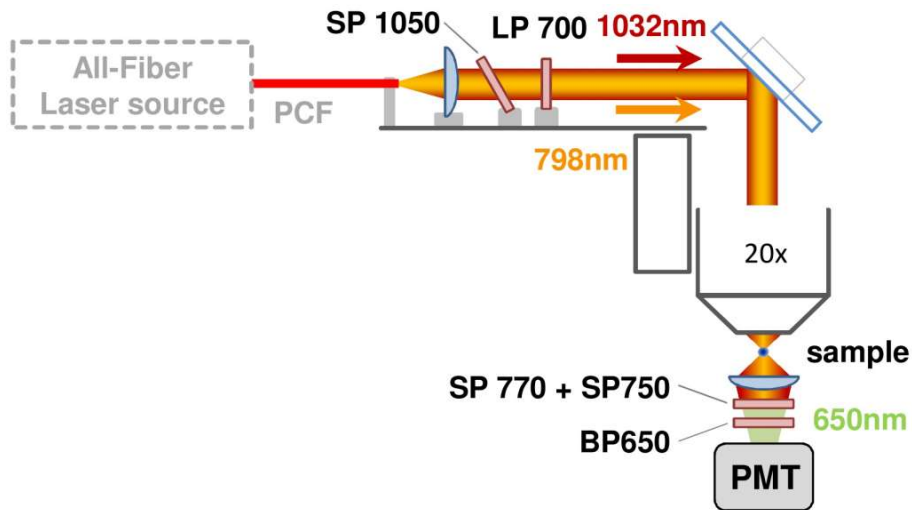


**Figure 5** – Schematic of the CARS microscopy setup, SP short pass, LP long pass, BP band pass, PMT photo multiplier tube.

for alignment. The collimated beam is deflected by a pair of scanning galvanometric mirrors and focused using a  $20 \times$  microscope objective with NA 0.4 (Mitutoyo Plan Apo NIR). Finally, the forward generated CARS signal is detected with a photomultiplier tube (PMT). All elements in the illumination path are designed for the near infrared reducing reflection losses. Furthermore, by minimizing the distance of the sample to the detector also scattered signal photons can be efficiently detected. For medical applications a large field of view (FOV) is beneficial, whereas most commercial microscopes have only a limited FOV, which is optically highly corrected. In contrast, the FOV of the microscope reported here has been maximized and exceeds  $1 \text{ mm}^2$  when using a  $20 \times$  objective.

To reduce the total power on the biological sample, the output of the PCF containing FWM signal, residual pump and idler is spectrally filtered. A short pass with

its edge at 1050 nm blocks the long-wavelength idler. Tilting this filter, moreover, allows one to continuously decrease the power fraction transmitted at 1032 nm. Hence, the amount of Stokes available for CARS can be adjusted. An additional long-pass filter blocks any light emitted at the CARS wavelength, which is generated in small amounts by non-phase-matched FWM in the PCF [17]. High-quality images are obtained with a total power of less than 20 mW on the sample. In front of the PMT the residual laser light is blocked by two short-pass filters, moreover, a band-pass filter ensures that only CARS photons are detected.

Multimodal nonlinear microscopic images utilizing CARS, SHG and TPEF of a human aorta section are presented in Fig. 6. These were recorded with a total average power on the sample of 50 mW (a)-(c) and 20 mW (d) respectively. Sections of  $1.2 \times 1.2 \text{ mm}^2$  were scanned with a pixel dwell time of  $1 \mu\text{s}$ . Figure 6(a) shows the image obtained when the CARS signal at 650 nm is detected. Probing the CH-stretching vibration with a laser frequency difference of  $2844 \text{ cm}^{-1}$ , lipid plaques are clearly visible in this image indicating atherosclerosis. The non-resonant signal contribution in the image is small; the ratio of resonant signal to non-resonant background for the lipid plaques is about 10:1, which has been measured by tuning off-resonance with a slightly modified setup. By exchanging the band-pass 650 nm filter in front of the detector with a short-pass 600 nm, the combined second harmonic generation (SHG) signal of collagen at 399 and 516 nm and the two-photon excited fluorescence signal (TPEF) of elastin is recorded (Fig. 6 (b)). Due their isotropic nature the lipid droplets appear dark in 6(b); while fibers composed of the structural proteins collagen and elastin become visible [18]. The multimodal composite image is shown in Fig. 6(c).

## Conclusion

In this contribution a completely alignment-free, simple and potentially low-cost all-fiber laser source for nonlinear and especially CARS microscopy is presented. The CARS pump pulses are produced by optical parametric generation via four wave mixing in a photonic-crystal fiber, which gives intrinsic passive synchronization of



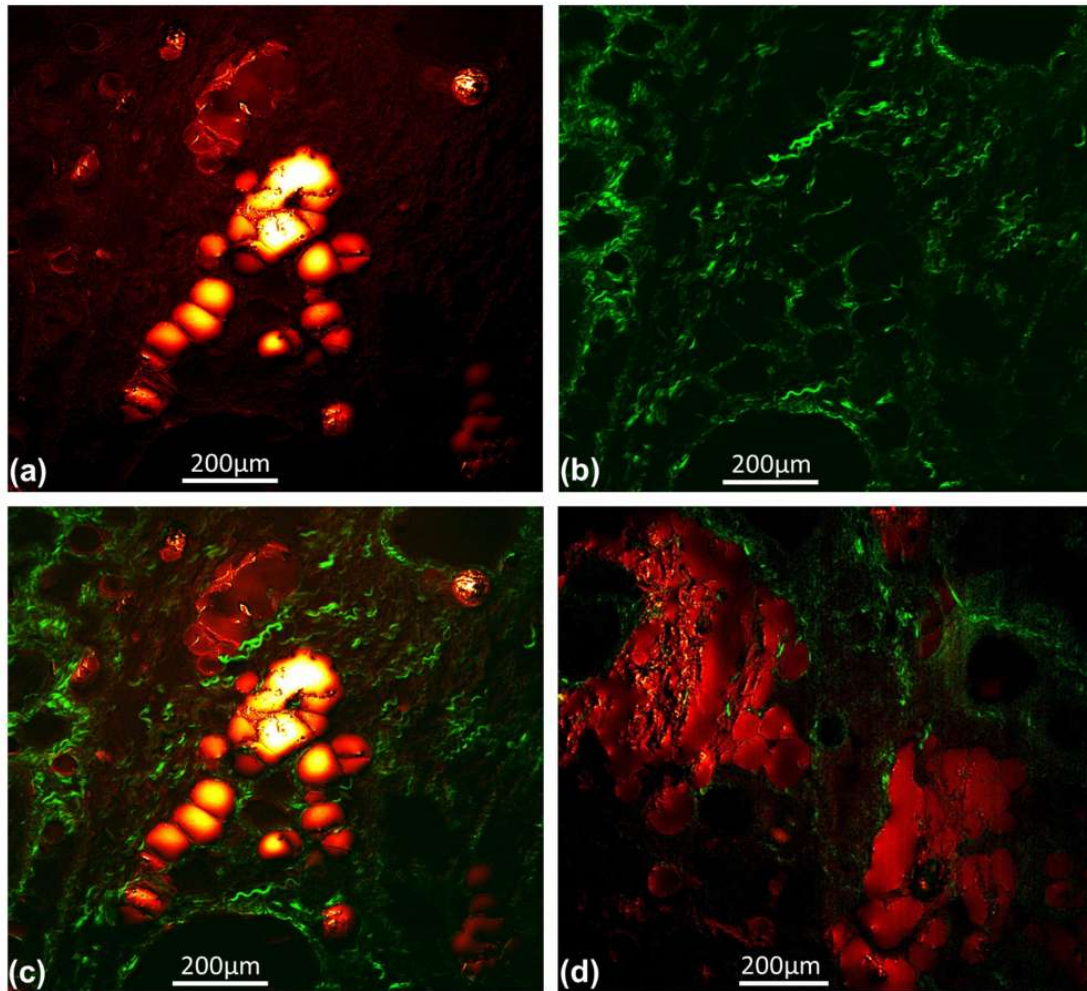


**Figure 6** – Microscopic images of atherosclerotic plaque deposition at the inner human arterial wall. (a)-(c) show the same sample section: (a) CARS image probing lipids at  $2844\text{ cm}^{-1}$ , the atherosclerotic plaques appear bright due to their high lipid content, (b) combined SHG and TPEF signal of the elastic fibers of the arterial wall predominantly composed of collagen (SHG) and elastin (TPEF), (c) Multimodal composite image showing an overlay of the CARS and the SHG/TPEF signals. The images were sampled with 16.8 Mpixels with a pixel dwell time of  $1\ \mu\text{s}$ , 2 scans averaged, 50 mW total laser power on the sample. (d) Multimodal composite image as in (c) showing a different aorta section, recorded with 20 mW total laser power on the sample.

the pump and Stokes pulses. The laser relies on a long-cavity passively mode-locked Yb fiber oscillator, developed to produce spectrally narrow 50 ps pulses with a low

repetition rate of 2 MHz. These parameters allow for direct amplification to 5 kW peak power using standard core-pumped single-mode fibers, which gives sufficiently high intensities to drive the frequency generation in the PCF. The complete setup is constructed of commercially available, polarization-maintaining fiber components which are fusion spliced eliminating any alignment.

CARS pump (798 nm) and Stokes (1032 nm) pulses are emitted from a single fiber end which is directly attached to a home-built laser scanning microscope. The single-fiber delivery drastically eases the experimental effort as the pulses are perfectly overlapped in space and time. This reduces the alignment to a minimum which is of particular importance for the user. The relatively long pulse durations are advantageous as they ensure temporal overlap even after additional optical elements, e.g. microscope objective lenses.

High-quality multimodal nonlinear microscopic imaging is demonstrated, presenting resonant imaging of lipids at a wavenumber shift of  $2845\text{ cm}^{-1}$  in combination with SHG and TPEF showing plaque deposition by arteriosclerosis in a human aorta section.

With its hands-off operation and compact dimensions the presented light source makes the application of CARS microscopy interesting for a wider community. Additional features as the fiber delivery and the extremely simplified handling particularly pave the way to the application of CARS in clinics.

## **Acknowledgments**

This work was supported by the German Federal Ministry of Education and Research (BMBF) [13N10773], [13N10774]; the European network of excellence P4L (Photonics4Life); and the Ministerio de Economía y Competitividad of Spain [TEC2008-05490]. M.B. acknowledges support from the Carl-Zeiss-Stiftung. The authors like to thank Christian Matthäus for providing the biological sample.

## References

- [1] Evans, C. L. and Xie, X. S. *Annual Review of Analytical Chemistry* (2008) **1**(1), 883–909 (2008).
- [2] Krafft, C., Dietzek, B., and Popp, J. *The Analyst* **134**(6), 1046–1057 (2009).
- [3] Bégin, S., Burgoyne, B., Mercier, V., Villeneuve, A., Vallée, R., and Côté, D. *Biomedical Optics Express* **2**(5), 1296–1306 (2011).
- [4] Andresen, E. R., Nielsen, C. K., Thøgersen, J., and Keiding, S. R. *Optics Express* **15**(8), 4848–4856 April (2007).
- [5] Pegoraro, A. F., Ridsdale, A., Moffatt, D. J., Pezacki, J. P., Thomas, B. K., Fu, L., Dong, L., Fermann, M. E., and Stolow, A. *Optics Express* **17**(23), 20700–20706 November (2009).
- [6] Krauss, G., Hanke, T., Sell, A., Träutlein, D., Leitenstorfer, A., Selm, R., Winterhalder, M., and Zumbusch, A. *Optics Letters* **34**(18), 2847–2849 (2009).
- [7] Baumgartl, M., Chemnitz, M., Jauregui, C., Meyer, T., Dietzek, B., Popp, J., Limpert, J., and Tünnermann, A. *Optics Express* **20**(4), 4484–4493 (2012).
- [8] Lefrancois, S., Fu, D., Holtom, G. R., Kong, L., Wadsworth, W. J., Schneider, P., Herda, R., Zach, A., Xie, X. S., and Wise, F. W. *Optics Letters* **37**(10), 1652–1654 (2012).
- [9] Lavoute, L., Knight, J. C., Dupriez, P., and Wadsworth, W. J. *Optics Express* **18**(15), 16193–16205 (2010).
- [10] Nodop, D., Jauregui, C., Schimpf, D., Limpert, J., and Tünnermann, A. *Optics Letters* **34**(22), 3499 November (2009).
- [11] Mosley, P. J., Bateman, S. A., Lavoute, L., and Wadsworth, W. J. *Optics Express* **19**(25), 25337 November (2011).
- [12] König, K., Becker, T. W., Fischer, P., Riemann, I., and Halbhuber, K.-J. *Optics Letters* **24**(2), 113–115 (1999).
- [13] Renninger, W. H., Chong, A., and Wise, F. W. *Optics Letters* **33**(24), 3025–3027 (2008).
- [14] Baumgartl, M., Ortaç, B., Limpert, J., and Tünnermann, A. *Applied Physics B* **107**(2), 263–274 (2012).
- [15] Tian, X., Tang, M., Cheng, X., Shum, P. P., Gong, Y., and Lin, C. *Optics Express* **17**(9), 7222–7227 April (2009).
- [16] Pezacki, J. P., Blake, J. A., Danielson, D. C., Kennedy, D. C., Lyn, R. K., and Singaravelu, R. *Nat Chem Biol* **7**(3), 137–145 (2011).
- [17] Balu, M., Liu, G., Chen, Z., Tromberg, B. J., and Potma, E. O. *Optics Express* **18**(3), 2380–2388 (2010).
- [18] Zipfel, W. R., Williams, R. M., Christie, R., Nikitin, A. Y., Hyman, B. T., and Webb, W. W. *Proceedings of the National Academy of Sciences of the United States of America* **100**(12), 7075–7080 (2003).



Adapted with kind permission from The Optical Society of America (OSA):

**Authors:** Mario Chemnitz, Martin Baumgartl, Tobias Meyer, Cesar Jau-regui, Benjamin Dietzek, Jürgen Popp, Jens Limpert, and Andreas Tünnermann.  
**Titel:** "Widely tuneable fiber optical parametric amplifier for coherent anti-Stokes Raman scattering microscopy"  
**Journal:** *Optics Express*, 20(24):26583–26595, **2012**

©Copyright 2012 The Optical Society of America (OSA).  
Reproduced with permission.



10 | Widely Tuneable Fiber Optical  
Parametric Amplifier for Cohe-  
rent Anti-Stokes Raman Scat-  
tering Microscopy

**Mario Chemnitz,<sup>1,\*</sup> Martin Baumgartl,<sup>1</sup> Tobias Meyer,<sup>2,3</sup> Cesar Jauregui,<sup>1</sup> Benjamin Dietzek,<sup>2,3</sup> Jürgen Popp,<sup>2,3</sup> Jens Limpert,<sup>1,4</sup> and Andreas Tünnermann<sup>1,4</sup>**

<sup>1</sup>Institute for Applied Physics, Abbe Center of Photonics, Friedrich-Schiller-University Jena, Albert-Einstein-Str. 15, 07745 Jena, Germany

<sup>2</sup> Institute of Physical Chemistry, Abbe Center of Photonics, Friedrich-Schiller-Universität Jena, Helmholtzweg 4, 07743 Jena, Germany

<sup>3</sup> Institute of Photonic Technology (IPHT) e.V., Albert-Einstein-Str. 9, 07745 Jena, Germany

<sup>4</sup> Fraunhofer Institute for Applied Optics and Precision Engineering, Albert-Einstein-Str. 7, 07745 Jena, Germany

\* corresponding author: mario.chemnitz@uni-jena.de

## **Abstract**

We present a narrow-bandwidth, widely tunable fiber laser source for coherent anti-Stokes Raman scattering (CARS) spectro-microscopy. The required, synchronized, two-color pulse trains are generated by optical-parametric amplification in a photonic-crystal fiber (PCF). The four-wave-mixing process in the PCF is pumped by a 140 ps, alignment-free fiber laser system, and it is seeded by a tunable continuous-wave laser; hence, a high spectral resolution of up to  $1\text{ cm}^{-1}$  is obtained in the CARS process. Since the PCF is pumped close to its zero-dispersion wavelength, a broad parametric gain can be accessed, resulting in a large tuning range for the generated signal and idler wavelengths. CARS spectroscopy and microscopy is demonstrated, probing different molecular vibrational modes within the accessible region between  $1200\text{ cm}^{-1}$  and  $3800\text{ cm}^{-1}$ .



## Introduction

Laser based spectroscopy and imaging have become important tools for biochemical and medical applications in the past decades. Nonlinear optical effects such as second (SHG) and third harmonic generation (THG) provide the opportunity for damage-free investigations in living cells (*in-vivo*). The missing chemical selectivity of these processes can be overcome by stimulated Raman scattering (SRS) and fluorescence microscopy, with the drawbacks of either a slightly lower imaging speed, due to a required lock-in data acquisition [1], or the sacrifice of label-free operation. Coherent anti-Stokes Raman scattering (CARS) provides both label-free chemical information and fast acquisition times [2, 3]. CARS is a third order non-linear interaction, where the stimulated emission of an anti-Stokes signal is related to resonant interactions with molecular energy states. This fact confers CARS chemical sensitivity. Thus, a suitable incident frequency set ( $\omega_{pump/probe}, \omega_{Stokes}$ ) is required in order to collect intense anti-Stokes signals. This resonant characteristic makes CARS a competitive technology to gain specific tissue information with high speed.

Due to the need of two widely separated and narrowband frequencies, the usual laser systems of choice are solid-state laser pumped optical parametric oscillators (OPO), which provide a high tuning range [2]. These systems have megahertz repetition rates and typical pulse durations between sub-picoseconds and ten picoseconds. This range of pulse durations has been found to be a good compromise between reasonable spectral resolution and the required high peak power. However, adjusting temporal and spatial overlap of the two pulse trains increases experimental difficulties. In addition the costs and size of such table-spanning systems prevent the spread of CARS systems in biochemical sciences.

Over the past few years new approaches were proposed for generating the required wavelength set directly inside of optical fibers. Fiber technology offers the benefit of highly stable, compact and robust laser sources. The first fiber-based CARS pump sources used soliton self frequency shift (SSFS) [4] and super continuum (SC) generation [5, 6]. Despite of their good wavelength tunability, these systems come with a rather low spectral power density and poor spectral resolution. To overcome this

problem, efficient spectral compression by SHG was demonstrated [7], leading to an increased system complexity.

As an alternative approach, efficient, degenerately pumped four-wave-mixing (DFWM) in endlessly single-mode PCFs could be shown [6, 8, 9, 10, 11]. DFWM is an optical nonlinear third order process where one pump field interacts with the waveguide material generating both a signal and an idler field. The resulting frequency separation between the generated fields and the pump is given by the phase-matching condition; and, hence, it can be adjusted by the dispersion of the fiber and, consequently, by a proper design of the air-hole structure of the PCF. Using pump pulses with a width of tens of picoseconds, the DFWM provides temporally and spatially overlapping pulses out of one fiber end. The spectral components have a well-separated spectral distribution with bandwidths of few nanometers, leading to a spectral resolution of a few ten wavenumbers [10, 11]. Such sources were successfully applied to CARS microscopy providing fast imaging with pixel-dwell-times of one microsecond.

As other parametric processes in bulk media, DFWM in PCFs also yields a spectrally distributed parametric gain [12]. Due to the high nonlinearity of small-core PCFs this gain is so high that the DFWM signal is generated out of quantum noise over fiber lengths of several ten centimeters. As optical parametric amplification (OPA) theory predicts [13], this gain can also be used for the amplification of an external seed signal. Especially a continuous wave (cw) seed signal is beneficial for CARS applications due to the generation of narrow, transform-limited signal and idler pulses. Furthermore, a cw-seed ensures permanent temporal overlap with the pump pulses, without any need of complicated locking or delay schemes. Parametric amplification of a cw seed signal could efficiently be demonstrated previously [14, 15, 16]. Most recently a fiber optical parametric amplifier (FOPA) has been used for CARS [16]. By tuning the pump and seed wavelengths, excitation frequencies between  $2700\text{ cm}^{-1}$  and  $3200\text{ cm}^{-1}$  were potentially addressable.

With regard to the application of the FOPA to CARS, two main aspects are of interest - the spectral resolution and the accessible tuning range. In this contribution we present a tunable FOPA system with an increased accessible frequency range, desi-

igned to address both the characteristic fingerprint region and the excitation region for the CH stretching modes with a high spectral resolution of a few wavenumbers. In contrast to the source presented in [16] significantly longer pulses are used giving some major advantages. First of all a significantly increased spectral resolution is obtained, which improves image contrast and is also advantageous for differentiating structurally similar molecules. In addition, the potential measurement of subtle frequency changes caused by the chemical environment of the molecule would require high spectral resolution. Further significant advantages of the longer pulse duration are the more compact setup and simplified experimental handling. The increased robustness of the pulses against nonlinear spectral broadening and temporal walk-off allows for alignment-free all-fiber implementation and fiber pulse delivery. The simultaneous emission of all-pulses from a single PCF with intrinsic temporal and spatial overlap, as presented herein, simplifies handling as no adjustable delay line is required, furthermore, the alignment-free, perfect spatial overlap allows to illuminate a larger field of view more homogeneously.

The presented source consists of a pulsed all-fiber laser which provides parametric gain inside of a PCF. This gain is used to amplify a cw Ti:Sapphire seed signal generating a narrow-band signal and its idler, respectively. This setup will be presented in section 2 while the output characteristics of the FOPA will be described in section 3. The different combination possibilities of the three output wavelengths give access to both of the above mentioned excitation bands. By tuning the cw seed within the parametric gain bandwidth, high resolution CARS spectroscopy and multi-excitation CARS microscopy are demonstrated in section 4.

## Setup of the fiber optical parametric amplifier

To drive the fiber optical parametric amplifier (FOPA) used in our experiments two laser systems are applied - a pulsed fiber laser for pumping and a bulk laser for seeding the nonlinear process in the photonic crystal fiber (PCF). Figure 1 shows the scheme of the setup.

A spectrally filtered and amplified mode-locked fiber laser similar to the one pre-

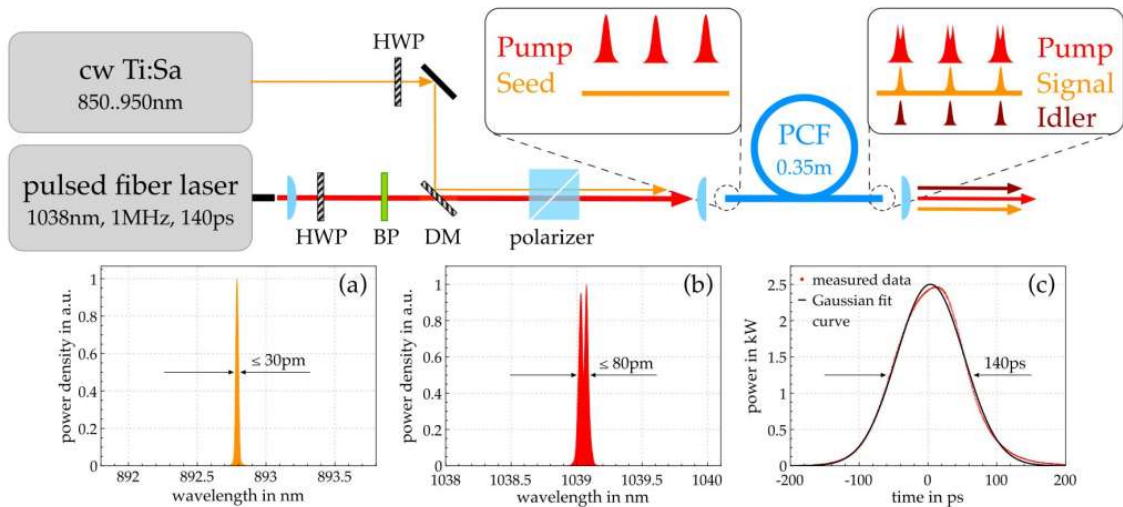


**Figure 1** – Schematic setup of the seeded fiber optical parametric amplifier. Pump and seed will be coupled into a PCF with a length of 0.35 m. Labels: BP - band pass, DM - dichroic mirror, HWP - half-wave plate. The graphs below show the characteristics of the incident laser pulses: (a) spectrum of the Ti:Sa seed signal; (b) spectrum of the fiber laser pump; (c) temporal shape of the pulsed pump

sented in [10] is used to pump the parametric process. The emission wavelength is selected by an internal FBG, which is centred at 1038 nm. By mechanical expansion or compression such a grating can easily be tuned by  $\pm 3$  nm when placed in a suited mounting [17]. This approach provides a simple tuning mechanism of the central wavelength of the pump laser system. The grating, moreover, determines the bandwidth and pulse duration of the laser. For the chosen grating bandwidth of 15 pm, a pulse duration of 140 ps was obtained (Fig. 1(c)). The pulses are transmitted through a bandpass filter, which blocks unwanted ASE, and a polarizer, which ensures a correct excitation of the PM fiber. Due to self-phase-modulation within the amplifier fibers, the bandwidth of the pump is broadened to 0.08 nm. The resultant spectrum, visible in Fig. 1(b), shows beginning modulations (double peak structure). Finally, an average power of 400 mW is coupled into the PCF, corresponding to a peak power of about 2.7 kW. This generates the necessary parametric gain in the FOPA. Including the PCF, the whole system is polarisation maintaining, which helps in mitigating parasitic effects such as nonlinear polarisation rotation [18].

For efficient frequency conversion, the selection of a suitable nonlinear fiber is im-

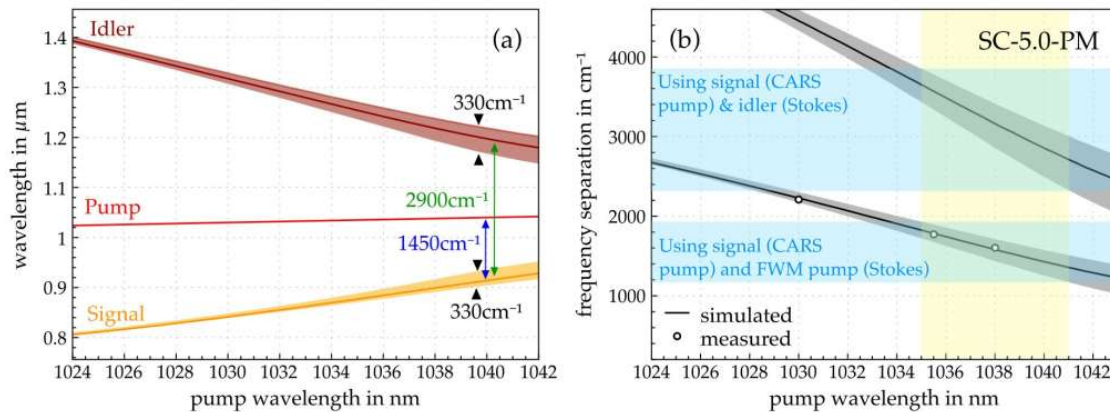


**Figure 2** – Simulation results for a 0.35 m long 5  $\mu\text{m}$  core PCF pumped with 2.5 kW. (a) shows the signal and idler wavelength position for the gain maximum as a function of the pump wavelength. The coloured areas illustrate the theoretical FWHM bandwidth of each band. (b) shows the calculated frequency separation between signal and pump or signal and idler as a function of the pump wavelength. The blue boxes illustrate the theoretically accessible Raman excitation regions by mechanically tuning the internal FBG by  $\pm 3$  nm (yellow box).

portant. The process of DFWM works most efficiently for perfect phase-matching, e.g.  $\kappa = 2k_p - k_i - k_s + 2\gamma P_p = 0$  with  $2\omega_p = \omega_i + \omega_s$  [12]. Consequently, the spectral distribution of the effective refractive index of the chosen fiber determines the signal and idler wavelengths. The resulting parametric gain  $g = g(\kappa)$  is dependent on the net-phase-matching  $\kappa$ . The resulting spectral gain distribution leads to the line shape of the generated FWM bands in unseeded FWM laser sources [10]. The bandwidth of this shape can significantly be broadened by pumping closer to the zero dispersion wavelength (ZDW) of the fiber. With some orders of magnitude the parametric gain enables the amplification of an external seed signal with only very low power. This allows the use of a continuous wave (cw) seed source which is beneficial due to the automatic temporal overlap with the pump pulses. The insets in the setup in Fig. 1 sketch the temporal pulse trace in front of and behind the PCF in case of cw seeded FOPA. Only in presence of pump intensity the cw signal is amplified and a respective idler pulse is generated. The non-amplified temporal regions between the signal pulses yield in a low power background not having any effect in a CARS sample.

We decided to use NKT PHOTONIC's SC-5.0-PM (pitch: 3.22, doL: 0.5, ZDW:

1040 nm, mode field diameter: 5  $\mu\text{m}$ ) for frequency conversion because it has its ZDW close to the emissions bandwidth of Ytterbium. Due to the flat dispersion characteristics near the ZDW, small frequency separations between pump and signal and broad gain bandwidths can be expected. This is confirmed by the numerical calculations shown in Fig. 2. The narrow bandwidth of the fiber pump output was neglected in the numerical calculations. Figure 2(a) shows two typical features: the signal wavelength gets closer to the pump wavelength when the pump wavelength of the fiber laser system approaches the ZDW of the PCF. At the same time the signal becomes spectrally broader, since the phase-matching condition is fulfilled for a broader spectral region. Choosing a pump wavelength around 1040 nm we were expecting CARS excitation frequencies around  $1450\text{ cm}^{-1}$  with a bandwidth of several hundred wavenumbers. In the following experiments the DFWM signal of the three-color output is always used as CARS pump, while either the residual DFWM pump or the idler serves as the Stokes wave for the CARS process. Therefore two excitation frequency bands are available from the FOPA as depicted in Fig. 2(b). Thus with this system we should be able to generate two tuning bands - the *soft* tuning of the input seed signal's wavelength and the *hard* tuning by slightly tuning the pump laser's FBG by  $\pm 3\text{ nm}$  around its center wavelength. By using both bands, the system theoretically provides an overall tunability of the CARS excitation frequency from  $1200\text{ cm}^{-1}$  up to  $3800\text{ cm}^{-1}$  with a  $400\text{ cm}^{-1}$  wide gap around  $2100\text{ cm}^{-1}$ , which contains only a few molecular modes of minor importance.

To sample the spectral accessibility of the predicted parametric gain, a continuously emitting Ti:Sapphire oscillator is used. This system provides a tunable continuous wave output from 850 up to 950 nm at constant narrow bandwidth of  $< 0.03\text{ nm}$  (resolution limit of the optical spectrum analyzer employed) (Fig. 1(b)).

## Fiber optical parametric amplification

The FOPA system described above has four input parameters available which were adjusted to the intended application - pump and seed power as well as pump and seed wavelength. First, the basic influence of a seed on the spectral distribution is

investigated. The fiber laser pump provides the necessary peak power to drive optical parametric generation (OPG) from quantum noise along the 35 cm fiber. The corresponding broadband signal and its respective idler spectrum are plotted light gray in Fig. 3(a). As expected, the frequency separation between the two possible wavelength combinations touches the fingerprint region as well as the CH-stretching bands. The average power of the signal is 33 mW which is perfectly suited for doing CARS spectro-/microscopy. With a pump power of 390 mW the energy conversion efficiency can be calculated to be 9.4% which compares well with former results [10].

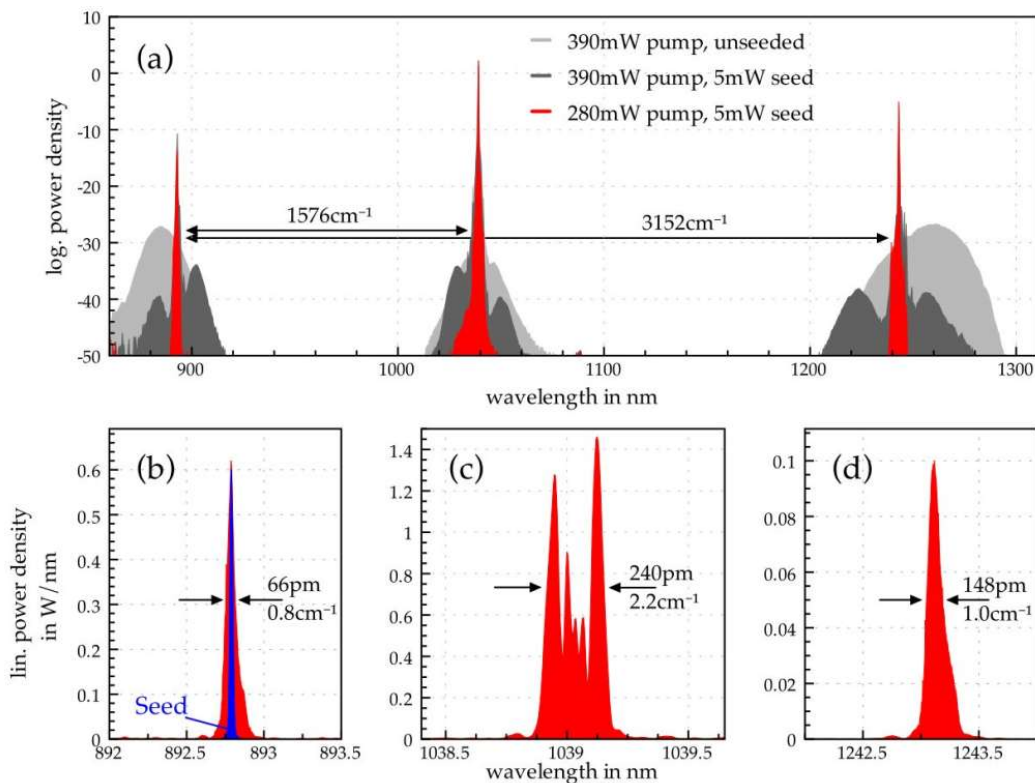


**Figure 3** – (a) Spectrum measured at the output of the PCF for three cases: high pump power without seed (light gray), high pump power with 5 mW seed (dark gray) and lower pump power with 5 mW seed (red). In the first and in the last case the signal output power was the same (33 mW). The spectra below show (b) signal (including unamplified seed spectrum), (c) pump and (d) idler for the last case in more detail. The frequency separation between signal and pump is within the so-called fingerprint region. This frequency separation can be increased by a factor of two when using signal and idler.

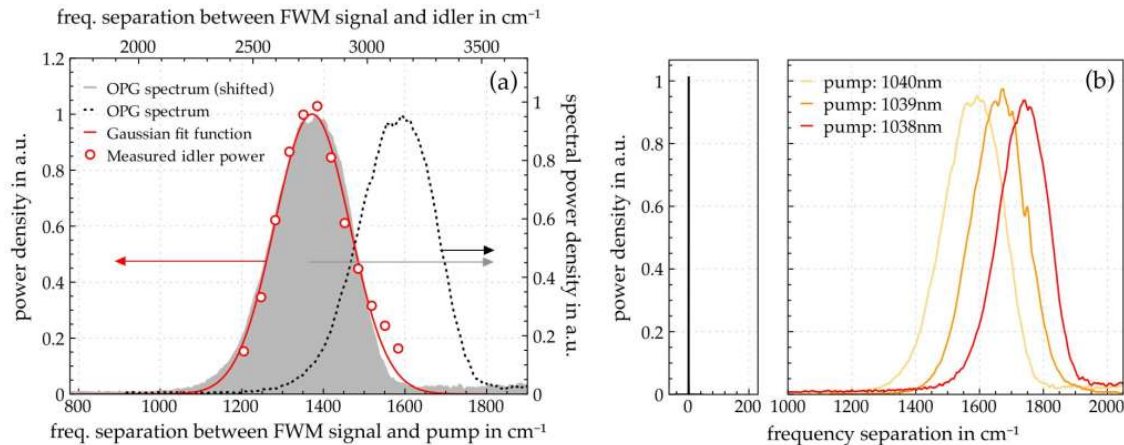
In presence of a 5 mW narrowband seed, the signal average power (without cw under-ground) increases to 55 mW. Simultaneously, in the spectrum the maximum power density increases more than one order of magnitude whereas the spectral width of the signal decreases significantly from several nanometers to few tens of picometers (dark grey spectrum of Fig. 3(a)). A pedestal of spontaneous OPG is still visible, which could deteriorate the spectral resolution of the presented CARS pump system. To prevent this pedestal from appearing, the pump power is reduced to 280 mW, where the signal power is the same as in the unseeded case (33 mW). By doing this, the pedestal strongly reduced while the peak spectral power density remains nearly the same (compare with red spectrum in Fig. 3).

Figure 3(b-d) show the different spectral bands in more detail. All three bands provide a remarkable narrow FWHM bandwidth. The broadest line corresponds to the pump, whose bandwidth increases from initially 0.08 nm to 0.24 nm due to self-phase modulation (SPM) in the single-mode PCF. However, the SPM-induced spectral structure (Fig.3(c)) is stable over time and its full width corresponds to a still small value of  $2.2 \text{ cm}^{-1}$ . Even narrower are the signal and the idler with 0.06 nm and 0.14 nm or  $0.8 \text{ cm}^{-1}$  and  $1.0 \text{ cm}^{-1}$ , respectively. The spectrum of the signal pulses is broader as the calculated time-bandwidth product due to SPM and parametric processes taking place near the signal wavelength. Nevertheless, this FOPA system provides a spectral resolution of few wavenumbers for both usable spectral band combinations. Especially in case of using signal and idler, the spectral resolution is more than one order of magnitude lower than other optical parametric fiber laser sources demonstrated previously [10, 11, 16]. Considering these bandwidths, the system performs even better than commercial table top bulk OPO systems (typically  $> 10 \text{ cm}^{-1}$ ).

Such a high spectral resolution requires a fine tunability to adjust the desired CARS excitation frequency exactly. The tuning range of the FOPA is based on the accessible parametric gain of the PCF. The shape of the signal or idler spectrum in absence of seed gives a first estimation of the spectral gain distribution. The statistical nature of the quantum noise leads to the amplification of all frequencies located inside the parametric gain spectrum. Thus the OPG spectrum resembles directly the shape



of the gain. Figure 4(a) shows the OPG spectral density of the idler as a function of the calculated frequency separation measured for a pump power of 350 mW (dashed line).



**Figure 4** – (a) Measured OPG spectrum (350 mW pump power) (dashed line, gray area) and measured idler power (300 mW pump power, 5 mW seed power) at the output of the PCF for different signal seed wavelengths (red circles) with respective Gaussian fit (red). Depending on the chosen wavelength pair, two excitation frequency bands (lower and upper abscissa) are addressable. (b) OPG spectra for different pump wavelengths and 350 mW pump power.

The accurate way to measure the shape of the gain spectrum is to detect the idler power for different seed wavelengths. As the non-seeded part of the parametric conversion, the idler is obtained without any cw background power. The idler measurement shown in Fig. 4 (a) was done with 300 mW of pump power and a 5 mW seed power. The measured power distribution represents the accessible soft tuning range of the FOPA. Compared to the OPG spectrum mentioned above, the maximum of the curve is shifted due to the different pump power used in both experiments. This observation fits to numerical calculations predicting that the frequency distance between signal and pump decreases by  $180 \text{ cm}^{-1}$  for a 50 mW lower pump power. In good agreement a shift of  $200 \text{ cm}^{-1}$  was measured experimentally.

Furthermore, it has to be noticed that the gain bandwidth remains nearly constant in the pump peak power range of 2.5 kW to 3.5 kW. The behaviour of the measured idler power (red) closely follows the OPG spectrum (gray). The FWHM bandwidth

of both (OPG and seeded idler power) amounts to  $230\text{ cm}^{-1}$ . This tuning range is doubled when signal and idler are used for CARS as signal and idler shift in opposite directions during tuning. The tuning range can be expanded further by tuning the FBG of the fiber pump laser as demonstrated by the OPG spectra shown in Fig. 4(b) exemplarily for three pump wavelengths and a constant pump power of 350 mW. By detuning the FBG from 1038 nm to 1040 nm, the frequency difference between signal and pump decreases from  $1740\text{ cm}^{-1}$  down to  $1590\text{ cm}^{-1}$ . In addition, the FWHM width increases slightly from  $175\text{ cm}^{-1}$  up to  $230\text{ cm}^{-1}$  in good agreement with the theoretical expectations. Not only spectral purity but also pulse peak power

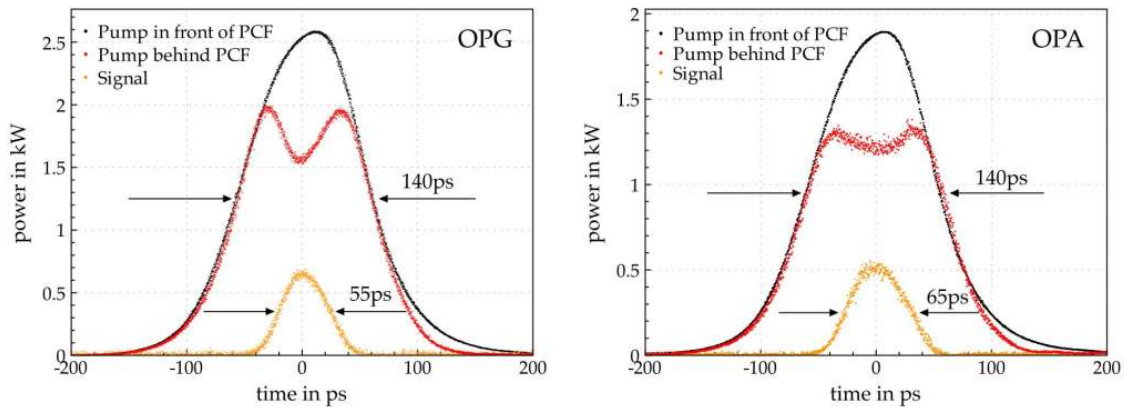


**Figure 5** – OPG: temporal pulse shape of DFWM pump (black, red) and signal (orange) in case of optical parametric generation (no seed). OPA: temporal pulse shape of DFWM pump (black, red) and signal (orange) in case of optical parametric amplification of a 5 mW cw seed signal.

is important to excite nonlinear processes such as CARS. Thus, a measurement of the temporal pulse shape is mandatory. For both cases - absence (OPG) and presence of a 5 mW seed signal (OPA) - the temporal pulse traces were measured with a 18 ps response time photodiode and a 70 GHz sampling oscilloscope. For both measurements the pump power was chosen to achieve the same signal average power of 33 mW. As can be seen in Fig. 5, less pump peak power is needed in the seeded case to reach the same signal power level as in the unseeded case. The measured pulse widths are very similar with 55 ps (OPG case) and 65 ps (OPA case). The difference of the inverse group velocity between signal and pump is numerically calculated to

be 2.3 ps/m and between signal and idler to be just 0.8 ps/m. Hence, the usage of a few tens of picoseconds long pulses and short fiber length leads to an automatic temporal overlap of all three colors out of one fiber end, as demonstrated before in [10]. In addition, such long pulse widths are beneficial in terms of application with standard microscope optical lenses and filters due to a relatively small group velocity mismatch in glass (lower than 10 ps/m for both possible wavelength combinations).

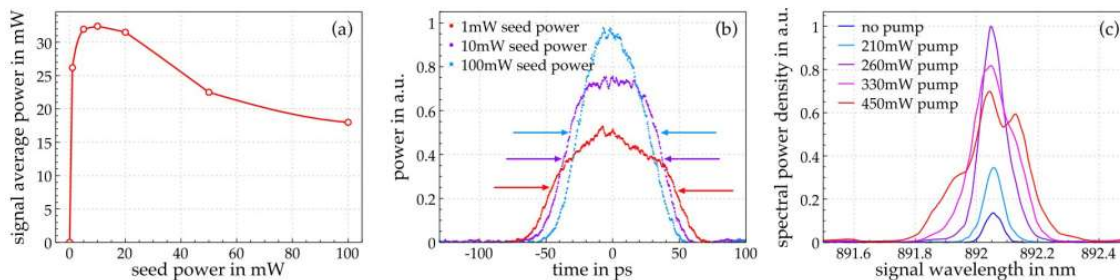


**Figure 6** – (a) Power of the amplified signal (cw background subtracted) over incident seed power. (b) Development of the temporal signal pulse shape with increasing seed. (c) Development of the signal output spectrum with increasing pump power and constant 5 mW seed power.

With the measured signal pulse width, the peak power of the FOPA signal output can be estimated to be 530 W. This corresponds to an amplification of 50 dB in peak power. Furthermore 28% of pump peak power could be converted into the signal. Besides the ease of use of the presented FOPA system, the seed power is one critical parameter that the user has always to take care of. Due to saturation effects, increasing the seed power will not lead in every case to a higher energy of the signal pulses. Figure 6 (a) shows the development of the amplified net signal average power as a function of the incident seed power. As can be seen, DFWM gets saturated already for a few milliwatts of seed power. Any further increase of the seed power leads only to a drop of the signal output power due to saturation effects. Furthermore, a degradation of the temporal pulse shape with increasing seed power (see Fig. 6 (b)) could be observed. Simulations show that back conversion in the most intense regions of the pulse is one reason for the pulse deformation. This results not only in a broadening of the pulses but also in a significant loss in peak power.

Consequently, tuning the seed power above the saturation limit is not an option for up-scaling the signal peak power. Only by keeping the input seed power below this limit, the peak power of Gaussian-like signal pulses increases with higher input seed as expected. To raise the saturation threshold, the pump power can be increased. Doing so one has to be aware of a further spectral broadening of all three wavelengths due to stronger self- and cross-phase-modulation effects as exemplarily shown in Fig. 6 (c) for the signal. A possibility to avoid further spectral broadening while up-scaling the signal peak power is to use a shorter PCF together with higher pump powers.

## Application of the FOPA system to CARS spectroscopy and imaging

We could show previously that the FOPA provides a self-synchronized, very narrowband three-color output with peak powers of at least several hundred Watts. This performance is perfectly suited for CARS applications. Especially, doing CARS spectroscopy provides the possibility to probe the actual spectral resolution and the tunability of the system. Accordingly we applied the FOPA to a mixture of n-hexane ( $C_6H_{14}$ ) and toluene ( $C_7H_8$ ) by focusing the collimated output into a cuvette containing both liquids. The beam is filtered previously to exclude any parasitic, non-phase-matched FWM between all three generated wavelengths in the PCF. This spurious signal would induce a broad CARS background in the sample, which would deteriorate the spectral characteristics of the resonance and therefore it has to be avoided. A second filter selects two of the three DFWM output wavelengths. Thus the CARS pump, which is always the DFWM signal (893–913 nm), excites, together with one of the filtered Stokes wavelength (DFWM pump at 1039 nm or the DFWM idler at 1205–1242 nm), molecular vibrational modes in the sample. Behind the glass cuvette the generated CARS signal is filtered out of all other spectral components and it is measured with a multimode fiber connected to an digital spectroscope.

The CARS spectrum for different excitation frequencies was integrated and asso-

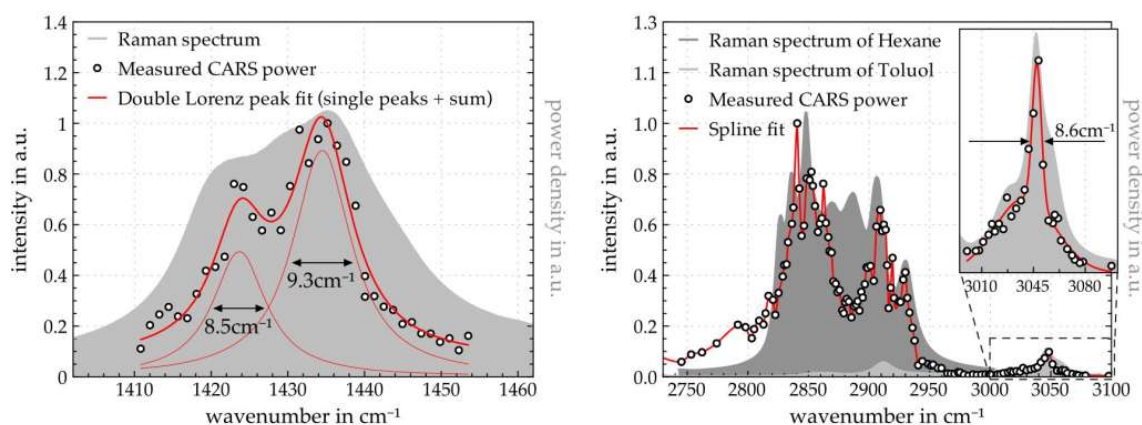


**Figure 7** – Raman and CARS intensity of a mixture of n-hexane and toluene as a function of the wavenumber. The left panel displays the deformation vibration spectrum around  $1430\text{ cm}^{-1}$  belonging to n-hexane, whereas the right one corresponds to the CH stretching around  $2900\text{ cm}^{-1}$ . All curves are normalised to their maxima.

ciated with the corresponding excitation wavenumber calculated from the CARS pump and Stokes wavelengths. This leads to a spectral distribution reflecting the Raman response of the sample. The tuning could be realized within the fingerprint region  $1325\text{ cm}^{-1} - 1580\text{ cm}^{-1}$  and the CH stretching regime  $2670\text{ cm}^{-1} - 3160\text{ cm}^{-1}$ , respectively, while keeping the pump wavelength constant at  $1039\text{ nm}$ . The seed power was adjusted to keep the excitation power constant during the scan. To this end, for every wavelength setting, the CARS pump and Stokes power as well as their spectral widths were monitored to ensure constant excitation conditions. Thus the FOPA is able to provide  $255\text{ cm}^{-1}$  of tuning bandwidth for the first region, without wavelength tuning of the fiber laser, and  $490\text{ cm}^{-1}$  in the second one.

Figure 7 shows the spectral CARS power distribution within selected parts of both interesting frequency regions. Whereas Fig. 7(b) pictures a wide wavelength scan range over the CH stretching resonances of toluene and hexane, Fig. 7(a) details the CH deformation vibration of hexane. In both regions high resolution Raman spectra are displayed for comparison. These are shifted a few tens of wavenumbers to lower frequencies. Although a direct comparison of CARS lineshapes with pure Raman spectra is only hardly possible due to the complex single-resonance distribution of the CARS signal, it is obvious that the spectral CARS distribution fits roughly to

the Raman measurements. Furthermore, with the aid of Fig. 7 (a) or the inset of Fig. 7 (b), it is possible to see that the system is able to resolve single resonances with bandwidths lower than  $10\text{ cm}^{-1}$ . This demonstrates the high spectral resolution of the presented FOPA system.

For image acquisition the laser was coupled into a home-built laser scanning microscope shown schematically in Fig. 8. The collimated beam is focused onto the sample using a NIR corrected microscope objective with a numerical aperture of 0.4 (Plan Apo NIR, Mitutoyo, Japan). The sample is imaged by raster scanning the laser focus across the sample by a galvanometric mirror. The CARS pump and Stokes wavelengths are filtered in a similar way as described for the spectroscopy experiments above. The power at the sample was kept low (30 mW) in order to avoid photodamage. However, the peak power of signal, residual pump and idler pulses is sufficiently high to generate besides CARS also second harmonic generation (SHG) and two photon excited fluorescence (TPEF) signals in tissue. The light emitted in forward direction was recollimated and separated from the incident laser light using two short pass filters. For detection of the SHG and TPEF signals an additional short pass filter with a cut-off wavelength of 600 nm was used. The CARS and SHG signals were then detected by a photomultiplier tube.

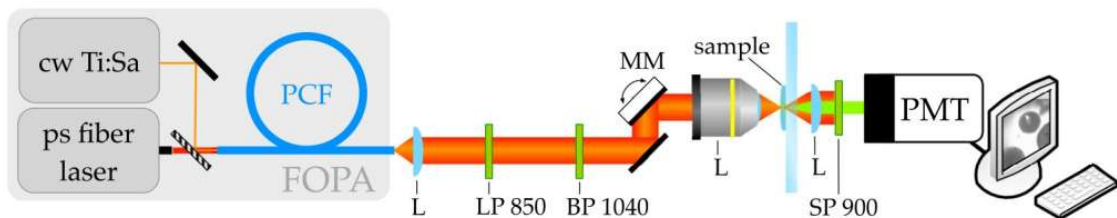


**Figure 8** – Schematic setup of the CARS microscope. L: achromatic lenses, LP: long pass filter at 850 nm, BP: band pass filter at 1040 nm, SP: short pass filter at 900 nm, MM: moveable xy-scanning mirror, PMT: photo multiplier tube.

For a microscopic image two frames of size  $2048 \times 2048$  pixels were averaged with a pixel dwell time of  $1\ \mu\text{s}$ . The system provides diffraction limited spatial resolution which results in a lateral resolution of  $1\ \mu\text{m}$ . The presented light source is, due to its small footprint and compact and robust design, potentially suited for imple-

mentation into biomedical instruments. In order to demonstrate the capabilities of the described light source for simultaneous SHG, TPEF and spectrally highly resolved CARS imaging, a human arterial wall with atherosclerotic plaque deposition has been subsequently imaged. The excitation frequencies were chosen to excite the symmetric aliphatic methylene stretching vibration at  $2845\text{ cm}^{-1}$  and the methyl stretching vibration at  $2930\text{ cm}^{-1}$ , in order to visualize the protein and lipid distribution.

The results of investigating the protein and lipid distribution at the inner arterial wall are displayed in Fig. 9. In panel (a) the combined SHG, TPEF and CARS signals are displayed simultaneously showing the lipid and protein distributions, while the separate channels are displayed in panels (b)-(d) on the right: SHG and TPEF (red), CARS  $2850\text{ cm}^{-1}$  (blue) and CARS  $2930\text{ cm}^{-1}$  (green) channels. Imaging at  $2850\text{ cm}^{-1}$  and  $2930\text{ cm}^{-1}$  allows qualitatively distinguishing proteins from lipids, since the ratio of  $CH_2/CH_3$  functional groups is significantly higher in lipids than in proteins. Large lipid clusters are visible, coloured in turquoise due to the combination of intense CARS signals at  $2850\text{ cm}^{-1}$  ( $CH_2$ , blue channel (Fig. 9 (b))) and weaker signals at  $2930\text{ cm}^{-1}$  ( $CH_3$ , green channel (Fig. 9 (c))). The areas of high protein content appear greenish, due to a lower  $CH_2/CH_3$  ratio than in lipids. The protein distribution is very similar to the collagen and elastin distribution of the elastic fibers of the inner arterial wall visualized in the SHG and TPEF channel. Thus, these elastic fibers are the major source of the observed CARS protein signal.

The CARS contrast, i.e. the intensity ratio of the CARS signal in resonance to the off resonant signal, determines the detection limit in CARS microscopy and can therefore be used for evaluating the image quality of the CARS light source. In order to demonstrate high CARS image contrast using a light source with high spectral resolution, intensity profiles of vibrationally resonant ( $2850\text{ cm}^{-1}$ ) and off-resonant ( $3000\text{ cm}^{-1}$ ) illuminated images were compared. The position of the profile is indicated in Fig. 10 (right) in case of the image at  $2850\text{ cm}^{-1}$ . For improved visualization of the changing average intensities, the profiles were filtered using a 10 point moving average filter. Only the strongest features - the brightest lipid deposits - are visible in the off-resonant image. Thus, the image contrast is 30 times higher in

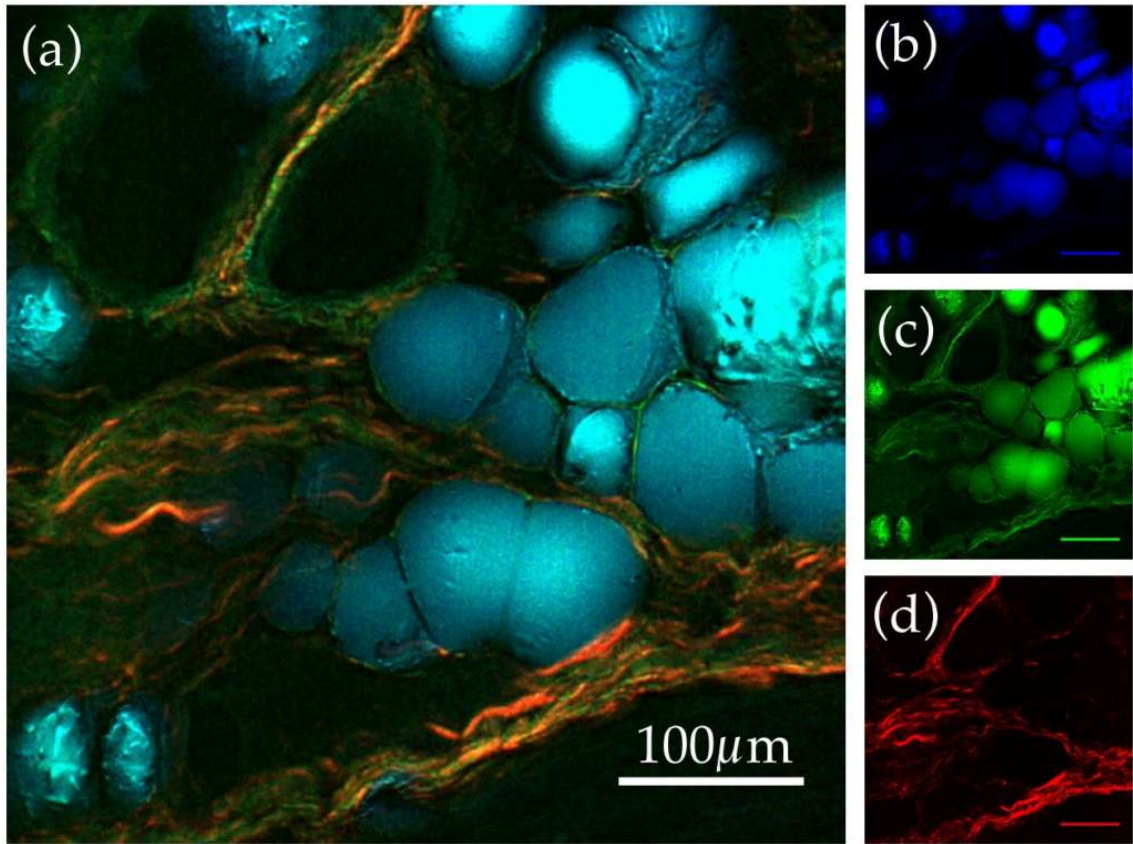


**Figure 9** – Multimodal nonlinear microscopic image of an atherosclerotic plaque deposition at a human artery wall. In panel (a) the combined CARS microscopic images acquired at the aliphatic methylene stretching vibration at  $2845\text{ cm}^{-1}$  (blue) and the methyl stretching vibration at  $2930\text{ cm}^{-1}$  (green) for imaging the lipid and protein distribution are contrasted to the combined TPEF and SHG signal of collagen and elastin (red). Lipids are coloured turquoise due to their high  $CH_2/CH_3$ , while proteins appear greenish. The single channels are separately displayed in panels (b)-(d). The images of the area of  $450 \times 450\ \mu\text{m}^2$  were acquired ( $2048 \times 2048$  pixels) illuminating the sample with 30 mW of laser power.

the resonant case. This improvement has been estimated by calculating the ratio of the difference of the signal peak to the background intensity in the resonant and off resonant image. The high contrast was additionally verified with an off-resonant measurement at  $2740\text{ cm}^{-1}$ . In the presented experiment the image contrast depends primarily on the concentration of the vibrational modes under investigation in contrast to lower spectral resolution light sources according to previous reports [19]. Therefore, no complicated detection schemes are required e.g. frequency modulation



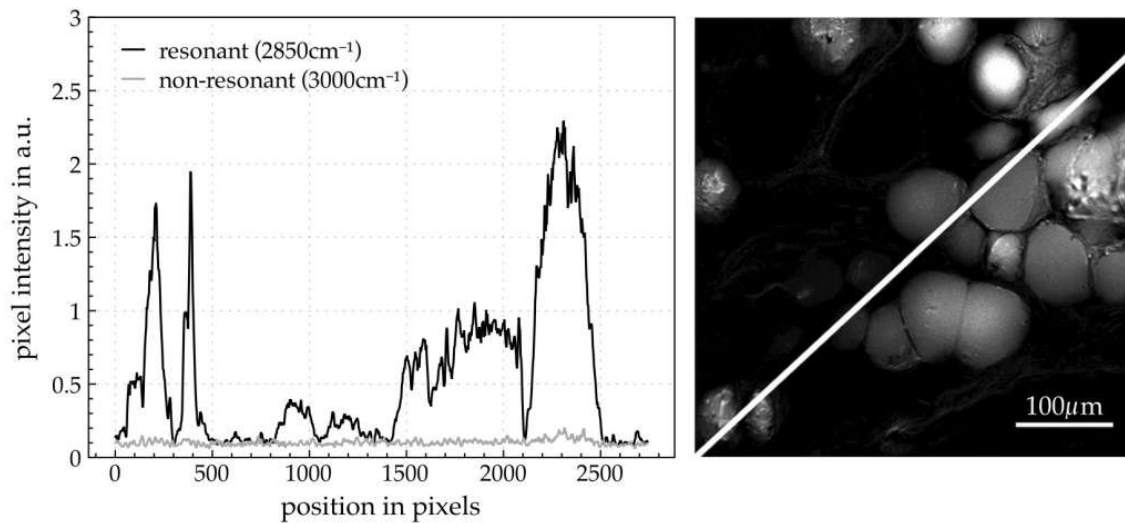


**Figure 10** – Line intensity profiles across the selected region of the sample for vibrationally resonant and off-resonant excitation.

CARS in order to detect molecular species at low concentration.

## Conclusion

In this work we have demonstrated a widely tunable, fiber-based CARS laser source with high spectral resolution. An efficient fiber optical parametric amplifier generates a three-color output (pump, signal, idler) based on four-wave-mixing in a photonic crystal fiber. The nonlinear frequency conversion is pumped by a 1040 nm fiber laser while it is seeded by a wavelength tunable cw Ti:Sapphire system. The whole system is polarisation maintaining and, therefore, fully controllable and reproducible in its output power, wavelength set and polarization. A 5  $\mu\text{m}$ -core PCF provides a several  $100\text{ cm}^{-1}$  broad parametric gain for amplification of the tunable seed. Either combination of the three wavelengths can be used for CARS, resulting in two accessible excitation bands (signal & pump or signal & idler). The use of 140 ps pump pulses leads to an intrinsic temporal overlap of all three generated wavelengths, which simplifies the experimental handling compared to previously presented FOPA systems [16]. Beside its temporal alignment-free output the whole system is

potentially all-fiber and thus prospectively alignment-free, if using a fiber-coupled, tunable, external-cavity diode laser (ECDL) as seed source.

With the chosen fiber and DFWM pump source, CARS generation is theoretically possible for Raman modes between  $1200 - 1900 \text{ cm}^{-1}$  and  $2300 - 3800 \text{ cm}^{-1}$  by hard- (DFWM pump wavelength) and soft-tuning (seed wavelength) touching the fingerprint region and CH stretching molecular modes. Actually both excitation bands could be applied to CARS spectro- and microscopy with one fixed DFWM pump wavelength showing a tuning bandwidth of  $255 \text{ cm}^{-1}$  around  $1450 \text{ cm}^{-1}$  and  $490 \text{ cm}^{-1}$  around  $2915 \text{ cm}^{-1}$ . This spectral region can be further extended by adapting the pump wavelength. Significant resonances of Hexane and Toluene with a bandwidth narrower than  $10 \text{ cm}^{-1}$  could be resolved. With approx.  $1 \text{ cm}^{-1}$ , the actual spectral resolution of the FOPA system is higher than that of typical commercially available picosecond OPO systems (typically  $> 10 \text{ cm}^{-1}$  bandwidth of signal output). Finally, the tuning abilities of the FOPA system could be applied to acquire chemically selective image information based on the CARS excitation of two spectrally separated CH-stretching bonds of both lipids and proteins. Due to the narrow excitation bandwidth the contrast of resonant signal and non-resonant background is as high as 30, which results in high image quality and, moreover, gives the opportunity to resolve even closely neighbouring resonances. The capabilities could be demonstrated by clearly resolving lipids and proteins in an aorta section.

Consequently, the FOPA system demonstrated represents a robust, quasi alignment-free CARS laser source providing a high spectral resolution, tunable three-color wavelength set out of one single fiber end. With this performance, this fiber source directly competes with state-of-the-art OPO systems, while, at the same, it offers a compact size and simplified handling.

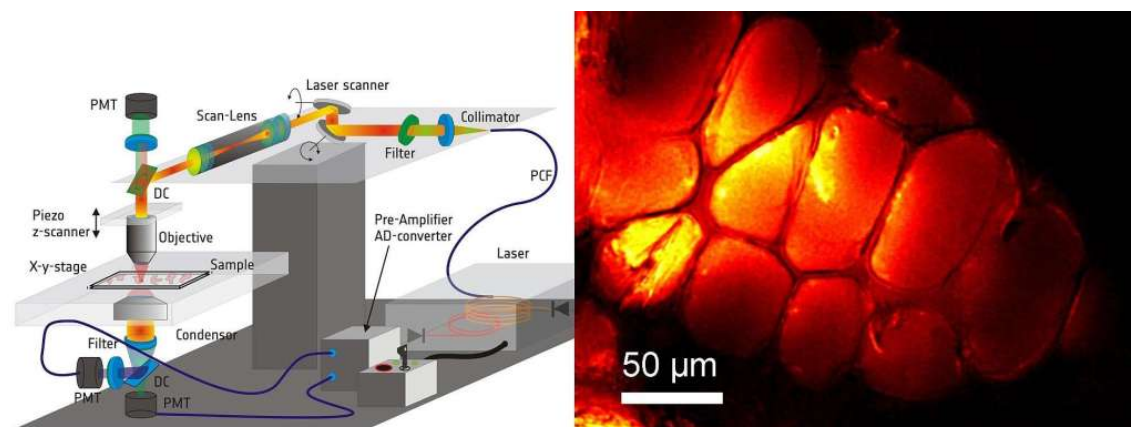
## **Acknowledgments**

This work was supported by the German Federal Ministry of Education and Research (BMBF) contract [13N10773] and [13N10774]; the European Network of Excellence Photonics4Life; and the Carl-Zeiss-Stiftung (M.B.). The authors thank Christian Matthäus for providing the biological samples.

## References

- [1] Saar, B. G., Freudiger, C. W., Reichman, J., Stanley, C. M., Holtom, G. R., and Xie, X. S. *Science* **330**(6009), 1368–1370 (2010).
- [2] Evans, C. L. and Xie, X. S. *Annual Review of Analytical Chemistry (2008)* **1**(1), 883–909 (2008).
- [3] Krafft, C., Dietzek, B., and Popp, J. *The Analyst* **134**(6), 1046–1057 (2009).
- [4] Krauss, G., Hanke, T., Sell, A., Träutlein, D., Leitenstorfer, A., Selm, R., Winterhalder, M., and Zumbusch, A. *Optics Letters* **34**(18), 2847–2849 (2009).
- [5] Selm, R., Winterhalder, M., Zumbusch, A., Krauss, G., Hanke, T., Sell, A., and Leitenstorfer, A. *Optics Letters* **35**(19), 3282–3284 (2010).
- [6] Gottschall, T., Baumgartl, M., Sagnier, A., Rothhardt, J., Jauregui, C., Limpert, J., and Tünnermann, A. *Optics Express* **20**(11), 12004 (2012).
- [7] Marangoni, M., Gambetta, A., Manzoni, C., Kumar, V., Ramponi, R., and Cerullo, G. *Optics Letters* **34**(21), 3262–3264 November (2009).
- [8] Wadsworth, W. J., Joly, N., Knight, J. C., Birks, T. A., Biancalana, F., and Russell, P. S. J. *Optics Express* **12**(2), 299 (2004).
- [9] Nodop, D., Jauregui, C., Schimpf, D., Limpert, J., and Tünnermann, A. *Optics Letters* **34**(22), 3499 November (2009).
- [10] Baumgartl, M., Chemnitz, M., Jauregui, C., Meyer, T., Dietzek, B., Popp, J., Limpert, J., and Tünnermann, A. *Optics Express* **20**(4), 4484–4493 (2012).
- [11] Baumgartl, M., Gottschall, T., Abreu-Afonso, J., Diez, A., Meyer, T., Dietzek, B., Rothhardt, J., Popp, J., Limpert, J., and Tünnermann, A. *Optics Express* **20**(21010-21018) (2012).
- [12] Agrawal, G. P. In *Nonlinear Science at the Dawn of the 21st Century*, Christiansen, P. L., Sørensen, M. P., and Scott, A. C., editors, number 542 in *Lecture Notes in Physics*, 195–211. Springer Berlin Heidelberg (2000).
- [13] Boyd, R. W. *Nonlinear Optics*. Academic, (2008).
- [14] Hädrich, S., Gottschall, T., Rothhardt, J., Limpert, J., and Tünnermann, A. *Optics Express* **18**(3), 3158–3167 (2010).
- [15] Mosley, P. J., Bateman, S. A., Lavoute, L., and Wadsworth, W. J. *Optics Express* **19**(25), 25337 November (2011).
- [16] Lefrancois, S., Fu, D., Holtom, G. R., Kong, L., Wadsworth, W. J., Schneider, P., Herda, R., Zach, A., Sunney Xie, X., and Wise, F. W. *Optics Letters* **37**(10), 1652–1654 (2012).
- [17] Ball, G. A. and Morey, W. W. *Optics Letters* **19**(23), 1979–1981 (1994).
- [18] Steel, D. G., Lind, R. C., Lam, J. F., and Giuliano, C. R. *Applied Physics Letters* **35**(5), 376–379 September (1979).
- [19] Bergner, G., Chatzipapadopoulos, S., Akimov, D., Dietzek, B., Malsch, D., Henkel, T., Schlücker, S., and Popp, J. *Small* **5**(24), 2816–2818 (2009).





Adapted with kind permission from The Royal Society of Chemistry:

**Authors:** Tobias Meyer, Martin Baumgartl, Thomas Gottschall, Torbjörn Pascher, Andreas Wuttig, Christian Matthäus, Bernd F. M. Romeike, Bernhard R. Brehm, Jens Limpert, Andreas Tünnermann, Orlando Guntinas-Lichius, Benjamin Dietzek, Michael Schmitt, and Jürgen Popp.

**Titel:** "Compact microscope setup for multimodal nonlinear imaging in clinics and application to disease diagnostics."

**Journal:** *Analyst*, 138(14):4048–4057, 2013.

©Copyright 2013 The Royal Society of Chemistry (RSC).

Reproduced with permission.

The original article has been published at <http://www.rsc.org>.



11 | Compact Microscope Setup for  
Multimodal Nonlinear Imaging  
in Clinics and Application to Di-  
sease Diagnostics

**Tobias Meyer,<sup>1</sup> Martin Baumgartl,<sup>2</sup> Thomas Gottschall,<sup>2</sup> Torbjörn Pascher,<sup>3</sup> Andreas Wuttig,<sup>1</sup> Christian Matthäus,<sup>1</sup>, Bernd F. M. Romeike,<sup>4</sup> Bernhard R. Brehm,<sup>5</sup> Jens Limpert,<sup>2</sup> Andreas Tünnermann,<sup>2,6</sup> Orlando Guntinas-Lichius,<sup>7</sup> Benjamin Dietzek,<sup>1,8</sup> Michael Schmitt,<sup>8</sup> and Jürgen Popp<sup>1,8\*</sup>**

<sup>1</sup> Institute of Photonic Technology e.V., Albert-Einstein-Strasse 9, 07745 Jena, Germany

<sup>2</sup> Institute of Applied Physics and Abbe Center of Photonics, Friedrich-Schiller-University Jena, Albert-Einstein-Str. 15, 07745 Jena, Germany.

<sup>3</sup> Pascher Instruments AB, Stora Rabybyaväg 24, 22478 Lund, Sweden and Department of Chemical Physics Lund University, Kemencentrum, Getingevägen 60, 22241 Lund, Sweden.

<sup>4</sup> Institute of Pathology, Department of Neuropathology, Jena University Hospital, Erlanger Allee 101, 07740 Jena, Germany.

<sup>5</sup> Catholic Clinic – Koblenz, Internal Medicine & Cardiology, Rudolf Virchow Str. 9, 56073 Koblenz, Germany.

<sup>6</sup> Fraunhofer Institute for Applied Optics and Precision Engineering, Albert-Einstein-Str. 7, 07745 Jena, Germany.

<sup>7</sup> Department of Otorhinolaryngology, University Hospital, Lessingstr. 2, 07743 Jena, Germany.

<sup>8</sup> Institute of Physical Chemistry and Abbe Center of Photonics, Friedrich-Schiller-University Jena, Helmholtzweg 4, 07743 Jena, Germany

\* corresponding author: juergen.popp@ipht-jena.de



## **Abstract**

The past years have seen an increasing interest in nonlinear optical microscopic imaging approaches for the investigation of diseases due to the method's unique capabilities of deep tissue penetration, 3D sectioning and molecular contrast. Application in clinical routine diagnostics, however, is hampered by large and costly equipment requiring trained staff and regular maintenance, hence not yet matured to a reliable tool for application in clinics. In this contribution implementing a novel compact fiber laser system into a tailored designed laser scanning microscope results in a small footprint easy to use multimodal imaging platform enabling simultaneously highly efficient generation and acquisition of second harmonic generation (SHG), two photon excited fluorescence (TPEF) as well as coherent anti-Stokes Raman scattering (CARS) signals with optimized CARS contrast for lipid imaging for label-free investigation of tissue samples. The instrument combining laser source and microscope features a unique combination of highest NIR transmission, four-fold enlarged field of view suited for investigating large tissue specimen. Despite its small size and turnkey operation rendering daily alignment dispensable the system provides highest flexibility, imaging speeds of 1 Mpixel per second and diffraction limited spatial resolution. This is illustrated by imaging samples of squamous cell carcinoma of head and neck (HNSCC) and atherosclerosis allowing for a complete characterization of the tissue composition and morphology, i.e. the tissue's morphochemistry. Highly valuable information for clinical diagnostics, e.g. monitoring the disease progression on a cellular level with molecular specificity, can be retrieved. Future combination with microscopic probes for in vivo imaging or even implementation in endoscopes will allow for in vivo grading of HNSCC and characterization of plaque deposits towards the detection of high risk plaques.

## Introduction

Multimodal nonlinear microscopy combining the effects of second harmonic generation SHG, two photon excited fluorescence TPEF and coherent anti-Stokes Raman scattering CARS for label-free imaging of native tissue has gained much interest during the past years as a versatile imaging tool in fundamental research on diseases [1, 2, 3, 4]. This is due to the unique set of properties in comparison to established biomedical visualization methods like e.g. MRI, ultrasound and X-ray tomography, which render multimodal nonlinear imaging particularly powerful for disease diagnostics. Nonlinear microscopy utilizing near infrared NIR laser wavelengths provides label-free molecule specific image contrast combined with diffraction limited spatial, i.e. lateral and axial resolution accessing depths of up to 1 mm in scattering tissue [5, 6] with video rate image acquisition [7]. It has been demonstrated for a wide range of clinical patterns, that similar information about the tissue morphology and composition is accessible by SHG/TPEF/CARS multimodal imaging as compared to the golden standard of *ex vivo* histopathology using multiple staining agents and immunohistochemical markers, e.g. for brain tumors [8, 9, 10], colon [11] and skin cancer [12]. CARS microscopy is particularly useful for investigating diseases associated with the lipid metabolism [13]. The most prominent diseases related to lipid biology are cardiovascular diseases (CVD). CVD account for more than 40% of deceases in Germany [14] constituting the leading cause of death worldwide. Atherosclerosis is the most prevalent among the manifold manifestations of cardiovascular diseases. Though disease progression is influenced by many risk factors and abundance increases with age, in particular in case of atherosclerosis the disease development is initiated as early as in the second or third decade of life [15] and therefore there is sufficient time for treatment to mitigate the etiopathology. However, to do so early recognition in absence of unambiguous symptoms is required. Atherosclerosis is a chronic disease of the arteries resulting in deposition of lipid plaques at the vessel wall. Therefore early diagnosis when the plaque burden is still low is very important to abort the disease. But the visualization of lipid deposits within arteries alone is insufficient, since the pathological behaviour of a plaque is not only depending on its

size but more importantly on its molecular composition [16]. Hence, imaging tools providing insight into the plaque's morphology and its chemical composition are required, ideally allowing for a non-invasive or minimal invasive routine screening of patients. Vulnerable plaques, i.e. plaques of high risk to rupture, are characterized by large lipid cores, thin fibrous caps and surrounding inflammatory cell infiltrates [15, 16]. These structures serving as disease markers can be visualized by nonlinear imaging combining SHG, TPEF and CARS. SHG is particularly sensitive to collagen fibers and cholesterol [17, 18, 19], whereas TPEF visualizes the distribution of autofluorescing protein fibers, e.g. collagen and elastin, in the vessel wall [20, 21] and oxidized fatty acids within the plaques [22]. CARS is capable of determining the spatial distribution of in principle any Raman active molecule by exciting characteristic vibrational resonances. However, CARS is mostly used to visualize the lipid distribution at  $2850\text{ cm}^{-1}$  corresponding to the symmetric C-H-stretch vibration of methylene groups [23], which are not a unique structural characteristic of lipids, but in contrast to other major biomolecules highly abundant in lipids. Though the prospects of multimodal nonlinear imaging as a clinical imaging tool are recognized for investigating multiple disease patterns, e.g. cancer [3, 8, 9, 10, 11, 12] and lipid metabolism related diseases [13] as atherosclerosis [24, 25, 26, 27, 28], the widespread application is limited to fundamental research and has not yet spread to clinical routine diagnostics due to instrumental complexity of the apparatus. The state of the art multimodal imaging platform [20, 29, 30] is based on a commercial laser scanning microscope utilizing a two colour tunable ultrafast laser, which can be either of typically 80 MHz repetition rate combined with an optical parametric oscillator (OPO): The OPO generates by frequency conversion the second tunable laser wavelength required for CARS imaging. Hence, multimodal imaging platforms require large laser systems and sophisticated microscopes controlled by complex data acquisition hard- and software. Therefore, apart from high costs, instrument handling is difficult and requires trained staff for maintenance. In addition subtle changes in the environment, e.g. temperature or humidity, may require realignment of the setup. Thus the currently available equipment is not compatible with routine application in clinics, e.g. at the patient's bedside or in an operation theatre. Furthermore for 80

MHz laser systems there is a clear discrepancy between high spectral resolution requiring ps-lasers in case of CARS and high peak power optimal for SHG and TPEF imaging requiring fs-lasers [24, 30]. Hence either SHG and TPEF excitation efficiency is sacrificed by using ps-lasers [25], the spectral resolution of CARS is reduced by using fs lasers [30] or the instrument complexity and image acquisition time are significantly increased by subsequently using fs and ps lasers for efficiently exciting TPEF, SHG and CARS signals [24].

Most promising in order to reduce instrument size and alignment requirements appear fiber laser based approaches for generating multicolour laser beams. Here several concepts for in fiber frequency conversion have been introduced: supercontinuum generation [26, 31], soliton self frequency shift [32, 33] and four wave mixing [34]. However, supercontinuum generation results in spectrally broadband emission but low spectral power density requiring additional filtering for single band CARS. Soliton self frequency shift on the other hand generates red shifted radiation but requires short pulses. Compatible with high spectral resolution and long pulse duration, which simplifies alignment of the temporal pulse overlap, is only the four wave mixing process, which further allows for wavelength tuning by either tuning the pump wavelength or by seeding the FWM process which in addition increases the spectral resolution [34, 35]. Just recently novel all-fiber laser sources have been developed and successfully applied to multimodal nonlinear microscopy [36, 37, 38] generating synchronized laser radiation in a photonic crystal fiber by four wave mixing (FWM), however only proof of principle of operation has been so far demonstrated.

In this contribution a novel compact setup for multimodal nonlinear imaging is presented suited for clinical diagnostics. The system features a fourfold enlarged field of view along with highest NIR transmission of 60% from the laser onto the specimen, which enables using alignment-free ultracompact low power multi-colour fiber lasers. However, the instrument's performance in terms of imaging speed, image contrast and spatial resolution is despite the reduced size comparable to commercially available laser scanning microscopes in combination with solid state lasers. This system is suited to investigate a variety of disease patterns, in particular the most prevalent which are cardio vascular diseases and cancer. In order to demonstrate

the instruments' capabilities for biomedical imaging *ex vivo* samples of an animal model of atherosclerosis, of human perivascular tissue as well as a specimen of a carcinoma of the oropharynx have been investigated and the results are presented in the following. Due to the instruments compactness, simplicity and high image quality the microscopic platform represents a significant step towards establishing nonlinear multimodal imaging in clinical settings, hence application of this device to routine clinical imaging as a diagnostics tool is anticipated in the near future while further technological research will focus towards multimodal endoscopy.

## Materials and Methods

A schematic sketch of the compact microscope setup for multimodal nonlinear imaging is displayed in figure 1 panel A, while photographs of the setup shown in panels B through E provide a realistic impression of the system's size.

### 1. NIR fiber laser

A key element for constructing a small size and portable nonlinear microscope is the application of an ultracompact and portable laser light source. The multicolour fiber laser used is a customized design for CARS, TPEF and SHG microscopy based on an amplified ytterbium fiber laser of 1.9 MHz repetition rate and 51 ps pulse duration [37] spliced to a photonic crystal fiber PCF similar to the designs previously reported [36, 38]. Such a fiber laser is shown in panel E of figure 1 (activefiber systems, Germany). The PCF has been chosen such that the frequency difference between the FWM signal wavelength and the fundamental pump wavelength corresponds to the vibrational frequency of the symmetric C-H-stretching vibration of methylene groups, i.e.  $2850\text{ cm}^{-1}$ . For CARS both the FWM signal and ytterbium fundamental pulses have been used for imaging, while for SHG and TPEF excitation the ytterbium fundamental wavelength at 1032 nm has been used. The signal pulse train used as CARS pump is centred at 797 nm. The pulse duration is 19 ps providing a spectral width of  $40\text{ cm}^{-1}$  full width at half maximum (FWHM) and a power of 25 mW. The Ytterbium pump laser used as Stokes beam in the CARS process is

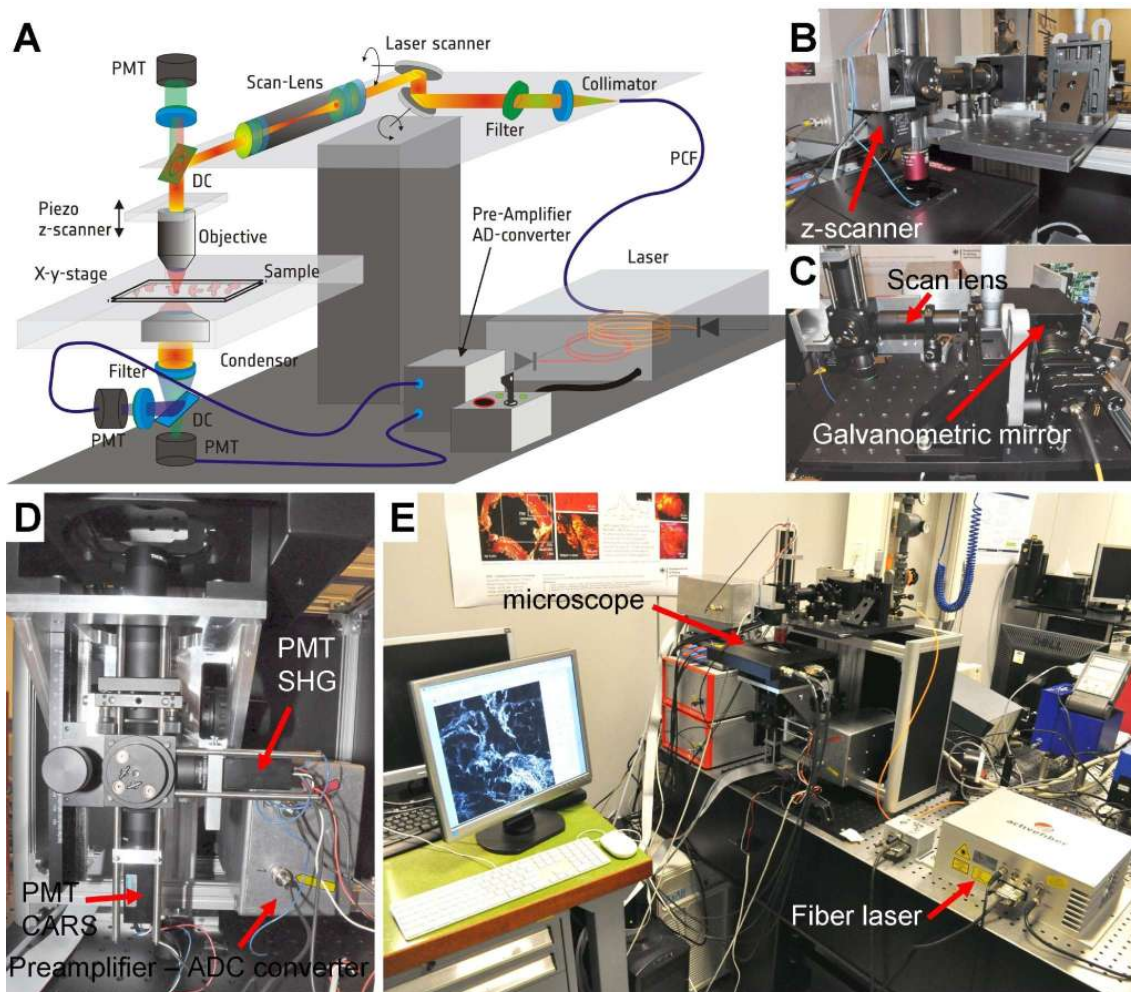


**Figure 1** – Schematic sketch of the complete nonlinear microscope (panel A) and photographs of the experimental setup (panels B – E). The footprint of the microscope is 60 cm × 45 cm enabling assembly also in areas with limited space. The illumination part of the microscope and the epidetection path are imaged in panels B and C. In panel D the optics and PMT detectors in forward direction are displayed. The box on the right contains the preamplifier and analogue to digital converter for processing the signals from the PMT detectors. The overview image in panel E shows the computer for system control, the laser and the microscope.

spectrally located at 1032 nm, providing more than 100 mW power and a spectral width of 6 cm<sup>-1</sup> FWHM, which is attenuated to 20 mW for imaging. The wavelength set of this laser is furthermore within the optimal window for tissue imaging, minimizing losses due to scattering and absorption, i.e. between the lowest electronic

absorption of haemoglobin and the highest vibrational absorption bands of water. This wavelength region spans the range from 750 nm to 1500 nm. For imaging at maximum 30 mW of pump and Stokes power were focused onto the sample using a  $20 \times$  NA 0.4 objective.

## 2. Compact nonlinear laser scanning microscope

The microscope design has been optimized to realize high optical throughput, hence the number of optical elements is minimized without affecting the optical performance, i.e. diffraction limited spatial resolution. In comparison to commercial laser scanning microscopes as used in alternative multimodal microscopes [8, 9], the optical layout of the microscope as displayed in figure 2 panel A provides a fourfold increased field of view for SHG/TPEF/CARS microscopy of large tissue samples by designing a short focal distance scan lens of only 70 mm featuring achromatic correction from 750 to 1100 nm and minimized reflection up to 1550 nm. A NIR transmission of the illumination beam path of 60% from the laser onto the specimen is realized, which is larger than the NIR transmission of alternative CARS imaging platforms providing NIR transmission ranging from 10% [39] to 40% [40]. This configuration enables using relatively low power but ultra compact, robust and maintenance free fiber lasers described in the preceding section. Since nonlinear imaging methods provide 3D sectioning, no confocal microscope design is required. The instrument is described in detail in the supplementary material. For the separation of the nonlinear signals from residual laser light in forward direction two short pass filters are used (SP770 and SP750, Semrock, USA). The forward emitted SHG and CARS signals are split by a longpass dichroic mirror (LP605, 24 mm  $\times$  36 mm, Thorlabs, USA), filtered by appropriate bandpass filters (CARS: bandpass 650/40 Thorlabs, SHG: bandpass 400/40 or 514/10, Thorlabs, USA) before being detected by PMT modules Hamamatsu, Japan. TPEF or alternatively backward scattered CARS/SHG signals are detected in epi-direction. In order to optimize the detection efficiency of the low intensity signals, the distance between sample and detectors is minimized in order to improve the collection of multiply scattered photons. The whole system is schematically depicted in figure 1 panel A, while panels B-E show

photographs of parts of the system. The arrangement of the optical elements is illustrated in figure 2 panel A.

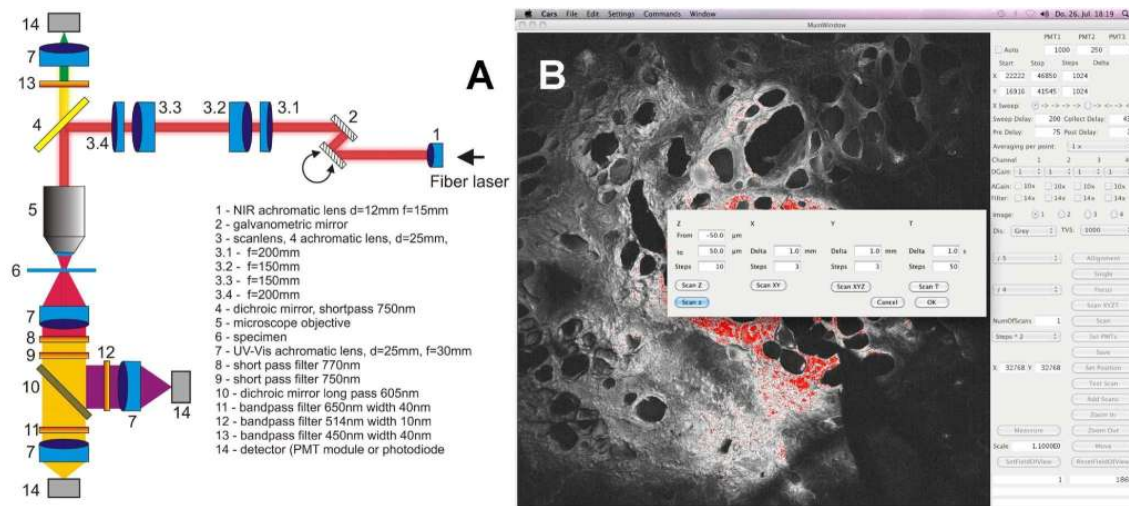


**Figure 2** – Panel A: scheme of the optical layout of the multimodal nonlinear microscope for simultaneous detection of SHG, TPEF and CARS signals. Manufacturers of the optical components: 1, 3, 4 – Edmund optics, USA, 7, 11, 12, 13 – Thorlabs, USA; 8, 9 Semrock, USA. Panel B: screen shot of the graphical user interface for controlling the nonlinear microscope. All elements for system control are displayed. When performing a multiple image scan, the menu in the center allows choosing one of 4 options for scanning multiple images, i.e. time series, z-, xy- and xyz-scans.

### 3. Data acquisition hardware & graphical user interface

The data acquisition soft- and hardware has been designed for controlling the galvanometric mirrors, the motorized xy microscope translation stage and the piezo z-focussing stage in addition to synchronized data acquisition of up to four channels simultaneously. The data acquisition system consists of two parts: the first part is a small desktop computer for running the graphical user interface for complete instrument control via USB and storage of the image data and the second device is the data acquisition hardware unit controlling the instrument, designed by T.P., Pascher Instruments AB, Sweden. The menus of the graphical user interface are clearly arranged in order to provide intuitive but complete control of the hardware. A screenshot of the software is displayed in figure 2 panel B.



As indicated in the screenshot shown in figure 2, four options are available: a time series scan for investigating dynamic processes, z-scan for depth resolved imaging of thick samples, xy-scan using the motorized stage for analysing sample areas exceeding the field of view of the scanner and xyz-scans for investigating extended thick specimen.

The key aspect for adaptation of the electronics' hardware of the instrument to nonlinear imaging is to optimize the detection system towards highly efficient and low noise acquisition of low intensity signals. This has been realized by using 16 bit data depth, which allows using the full dynamic range of a PMT module of 3 orders of magnitude in intensity to detect simultaneously weak and bright structures, thus enabling analysing small intensity fluctuations and avoiding loss of information due to analogue to digital conversion. In addition a large set of averaging options, e.g. pixel dwell times up to 256  $\mu s$  and averaging of a specific number of frames as well as additional electronic low pass filtering and pre amplification preceding analogue to digital conversion, have been implemented. The in depth description of the data acquisition hardware design can be found in the supplementary section. The most important parameters of the hardware control unit are summarized in table S 2.

In summary key imaging specifications of the instrument are condensed in table 1.

**Table 1** – Summary of specifications of the multimodal nonlinear microscope

<b>Parameter</b>	<b>Custom built LSM</b>
Field of view 20 ×	$1.2 \times 1.2 \text{ mm}^2$
Scanning speed @ 1024 <sup>2</sup>	2 s
NIR T[%] 800/1000 nm	> 60%
Image size pixels	$128 \times 128 - 4096 \times 4096$
Pixel dwell time	$1 \mu s - 256 \mu s$
Data depth	16 bit

#### 4. Investigated tissue samples

Adult male New Zealand white rabbits Harlan, Borchon, Germany were fed with a 0.5% cholesterol diet to initiate atherosclerotic plaque deposition. The rabbits were sacrificed by an overdose of an anaesthetic solution of ketamine and xylazine. The aortic artery was excised and preserved in 5% formalin solution Oscar Fischer GmbH, Saarbrücken, Germany either for in vitro non-linear imaging or preparation of 5  $\mu\text{m}$  cross sections using a microtome. For preparing thin dried tissue sections no standard embedding medium has been used to avoid signal contributions from the embedding matrix. The cross sections were placed on  $\text{CaF}_2$  slides. For in vitro multi-modal imaging of plaque deposits at the inner arterial wall the blood vessel was cut open, immersed in physiological buffer and sandwiched between two microscope coverslides, thus avoiding denaturation and shrinkage during the measurement. For determining the contrast and as control tissue human tissue was investigated. The specimen was obtained from routine biopsy at the University hospital, Jena, Germany.

The section of a head and neck squamous cell carcinoma (HNSCC) sample was obtained from a biopsy of a patient with a pT3N2bM0 carcinoma of the left tonsil. The biopsy was taken from the primary tumor site and its environment. A cryosection of 20  $\mu\text{m}$  thickness was investigated without further tissue processing. Usage of material from routine biopsies was approved by the ethics committee for human research at the Medical Faculty, Friedrich-Schiller-University Jena, Germany.

#### 5. Image analysis

For image analysis ImageJ [41] has been used.

### Results and Discussion

In comparison to multimodal imaging platforms based on highly integrated commercial laser scanning microscopes in combination with solid state ultrafast lasers [9, 18, 26, 30], the presented homebuilt microscopic setup can be quickly moved and

reinstalled, provides highest NIR transmission of 60%, high flexibility by direct access to all optical and mechanical elements and an enlarged field of view. Due to the custom optical layout of the scan lens the FOV of the homebuilt instrument is four times larger enabling faster investigation of extended tissue specimen as illustrated in figure 3 panel A. Here a CARS image at  $2850\text{ cm}^{-1}$  of an aorta cross section of an animal model for atherosclerosis is displayed. The large white box marks the FOV of this microscope in combination with a  $20\times$  objective, while the small dashed square corresponds to the FOV of a standard commercial laser scanning microscope used in previous multimodal nonlinear imaging investigations [9].

The small footprint allows installation in areas with space constraints. While most laser scanning systems are installed at fixed position on laser tables due to the large ultrafast lasers, the setup here can be disassembled and reconstructed within a few hours. Most commercial laser scanning systems used for nonlinear microscopy are based on confocal instruments initially designed for fluorescence microscopy using visible lasers. This results in limited NIR transmission [39] in comparison to 60% as reported herein and unnecessary complexity of the instrument, e.g. integrated internal descanned confocal detectors. Confocal detection design limits the system to the detection of ballistic signal photons, a with tissue depth exponentially decreasing fraction of all signal photons. The instrument described herein has no confocal design thus reducing the instruments complexity and improving the overall transmission. The lateral and axial resolution is not reduced, since nonlinear microscopy provides intrinsically 3D sectioning with xyz-resolution comparable to confocal microscopy [5, 42].

Another major benefit of the instrument is related to the novel turn-key and small footprint fiber laser light source characterized by low repetition rate and long, i.e. tens of ps, pulse duration. As can be seen in figure 1 panel E the size of the laser is significantly smaller than a conventional laser source for CARS microscopy. The simultaneous emission of the long duration, i.e. tens of ps temporal pulse width, ytterbium fundamental and the FWM signal and idler wavelengths from the same small core fiber end results in perfect spatial and temporal overlap of pump and Stokes wavelengths rendering daily alignment dispensable and is a unique feature of

only this laser concept. In contrast to alternatively used ultrafast solid state laser systems applied to multimodal nonlinear imaging, e.g. either two synchronized oscillators [24, 25], a single oscillator in combination with an optical parametric oscillator (OPO) [30, 43], or single broadband laser sources incorporating free space optics and pulse shapers [44], which require regular adjustment, this laser is designed for maintenance free operation. Also alternative compact fiber laser concepts based on soliton self frequency shift [32, 33], supercontinuum generation [26, 31], four wave mixing [34, 35, 36, 37, 38], a fiber optic parametric oscillator [45] or two synchronized ps fiber lasers [40] still rely on mechanical delay lines and dichroic mirrors to overlap pump and Stokes pulses temporally and spatially, which results in higher sensitivity to environmental changes and regular adjustment in contrast to the fully fiber integrated approach presented here. In particular except from the concept of two synchronized ps fiber lasers [40], all other laser sources are based on much shorter pulses, hence pulse dispersion in the microscope optics results in significant temporal walk off of the pulses, which needs to be corrected for by the mechanical delay and adjusted, when changing the objective. Due to the longer pulse duration of several tens of ps of the laser presented herein [37], the velocity difference between pump and Stokes pulses in the microscope optics results only in a negligible temporal walk off of a small fraction of the pulse length and therefore the temporal pulse overlap is always preserved. This laser characteristic enables to greatly simplify the microscope optics, in particular the number of optical elements can be reduced, and thus is the key to improve the overall NIR transmission as described in the preceding section.

Furthermore, commercial CARS lasers of 80 MHz repetition rate and ps pulse duration excite SHG and TPEF signals less effectively [24, 46]. On the other hand, fs lasers of 80 MHz repetition rate provide efficient SHG and TPEF excitation but come at the cost of a poor spectral resolution of only  $100 \text{ cm}^{-1}$  for CARS imaging [30]. Additionally due to the much shorter pulse duration temporal walk off of the pulses as well as group velocity dispersion significantly complicate the alignment. The peak power of the laser used in this work [37] is the same as for a 500 fs laser systems of 80 MHz repetition rate but provides a spectral resolution better than

40  $\text{cm}^{-1}$  for the pump and below 6  $\text{cm}^{-1}$  for the Stokes wavelength. As previously reported, the spectral resolution can be further increased to 1  $\text{cm}^{-1}$ , when the FWM process is seeded [35] using a continuous wave (cw) laser. Here spectral tuning in the range from 1200 to 3800  $\text{cm}^{-1}$  with a small gap around 2000  $\text{cm}^{-1}$  has been realized, which compares well with alternative tunable fiber lasers [32, 34, 40]. However, in order to minimize the system's complexity, we operate the fiber laser at a fixed spectral position tuned to be in resonance with the aliphatic CH-stretching vibration of methylene groups at 2850  $\text{cm}^{-1}$ .

Another advantage of the presented low MHz repetition rate fiber laser design is to enable simultaneously highly efficient generation of SHG, TPEF and CARS signals, without severely reducing the spectral resolution required for CARS microscopy, while alternative approaches are experimentally more complex, e.g. use either experimentally complex subsequent fs and ps excitation [24], sacrifice SHG and TPEF excitation efficiency by 80 MHz ps laser [25] or CARS spectral resolution by 80 MHz fs excitation [30]. The key parameters to describe the efficiency for the generation of nonlinear signals are the peak power of the laser and the peak intensity at the specimen. These values can be calculated using the laser repetition rate  $k$ , pulse duration  $\tau$ , the average power  $P_{av}$  and the laser spot size in the specimen plane  $A$  or the lateral resolution of the system  $d$ :

$$P_{max} = \frac{P_{av} \cdot t}{k \cdot \tau} \Leftrightarrow I_{max} = \frac{P_{max}}{A} = \frac{4P_{max}}{\pi d^2} \quad (1)$$

An alternative laser for multimodal nonlinear imaging [30] working at similar wavelengths provides 100 fs pulses at 80 MHz repetition rate using 3.1 mW of laser power at the sample for CARS imaging generating a laser spot diameter of 310 nm. This translates according to equation 1 to a peak power of 387 W and a peak intensity in the specimen plane of  $5 \times 10^{15} \text{W}/\text{m}^2$ . The laser used in this contribution provides 20 ps pulses at 1.9 MHz repetition rate using 30 mW at the sample. This results in a peak power of 790 W and a tenfold lower peak intensity of  $5 \times 10^{14} \text{W}/\text{m}^2$  in the specimen plane, while still allowing for image acquisition with pixel dwell time of only 1  $\mu\text{s}$ . This calculation in addition to the high quality nonlinear images presented in figures 3 to 6 prove that this laser source is in terms of imaging performance

at moderate power levels of 30 mW in the specimen plane comparable to alternative laser sources for multimodal nonlinear microscopy, unless higher average powers are required, at the sample e.g. for imaging deeper than 100  $\mu\text{m}$  within scattering tissue. However, the spectral resolution in CARS microscopy is significantly improved in comparison to a 100 fs laser. The laser described herein provides 40  $\text{cm}^{-1}$  spectral resolution in contrast to more than 100  $\text{cm}^{-1}$  for a 100 fs 80 MHz repetition rate laser used by Chen et al. [30]. In addition, further substantial improvement of the spectral resolution to 1  $\text{cm}^{-1}$  for CARS imaging is possible by seeding the FWM process [35].

Since the laser design is completely spliced and uses only polarization-maintaining fiber components [37] it provides unparalleled stability with respect to environmental changes. While the laser parameters differ substantially from alternative laser sources, no photodamage when using average laser power of below 30 mW in the specimen plane have been observed for this low repetition rate laser. Thus, this light source is perfectly suited for the application in clinical settings. In summary this alignment-free turn-key laser source is due to its small footprint, insensitivity to environmental changes and simple operation combined with highly efficient CARS, SHG and TPEF signal generation ideally suited for routine clinical application.

In the following results from imaging samples from a rabbit model for atherosclerosis and human perivascular tissue as well as tissue from an oropharyngeal squamous cell carcinoma is presented to demonstrate the systems capabilities for tissue imaging.

In figure 3 images from an artery tissue of a rabbit fed with a high cholesterol diet to induce atherosclerosis are displayed. In figure 3 panel A a CARS image at the symmetric  $\text{CH}_2$  stretch vibration of 2850  $\text{cm}^{-1}$  for a whole artery cross section is generated by fusing four single CARS images. It can be seen that the plaque deposits are not uniformly distributed at the vessel wall, but the plaque thickness varies across the circumference. In order to investigate areas of different plaque thickness in more detail, high resolution images have been acquired in panels B, C and D as indicated in panel A. These images visualize the curly structure of the elastic fibers of the vessel wall. The composition of the plaque is different in areas of high (figure 3 B) and low lipid deposition (figure 3 C). While the plaque's foam like structure ap-

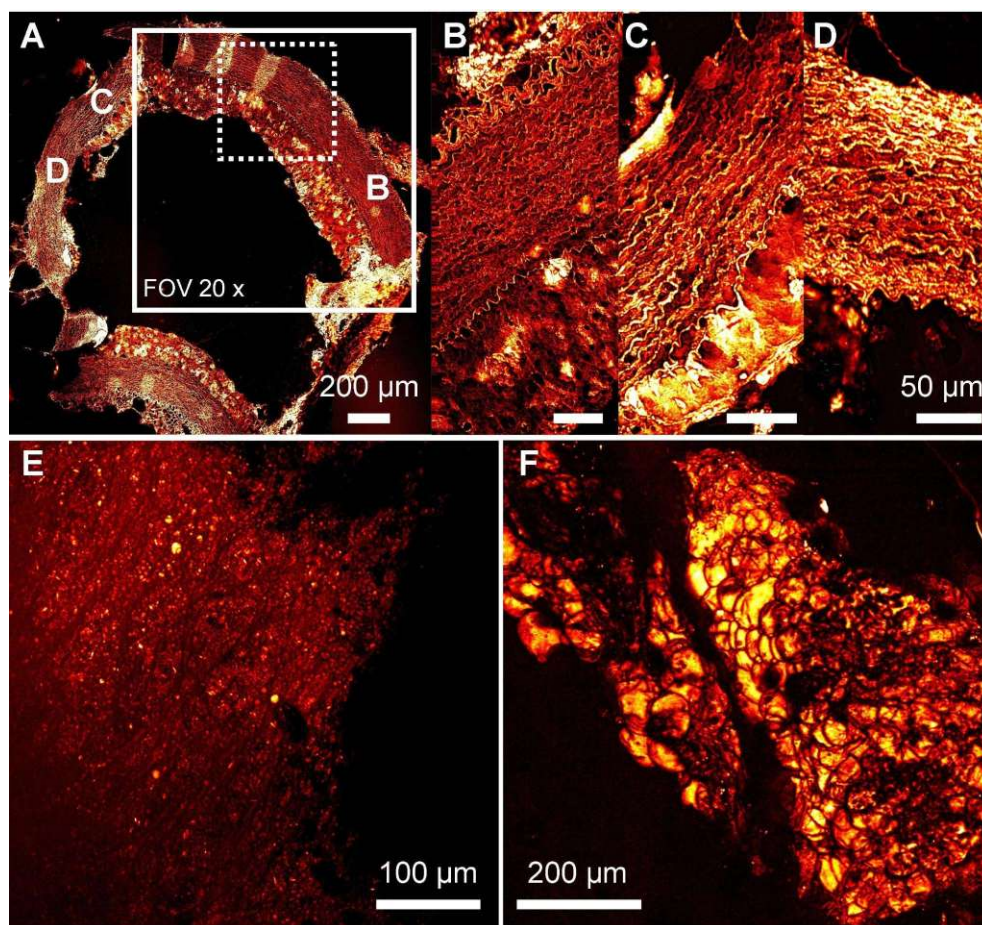


**Figure 3** – CARS imaging of tissue samples from an animal model for atherosclerosis, i.e. a rabbit fed with high cholesterol diet for several weeks. Imaging was performed at the symmetric aliphatic C-H-stretch vibration of methylene groups,  $2850\text{ cm}^{-1}$ . In panel A the large field of view (FOV) of the customized microscope is indicated as a white square, while the small dashed square corresponds to the FOV of a commercial standard laser scanning microscope. Especially for medical use orientation on large specimen is improved due to a larger FOV. For investigating areas of several mm extension, multiple images obtained by xy translation of the sample are fused as in the case of the whole artery cross section, panel A. In panels B, C and D areas of different plaque deposition are displayed as indicated in panel A. The curly elastic protein fiber strands of the arterial wall are clearly visualized, as well as the lipid deposits and its structure at the inner vessel wall. Different brightness indicates, that the plaque composition varies, since the concentration of methylene groups is visualized. In panels E and F the microscope's z-scanning option and deep tissue penetration of the NIR laser are demonstrated by imaging of plaque deposits from the lumen of the artery in buffer solution and detecting the CARS signal through  $500\text{ }\mu\text{m}$  of tissue in forward direction. In panel E an area of low plaque deposition is shown, the depth of this z-projection corresponds to  $40\text{ }\mu\text{m}$ . In panel F a lipid deposit of  $100\text{ }\mu\text{m}$  thickness is displayed.

pears medium intense in an area of high deposition (figure 3 B), the plaque is more uniform in the area of thin deposition and the average CARS intensity is higher, indicating higher lipid content (figure 3 C). To investigate these differences further, axially resolved in vitro imaging of a large aorta specimen with plaque deposits at the inner arterial wall has been performed. Z projections of the lipid deposits at the inner vessel walls in areas of low and high deposition are displayed in figure 3 panels E and F. The CARS signal at  $2850\text{ cm}^{-1}$  corresponding to the symmetric C-H-stretch vibration of methylene groups highlights areas of dense fatty acid deposition. While there are non noticeable lipid deposits at the vessel wall in figure 3 panel E, there is an extended plaque structure exceeding  $100\text{ }\mu\text{m}$  in thickness in figure 3 panel F. To demonstrate the chemical origin of the contrast of the CARS images a sample of human perivascular tissue surrounding an artery has been investigated in resonance with the symmetric C-H-stretch vibration of methylene groups at  $2850\text{ cm}^{-1}$  and off resonance at  $2990\text{ cm}^{-1}$  as displayed in figure 4. In panel A of figure 4 the resonant image is displayed, while the inset corresponds to the off resonant image, which has been multiplied by a factor of 5 in order to visualize the adipose cells more clearly. Panel B2 displays an intensity profile along the white line shown in panel A of figure 4. Panel B1 displays a CARS spectrum of lipids acquired by tuning the frequency difference between the pump and Stokes lasers across the C-H-stretching region. The spectral positions for acquiring resonant and off resonant CARS images and the intensity profiles are indicated and colour coded in the CARS spectrum shown in figure 4 panel B1. As shown in figure 4 panel B2, the image contrast vanishes almost completely, if the difference frequency of the lasers is tuned off resonant. From the ratio of the intensities, the contrast has been calculated to 10. This represents only a lower bound to the Raman resonant contrast, since for low light levels a large background contribution due to noise of the readout circuit is observed. When estimating the readout noise and subtracting this contribution from the signal intensity, the image contrast is in the range of 20, which is a factor of 3 better than for fs light sources for multimodal imaging in the same wavelength range [30] or even a factor of 10 better compared to 2 ps laser system operating in the visible range [47].



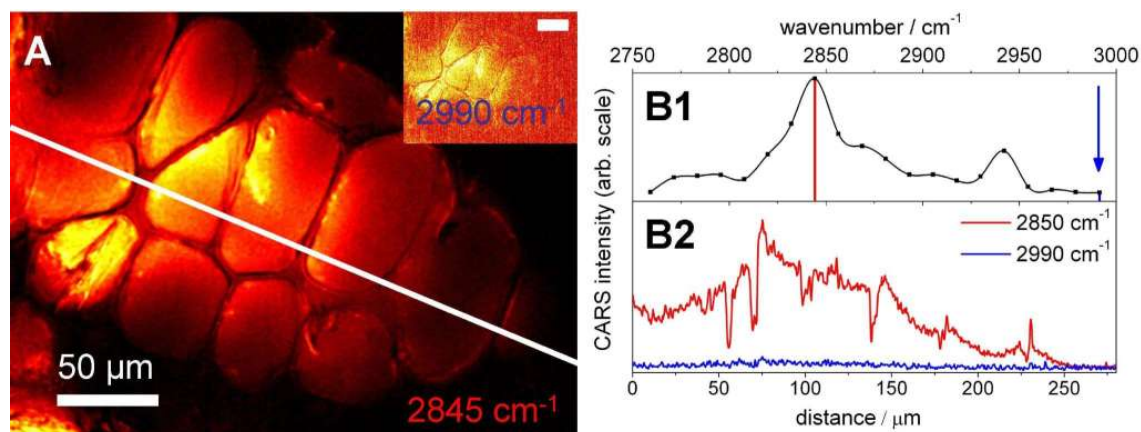


**Figure 4** – The high molecular contrast of CARS at the aliphatic C-H-stretching vibration of methylene groups when using NIR lasers is exemplarily demonstrated for adipocytes and connective tissue surrounding a human artery. In resonance the lipid droplets appear bright, while cytoplasm and membrane of the adipocytes are darker due to lower relative lipid content. The small inset shows the same image at  $2990\text{ cm}^{-1}$ . The intensity is magnified by 5 and the contrast enhanced. In panel B1 a CARS spectrum of lipids is shown and the spectral positions for acquisition of the images in panel A and the intensity profiles of panel B2 are indicated. Panel B2 displays intensity profiles in and off resonant. The contrast is 20 times higher in the resonant case for pure triglycerides, i.e. the lipid droplets in adipocytes.

However, as already mentioned, the strength of the presented setup is based on the ability to not only record CARS images but also simultaneously SHG and TPEF signals. SHG and TPEF signals are very efficiently excited in parallel to CARS, but provide information about the spatial distribution of further tissue components, in particular protein fibers [21, 48], oxidized fatty acids [22] and cholesterol [18]. This multitude of signals therefore provides a detailed morphochemical map of the tissue, which prospectively allows the determination of the type of atherosclerotic plaque and therefore also its risk to rupture, even without surgical excision and labelling of tissue.

In detail TPEF displays the distribution of autofluorophors. In blood vessel walls a prominent source of autofluorescence are elastic fibers composed of the fluorescing proteins elastin and collagen [21]. Within atherosclerotic plaque deposits oxidized lipids are associated with fluorescence [22]. SHG is sensitive to highly ordered structures, which are the proteins myosin and collagen. Myosin is concentrated within the smooth muscle cells, thus especially in the blood vessel wall. Collagen is arranged in

the protein fibers of connective tissue [49]. However, recently also different sources of SHG within lipid deposits have been reported [18], especially cholesterol crystals. Therefore the multimodal combination of these three nonlinear imaging modalities CARS, SHG and TPEF provides manifold information not only on the tissue morphology but also on the chemical composition, comparable to the information content of multiple histological stains, e.g. the elastic van Gieson (EVG) stain for elastic fibers. This is demonstrated in figure 5. In panel A of figure 5 a multimodal image of an artery section of a rabbit fed with a high cholesterol diet is displayed combining SHG blue CARS at  $2850\text{ cm}^{-1}$  red and TPEF green signals to a false colour image. The individual signals are displayed in figure 5 panels B-D. TPEF and SHG signals figure 5 panels C and D are highly co-localized. The SHG and TPEF signals are more intense in the outermost layer, the tunica externa or tunica adventitia, which is composed of connective tissue and thus rich in collagen, which is a source of both autofluorescence and second harmonic signals. CARS at  $2850\text{ cm}^{-1}$  visualizes the morphology of the vessel wall: the fibrous structure of the proteins and the plaque deposits. Interestingly the plaque is not uniformly rich in lipids. The highest signal intensity is visible in the outermost layer. Some bright lipid deposits are also origin of intense SHG and TPEF signals, but not all. Therefore, cholesterol crystals and oxidized low density lipoprotein as sources of SHG and TPEF signals are not uniformly distributed within the plaque. These are interesting findings, since the plaque composition is directly related to the risk of rupture causing an acute life threatening event like a stroke or heart attack.

But possible clinical applications of the compact multimodal nonlinear microscope are not limited to cardiovascular diseases. This is illustrated in figure 6. In panels A-C of figure 6 multimodal images of invasively growing tumor nests of a head and neck squamous cell carcinoma are displayed. The tumor is growing into the connective tissue at an oropharyngeal site. In Figure 6 panel A both the CARS signal at the symmetric CH stretching vibration of methylene groups at  $2850\text{ cm}^{-1}$  and SHG signals of collagen fibers of the connective tissue are displayed, while the single CARS and SHG signals are presented in panels B and C, respectively. In particular the visualization of collagen represents an important marker for diagnosing the transition

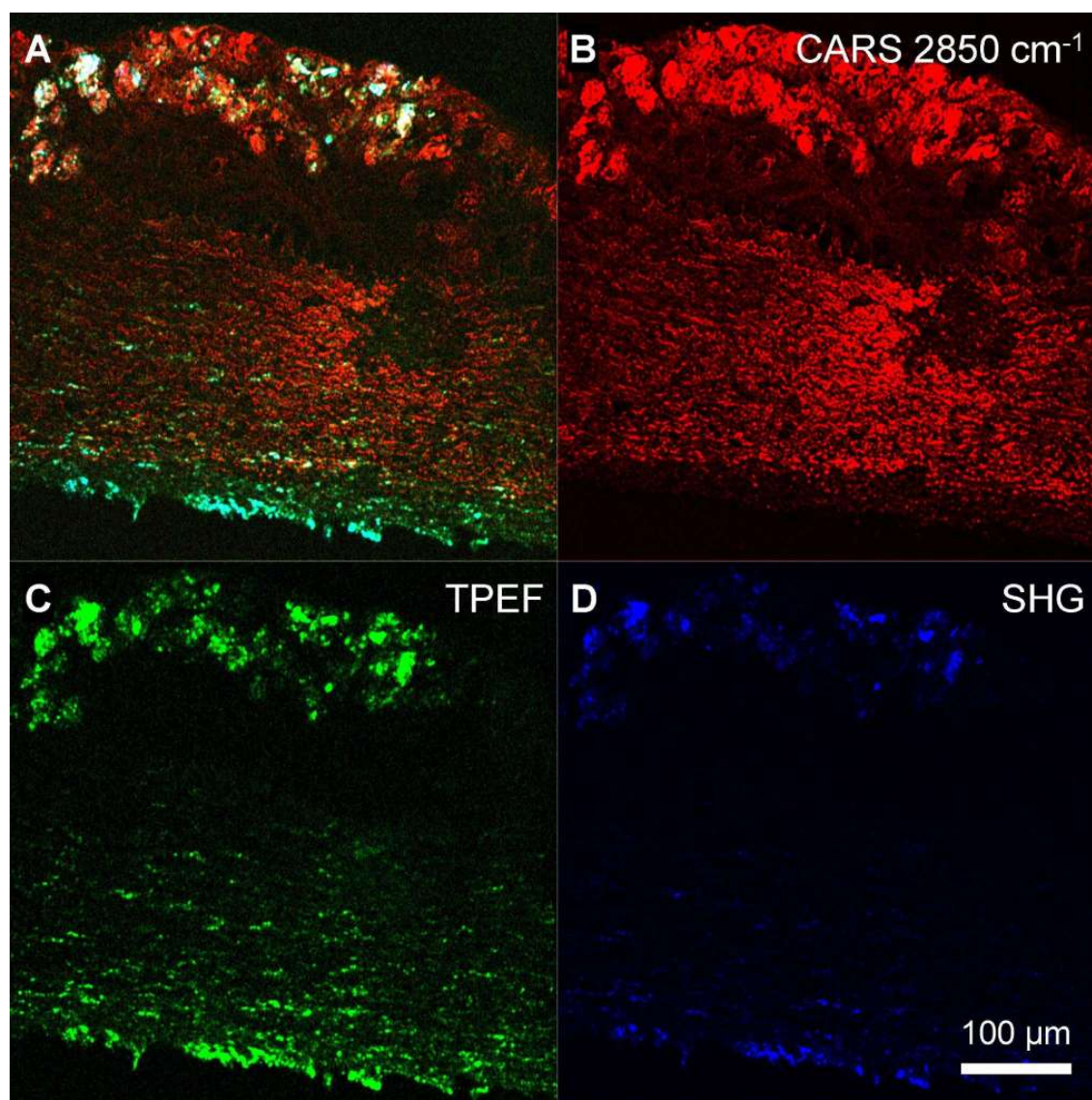


**Figure 5** – Composite multimodal nonlinear microscopic image of an artery section of an animal model for atherosclerosis. In panel A CARS, TPEF and SHG image are combined to a false colour molecular map of the artery section. CARS imaging at the symmetric C-H-stretching vibration of methylene groups at  $2850\text{ cm}^{-1}$  abundant in all major biomolecules reveals the morphology of the artery. Furthermore, it highlights lipid deposits and protein fibers due to the high concentration of scattering functional groups. TPEF in green, panel C, is used to display autofluorescing molecules, in particular fluorescing protein fibers like elastin and collagen in addition to NADPH and oxidized fatty acids in the plaques. SHG displayed in blue in panel D is sensitive to protein fibers composed of collagen and actin of smooth muscle cells, but cholesterol within the plaque does also generate signals. SHG and TPEF are to a large extent co-localized.

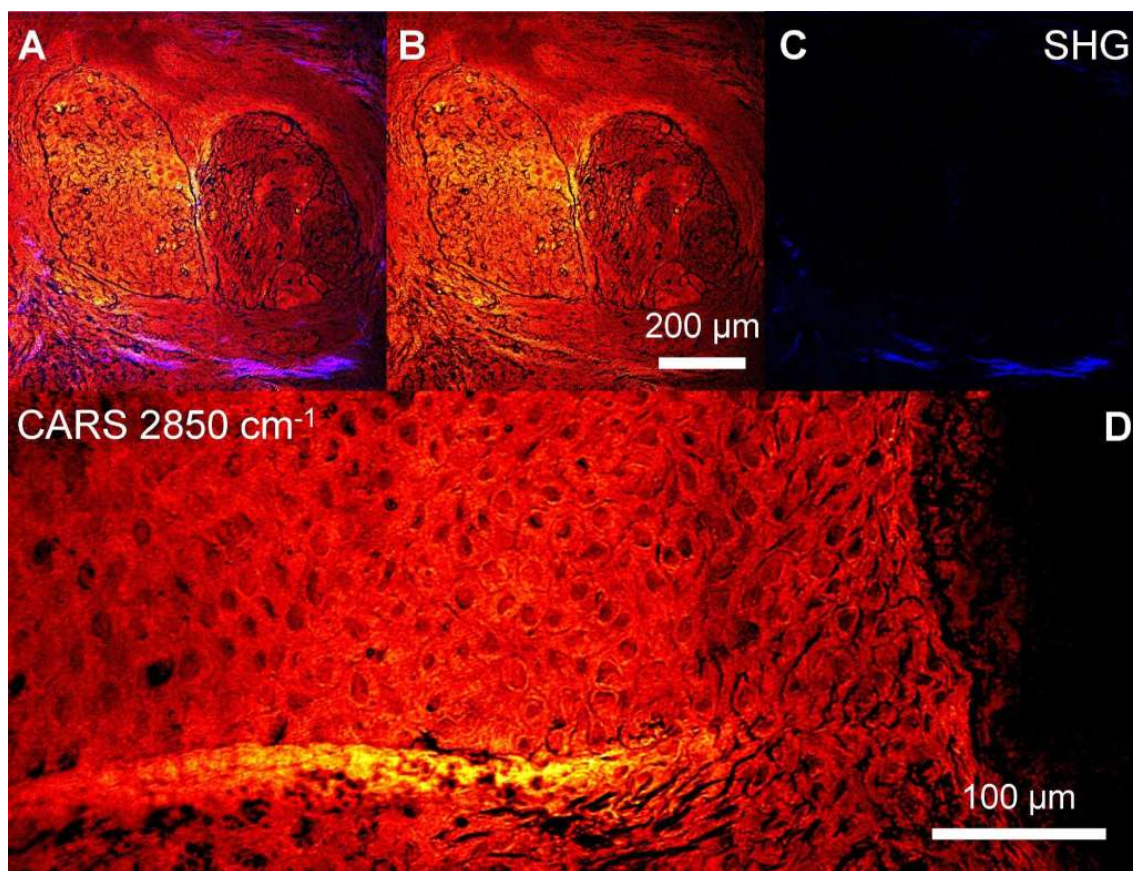


**Figure 6** – Multimodal nonlinear imaging of a head and neck squamous cell carcinoma sample from an oropharyngeal site. In panels A-C tumor nests are invasively growing into the connective tissue. In panel A both the CARS signal at the symmetric CH stretching vibration of methylene groups at  $2850\text{ cm}^{-1}$  and SHG signals of collagen fibers of the connective tissue are displayed, CARS and SHG signals are represented in panels B and C. Epithelium without pathological findings is depicted in panel D (CARS,  $2850\text{ cm}^{-1}$ ). Single epithelial cells and nuclei are visualized.

from grade 3 to invasively growing grade 4 carcinoma. Grade 4 is defined by tumor cells breaking through the basement membrane and invading the connective tissue [3, 50, 51]. For comparison adjacent epithelium without pathological findings is depicted in panel D utilizing CARS at  $2850\text{ cm}^{-1}$ . In figure 6 panel D single epithelial cells and nuclei are visualized, demonstrating the potential for tissue imaging for diagnostic purposes, since grading of HNSCC relies on the visualization of architectural and cytological changes accompanying the process of carcinogenesis [50, 51],

e.g. cell density, size and shape of individual cells and nuclei as well as the nuclei to cytoplasm ratio. Therefore also in case of tumor diagnostics, multimodal nonlinear microscopy represents a promising imaging tool.

## Conclusion

Application of imaging tools in clinical settings poses strict constraints on the system in terms of cost effectiveness, size, complexity in handling and robustness. While the past years have seen an increasing number of studies proving that multimodal nonlinear imaging approaches are valuable tools for illuminating aspects of disease progression on cellular and sub cellular level, the equipment was yet too complex for other than research applications. The compact multimodal nonlinear microscope presented herein represents a significant step towards establishing nonlinear microscopy in clinics for routine diagnostics due to its simplicity, high NIR transmission for use with low power compact lasers and large field of view and high image quality. The instrument will be tested on disease patterns, which are directly accessible, e.g. skin cancers and head and neck cancers in the near future.

But further progress will also point in different directions, especially towards in vivo endoscopy. In this respect the presented fiber laser light source is not only compatible with endoscopy, but intrinsically overcomes the difficulty of coherent Raman imaging in long glass fibers and thick tissue arising from the dispersion of pulses at different wavelengths. The resulting reduction of the temporal pulse overlap with increasing fiber length is greatly reduced by using 100 ps pulses allowing for endoscope fiber lengths of few m without precompensation. When additional spectral information and higher spectral resolution are required, the laser source can be modified to be spectrally tunable as discussed in detail elsewhere [35], resulting in a total tuning range from 1200 to 3800  $\text{cm}^{-1}$  and 1  $\text{cm}^{-1}$  spectral resolution. Furthermore, this source enables due to the low MHz repetition rate both efficient SHG and TPEF imaging together with high contrast CARS microscopy, thus overcoming the discrepancy between low peak power high spectral resolution ps-lasers ideal for CARS and low spectral resolution high peak power fs-lasers ideal for TPEF and

SHG, which apply to 80 MHz repetition rate oscillators [24, 30].

The great potential of the presented fiber laser microscope setup is exemplarily demonstrated by imaging atherosclerotic and HNSCC tissue specimen but it is explicitly not limited to examination of these particular disease patterns. The combination of SHG, TPEF and CARS imaging allows determining the distribution of fibrous proteins, smooth muscle cells, cholesterol and lipids with spatial resolution and contrast comparable to ex vivo staining histopathology, but with the advantage of potentially being applicable under in vivo conditions in the near future. Imaging the collagen network, the collagen organization and shape is of diagnostic relevance also for grading cancer tissue [3, 52, 53]. Especially implementation into endoscopes would have the benefit of enabling in vivo characterization of arterial plaque depositions in order to detect high risk plaques, e.g. plaques associated with a large lipid core and a thin fibrous cap, for further monitoring or direct treatment. Also in case of malignancies, multimodal nonlinear microscopy provides label-free excellent information on the tissue morphology and composition. During carcinogenesis first morphologic changes occur at the basement membrane. Nonlinear imaging combining depth penetrations up to 1 mm with cellular resolution is perfectly suited to detect these modifications in vivo. Hence, the method allows for non invasive in depth screening of suspicious lesions possibly reducing the number of biopsies taken in the future. By integration into surgical microscopes, the method may be prospectively useful for surgical guidance.

## **Acknowledgments**

Financial support of the European Union via the Europäischer Fonds für Regionale Entwicklung EFRE and the "Thüringer Ministerium für Bildung Wissenschaft und Kultur TMBWK" Projects: B714-07037, B578-06001, 14.90 HWP and via the European network of excellence P4L Photonics4Life as well as financial support from the German Ministry for Science and Education BMBF MediCARS FKZ: 13N10773 & 13N10774 is highly acknowledged. M.B. acknowledges support from the Carl-Zeiss-Stiftung.

## References

- [1] Yue, S., Slipchenko, M. N., and Cheng, J.-X. *Laser & Photonics Reviews* **5**(4), 496–512 (2011).
- [2] Krafft, C., Dietzek, B., Schmitt, M., and Popp, J. *Journal of Biomedical Optics* **17**(4), 40801 (2012).
- [3] Meyer, T., Guntinas-Lichius, O., von Eggeling, F., Ernst, G., Akimov, D., Schmitt, M., Dietzek, B., and Popp, J. *Head & Neck* (2012).
- [4] Cicchi, R., Sestini, S., De Giorgi, V., Massi, D., Lotti, T., and Pavone, F. S. *Journal of Biophotonics* **1**(1), 62–73 (2008).
- [5] Helmchen, F. and Denk, W. *Nature Methods* **2**(12), 932–940 (2005).
- [6] Kobat, D., Durst, M. E., Nishimura, N., Wong, A. W., Schaffer, C. B., and Xu, C. *Optics Express* **17**(16), 13354–13364 (2009).
- [7] Suhaim, J. L., Boik, J. C., Tromberg, B. J., and Potma, E. O. *Journal of Biophotonics* **5**(5-6), 387–395 (2012).
- [8] Evans, C. L., Xu, X., Kesari, S., Xie, X. S., Wong, S. T. C., and Young, G. S. *Optics Express* **15**(19), 12076–12087 (2007).
- [9] Meyer, T., Bergner, N., Bielecki, C., Krafft, C., Akimov, D., Romeike, B. F. M., Reichart, R., Kalff, R., Dietzek, B., and Popp, J. *Journal of Biomedical Optics* **16**(2), 21113 (2011).
- [10] Meyer, T., Bergner, N., Medyukhina, A., Dietzek, B., Krafft, C., Romeike, B. F. M., Reichart, R., Kalff, R., and Popp, J. *Journal of Biophotonics* **5**(10), 729–733 (2012).
- [11] Krafft, C., Ramoji, A. A., Bielecki, C., Vogler, N., Meyer, T., Akimov, D., Rösch, P., Schmitt, M., Dietzek, B., Petersen, I., Stallmach, A., and Popp, J. *Journal of Biophotonics* **2**(5), 303–312 (2009).
- [12] Vogler, N., Meyer, T., Akimov, D., Latka, I., Krafft, C., Bendsoe, N., Svanberg, K., Dietzek, B., and Popp, J. *Journal of Biophotonics* **3**(10-11), 728–736 (2010).
- [13] Le, T. T., Yue, S., and Cheng, J.-X. *Journal of Lipid Research* **51**(11), 3091–3102 November (2010).
- [14] *Todesursachen in Deutschland*. Statistisches Bundesamt Wiesbaden, (2011).
- [15] Choudhury, R. P., Fuster, V., and Fayad, Z. A. *Nature Reviews Drug Discovery* **3**(11), 913–925 (2004).
- [16] Owen, D. R. J., Lindsay, A. C., Choudhury, R. P., and Fayad, Z. A. *Annual Review of Medicine* **62**(1), 25–40 (2011).
- [17] Schenke-Layland, K. *Journal of Biophotonics* **1**(6), 451–462 (2008).
- [18] Suhaim, J. L., Chung, C.-Y., Lilledahl, M. B., Lim, R. S., Levi, M., Tromberg, B. J., and Potma, E. O. *Biophysical Journal* **102**(8), 1988–1995 (2012).
- [19] Cicchi, R., Vogler, N., Kapsokalyvas, D., Dietzek, B., Popp, J., and Pavone, F. S. *Journal of Biophotonics* **6**(2), 129–142 (2013).
- [20] Ko, A. C.-T., Ridsdale, A., Mostaçõ-Guidolin, L. B., Major, A., Stolow, A., and Sowa, M. G. *Biophysical Reviews* **4**(4), 323–334 (2012).
- [21] Monici, M. In *Biotechnology Annual Review*, El-Gewely, M. R., editor, volume 11 of *Biotechnology Annual Review*, 227–256. Elsevier (2005).
- [22] Arakawa, K., Isoda, K., Ito, T., Nakajima, K., Shibuya, T., and Ohsuzu, F. *Arteriosclerosis, Thrombosis, and Vascular Biology* **22**(6), 1002–1007 (2002).

- [23] Pezacki, J. P., Blake, J. A., Danielson, D. C., Kennedy, D. C., Lyn, R. K., and Singaravelu, R. *Nature Chemical Biology* **7**(3), 137–145 (2011).
- [24] Le, T. T., Langohr, I. M., Locker, M. J., Sturek, M., and Cheng, J.-X. *Journal of biomedical optics* **12**(5), 54007 September (2007).
- [25] Wang, H.-W., Langohr, I. M., Sturek, M., and Cheng, J.-X. *Arteriosclerosis, Thrombosis, and Vascular Biology* **29**(9), 1342–1348 (2009).
- [26] Ko, A. C. T., Ridsdale, A., Smith, M. S. D., Mostaco-Guidolin, L. B., Hewko, M. D., Pegoraro, A. F., Kohlenberg, E. K., Schattka, B., Shiomi, M., Stolow, A., and Sowa, M. G. *Journal of biomedical optics* **15**(2), 20501 (2010).
- [27] Mostaco-Guidolin, L. B., Ko, A. C. T., Popescu, D. P., Smith, M. S. D., Kohlenberg, E. K., Shiomi, M., Major, A., and Sowa, M. G. *Physics In Medicine and Biology* **56**(16) August (2011).
- [28] Matthäus, C., Dochow, S., Bergner, G., Lattermann, A., Romeike, B. F. M., Marple, E. T., Krafft, C., Dietzek, B., Brehm, B. R., and Popp, J. *Analytical Chemistry* August (2012).
- [29] Meyer, T., Akimov, D., Tarcea, N., Chatzipapadopoulos, S., Muschiolik, G., Kobow, J., Schmitt, M., and Popp, J. *The Journal of Physical Chemistry. B* **112**(5), 1420–1426 (2008).
- [30] Chen, H., Wang, H., Slipchenko, M. N., Jung, Y., Shi, Y., Zhu, J., Buhman, K. K., and Cheng, J.-X. *Optics Express* **17**(3), 1282–1290 (2009).
- [31] Kano, H. and Hamaguchi, H. *Optics Express* **14**(7), 2798–2804 April (2006).
- [32] Krauss, G., Hanke, T., Sell, A., Träutlein, D., Leitenstorfer, A., Selm, R., Winterhalder, M., and Zumbusch, A. *Optics Letters* **34**(18), 2847–2849 (2009).
- [33] Pegoraro, A. F., Ridsdale, A., Moffatt, D. J., Pezacki, J. P., Thomas, B. K., Fu, L., Dong, L., Fermann, M. E., and Stolow, A. *Optics Express* **17**(23), 20700–20706 November (2009).
- [34] Lefrancois, S., Fu, D., Holtom, G. R., Kong, L., Wadsworth, W. J., Schneider, P., Herda, R., Zach, A., Sunney Xie, X., and Wise, F. W. *Optics Letters* **37**(10), 1652–1654 (2012).
- [35] Chemnitz, M., Baumgartl, M., Meyer, T., Jauregui, C., Dietzek, B., Popp, J., Limpert, J., and Tünnermann, A. *Optics Express* **20**(24), 26583–26595 November (2012).
- [36] Baumgartl, M., Chemnitz, M., Jauregui, C., Meyer, T., Dietzek, B., Popp, J., Limpert, J., and Tünnermann, A. *Optics Express* **20**(4), 4484–4493 (2012).
- [37] Baumgartl, M., Gottschall, T., Abreu-Afonso, J., Diez, A., Meyer, T., Dietzek, B., Rothhardt, J., Popp, J., Limpert, J., and Tünnermann, A. *Optics Express* **20**(21010-21018) (2012).
- [38] Gottschall, T., Baumgartl, M., Sagnier, A., Rothhardt, J., Jauregui, C., Limpert, J., and Tünnermann, A. *Optics Express* **20**(11), 12004 (2012).
- [39] Nan, X. L., Potma, E. O., and Xie, X. S. *Biophysical Journal* **91**(2), 728–735 (2006).
- [40] Bégin, S., Burgoyne, B., Mercier, V., Villeneuve, A., Vallée, R., and Côté, D. *Biomedical Optics Express* **2**(5), 1296–1306 (2011).
- [41] Abramoff, M. D., Magalhães, P. J., and Ram, S. J. *Biophotonics international* **11**(7), 36–42 (2004).
- [42] Cheng, J.-x., Volkmer, A., Book, L. D., and Xie, X. S. *The Journal of Physical Chemistry B* **106**(34), 8493–8498 August (2002).
- [43] Ganikhanov, F., Evans, C. L., Saar, B. G., and Xie, X. S. *Optics Letters* **31**(12), 1872–1874 (2006).



- [44] Dudovich, N., Oron, D., and Silberberg, Y. *Nature* **418**(6897), 512–514 August (2002).
- [45] Zhai, Y.-H., Goulart, C., Sharping, J. E., Wei, H., Chen, S., Tong, W., Slipchenko, M. N., Zhang, D., and Cheng, J.-X. *Applied Physics Letters* **98**(19) (2011).
- [46] Huff, T. B., Shi, Y., Fu, Y., Wang, H., and Cheng, J.-X. *Ieee Journal of Selected Topics In Quantum Electronics* **14**(1), 4–9 (2008).
- [47] Bergner, G., Chatzipapadopoulos, S., Akimov, D., Dietzek, B., Malsch, D., Henkel, T., Schlücker, S., and Popp, J. *Small* **5**(24), 2816–2818 (2009).
- [48] Zipfel, W. R., Williams, R. M., Christie, R., Nikitin, A. Y., Hyman, B. T., and Webb, W. W. *Proceedings of the National Academy of Sciences of the United States of America* **100**(12), 7075–7080 (2003).
- [49] Campagnola, P. *Biophysical Journal* **82**(1), 493–508 (2002).
- [50] Sapp, J. P., Eversole, L., and Wysocki, G. *Contemporary Oral and Maxillofacial Pathology*. Elsevier, (2003).
- [51] Reibel, J. *Critical Reviews in Oral Biology and Medicine: An Official Publication of the American Association of Oral Biologists* **14**(1), 47–62 (2003).
- [52] Medyukhina, A., Vogler, N., Latka, I., Kemper, S., Böhm, M., Dietzek, B., and Popp, J. *Journal of Biophotonics* **4**(9), 627–636 September (2011).
- [53] Cicchi, R., Kapsokalyvas, D., Giorgi, V. D., Maio, V., Wiechen, A. V., Massi, D., Lotti, T., and Pavone, F. S. *Journal of Biophotonics* **3**(1-2), 34–43 (2010).

## Supplementary Material

### S1. Compact nonlinear laser scanning microscope

The optical layout of the microscope as displayed in figure 2 panel A has been designed to fit the requirements of nonlinear SHG/TPEF/CARS microscopy for tissue imaging. Therefore all optical elements in the illumination beam path are optimized for highest NIR transmission. This configuration enables using relatively low power but ultra compact, robust and maintenance free fiber lasers described in the preceding section. In order to realize high optical throughput, the number of optical elements is minimized without affecting the optical performance, i.e. diffraction limited spatial resolution. Since nonlinear imaging methods provide 3D sectioning, no confocal microscope design is required. A NIR anti reflective coated achromatic lens (NIR achromatic lens, 12 mm diameter, 15 mm focal length, Edmund optics, USA) is used to collimate the beam to 6 mm diameter, allowing to fully illuminate the back aperture of the microscope objectives and the galvanometric mirror pair (model 6210HSM40, Camtech, USA). The scanning system is equipped with protected silver coated mirrors of 6 mm diameter providing a surface flatness of  $\lambda$ . Adapting the beam diameter to the size of the objective's back aperture guarantees, that the system's spatial resolution is limited by diffraction of the focusing objective. A scan lens system has been designed to image the centre of the galvanometric mirror pair onto the back aperture of the microscope objective. This scanlens system is optimized for minimal chromatic aberrations in the NIR spectral range and to provide a large field of view. Furthermore, the distance between scan lens and objective enables insertion of a short pass dichroic mirror (short pass 750 nm, size 24 mm x 36 mm, Edmund optics, USA) and a 400  $\mu\text{m}$  piezo driven stage. The dichroic mirror allows for detection of signals in backward direction and the piezo driven stage provides 400  $\mu\text{m}$  travel along the z axis for fine focusing (PIFOC P-725.4CD, PI, Germany) and automated acquisition of z-stacks. The scan lens system consists of 4 NIR coated achromatic lenses arranged in two pairs in a 4f-configuration: 200 mm – 150 mm – 150 mm – 200 mm (NIR achromatic lens, 25 mm diameter, Edmund optics, USA). Optimization of the scan lens design was performed using Zemax (Radian Zemax,

USA). The microscope objective is mounted to the z-stage. For large area scanning a  $20 \times 0.4$  NA NIR corrected long working distance objective is used (Mitutoyo, Japan). The sample is fixed on a motorized xy-stage providing 75 mm by 50 mm of travel and 1  $\mu\text{m}$  positioning accuracy (ScanPlus, Märzhäuser, Germany). Residual laser light and signals are collimated in forward direction by a NA matched VIS achromatic lens of 25 mm diameter and 30 mm focal length (Thorlabs, USA). For the separation of the nonlinear signals in forward direction two short pass filters are used (SP770 and SP750, Semrock, USA). The forward emitted SHG and CARS signals are splitted by a longpass dichroic mirror (LP605, 24 mm  $\times$  36 mm, Thorlabs, USA), filtered by appropriate bandpass filters (CARS bandpass 650/40 Thorlabs, SHG bandpass 400/40 or 514/10, Thorlabs, USA) and focused onto the PMT detectors by achromatic lenses (diameter 25 mm, 30 mm focal length, Thorlabs, USA). TPEF or alternatively backward scattered CARS/SHG signals are detected by a PMT module in epi-direction. Alternatively also TPEF signals can be detected in forward direction. For detection of CARS signals, PMT modules of enhanced sensitivity in the red spectral range are used (H6780-20, H10721-20 and H9305-03, Hamamatsu, Japan), whereas for detecting SHG and TPEF signals in the visible range VIS sensitive PMTs are used (H6780, Hamamatsu, Japan). A summary of the key components of the instrument is given in table S 1. The whole system is schematically depicted in figure 1 panel A, while panels B-E show photographs of parts of the system.

**Table S 1** – List of main components of the compact laser scanning microscope

<b>Model</b>	<b>Part</b>	<b>Manufacturer</b>
6210HSM40	xy-galvanometric mirror	Cambridge Technology, USA
ScanPlus 75 x 50	xy-translation stage	Märzhäuser Wetzlar, Germany
P-725.4CD	400 $\mu\text{m}$ Piezo z-stage	Physikinstrumente, Germany
	Customized Data acquisition hardware	Pascher instruments, Sweden
H10721-20	8 mm head on PMT module	Hamamatsu, Japan
H6780-20	8 mm head on PMT module	Hamamatsu, Japan
H6780	8 mm head on PMT module	Hamamatsu, Japan
H9305-03	Side on PMT modules	Hamamatsu, Japan
BXFM-F	manual z-focussing unit	Olympus, Japan
Plan Apo NIR	20 $\times$ NA 0.4 LWD objective	Mitutoyo, Japan

## **S2. Data acquisition hardware & graphical user interface**

The data acquisition soft- and hardware has been designed for controlling the galvanometric mirrors, the motorized xy microscope translation stage, the piezo z-focussing stage and for synchronized data acquisition of up to 4 channels simultaneously. The data acquisition system consists of two parts: the first part is a small desktop computer for running the graphical user interface for complete instrument control via USB and storage of the image data and the second device is the data acquisition hardware controlling the instrument. Both the data acquisition hardware as well as the graphical user interface were specifically designed for this microscope by T.P., Pascher Instruments AB, Sweden. The menus of the graphical user interface are clearly arranged in order to provide intuitive but complete control of the hardware. A screenshot of the software is displayed in figure 2 panel B. From the user interface the scanning start position, stop position and step length for both directions are sent to the data acquisition hardware control unit. The data acquisition hardware has two major parts. The first part is the scan mirror control unit which re-

gulates the position of the x and y mirrors during scanning and the second part deals with the data readout synchronized with the laser scanner. In the hardware control unit the information about the image size combined with several adjusted electronic delay is converted such, that the unit performs the full 2D sweep without computer intervention. The hardware control unit contains power supplies for preamplifier and analogue to digital conversion electronics in addition to slots for insertion of controller cards. The first card is used for driving the galvanometric scanner and setting the voltages of the photomultiplier tube modules (PMT), the second card controls the motorized xy stage and the piezo z stage via RS-232 serial ports. Another two cards are used for receiving data from a preamplifier and ADC of two detectors via parallel interface ports. In the following the workflow of performing a 2D scan is described in detail. The location of each point on the sample is determined by the position of the galvanometric mirrors. During the collection of an image the y direction corresponds to the slow axis which is moved in steps. The fast scan direction is the x axis. In x direction the mirror sweeps from one end position to the other in continuous motion at constant angular speed. The image size is quadratic and can be chosen from  $128 \times 128$  up to  $4096 \times 4096$  pixels. According to the chosen frame size the digitizing electronic collects during the sweep of the fast x-axis the required number of data points, which are equally spaced in time. The first part of the hardware control unit moves the galvanometric mirror pair by automatically performing a full xy-scan digitally. The digital position values are converted to voltages by two 16-bit digital to analogue converters (DAC) and the resulting driving voltage signal is sent to the galvanometric scanner. The resolution of the system is sufficient to enable diffraction limited spatial resolution. 20 voltage steps in the digital position correspond to a beam displacement of  $1 \mu\text{m}$  in the image plane in combination with a  $20 \times$  objective. The control unit also provides a trigger signal for each sweep of the X direction mirror to synchronize the data readout with the mirror motion. The second part of the control unit deals with synchronized readout of the detector signals. The readout circuitry is divided into three parts. The first part includes a PMT or diode detector pre amplifier with different computer controllable gain and analogue low pass filters. These settings enable optimisation of the signal to noise

ratio for the available absolute signal amplitudes and readout speeds ranging from 1 to 256  $\mu s$  per pixel. The second component contains a digitizing part consisting of an 18-bit analogue to digital converter (ADC) running at 2 MHz (mega samples per second), which allows averaging a number of readings for each data point. Upon each line triggering event this unit sends the predetermined number of appropriately averaged data points representing a full sweep of the X direction mirror to the data storage card. The storage card as the third component has two memory banks used in ping pong fashion. While the digitizing part files the signal in one storage bank the computer reads out the other one containing the signals of the previous complete line sweep. In principle bidirectional and unidirectional scanning of the sample is possible. For data acquisition the unidirectional scan mode is used, since for bidirectional scans certain delays have to be adjusted depending on image size and the scanning field of view in order to correct for a spatial position offset of the laser beam. The graphical user interface enables complete instrument control, i.e. setting the PMT voltages, zooming into the image, setting the image parameters, e.g. frame size and the number of pixels, additional filtering, analogue and digital gain as well as point averaging by slow scanning or frame averaging in order to detect weak signals. The options are accessible by drop down lists. An additional menu is popping up for performing a series of images. As indicated in the screenshot shown in figure 2, four options are available: a time series scan for investigating dynamic processes, z-scan for depth resolved imaging of thick samples, xy-scan using the motorized stage for analysing sample areas exceeding the field of view of the scanner and xyz-scans for investigating extended thick specimen. There is no limit on the number of individual images per scan apart from the capacity of the hard disk. Each image of an individual detector is stored as a separate 16 bit TIFF file in addition to a text file containing the settings of the electronics. For adjustment, two fast scan options are implemented. The alignment mode performs a fast scan by reducing the number of lines per image and thus speeding up the image update rate. In the focus mode a fraction of the image is displayed at full resolution for focusing purposes. The key aspect for adaption of the electronics' hardware of the instrument to nonlinear imaging is a large set of options to optimize the detection

of weak signals. These options include low pass filtering of the signal, an additional tenfold analogue gain setting, pixel dwell times up to  $256 \mu s$  and averaging of a specific number of frames. The most important parameters of the hardware control unit are summarized in table S 2.

Photon counting as the most sensitive method of light detection is not used, because this method does not enable to count a number of photons arriving at the same time, as it is the case for coherent CARS and SHG signals excited by pulsed light sources.

**Table S 2** – Summary of parameters of the data acquisition hardware control unit

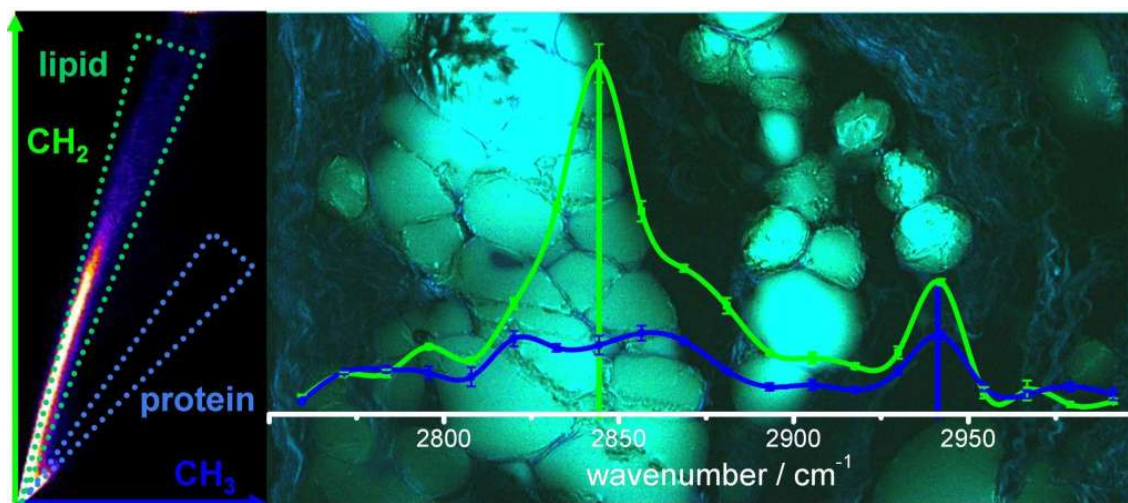
---

Resolution	$128 \times 128 - 4096 \times 4096$ pixels
Scanning speed @ $128^2$	8 fps
Scanning speed @ $4096^2$	24 s
Detection channels	3 PMTs + 1 photodiode
Pixel dwell time	$1 \mu s - 256 \mu s$
Data depth	16 bit
ADC	2 MHz

---







Adapted with kind permission of the American Chemical Society (ACS) from the following source:

**Authors:** Tobias Meyer, Mario Chemnitz, Martin Baumgartl, Thomas Gottschall, Torbjörn Pascher, Christian Matthäus, Bernd F. M. Romeike, Bernhard R. Brehm, Jens Limpert, Andreas Tünnermann, Michael Schmitt, Benjamin Dietzek, and Jürgen Popp.

**Titel:** "Expanding Multimodal Microscopy by High Spectral Resolution Coherent Anti-Stokes Raman Scattering Imaging for Clinical Disease Diagnostics."

**Journal:** *Analytical Chemistry*, 85(14):6703–6715, 2013.

©Copyright 2013 American Chemical Society (ACS).

Reproduced with permission.



12 | Expanding Multimodal Microscopy by High Spectral Resolution Coherent Anti-Stokes Raman Scattering Imaging for Clinical Disease Diagnostics

**Tobias Meyer,<sup>1</sup> Mario Chemnitz,<sup>2</sup> Martin Baumgartl,<sup>2</sup> Thomas Gottschall,<sup>2</sup> Torbjörn Pascher,<sup>3</sup> Christian Matthäus,<sup>1</sup> Bernd F. M. Romeike,<sup>4</sup> Bernhard R. Brehm,<sup>5</sup> Jens Limpert,<sup>2</sup> Andreas Tünnermann,<sup>2,6</sup> Michael Schmitt,<sup>7</sup> Benjamin Dietzek,<sup>1,7</sup> and Jürgen Popp<sup>1,7\*</sup>**

<sup>1</sup> Institute of Photonic Technology e.V., Albert-Einstein-Strasse 9, 07745 Jena, Germany

<sup>2</sup> Institute of Applied Physics and Abbe Center of Photonics, Friedrich-Schiller-University Jena, Albert-Einstein-Str. 15, 07745 Jena, Germany.

<sup>3</sup> Pascher Instruments AB, Stora Rabybyaväg 24, 22478 Lund, Sweden and Department of Chemical Physics Lund University, Kemicentrum, Getingevägen 60, 22241 Lund, Sweden.

<sup>4</sup> Institute of Pathology, Department of Neuropathology, Jena University Hospital, Erlanger Allee 101, 07740 Jena, Germany.

<sup>5</sup> Catholic Clinic – Koblenz, Internal Medicine & Cardiology, Rudolf Virchow Str. 9, 56073 Koblenz, Germany.

<sup>6</sup> Fraunhofer Institute for Applied Optics and Precision Engineering, Albert-Einstein-Str. 7, 07745 Jena, Germany.

<sup>7</sup> Institute of Physical Chemistry and Abbe Center of Photonics, Friedrich-Schiller-University Jena, Helmholtzweg 4, 07743 Jena, Germany

\* corresponding author: [juergen.popp@ipht-jena.de](mailto:juergen.popp@ipht-jena.de)

## Abstract

Over the past years fast label-free nonlinear imaging modalities providing molecular contrast of endogenous disease markers with subcellular spatial resolution have been emerged. However, applications of these imaging modalities in clinical settings are still at the very beginning. This is because single nonlinear imaging modalities such as second-harmonic generation (SHG) and two-photon excited fluorescence (TPEF) have only limited value for diagnosing diseases due to the small number of endogenous markers. Coherent anti-Stokes Raman scattering (CARS) microscopy on the other hand can potentially be added to SHG and TPEF to visualize a much broader range of marker molecules. However, CARS requires a second synchronized laser source and the detection of a certain wavenumber range of the vibrational spectrum to differentiate multiple molecules, which results in increased experimental complexity and often inefficient excitation of SHG and TPEF signals. Here we report the application of a novel near-infrared (NIR) fiber laser of 1 MHz repetition rate, 65 ps pulse duration, and  $1\text{ cm}^{-1}$  spectral resolution to realize an efficient but experimentally simple SHG/TPEF/multiplex CARS multimodal imaging approach for a label-free characterization of composition of complex tissue samples. This is demonstrated for arterial tissue specimens demonstrating differentiation of elastic fibers, triglycerides, collagen, myelin, cellular cytoplasm, and lipid droplets by analyzing the CARS spectra within the C-H stretching region only. A novel image analysis approach for multispectral CARS data based on colocalization allows correlating spectrally distinct pixels to morphologic structures. Transfer of this highly precise but compact and simple to use imaging approach into clinical settings is expected in the near future.

## Introduction

Routine imaging in biomedical diagnostics demands methods which are ideally fast, noninvasive, label-free, and universally applicable to the various types of tissues in order to provide an all-optical biopsy allowing for an identification of disease-related changes. At the same time, these imaging methods should be also technically simple to operate, e.g., compatible with established clinical imaging platforms. Novel imaging tools are needed to diagnose the most prevalent disease patterns in the developed countries, i.e., cardiovascular diseases (CVD) and cancer, which account for 75% of the deceases in Germany,[1] at an early stage. This is crucial to improve the patient's prognosis, but also to reduce the ever-increasing costs for medical treatment. However, the disease-causing tissue changes are subtle requiring the visualization of the tissue structure with subcellular resolution and detection of molecular markers related to disease progression. The current golden standard in histopathology is staining microscopy performed on sectioned tissue biopsies *ex vivo*. However, mostly biopsies are taken not until severe disease symptoms occur. Furthermore, due to the invasive nature and possible complications of biopsies, this method is of only limited use for an early disease recognition, e.g., by routine screening of patients without positive symptoms. Thus, a fast, non- or minimally invasive label-free *in vivo* imaging technique is needed, which provides molecular contrast for the detection of first disease-related changes within the chemical composition of the tissue.

Promising imaging candidates for the above-mentioned envisioned biomedical application in the future are nonlinear microscopic methods. Nonlinear imaging,[2] e.g., two-photon excited fluorescence (TPEF) [3] and second-harmonic generation (SHG),[4] provide unique properties such as (1) diffraction-limited three-dimensional resolution of morphological tissue structures, (2) a significantly improved depth penetration of 1 mm in native tissue, [5, 6, 7] (3) label-free molecular contrast utilizing endogenous disease markers,[3, 8] and (4) high-speed image acquisition [2]at moderate average laser power tolerable by living tissue. [9, 10]

However, the limited number of endogenous molecular markers in tissue reduces the diagnostic value of SHG and TPEF alone for detecting diseases.[3, 8] This is pro-

cess intrinsic, since SHG requires noninversion symmetric structures, which are the quasi-crystalline protein fibers collagen, actin-myosin and tubuline, [11] and crystalline cholesterol,[12] while TPEF is limited to fluorescing molecular species, which are similarly rare in tissue, e.g., the proteins keratin, elastin, or NAD(P)H.[3] Furthermore, the generated signal intensity of endogenous markers is significantly weaker than that of dye labels, e.g., on the order of 0.01 GM ( $GM = 10^{-50}cm^4s/photon$ ) for NAD(P)H [13] in contrast to 30 GM for dyes like fluorescein.[14] The weak autofluorescence emission can be further decreased by light-induced destruction of the chromophore, i.e., photobleaching and quenching, e.g., non-emissive energy transfer. Since only a few endogenous marker molecules in tissue generate TPEF or SHG signals, the application to disease diagnostics is limited to such a few cases, where SHG- or TPEF-active molecular markers are involved, e.g., diseases related to collagen disorders,[4, 15, 16, 17, 18, 19] in particular for imaging various types of cancer [20] and atherosclerosis.[21]

An alternative spectroscopic method enabling the visualization of all molecules with high accuracy is vibrational imaging. This is because the vibrational spectrum of molecules is highly specific almost like a fingerprint. The vibrational spectrum is accessible by several methods, e.g., IR absorption and Raman scattering. Since the depth penetration and spatial resolution in tissue of IR absorption is not sufficient, only Raman-based techniques are suitable for thick tissue imaging and in vivo applications.[22, 23]

However, spontaneous Raman scattering suffers from its intrinsic low cross section [24] of approximately  $10^{-29}cm^2$ , i.e., orders of magnitude lower than UV-vis [25] and IR [26] absorption with cross sections of  $10^{-17}cm^2$  and  $10^{-19}cm^2$ , respectively. This property translates at nondestructive laser power levels into slow imaging speeds of 25 ms per Raman spectrum, which is already fast.[27] To increase the Raman signal resonance or surface enhancement effects are not suitable for in vivo application, because resonance enhancement is limited to absorbing species and often leads to photodegradation, while surface enhancement requires metal nanoparticles as labels.[28] Hence, nonlinear signal enhancement by coherent Raman imaging is the only option to realize video rate image acquisition speed [29, 30] which is a

key prerequisite for biomedical applications.[31] However, for fast nonlinear coherent Raman imaging only a part of the Raman spectrum can be used, since acquisition of the complete spectrum requires either a broad-band laser in combination with a spectrograph [32] or wavelength scanning of the laser,[33, 34] which results in significantly longer acquisition times. In order to maintain the speed advantage of coherent Raman over spontaneous Raman, a few selected Raman resonances or the high-wavenumber spectral region from 2500 to 3500  $\text{cm}^{-1}$  is scanned, which leads to the strongest coherent Raman signals. As has been shown for spontaneous Raman imaging,[35, 36, 37] the high-wavenumber Raman spectrum contains sufficient spectral information for disease diagnostics.

Recently several groups have implemented multispectral coherent Raman imaging for analyzing the composition of tissue. Coherent anti-Stokes Raman scattering (CARS)-based methods have been employed in combination with principal component analysis for differentiating cholesterol crystals from other lipids [34] and for discerning lipids within the meibomian gland from the extracellular matrix.[38] Stimulated Raman scattering (SRS)-based techniques allow for the discrimination of lipids, proteins, and water.[39] By combining multispectral coherent Raman imaging with other nonlinear imaging modalities the chemical specificity is increased, e.g., a combination of SRS and SHG has recently proved discrimination of cholesterol monohydrate crystals from other lipid structures in the tissue and even from condensed cholesteryl esters.[12]

Therefore, the multimodal combination of TPEF, SHG, and multispectral coherent Raman imaging, i.e., CARS imaging at multiple Raman resonances, enables a more specific characterization of the tissue composition than TPEF and SHG alone, since a significantly larger set of molecular markers are accessible for imaging various disease patterns.[19, 40, 41, 42] However, the realization of TPEF, SHG, and coherent Raman imaging combining simultaneously high signal generation efficiency with high specificity has not been demonstrated due to the different requirements of TPEF, SHG, and CARS on the laser source in particular with respect to spectral resolution and synchronization of different emission wavelengths. Coherent Raman imaging requires two synchronized laser beams to illuminate the sample such that the frequency



difference matches a vibrational resonance. Current lasers for coherent Raman imaging are based on either two synchronized lasers [43] or a combination of an ultrafast laser and an optical parametric oscillator [34, 44, 45] for frequency conversion providing picosecond pulses at usually 80 MHz repetition rate. On the contrary, common ultrafast lasers for SHG and TPEF imaging are tunable titanium-sapphire lasers of 80 MHz repetition rate and much shorter, e.g., 100 fs, pulse duration.[2, 3, 4]Both SHG and TPEF are efficiently excited by spectrally broad lasers owing to the large spectral width of an electronic absorption of several 10 nm in case of TPEF and no constraints on the spectral width in case of SHG. Therefore, the average power on the sample is reduced if shorter pulses are used since SHG and TPEF scale quadratically with the peak intensity, which increases for shorter pulse duration. The different requirements with respect to spectral resolution translate into different laser systems for multimodal imaging combining TPEF, SHG, and CARS, none of them simultaneously optimized for all three modalities. For multimodal imaging either two synchronized picosecond lasers for better CARS resolution, [46] two synchronized femtosecond lasers for an increased SHG and TPEF signal intensity, [47] chirped fs lasers for balancing CARS resolution and TPEF and SHG signal intensity [48] or even subsequent illumination with picosecond and femtosecond laser have been employed in order to excite all three signals most effectively.[49] However, all these laser concepts increase the experiment's complexity, the photon load of the sample, and the total acquisition time. However, low repetition rate and long pulse duration laser provide simultaneously high peak power and high spectral resolution at moderate average power.[50]

Among the different coherent Raman methods CARS,[51, 52, 53] stimulated Raman scattering (SRS) [54], and Raman-induced Kerr effect (RIKE) [55] come into consideration, but CARS is easiest implemented: RIKE and SRS rely on modulation transfer detection schemes requiring additionally a lock-in amplifier for detection; the CARS signal on the other hand is spectrally separable from the incident lasers as are SHG and TPEF signals and does therefore not require substantial modifications of an existing nonlinear microscope. All coherent Raman signals are due to the phase-matching condition predominantly emitted in forward direction, while

biomedical imaging requires detection of the generated signals in backward direction. CARS is compatible with backward detection,[56] while backward detection of RIKE and SRS signals is more difficult to realize, e.g., by large area detectors as in case of SRS.[30]

However, also CARS suffers from disadvantages: CARS is not background-free, since other third-order processes generate the so-called nonlinear nonresonant background, which ultimately limits the image contrast.[52] Interference of the nonlinear background and the resonant CARS signal results in dispersive CARS line shapes. Thus, the exact wavenumber position of the Raman resonances known from spontaneous Raman spectroscopy is often shifted to lower wavenumbers in CARS spectra. However, this spectral shift depends strongly on the laser parameters. In particular, the laser wavelength determines the magnitude of the nonresonant background by two-photon absorption enhancement.[57] For near-infrared (NIR) excitation of spectrally broad and in comparison to the nonresonant background intense Raman resonances as is the case for the C-H wavenumber region this effect is negligible. Due to interference with the nonlinear background the CARS signal intensity dependence on the concentration changes from linear in the low to quadratic in the high-concentration region. Hence, quantitative analysis is difficult. In order to exploit the potential of CARS microscopy, which allows discerning a great variety of molecular markers, multiple Raman resonances need to be scanned at a spectral resolution allowing for separation of the closest neighboring Raman resonances. Therefore, for high spectral resolution CARS measurements excitation pulses with rather long pulse durations are required (a resolution in the order of  $1\text{ cm}^{-1}$  corresponds to pulse durations of few 10 ps) in order to exploit the multiplexing capabilities of vibrational imaging, i.e., to differentiate between a selection of marker molecules.[33, 58] Just recently novel fiber laser based light sources have been developed utilizing four-wave mixing (FWM) in a photonic crystal fiber for the generation of multicolor laser beams. These lasers provide long pulse duration and high peak power; but due to the gain bandwidth of the parametric conversion process of FWM starting from quantum noise, the spectral width is on the order of  $30\text{ cm}^{-1}$ . However, the spectral resolution can be significantly increased by seeding the FWM process in photonic crystal fi-

bers [59] for pump and Stokes pulse generation providing  $1\text{ cm}^{-1}$  spectral width laser pulses [58] when the concept is applied to low repetition rate long pulse duration lasers.[50, 60, 61]

To prove the prospects of this novel light source *ex vivo* chemical selective imaging of connective tissue, proteins, and lipids has been performed in this contribution and compared to the golden standard of staining histopathology diagnostics of cardiovascular diseases. Atherosclerosis together with related cardiovascular diseases is the most prevalent cause of death in the developed countries.[62] It is a chronic process of the vessel walls evolving over years [63] and is accompanied by the deposition of lipid plaques at the luminal site and an increase of connective tissue, not only in the whole vessel wall but even in the perivascular space, i.e., the so-called periadventitial fibrosis. However, even though detection of early lesions is possible, it is difficult to predict imminent serious disease progression, e.g., a heart attack, caused by disruption of a plaque, leading to thrombotic occlusion of the vessel. Since the vulnerability of a plaque is associated with its composition,[64, 65, 66, 67] *in vivo* high-resolution imaging of structure and composition of the vessel wall may prove useful in order to evaluate the risk of rupture in the future.

In this contribution, results from the application of the above-mentioned novel low repetition rate high spectral resolution laser source to multimodal nonlinear imaging of tissue are presented in order to determine the distribution of multiple molecular markers. For human perivascular tissue as well as tissue specimen of an animal model for atherosclerosis it is exemplarily demonstrated that the synergistic combination of SHG, TPEF with high-resolution multispectral CARS enables one to analyze the composition of complex tissue samples in short acquisition time providing high signal intensities, high contrast, and high accuracy superior to lower spectral resolution systems. By applying a novel image analysis approach based on colocalization, CARS images at multiple resonances can be used to correlate spectrally distinct pixels with morphologic structures. Due to the experimental simplicity, the combination of fiber-based light source and multispectral image analysis is especially suited for application in clinical settings, in particular for imaging of atherosclerosis.

## Experimental Section

The fiber lasers used in this study have been described in detail elsewhere.[50, 58, 60, 61] The lasers are based on amplified ytterbium fiber lasers of 1 MHz pulse repetition rate and 120-140 ps pulse duration.[50, 58, 60] Signal and idler pulses of  $30\text{ cm}^{-1}$  spectral width are generated at 787 and 1427 nm by FWM. Ytterbium fundamental and FWM signal have been used as Stokes and pump beam for CARS imaging displayed in Figures 3 A and 4 A-E. Spectral tuning has been performed by stretching the fiber Bragg grating, thus increasing the ytterbium wavelength from 1030 to 1032 nm and in parallel tuning the FWM signal from 786.8 to 800 nm. By seeding the degenerately pumped FWM process in a photonic crystal fiber (PCF) using a continuous wave (cw) titanium-sapphire laser (Spectra Physics, Tsunami), which can be tuned from 700 to 1000 nm, the spectral width of the FWM signal (pump wavelength in CARS) and FWM idler (Stokes wavelength) pulses is significantly reduced by a factor of 30 to  $1\text{ cm}^{-1}$  at 65 ps pulse duration, while the spectral position coincides with the seed-laser wavelength.[58] Spectral tuning of the picosecond pulses has been realized by wavelength tuning the cw seed. For CARS imaging the FWM signal and idler pulses have been used, while the ytterbium fundamental has been blocked. The signal pulse train has been used to excite SHG and TPEF signal and as CARS pump. It has a spectral width (full width at half-maximum, fwhm) of  $0.8\text{ cm}^{-1}$ , while the center wavelength varies during spectral tuning from 900 to 920 nm. The idler with a fwhm of  $1\text{ cm}^{-1}$  is utilized as Stokes beam in the CARS process and spectrally scanned from 1236 to 1196 nm.

CARS, TPEF, and SHG microscopy were performed using a custom-built laser scanning microscope. The instrument has been specifically designed to meet the requirements for clinical applications that are small footprint, high NIR transmission, large field of view, high sensitivity in order to detect low-intensity signals in the vis-NIR spectral range, and, most importantly, simple operation. The laser is scanned across the sample using a galvanometric mirror pair. A  $20\times 0.4$  NIR objective (Mitutoyo, Japan) focuses the laser onto the sample. The CARS, TPEF, and SHG signals are spectrally filtered from the exciting laser light using two short-pass filters at 750

and 770 nm (Semrock, U.S.A.) and detected in forward direction by a NIR-sensitive photomultiplier tube (H6780-20, Hamamatsu, Japan). In order to separate CARS and the combined SHG/TPEF signals, an additional 600 nm long-pass filter has been used for CARS and a 600 nm short-pass filter for detecting the TPEF/SHG signals excited by the pump laser beam at 900 nm.

For testing, a thin tissue section of a human artery fixed on a  $CaF_2$  slide has been investigated by multispectral CARS microscopy in the C-H stretching vibrational range from 2700 to 3000  $cm^{-1}$  first using the seeded laser of 1  $cm^{-1}$  spectral resolution in steps of 13  $cm^{-1}$  and by TPEF-SHG microscopy utilizing 30 mW of laser power at the sample corresponding to peak intensity levels of  $80 \times 10^{12} W/m^2$  (for an objective NA 0.4, 1 MHz repetition rate, 65 ps pulse duration), which is tolerable by tissue samples (the tolerable peak intensity has been estimated to be  $750 \times 10^{12} W/m^2$  for 3 mW of a 190 fs 82 MHz pulse train at 830 nm focused by a NA 0.9 objective).[9] The peak intensity has been calculated as follows:  $I_{peak} = 4P_{sample}/(k\tau\pi d_{min}^2)$  Here  $I_{peak}$  represents the peak intensity,  $P_{sample}$  is the average power at the sample,  $k$  is the laser repetition rate,  $\tau$  is the pulse duration, the focal spot area is  $0.25\pi d_{min}^2$ , which is for a Gaussian beam according to the diffraction limit  $d_{min} = 1.22\lambda/NA$ . For imaging the following data acquisition parameters were employed: pixel dwell time  $1\mu s$ , image size  $402 \times 905\mu m^2$  corresponding to  $2048 \times 4096$  pixel, averaging of two frames, total image acquisition time 20 s per image. These parameters can be compared to measurements with the fiber laser of 30  $cm^{-1}$  spectral resolution resulting in the following parameters: image size of  $720 \times 360\mu m^2$ ,  $2700 \times 1350$  pixel,  $1\mu s$  pixel dwell time, two frames averaged. The specimen of perivascular, i.e., periadventitial tissue of a human artery, was procured at the University Hospital, Jena. After multimodal nonlinear microscopic investigation the tissue section was histopathologically examined utilizing elastic van Gieson's stain (EVG) for visualizing elastic as well as collagen fibers and cell nuclei. The second specimen under investigation is a cross section of an artery of a rabbit model for atherosclerosis fed with a high-cholesterol diet. The specimen has been imaged utilizing multimodal nonlinear imaging combining SHG, TPEF, and single-band CARS at 2850  $cm^{-1}$  of low spectral resolution with multispectral CARS of 1  $cm^{-1}$  spectral resolution.

Constant laser intensity was ensured prior to each individual scan by monitoring the laser power using a power meter. Deviations were corrected by a polarizing beam splitter. The data were analyzed using imageJ.[68, 69, 70, 71] All images were corrected for residual small laser intensity drifts by normalizing the images to an area of purely nonresonant FWM. The nonresonant FWM signal is affected by the same intensity dependence as the CARS signal of interest, i.e.,  $I_{CARS/FWM} \propto I_{Pump}^2 \cdot I_{Stokes}$ . This area is indicated by a red square in Figure 2 and was chosen such that it contains only a piece of the  $CaF_2$  slide. To correct for a laser beam drift of the pointing direction and motion of the sample due to vibrations during acquisition of the whole image series, the images were realigned and combined to an image stack, using the TransformJ and the registration plug-in linear stack alignment with SIFT (Fiji). To reduce system noise the raw images have been median-filtered by two pixels radius, which is not affecting the spatial resolution, since one pixel corresponds to 250 nm and the diffraction-limited lateral resolutions is about  $1\mu m$ . CARS spectra were retrieved by plotting the intensity in a pixel or an area of the image as a function of the wavenumber shift of the exciting fiber laser using imageJ's built-in "plot z-axis profile" function. The net total acquisition time per CARS spectrum is  $40\mu s$  corresponding to  $2\mu s$  for each of the 20 wavenumber steps. The standard deviation was calculated from the eight surrounding pixels and is a good measure of fluctuations due to laser, electronic, and photon shot noise. Intensity profiles at specific wavenumber positions were calculated using the line profile function of ImageJ.[68] The intensity profiles were filtered by 50 point moving average filter to remove noise.

## Results and Discussion

The key aspect of multispectral CARS imaging is to acquire both spatially and spectrally highly resolved CARS images for subsequent analysis. Imaging at a single vibrational resonance is insufficient for determining the chemical composition, i.e., the morphochemistry, of a complex sample, since the observed spatial intensity fluctuations may originate from other sample properties than chemical gradients. Differences in absorption and scattering change the incident laser intensity and the-

refore also significantly the generated CARS signal intensity, in particular as CARS signal generation is a nonlinear process. Even after correction for changes in the incident intensity the residual fluctuations in the CARS intensity originate either from varying concentrations of the probed vibrational oscillator or from intensity fluctuations due to differences in the scattering properties of the tissue above the probed volume but also from contributions of other chemical species also possessing a vibrational resonance within the probed spectral width. Disentanglement of these contributions is impossible by single-band CARS imaging. Resolving this issue is especially demanding when CARS imaging is performed in the C-H stretching vibrational region as all biomolecules' vibrational spectra feature Raman resonances in this spectral window, which are spectrally broad and therefore overlapping. Nonetheless, CARS microscopy is primarily employed in this spectral range due to the large Raman scattering cross sections of C-H stretching vibrations allowing for high image acquisition speeds.[29] Thus, the Raman spectra of major biomolecules are more difficult to discern in the C-H stretching region than in the fingerprint spectral region. However, disease recognition solely within the C-H stretching spectral region has been recently demonstrated by spontaneous Raman spectroscopy.[35, 36] Thereby the differentiation of lipid, protein, and DNA contributions for the detection of cell nuclei has been successfully demonstrated in Raman imaging in the C-H stretching spectral window.[37] The same will be true but more demanding in the case of spectral CARS imaging as will be shown in the following.

To evaluate the potential of C-H multiplex CARS/SHG/TPEF multimodal imaging for highlighting the tissue's morphochemistry, i.e., the morphology along with the chemical composition, first a tissue section of human perivascular, i.e., periadventitial, tissue was investigated by SHG imaging in combination with multispectral CARS microscopy in the C-H stretching wavenumber region. The results are depicted in Figures 1–3. The two strong vibrational resonances around 2844 and 2942  $\text{cm}^{-1}$  are assigned to the aliphatic C-H stretching vibration of methylene and methyl groups.[72, 73, 74]

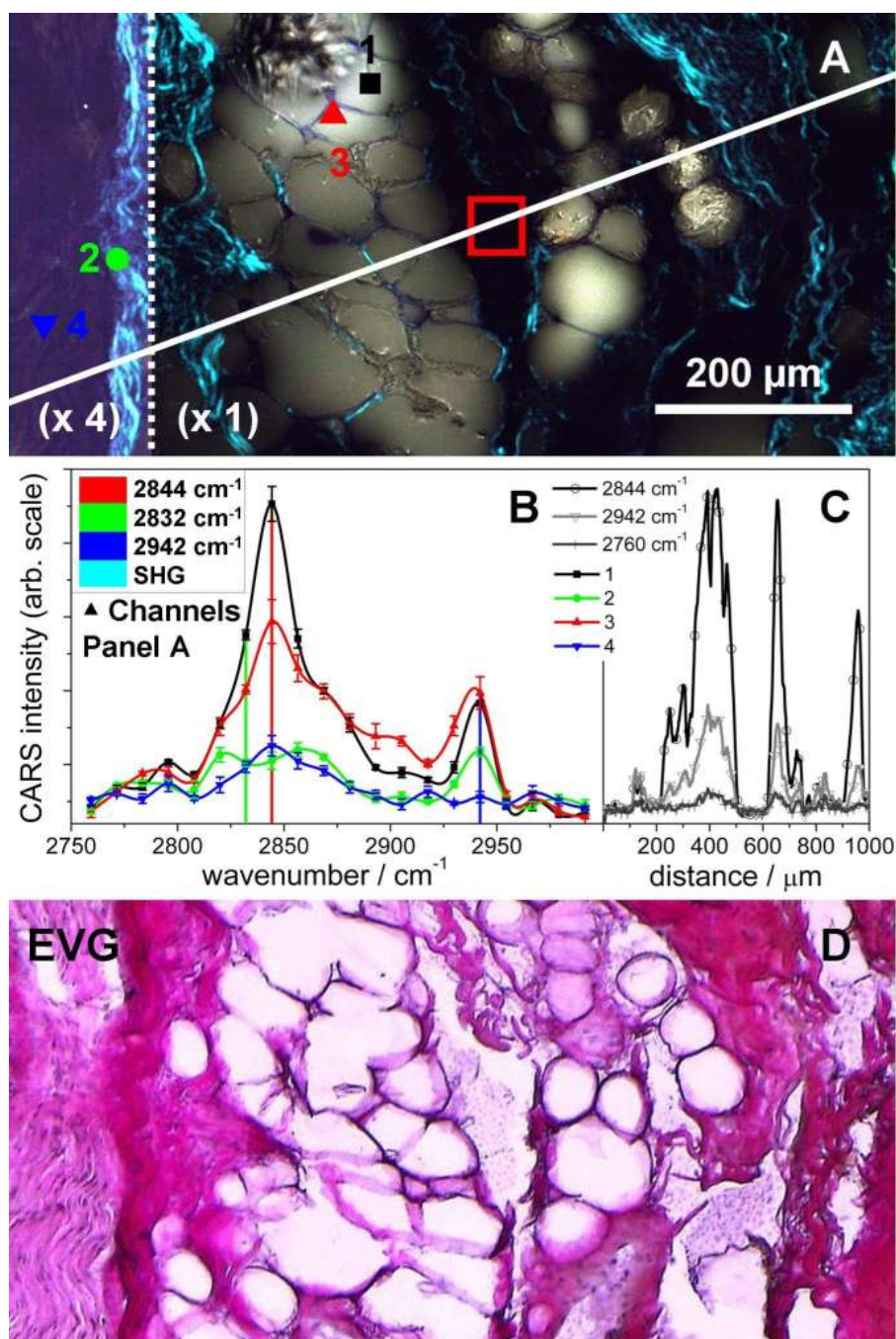


**Figure 1** – (A) Multimodal multispectral high spectral resolution CARS and SHG image of a human perivascular tissue section allows for high-contrast vibrational imaging of major constituents as indicated: (1) lipid droplets in adipocyte, (2) collagen fibers of the connective tissue blue (CARS)/cyan (SHG), (3) cell membranes and cytoplasm of the adipocytes, and (4) myelin sheaths around the axons of a bundle of nerves. To increase the visibility of the myelin sheets, the brightness of the left area of panel A has been enhanced as indicated.



**continued caption Figure 1** Red square: area of pure nonresonant signal from the  $CaF_2$  substrate has been used to normalize the CARS spectra in panel C to correct for residual laser intensity fluctuations. The detected structures are validated by consecutive EVG staining, panel B, demonstrating perfect correspondence. On the left a nerve bundle can be seen; the voids are adipocytes, and the red fibers correspond to collagen fibers in excellent agreement with label-free nonlinear microscopy. The distinct CARS spectra of the four structures within the C-H stretching region are reproduced in panel C. The error bars correspond to the standard deviation with respect to the eight neighboring pixels. Along the white line in panel A intensity profiles at three wavenumber positions off-resonant at  $2760\text{ cm}^{-1}$  and in resonance with  $CH_2$  and  $CH_3$  groups have been acquired and plotted in panel D to estimate the resonant image contrast. Apart from the Raman resonance the image contrast depends on the concentration and on the molecular species. In case of triglycerides within adipocytes the contrast is about 20 at  $2844\text{ cm}^{-1}$  and 5 at  $2942\text{ cm}^{-1}$ . In case of protein structures the contrast is 3-4 for collagen and 2 for myelin for both resonances (for more details see text). Image parameters: image size  $905 \times 402\ \mu\text{m}^2$ ,  $4096 \times 2048$  pixels, spectral resolution  $1\text{ cm}^{-1}$ , pixel dwell time  $1\ \mu\text{s}$ , averaging of two frames, acquisition time 20 s per image, 20 images in the range from  $2750$  to  $3000\text{ cm}^{-1}$ ,  $40\ \mu\text{s}$  per spectrum.

---

In panel A of Figure 1 a combined SHG and CARS image at three Raman resonances within the C-H stretching region is displayed, showing the SHG intensity in cyan, while the CARS intensity of the symmetric  $CH_2$  stretch vibration is displayed in red at  $2844\text{ cm}^{-1}$  and in green at  $2832\text{ cm}^{-1}$ , whereas the resonance at  $2942\text{ cm}^{-1}$  assigned to the Fermi resonance of the symmetric  $CH_3$  stretch vibration is depicted in blue.[74] This multiplex CARS image set of a human tissue section of adipose tissue in the C-H stretching wavenumber region was recorded with  $1\text{ cm}^{-1}$  spectral resolution and a step size of  $13\text{ cm}^{-1}$ . The nonresonant background, which has been used to correct the spectral data in Figure 1 B, Figure 2, panels D and E, and Figure 3 F for residual intensity differences. Figure 1 A allows for discerning four different structures as indicated: lipid droplets in adipocytes in yellow (1), collagen fibers of the connective tissue blue (CARS), cyan (SHG) (2), cell membranes and cytoplasm of the adipocytes in blue (3), and myelin sheaths around the axons of a bundle of nerves (4). The discrimination of the four morphologic structures is based

---

on differences in the chemical composition, which are reflected in the CARS spectra within the C-H stretching region plotted in panel B of Figure 1.

The quality of the CARS spectra is excellent taking into account the short net acquisition time of each spectrum of only  $40\mu\text{s}$ , which corresponds to the accumulated pixel dwell time of 20 wavenumber steps, whereas Raman spectra possessing a similar signal-to-noise ratio require typically orders of magnitude longer integration times.[27] In order to visualize the myelin sheaths clearly, the contrast on the left of the image shown in Figure 1 A has been enhanced by a factor of 4. Position 1 in Figure 1 A corresponds to the lipid droplet of an adipocyte filled mainly with triglycerides. Indeed, the CARS spectrum (see Figure 1 B) is characterized by high signal intensity and a stronger signal at  $2844\text{ cm}^{-1}$  than at  $2942\text{ cm}^{-1}$ . This corresponds structurally to a ratio of  $\text{CH}_2$  to  $\text{CH}_3$  functional groups of greater than 1 which is in agreement with the structure of triglycerides containing fatty acids of chain lengths starting from four carbon atoms. The spectrum of protein fibers (Figure 1 A, position 2) is different from that recorded at position 1 in showing two separate bands at  $2820$  and  $2856\text{ cm}^{-1}$  assigned to the symmetric  $\text{CH}_2$  and  $\text{CH}_3$  stretching vibrations and a similarly intense band at  $2942\text{ cm}^{-1}$  of the Fermi resonance of the  $\text{CH}_3$  stretch vibrations.[74] These differences in the intensity ratio of the bands around  $2844$  and  $2942\text{ cm}^{-1}$  are due to the different ratio of  $\text{CH}_2/\text{CH}_3$ -functional groups in lipids and proteins. This ratio is high in lipids (on average  $> 10$ ) and close to 2 in proteins. Additional variations in the peak position of protein and triglyceride CARS spectra are based on strong variations in the chemical environment of the methylene and methyl groups of proteins in comparison to the highly uniform methylene groups in long-chain fatty acids of triglycerides. The on average lower intensity of the CARS spectrum of protein fibers is due to a lower Raman cross section and a lower number density of the scattering structures in proteins in comparison to triglycerides condensed in lipid droplets of adipocytes. In position 3 of Figure 1 A both the proteins of the cytoplasm as well as the lipid cell membrane of the adipocytes contribute to the CARS signals. Therefore, the CARS spectrum of the cytoplasm is characterized by shoulders at the peak positions of the protein bands in addition to the two strong lipid bands. Furthermore, it is weaker in intensity than the spectrum of triglycerides.

The CARS spectrum of myelin in location 4 of Figure 1 A is very weak in intensity with respect to the triglyceride spectrum, but clearly a lipid and not a protein spectrum. This is evident from the strong symmetric  $CH_2$  stretching band at  $2844\text{ cm}^{-1}$ . Due to the low intensity, further spectral characteristics are not assignable.

For comparison the multimodal image is contrasted to a standard histopathologic EVG staining image plotted in panel D of Figure 1, which is a standard stain of connective tissue to detect and discern collagen and elastin. In agreement with SHG imaging, the visible protein fibers are composed of collagen, while no elastic fibers can be seen, which would be colored dark blue to black.

In the following the spectral assignment will be discussed in more detail, since it is not clear that the peak position in CARS spectroscopy coincides with the band positions known from linear vibrational, i.e., infrared and Raman spectroscopy, because as mentioned above this depends on another parameter, the nonlinear background. The chemical specificity as a key parameter for molecular CARS imaging depends on the nonlinear background. The molecule unspecific nonresonant background originates from FWM processes not incorporating Raman resonances and generates within a spectral width of several  $10\text{ cm}^{-1}$  a constant signal, which interferes with the vibrationally resonant CARS signal. The molecular contrast is the ratio of the CARS intensities in and off a Raman resonance and is a measure of the molecular specificity. The molecular contrast has been estimated for the measurement displayed in Figure 1A by plotting intensity profiles (Figure 1C) along the white line shown in Figure 1A at the  $CH_2$  and  $CH_3$  Raman resonances at  $2844$  and  $2942\text{ cm}^{-1}$  well as in off-resonance at  $2760\text{ cm}^{-1}$ . Apart from the line shape, i.e., bandwidth, and Raman scattering cross section of the molecule, the molecular contrast depends also on the number density of scattering molecules itself. In case of triglycerides within adipocytes the molecular contrast is about 20 at  $2844\text{ cm}^{-1}$  and 5 at  $2942\text{ cm}^{-1}$ . In case of protein structures the contrast is 3-4 for collagen for both Raman resonances and 2 for myelin at  $2850\text{ cm}^{-1}$ . However, the background level does not only originate from the contrast limiting nonresonant background, but a major source of the detected signal at a vibrationally silent spectral position originates from residual stray light and noise of the detection electronics.

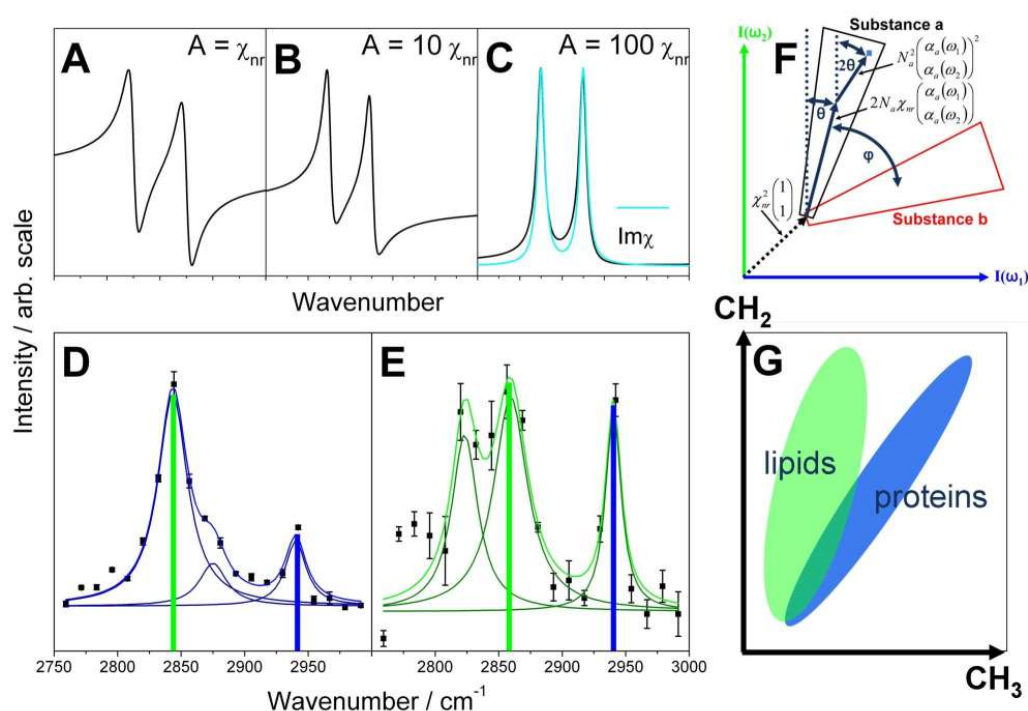


**Figure 2** – Comparison of artificial CARS spectra of two resonances of  $30 \text{ cm}^{-1}$  spectral width for varying ratios of nonresonant background  $\chi_{nr}$  to the Lorentzian peak area  $A$  in panels A-C with normalized CARS spectra of a lipid droplet of an adipocyte (D) and a collagen fiber (E) measured by high spectral resolution CARS imaging. In case of low nonresonant background (C), the CARS spectrum agrees well with the Raman spectrum, which corresponds to the imaginary part of the third-order susceptibility  $\chi^{(3)}$ . The CARS spectra can be analyzed by fitting Lorentzian peak functions. The peak positions agree well with the position of Raman resonances of methylene and methyl groups and are not significantly shifted by interference with the nonresonant background. The error bars originate from photon shot noise as well as pixel-to-pixel concentration differences in locations 1 and 2 of Figure 1. Panel G illustrates that biomolecules like proteins and triglycerides are characterized by distinct ratios of methylene to methyl groups. This structural difference is used to discern lipids and proteins in CARS imaging at two resonances characteristic for  $\text{CH}_3$  and  $\text{CH}_2$  groups by calculating the frequency scatter plot, i.e., the 2D histogram, displayed in Figures 3 and 4. A two-dimensional histogram of CARS images at two resonances  $\omega_1$  and  $\omega_2$  is displayed in panel F. Three vectorial components contribute to the intensity pair in the plot, as shown in equation 2, which results in changing pointing direction of the segment from  $\theta$  to  $2\theta$  for high-intensity pixels. Bright areas correspond to highly abundant pixel intensity values. Molecules of similar CARS intensity ratio at two frequencies  $\omega_1$  and  $\omega_2$  cluster in specific segments of the plot, marked by a and b. The segments of the molecular markers of different intensity ratios  $\omega_1$  and  $\omega_2$  are separated by the separation angle  $\phi$ , which increases for high spectral resolution CARS (D). High concentrations correspond to a large distance to the origin. Here the separation of the markers is better than for the laser in panel C. At low intensity, discrimination of markers a and b is more difficult due to lower signal-to-noise ratio and the decreasing separation. Back-projecting of the segmented areas onto the original image allows locating lipid and protein contributions in the original image (see Figure 4).

Another option to estimate the nonlinear background intensity is based on the shape of the CARS spectra, since the spectral shape is highly influenced by interference with the nonresonant background. The detected CARS intensity at the laser frequency difference  $\Delta\omega = \omega_{pump} - \omega_{Stokes}$  is given by:[75, 76]

$$I_{CARS}(\Delta\omega) = |\chi_{nr} + \sum_k \sum_i \chi_r^{ki}(\Delta\omega)|^2 \longleftrightarrow \chi_r^i = \frac{A_i}{\omega_0^i - \Delta\omega - i\Gamma_i} \quad (1)$$

The index  $k$  denotes the molecular species within the laser focus, and the index  $i$  counts the number of Raman resonances  $\omega_0^i$  of each Raman-active substance  $k$ . The bandwidth of each vibration is given by  $\Gamma$ , whereas the intensity is governed by  $A$ . This constant depends in detail on the number density as well as the cross section for the Raman scattering process. For a constant width  $\Gamma$  the band shape is determined by the ratio of  $A$  to the magnitude of the nonresonant background  $\chi_{nr}$ . In Figure 2 simulations of CARS spectra consisting of two isolated resonances have been calculated for a fixed  $\Gamma = 30\text{cm}^{-1}$  and three different ratios of  $A$  to  $\chi_{nr}$  ranging from 1 to 100 in panels A-C. These artificial spectra are contrasted to average CARS spectra of a lipid droplet (position 1 Figure 1A) and a collagen protein fiber (position 2 Figure 1A) displayed in panels D and E of Figure 2. As can be seen in Figure 2 A-C, when the nonresonant background is small, the spectral shift of CARS resonances to lower wavenumber with respect to the corresponding Raman resonance is negligible and the band shape is almost Lorentzian. When fitting the experimental CARS spectra with three Lorentzian peak functions the spectral shape is very well reproduced within the margin of error of the experimental data. Thus, the molecular contrast for the observed structures corresponds to  $A/\chi_{nr}$  ratios in the range from 10 to 100, which simplifies interpretation of the CARS data, since the band positions are within the accuracy of the measurement identical to the ones in the Raman spectra, as indicated in Figure 2C. For a high  $A/\chi_{nr}$  ratio the CARS spectrum can be approximated by the imaginary part of the third-order susceptibility  $\chi_r^i$ , which corresponds to the Raman spectrum. Table 1 summarizes the data from a Lorentzian fit of the CARS spectra shown in Figure 2, panels D and E. Here, the Raman resonance frequency  $\omega_0$ , resonance bandwidth  $\Gamma$ , and amplitude  $A$  ha-

ve been fitted. Given are resonance frequency  $\omega_0$  and bandwidth  $\Gamma$  as characteristic parameters for comparison with Raman spectroscopy of biomolecules.[72, 73, 74, 77]

**Table S 1** – Resulting Fit-Parameters Resonance Frequency  $\omega_0$  and Spectral Bandwidth  $\Gamma$  from Fitting Lorentzian Peak Functions to the CARS Spectra of Triglycerides and Proteins, see Figure 2, panels D and E

<b>triglycerides</b>		<b>proteins</b>	
$\omega_0$	$\Gamma$	$\omega_0$	$\Gamma$
( $cm^{-1}$ )	( $cm^{-1}$ )	( $cm^{-1}$ )	( $cm^{-1}$ )
2843	28	2823	25
2875	26	2859	32
2940	20	2940	15

Interestingly, within the accuracy of the spectral CARS measurement, which corresponds in this case to the spectral step size of  $13\text{ cm}^{-1}$ , no shift in band position with respect to other vibrational spectroscopy tools is evident.[72, 73, 74, 77] Therefore, when imaging strong resonances and high-concentrated species in the C-H stretching vibrational region of biological tissue, i.e., when the resonant signal is significantly larger than the nonresonant background, the band shape is not distorted. Interference effects become significant if the ratio of  $A/\chi_{nr}$  approaches 1. This is the case if the nonresonant background is large, e.g., when using UV-vis and/or spectrally broad femtosecond lasers for CARS imaging, but also when either a weak Raman resonance or a resonance of a dilute species is to be detected.

Nevertheless, the relative intensity ratios of the bands are different comparing CARS and Raman spectroscopy. This is due to the fact that in Raman spectroscopy the signal intensity is linearly dependent on the concentration. In case of CARS, however, the concentration dependence of the signal intensity changes from a quadratic behavior for high concentrations to a linear behavior for low concentrations of scattering molecules. This is again a consequence of the coherent mixing of the resonant

and nonresonant CARS susceptibility contributions and the proportionality of the CARS signal intensity to the squared modulus of the overall third-order susceptibility. Due to the nonlinear concentration dependence of the signal, quantification is difficult.[46, 78, 79] Furthermore, due to interference the CARS spectrum of a mixture of analytes is not only the weighted sum of the CARS spectra of the individual components. However, qualitative analysis of the tissue composition equivalent to staining histopathology can be performed by multispectral CARS imaging in a fast and simple way for a few wavenumber steps.

An intuitive way to qualitatively correlate the intensity at different wavenumber positions to the composition is sketched in panels F and G of Figure 2. In panel G a two-dimensional plot of the number of methylene and methyl groups per protein and lipid molecule is shown. The axes correspond to the number of  $CH_3$  and  $CH_2$  functional groups within a single molecule. Lipids are characterized by a higher ratio of  $CH_2$  to  $CH_3$  functional groups than proteins, which is why both groups of biomolecules cluster in different areas of the plot. This structural difference can be used for a discrimination by multispectral CARS imaging utilizing colocalization analysis. A two-dimensional histogram, the frequency scatter plot, enables differentiation of lipids and proteins by their distinct  $CH_2/CH_3$  ratio, when CARS images at two resonances characteristic for  $CH_2$  and  $CH_3$  functional groups are used. Such scatter plots are known from colocalization analysis in order to separate multiple fluorescent labels with overlapping fluorescence emission spectra.[70] However, the interpretation is different in CARS imaging. In the three-dimensional frequency scatter plots, the x and y coordinates correspond to the intensity values of two image channels. The intensity of a pixel in the scatter plot complies with the abundance of the respective pair of intensity values in the two images. When performing this analysis for two characteristic Raman resonances for methyl and methylene groups as indicated in the CARS spectra of proteins and lipids in panels D and E of Figure 2, molecules with the same ratio of methyl to methylene groups concentrate in characteristic areas of the plot. In detail, the relationship between pixel intensity and concentration is more complex as indicated in eq 2, since the nonlinear susceptibilities  $\chi$  depend on the number  $N$  of scattering particles  $k$  within the probed focal

volume weighted by the scattering cross section  $\alpha_k$  of the particular molecule. The two-dimensional vector of CARS signal intensities of the molecule  $k$  at two frequencies  $\omega_1$  and  $\omega_2$  is related to the modulus squared of the third-order susceptibility  $\chi^{(3)}$ . For a molecule  $k$ , this quantity can be expressed as the number of molecules  $k$ , denoted  $N_k$  times the molecules' polarizability  $\alpha$  at the respective frequency. When rearranging the terms, three vectorial components can be discerned. The first is the nonresonant background, which corresponds to an offset of the origin along the diagonal. Since the background is low, as discussed above, this offset is only small under the applied imaging conditions. The other two components correspond to terms linear and quadratic in the number of molecules. For small concentrations, the linear term dominates. This vector is aligned at an angle  $\theta$  to the  $y$  axis. For high concentrations the component quadratic in the concentration contributes markedly to the overall signal, oriented at the angle  $2\theta$  to the  $y$  axis. Therefore, the cloud in the scatter plot changes the direction at higher concentration. As evident from eq 2, the position in the scatter plot is not directly related to the concentration, but the number of molecules is weighted with the polarizability  $\alpha$  at the frequency  $\omega$ .

$$\begin{pmatrix} I^k(\omega_1) \\ I_a^k(\omega_2) \end{pmatrix} \propto \begin{pmatrix} |\chi_{nr} + \chi_r^k(\omega_1)|^2 \\ |\chi_{nr} + \chi_r^k(\omega_2)|^2 \end{pmatrix} \longleftrightarrow \chi^{(3)} = N \cdot \alpha^{(3)} \quad (2)$$

$$\begin{pmatrix} I^k(\omega_1) \\ I_a^k(\omega_2) \end{pmatrix} \propto N_k^2 \cdot \begin{pmatrix} \alpha^k(\omega_1)^2 \\ \alpha^k(\omega_2)^2 \end{pmatrix} + N_k \begin{pmatrix} \alpha^k(\omega_1) \\ \alpha^k(\omega_2) \end{pmatrix} + \chi_{nr}^2 \begin{pmatrix} 1 \\ 1 \end{pmatrix} \quad (3)$$

In Figure 2F, the three vectorial CARS signal contributions at a certain pixel position in the scatter plot are separately sketched and the angles of  $\theta$  and  $2\theta$  to the  $y$  axis are indicated. Substances of different intensity ratios at the two frequencies concentrate in different areas of the plot, indicated by the red and black segments. The central directions of the segments are separated by the angle  $\phi$ . A larger spectral separation results in a larger separation angle  $\phi$  allowing one to discern marker  $a$  from  $b$ . Furthermore, the separation angle  $\phi$  as a measure of spectral distance of two molecular markers is maximized for higher spectral resolution as illustrated in Figure 3 by comparing panels C and D, which substantiates the proposed improvement in chemical contrast for high spectral resolution CARS imaging. The origin of



the coordinate system corresponds to the zero intensity in both images used to construct the frequency scatter plots. The lowest intensity in CARS images is usually a nonzero intensity, the nonresonant background. In experimental data, further offset contributions arise from noise of the detection electronics and stray light. Separation of two marker substances in the low-intensity region is difficult. In particular, the relative intensity error due to photon shot noise, which is proportional to the square root of the intensity values, increases for low-intensity pixels. The larger the distance to the origin, the higher the intensity value, and therefore, the better the separation of the markers, exemplarily illustrated for two marker substances labeled a and b in panel F of Figure 2. Areas in the upper left and lower right of the frequency scatter plot are occupied by pixels of high intensity in only one of the two channels, but not in both. In traditional colocalization analysis, these areas are not due to colocalized pixels, but reflect pixels occupied by a single marker. However, as evident from Figure 2G, for organic substances this configuration is rare for imaging  $CH_2$  and  $CH_3$ , since abundant biomolecules carry both functional groups. Pixels in which marker a and b are both present will be located in between the sketched segments of both pure substances.

Quantitative analysis of the signals is difficult, due to the complex relation between the number  $N$  and the pixel intensity (eq 2). However, qualitatively, the pixel color directly correlates with the composition and the distance to the origin in the scatter plot is still a relative measure of the number  $N$  of scattering molecules of index  $k$ , e.g., proteins or lipids, as will be shown in the following.

In Figure 3 CARS imaging at two different wavenumber positions has been performed utilizing a  $30\text{ cm}^{-1}$  spectral resolution fiber laser in panel A and a fiber laser of  $\text{cm}^{-1}$  spectral resolution in panel B. CARS signals at the symmetric C-H stretching resonance frequency of methylene groups at  $2850\text{ cm}^{-1}$  are displayed in green, while the intensity of C-H stretching resonance characteristic for methyl groups at  $2930\text{ cm}^{-1}$  is plotted in blue. The precise wavenumber positions may vary in Figures 1, 3, and 4, representing the exact spectral position for the CARS measurements shown. However, taking into account the spectral widths of the respective resonances (Figure 2, panels D and E), the differences in spectral position are negligible. The

resulting images allow for a differentiation of proteins and lipids due to different coloring. Proteins concentrated in the cytoplasm appear bluish, e.g., blue triangles in panels A and B, as well as collagen fibers displayed in panel B (which were too faint to be imaged in panel A), while triglycerides concentrated in the lipid droplets of adipocytes appear bright green in both images (green triangles). In order to quantify that higher spectral resolution improves the discrimination of chemically similar structures, frequency scatter plots of the images in panels A and B are displayed in panels C and D. Two spectrally separate components are discernible. The larger and more intense lipid droplets dominate the plot in a segment of larger slope. The protein component, i.e., cytoplasm and protein fibers, appears in a segment of smaller slope and maximum intensity below the adipocyte signal. As evident, the separation angle is increased in case of high-resolution imaging, which improves the separation and discrimination of both signals significantly. In case of spectrally well-separated resonances this is less critical than for spectrally close-lying resonances. The advantage of higher spectral resolution is also apparent when comparing the CARS spectra corresponding to both laser concepts in panels E and F of Figure 3. The spectra from triglycerides and the cytoplasm obtained with the low spectral resolution laser source show a broad resonance peak without structure, while the laser of  $1\text{ cm}^{-1}$  spectral resolution provides two distinct CARS resonances together with shoulders allowing one to discern four structures by their characteristic CARS spectra as already illustrated in Figure 1 C. As indicated by the black dotted lines in Figure 3, panels C and D, the direction of the lipid component slightly bends at higher intensities due to the increasing contribution of the term quadratic in concentration.

In summary imaging at two resonances only enables the differentiation of protein and lipid structures while further Raman resonances provide evidence for additional constituents. Therefore, multispectral CARS imaging at high spectral resolution complements data from single-band CARS multi-modal nonlinear imaging and is as such particularly important for biomedical imaging. This is illustrated for an animal model for atherosclerosis in Figure 4. Panel A shows the combined multimodal image fusing data from SHG, TPEF, and CARS at the aliphatic C-H stretching frequency

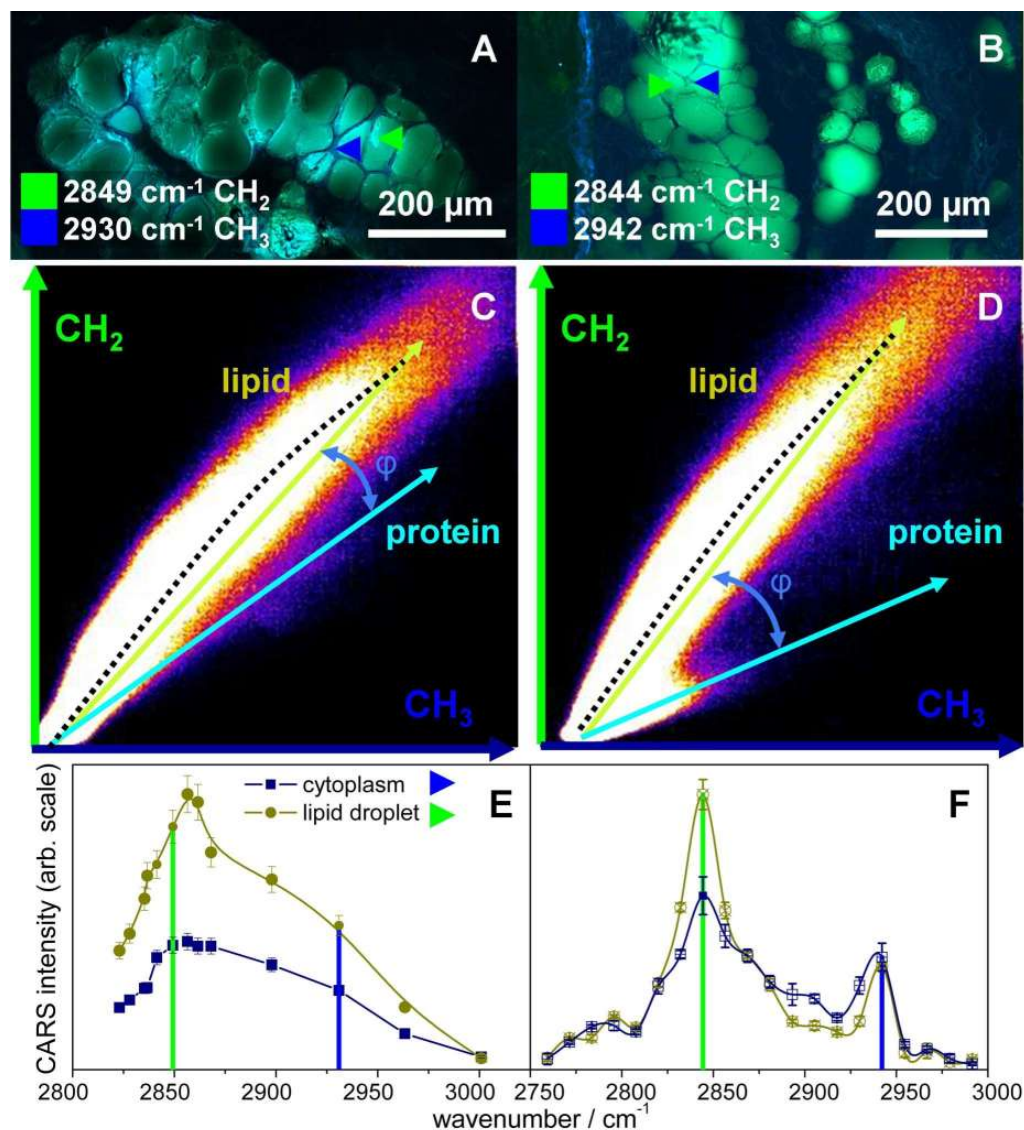


**Figure 3** – Advantages of  $1\text{ cm}^{-1}$  high spectral resolution CARS imaging are contrasted by comparison with  $30\text{ cm}^{-1}$  CARS data for qualitatively discerning protein from lipid structures in a two-color CARS image at the C-H stretching resonance of  $CH_3$  (blue) and  $CH_2$  (green) groups. The protein-rich cytoplasm is displayed in blue and lipids in green. The spectral separation of both components is characterized by the separation angle  $\phi$  in the frequency scatter plots C and D, which is significantly increased for high spectral resolution CARS (D). Thus, high spectral resolution allows for a lower detection limit. Note also that the nonlinear concentration dependence manifests itself in a bending of the histogram point cloud corresponding to the lipid components, indicated by the black dotted line in panels C and D. Better separation of lipids and proteins at higher spectral resolution is also evident by comparing CARS spectra of lipid droplets and cytoplasm of adipocytes measured at  $30\text{ cm}^{-1}$  (E) and  $1\text{ cm}^{-1}$  spectral resolution (F).

of methylene groups at  $2850\text{ cm}^{-1}$ , while the images of the single modalities are plotted in panels B-D. While dense lipid contributions can be identified due to their high intensity in the single-band CARS image shown in Figure 4B by thresholding, lower concentrations of lipids and protein fibers of the arterial wall are of similar average intensity and therefore not discernible by single-band CARS. Therefore, the single-frequency CARS image is displaying mainly the morphology but does not reveal further insight into the composition. TPEF signals are generated within the lipid deposits as well as within the vessel walls composed of elastic fibers as illustrated in Figure 4C. Within the plaque, oxidized fatty acids[46, 80] and fat-soluble dyes like carotenoids are major sources of autofluorescence, while TPEF signals within the tunica media originate from the fluorescent elastic protein elastin,[49, 81, 82] which is a major protein component of the artery. The TPEF signals are highly colocalized with SHG from collagen and smooth muscle cells.[49] Collagen as well as actin-myosin are major sources of SHG within the tunica media.[11] High concentrations of collagen can be also seen in the outermost layer, the tunica externa, composed of connective tissue and thus characterized by a high collagen content. Strong SHG signals are also apparent within the plaque deposits, which have been recently assigned to crystalline cholesterol, which is discussed as a possible cause of acute coronary death.[12] Hence, multimodal nonlinear imaging provides information on the distribution of protein fibers composed of collagen and elastin, oxidized fatty acids, crystalline cholesterol, and triglycerides, but the assignment is not definite. In particular, implicit knowledge on the abundance of certain molecules in morphologic structures is used to assign the fluorescence within plaques to different fluorophors than within the tunica media, even though no spectral difference is observed. Another complication arises from the fact that fluorescence signals are affected by processes like quenching or bleaching, which can significantly reduce the autofluorescence. This is especially critical, since autofluorescence signals are orders of magnitude weaker than that of efficient dye labels like rhodamine 6G or fluorescein, e.g., at 700 nm excitation wavelength the cross section of NADPH is  $0.04\text{ GM}$  ( $1\text{GM} = 10^{-50}\text{ cm}^4\text{s}$  per photon and per molecule),[13] while that of rhodamine exceeds 100 GM.[14] Similarly, SHG signals of collagen have been observed to vanish if the structure of the quasi-crystalline

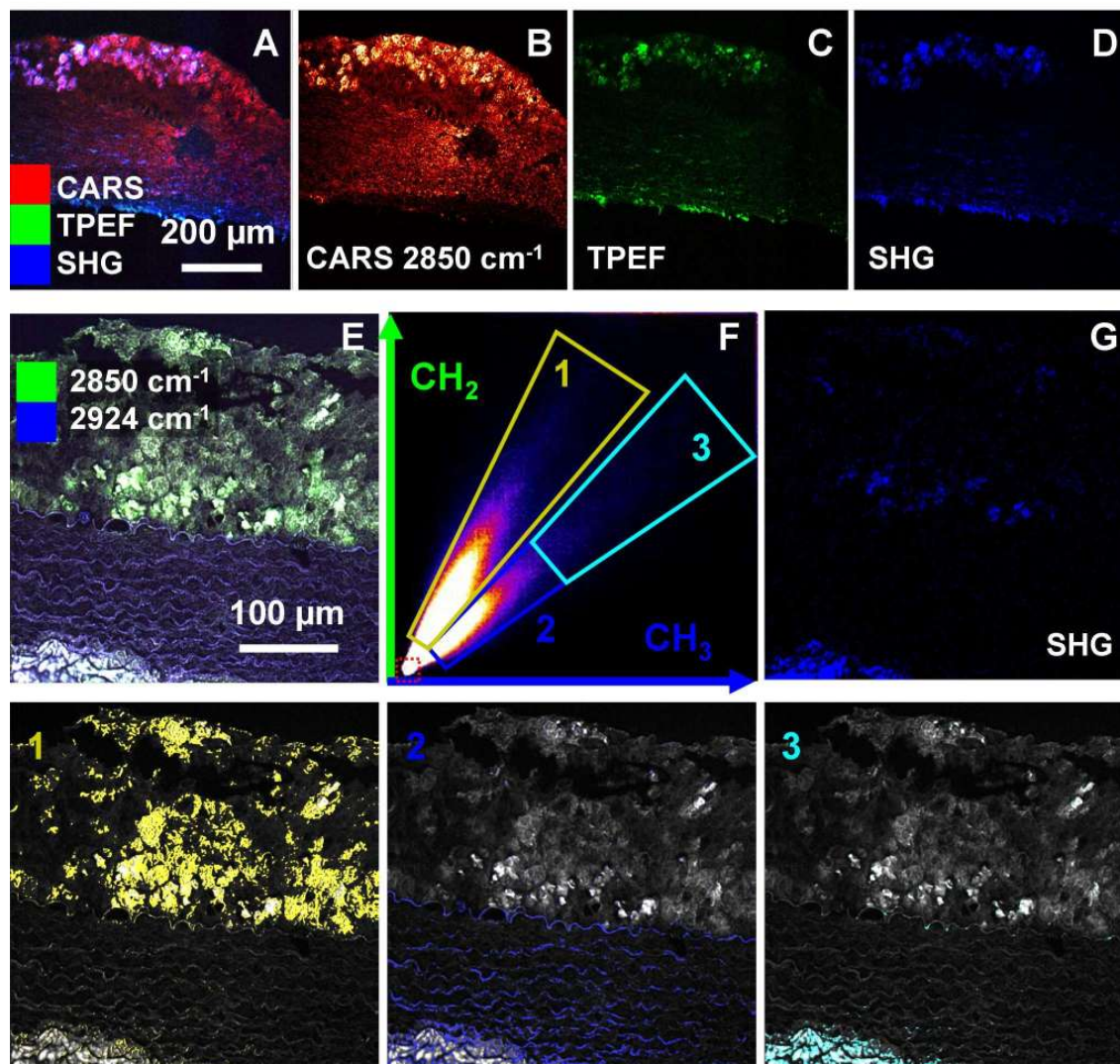


**Figure 4** – Analysis of the composition of an atherosclerotic lesion of a rabbit model for atherosclerosis by multimodal nonlinear imaging combining CARS at 2850  $\text{cm}^{-1}$ , SHG, and TPEF (A-D), which can be significantly improved by multispectral high-resolution CARS (E-G). CARS at 2850  $\text{cm}^{-1}$  allows detection of high-concentrated lipids (B) and visualization of the morphology but cannot discern low-concentrated lipids from protein. Fluorescent lipids and elastin are visualized by TPEF (C), while SHG detects cholesterol crystals and collagen (D) colocalized with elastin. CARS at  $\text{CH}_3$  (blue) and  $\text{CH}_2$  (green), panel E, allows discerning protein from lipid contributions. The frequency scatter plot (F) shows distinct segments of protein and lipid pixels. Back-projection localizes the lipid component within the plaque (1), the low-intensity protein component within the tunica media (2), and the high-intensity protein within the tunica externa (3), which allows identification of the SHG-active component in panel G in the tunica externa as collagen, while the SHG-active marker within the plaque is assigned to crystalline cholesterol.

collagen is altered during disease progression.[83] Therefore, alternative methods are needed for an assignment of SHG and fluorescent signals without knowledge of the abundance of SHG and TPEF markers in tissue structures and to detect collagen and elastin in tissue, even when their structure is altered such that SHG and TPEF signals vanish. This is accomplished by multispectral CARS as illustrated in the following. In panel E of Figure 4 a combined CARS image at 2850 and 2924  $\text{cm}^{-1}$  is displayed, allowing one to separate protein from lipid components. The frequency scatter plot in panel F underlines that two distinct molecular classes are present, proteins and lipids, clearly separated by a larger angle  $\phi$  than what has been observed for a low spectral resolution laser source (Figure 3C). By back-projecting the three boxed areas of the scatter plot onto the original image, the composition of different areas of the image becomes clear. The components 1-3 are plotted in the third row of Figure 4. The lipid component 1 is localized predominantly within the plaque, as expected, while the tunica media composed of low-intensity protein fibers corresponds to component 2. The tunica externa is also composed of protein, but of higher concentration, which is why component 3 is brighter than the protein fibers of component 2. By comparing the SHG image G with panels 1-3 it is evident that the SHG signal within the plaque originates in a lipid structure as is crystalline cholesterol, since only few molecules generate strong SHG signals. Furthermore, the fluorescence and SHG signals within tunica externa and tunica media are colocalized with protein structures detected by multispectral CARS imaging; therefore, the SHG signal originates in collagen and actin-myosin, while the TPEF signal is due to elastin, which are colocalized.[49] Therefore, multispectral CARS allows one to paint a more detailed map of the chemical composition of complex tissue samples enabling discrimination of distinct fluorescing markers and SHG-active molecules. In addition, the distribution of further Raman-active molecules can be visualized by multispectral CARS imaging at additional Raman resonances.

## Conclusion

High-resolution multispectral CARS imaging is a powerful method for high-speed visualization of the composition of complex tissue samples and as such a very expedient complement of nonlinear SHG and TPEF imaging. The presented low repetition rate laser source coupled to a home-built microscope resolves the incongruity of currently widespread 80 MHz lasers, which cannot provide simultaneously high peak power and high spectral resolution. Thus, this light source of high spectral resolution characterized by 65 ps pulse duration and 1 MHz repetition rate provides for the first time simultaneously high peak intensities for efficient SHG and TPEF generation in addition to high spectral resolution multispectral CARS imaging. In particular with respect to the spectral resolution this approach represents a significant improvement over previous attempts. To the best of our knowledge, only one reported light source enables spectrally higher resolved multispectral CARS imaging,[33] but this is due to the longer excitation wavelengths and lower peak power not suited for similarly efficient SHG and TPEF imaging. The presented method allows for orders of magnitude faster acquisition of CARS spectra with diffraction-limited spatial resolution than what can be obtained by state-of-the-art spontaneous Raman imaging.[27] Specifically, the CARS spectra in the C-H stretching region were obtained in 40 $\mu$ s per spectrum data acquisition time, while the acquisition of a single Raman spectrum takes at least 25 ms.[27] The pixel dwell time of 2 $\mu$ s is comparable to the fastest alternative multispectral Raman imaging systems using pixel dwell times of 4 $\mu$ s per wavenumber step [38] or even 200 $\mu$ s in SRS required for a more precise quantitative analysis.[84] Interpretation of the band position in the C-H stretching region is simple due to low nonresonant background and high concentrations of lipids and protein fibers. Hence, interference of CARS signals from different substances does not alter the peak position significantly. While quantitative analysis remains challenging due to the quadratic concentration dependence, qualitative decomposition into major compounds is possible. In this work for the first time colocalization analysis of CARS images at selected Raman resonances has been applied to analyze multispectral CARS data. Back-projection of areas of the scatter plot, which correspond to

pixels of similar color and therefore similar composition, substantiates and improves the assignment of colocalized TPEF and SHG signals to the originating molecular markers, e.g., SHG within atherosclerotic plaque deposits could be assigned to a lipid structure, i.e., crystalline cholesterol, while fluorescence and SHG signals within the tunica media and tunica externa originate in protein structures, i.e., elastin and collagen. Colocalization analysis specifically applied to two-color CARS imaging at 2850 and 2930  $\text{cm}^{-1}$  allows discrimination of lipid and protein structures by their characteristic color, which reflects their distinct ratio of  $\text{CH}_3$  to  $\text{CH}_2$  functional groups. Colocalization analysis further documents that the molecular contrast is significantly improved by high spectral resolution CARS imaging, since the separation angle  $\phi$  in the frequency scatter plot is substantially increased for higher spectral resolution. This observation suggests that high spectral resolution light sources are essential in order to discern Raman markers characterized by resonances in spectral proximity, e.g., separated at the spectral resolution limit.

CARS spectra in the C-H stretching region from 2750 to 3000  $\text{cm}^{-1}$  allow additionally discerning the protein-rich cytoplasm of adipocytes from the lipid droplets and from collagen fibers, while myelin around axons is identified as a lipid-rich structure. In summary, label-free nonlinear imaging utilizing multispectral CARS imaging at high spectral resolution provides detailed maps on the composition and morphology of tissue samples. The results perfectly agree with the golden standard of staining histopathology as demonstrated for a specific stain for elastic fibers, the EVG stain. Furthermore, the laser source is maintenance- and adjustment-free highly relevant for routine application, e.g., in clinical diagnostics. Due to the synchronized emission of pump and Stokes beam from a single fiber end, the spatial overlap of both colors is almost perfect, while the long pulse duration minimizes dispersion in the sample and focusing optics; therefore, no adjustment of the spatial or temporal overlap is required. Setting up the multimodal imaging platform is as simple as to chose the right filters and couple the laser into the microscope, which is a tremendous advantage for widespread application and to the best of our knowledge a unique feature of the presented approach. Thus, this method is in this experimentally facile realization combined with high signal yields, high spectral resolution, and imaging speeds up



to 1 Mpixel per second ready to use for label-free imaging in clinical environment and other more advanced biomedical imaging applications, e.g., surgical guidance, in the near future. Extension to imaging at Raman resonances within the fingerprint spectral region will very likely allow detecting additional marker molecules.

## Author Information

**Corresponding author:** \* Phone: +493641206300. Fax: +493641206399. E-mail: juergen.popp@ipht-jena.de.

**Notes:** The authors declare no competing financial interest.

## Acknowledgments

Financial support of the European Union via the Europäischer Fonds für Regionale Entwicklung (EFRE) and the "Thüringer Ministerium für Bildung Wissenschaft und Kultur (TMBWK)" (Projects: B714-07037, B578-06001, 14.90 HWP) and via the European network of excellence P4L (Photonics4Life) as well as financial support by the German Ministry for Science and Education (BMBF) *MediCARS* (FKZ 13N10773 and 13N10774) and the Carl-Zeiss-Stiftung is highly acknowledged.

## References

- [1] *Todesursachen in Deutschland*. Statistisches Bundesamt Wiesbaden, (2011).
- [2] Helmchen, F. and Denk, W. *Nature Methods* **2**(12), 932–940 (2005).
- [3] Wang, B.-G., König, K., and Halhuber, K.-J. *Journal of Microscopy* **238**(1), 1–20 (2010).
- [4] Campagnola, P. *Anal. Chem.* **83**(9), 3224–3231 (2011).
- [5] Theer, P., Hasan, M. T., and Denk, W. *Optics Letters* **28**(12), 1022–1024 (2003).
- [6] Theer, P. and Denk, W. *Journal of the Optical Society of America A* **23**(12), 3139–3149 (2006).
- [7] Kobat, D., Horton, N. G., and Xu, C. *Journal of Biomedical Optics* **16**(10), 106014 (2011).
- [8] Zipfel, W. R., Williams, R. M., Christie, R., Nikitin, A. Y., Hyman, B. T., and Webb, W. W. *Proceedings of the National Academy of Sciences of the United States of America* **100**(12), 7075–7080 (2003).
- [9] Hopt, A. and Neher, E. *Biophysical Journal* **80**(4), 2029–2036 April (2001).
- [10] König, K., Becker, T. W., Fischer, P., Riemann, I., and Halhuber, K.-J. *Optics Letters* **24**(2), 113–115 (1999).
- [11] Mohler, W., Millard, A. C., and Campagnola, P. J. *Methods* **29**(1), 97–109 (2003).

- [12] Suhalim, J. L., Chung, C.-Y., Lilledahl, M. B., Lim, R. S., Levi, M., Tromberg, B. J., and Potma, E. O. *Biophysical Journal* **102**(8), 1988–1995 (2012).
- [13] Huang, S., Heikal, A. A., and Webb, W. W. *Biophysical Journal* **82**(5), 2811–2825 (2002).
- [14] Xu, C. and Webb, W. W. *Journal of the Optical Society of America B* **13**(3), 481–491 (1996).
- [15] Cicchi, R., Sestini, S., De Giorgi, V., Massi, D., Lotti, T., and Pavone, F. S. *Journal of Biophotonics* **1**(1), 62–73 (2008).
- [16] Cicchi, R., Kapsokalyvas, D., Giorgi, V. D., Maio, V., Wiechen, A. V., Massi, D., Lotti, T., and Pavone, F. S. *Journal of Biophotonics* **3**(1-2), 34–43 (2010).
- [17] Cicchi, R., Vogler, N., Kapsokalyvas, D., Dietzek, B., Popp, J., and Pavone, F. S. *Journal of Biophotonics* **6**(2), 129–142 (2013).
- [18] Medyukhina, A., Vogler, N., Latka, I., Kemper, S., Böhm, M., Dietzek, B., and Popp, J. *Journal of Biophotonics* **4**(9), 627–636 September (2011).
- [19] Vogler, N., Medyukhina, A., Latka, I., Kemper, S., Böhm, M., Dietzek, B., and Popp, J. *Laser Physics Letters* **8**(8), 617–624 (2011).
- [20] Perry, S. W., Burke, R. M., and Brown, E. B. *Annals of Biomedical Engineering* (2012).
- [21] van Zandvoort, M., Engels, W., Douma, K., Beckers, L., oude Egbrink, M., Daemen, M., and Slaaf, D. W. *Journal of Vascular Research* **41**(1), 54–63 (2004).
- [22] Krafft, C., Dietzek, B., and Popp, J. *The Analyst* **134**(6), 1046–1057 (2009).
- [23] Krafft, C., Dietzek, B., Schmitt, M., and Popp, J. *Journal of Biomedical Optics* **17**(4), 40801 (2012).
- [24] Trulson, M. O. and Mathies, R. A. *The Journal of Chemical Physics* **84**(4), 2068–2074 (1986).
- [25] Kastrup, L. and Hell, S. W. *Angewandte Chemie International Edition* **43**(48), 6646–6649 (2004).
- [26] Barney, W. S., Wingen, L. M., Lakin, M. J., Brauers, T., Stutz, J., and Finlayson-Pitts, B. J. *The Journal of Physical Chemistry A* **104**(8), 1692–1699 (2000).
- [27] Okuno, M. and Hamaguchi, H.-o. *Optics Letters* **35**(24), 4096–4098 (2010).
- [28] Kneipp, J., Kneipp, H., and Kneipp, K. *Chemical Society Reviews* **37**(5), 1052–1060 April (2008).
- [29] Evans, C. L., Potma, E. O., Puoris'haag, M., Cote, D., Lin, C. P., and Xie, X. S. *Proc Natl Acad Sci U S A* **102**(46), 16807–16812 November (2005).
- [30] Saar, B. G., Freudiger, C. W., Reichman, J., Stanley, C. M., Holtom, G. R., and Xie, X. S. *Science* **330**(6009), 1368–1370 (2010).
- [31] Suhalim, J. L., Boik, J. C., Tromberg, B. J., and Potma, E. O. *Journal of Biophotonics* **5**(5-6), 387–395 (2012).
- [32] Kano, H. and Hamaguchi, H. *Optics Express* **13**(4), 1322–1327 (2005).
- [33] Bégin, S., Burgoyne, B., Mercier, V., Villeneuve, A., Vallée, R., and Côté, D. *Biomedical Optics Express* **2**(5), 1296–1306 (2011).
- [34] Lim, R. S., Suhalim, J. L., Miyazaki-Anzai, S., Miyazaki, M., Levi, M., Potma, E. O., and Tromberg, B. J. *The Journal of Lipid Research* **52**(12), 2177–2186 September (2011).
- [35] Mo, J., Zheng, W., Low, J. J. H., Ng, J., Ilancheran, A., and Huang, Z. *Analytical Chemistry* **81**(21), 8908–8915 November (2009).

- [36] Koljenovic', S., Bakker Schut, T. C., Wolthuis, R., de Jong, B., Santos, L., Caspers, P. J., Kros, J. M., and Puppels, G. J. *Journal of Biomedical Optics* **10**(3), 31116 (2005).
- [37] Meyer, T., Bergner, N., Medyukhina, A., Dietzek, B., Krafft, C., Romeike, B. F. M., Reichart, R., Kalff, R., and Popp, J. *Journal of Biophotonics* **5**(10), 729–733 (2012).
- [38] Lin, C.-Y., Suhaim, J. L., Nien, C. L., Miljković, M. D., Diem, M., Jester, J. V., and Potma, E. O. *Journal of Biomedical Optics* **16**(2), 21104 (2011).
- [39] Zhang, D., Wang, P., Slipchenko, M. N., Ben-Amotz, D., Weiner, A. M., and Cheng, J.-X. *Analytical Chemistry* **85**(1), 98–106 (2013).
- [40] Meyer, T., Bergner, N., Bielecki, C., Krafft, C., Akimov, D., Romeike, B. F. M., Reichart, R., Kalff, R., Dietzek, B., and Popp, J. *Journal of Biomedical Optics* **16**(2), 21113 (2011).
- [41] Meyer, T., Guntinas-Lichius, O., von Eggeling, F., Ernst, G., Akimov, D., Schmitt, M., Dietzek, B., and Popp, J. *Head & Neck* (2012).
- [42] Vogler, N., Meyer, T., Akimov, D., Latka, I., Krafft, C., Bendsoe, N., Svanberg, K., Dietzek, B., and Popp, J. *Journal of Biophotonics* **3**(10-11), 728–736 (2010).
- [43] Cheng, J. X., Jia, Y. K., Zheng, G. F., and Xie, X. S. *Biophysical Journal* **83**(1), 502–509 (2002).
- [44] Yakovlev, V. V. *Journal of Raman Spectroscopy* **34**(12), 957–964 (2003).
- [45] Ganikhanov, F., Carrasco, S., Xie, X. S., Katz, M., Seitz, W., and Kopf, D. *OPTICS LETTERS* **31**(9), 1292–1294 (2006).
- [46] Wang, H.-W., Langohr, I. M., Sturek, M., and Cheng, J.-X. *Arteriosclerosis, Thrombosis, and Vascular Biology* **29**(9), 1342–1348 (2009).
- [47] Chen, H., Wang, H., Slipchenko, M. N., Jung, Y., Shi, Y., Zhu, J., Buhman, K. K., and Cheng, J.-X. *Optics Express* **17**(3), 1282–1290 (2009).
- [48] Pegoraro, A. F., Ridsdale, A., Moffatt, D. J., Jia, Y., Pezacki, J. P., and Stolow, A. *Optics Express* **17**(4), 2984–2996 (2009).
- [49] Le, T. T., Langohr, I. M., Locker, M. J., Sturek, M., and Cheng, J.-X. *Journal of biomedical optics* **12**(5), 54007 September (2007).
- [50] Baumgartl, M., Chemnitz, M., Jauregui, C., Meyer, T., Dietzek, B., Popp, J., Limpert, J., and Tünnermann, A. *Optics Express* **20**(4), 4484–4493 (2012).
- [51] Le, T. T., Yue, S., and Cheng, J.-X. *Journal of Lipid Research* (2010).
- [52] Evans, C. L. and Xie, X. S. *Annual Review of Analytical Chemistry (2008)* **1**(1), 883–909 (2008).
- [53] Pezacki, J. P., Blake, J. A., Danielson, D. C., Kennedy, D. C., Lyn, R. K., and Singaravelu, R. *Nat Chem Biol* **7**(3), 137–145 (2011).
- [54] Freudiger, C. W., Min, W., Saar, B. G., Lu, S., Holtom, G. R., He, C., Tsai, J. C., Kang, J. X., and Xie, X. S. *Science* **322**(5909), 1857–1861 (2008).
- [55] Freudiger, C. W., Roeffaers, M. B. J., Zhang, X., Saar, B. G., Min, W., and Xie, X. S. *J. Phys. Chem. B* **115**(18), 5574–5581 (2011).
- [56] Cheng, J. X., Volkmer, A., Book, L. D., and Xie, X. S. *The Journal of Physical Chemistry B* **105**(7), 1277–1280 (2001).
- [57] Levenson, M. D. and Bloembergen, N. *Physical Review B* **10**(10), 4447–4463 November (1974).

- [58] Chemnitz, M., Baumgartl, M., Meyer, T., Jauregui, C., Dietzek, B., Popp, J., Limpert, J., and Tünnermann, A. *Optics Express* **20**(24), 26583–26595 November (2012).
- [59] Mosley, P. J., Bateman, S. A., Lavoute, L., and Wadsworth, W. J. *Optics Express* **19**(25), 25337 November (2011).
- [60] Baumgartl, M., Gottschall, T., Abreu-Afonso, J., Diez, A., Meyer, T., Dietzek, B., Rothhardt, J., Popp, J., Limpert, J., and Tünnermann, A. *Optics Express* **20**(21010-21018) (2012).
- [61] Gottschall, T., Baumgartl, M., Sagnier, A., Rothhardt, J., Jauregui, C., Limpert, J., and Tünnermann, A. *Optics Express* **20**(11), 12004 (2012).
- [62] Roger, V. L., Go, A. S., Lloyd-Jones, D. M., Benjamin, E. J., Berry, J. D., Borden, W. B., Bravata, D. M., Dai, S., Ford, E. S., Fox, C. S., Fullerton, H. J., Gillespie, C., Hailpern, S. M., Heit, J. A., Howard, V. J., Kissela, B. M., Kittner, S. J., Lackland, D. T., Lichtman, J. H., Lisabeth, L. D., Makuc, D. M., Marcus, G. M., Marelli, A., Matchar, D. B., Moy, C. S., Mozaffarian, D., Mussolino, M. E., Nichol, G., Paynter, N. P., Soliman, E. Z., Sorlie, P. D., Sotoodehnia, N., Turan, T. N., Virani, S. S., Wong, N. D., Woo, D., and Turner, M. B. *Circulation* **125**(1), 188–197 (2012).
- [63] Choudhury, R. P., Fuster, V., and Fayad, Z. A. *Nature Reviews Drug Discovery* **3**(11), 913–925 (2004).
- [64] Stolzmann, P., Subramanian, S., Abdelbaky, A., Maurovich-Horvat, P., Scheffel, H., Tawakol, A., and Hoffmann, U. *Radiographics: a review publication of the Radiological Society of North America, Inc* **31**(5), 1255–1269 (2011).
- [65] Finet, G., Ohayon, J., and Rioufol, G. *Coronary artery disease* **15**(1), 13–20 (2004).
- [66] Finet, G., Ohayon, J., Rioufol, G., Lefloch, S., Tracqui, P., Dubreuil, O., and Tabib, A. *Archives des maladies du coeur et des vaisseaux* **100**(6-7), 547–553 (2007).
- [67] Abdel-Wahab, M., Khattab, A. A., Liska, B., Toelg, R., El-Hammady, W., Farag, N., Geist, V., Ramzy, A., and Richardt, G. *EuroIntervention: journal of EuroPCR in collaboration with the Working Group on Interventional Cardiology of the European Society of Cardiology* **3**(4), 482–489 (2008).
- [68] Abramoff, M. D., Magalhães, P. J., and Ram, S. J. *Biophotonics international* **11**(7), 36–42 (2004).
- [69] Schindelin, J., Arganda-Carreras, I., Frise, E., Kaynig, V., Longair, M., Pietzsch, T., Preibisch, S., Rueden, C., Saalfeld, S., Schmid, B., Tinevez, J.-Y., White, D. J., Hartenstein, V., Eliceiri, K., Tomancak, P., and Cardona, A. *Nature Methods* **9**(7), 676–682 (2012).
- [70] Li, Q., Lau, A., Morris, T. J., Guo, L., Fordyce, C. B., and Stanley, E. F. *The Journal of Neuroscience* **24**(16), 4070–4081 April (2004).
- [71] Collins, T. J. *BioTechniques* **43**(1 Suppl), 25–30 (2007).
- [72] Schaller, R. D., Ziegelbauer, J., Lee, L. F., Haber, L. H., and Saykally, R. J. *The Journal of Physical Chemistry B* **106**(34), 8489–8492 August (2002).
- [73] Wang, H., Fu, Y., Zickmund, P., Shi, R., and Cheng, J.-X. *Biophysical Journal* **89**(1), 581–591 (2005).
- [74] Lu, R., Gan, W., Wu, B.-h., Zhang, Z., Guo, Y., and Wang, H.-f. *The Journal of Physical Chemistry B* **109**(29), 14118–14129 (2005).
- [75] Tolles, W. M., Nibler, J. W., McDonald, J. R., and Harvey, A. B. *Applied Spectroscopy* **31**(4), 253–271 (1977).
- [76] Volkmer, A. *Journal of Physics D: Applied Physics* **38**(5), R59—R81 (2005).
- [77] Colthup, N. B., Daly, L. H., and Wiberley, S. E. *Introduction to infrared and Raman spectroscopy*. Academic Press, (1990).

- [78] Li, L., Wang, H. F., and Cheng, J. X. *Biophysical Journal* **89**(5), 3480–3490 November (2005).
- [79] Bergner, G., Chatzipapadopoulos, S., Akimov, D., Dietzek, B., Malsch, D., Henkel, T., Schlücker, S., and Popp, J. *Small* **5**(24), 2816–2818 (2009).
- [80] Arakawa, K., Isoda, K., Ito, T., Nakajima, K., Shibuya, T., and Ohsuzu, F. *Arteriosclerosis, Thrombosis, and Vascular Biology* **22**(6), 1002–1007 (2002).
- [81] Wang, H.-W., Le, T. T., and Cheng, J.-X. *Optics Communications* **281**(7), 1813–1822 April (2008).
- [82] Ko, A. C.-T., Ridsdale, A., Mostaço-Guidolin, L. B., Major, A., Stolow, A., and Sowa, M. G. *Biophysical Reviews* **4**(4), 323–334 (2012).
- [83] Kim, B. M., Eichler, J., Reiser, K. M., Rubenchik, A. M., and Da Silva, L. B. *Lasers in surgery and medicine* **27**(4), 329–335 (2000).
- [84] Fu, D., Holtom, G., Freudiger, C., Zhang, X., and Xie, X. S. *The Journal of Physical Chemistry B* **117**(16), 4634–4640 April (2013).



## 13 | Peer Reviewed Publications

- [1] Torsten Frosch, Tobias Meyer, Michael Schmitt, and Jürgen Popp. Device for raman difference spectroscopy. *Analytical Chemistry*, 79(16):6159–6166, 2007.
- [2] Tobias Meyer, Denis Akimov, Nicolae Tarcea, Susana Chatzipapadopoulos, Gerald Muschiolik, Jens Kobow, Michael Schmitt, and Jürgen Popp. Three-dimensional molecular mapping of a multiple emulsion by means of CARS microscopy. *The Journal of Physical Chemistry B*, 112(5):1420–1426, 2008.
- [3] Christoph Krafft, Anuradha A. Ramoji, Christiane Bielecki, Nadine Vogler, Tobias Meyer, Denis Akimov, Petra Rösch, Michael Schmitt, Benjamin Dietzek, Iver Petersen, Andreas Stallmach, and Jürgen Popp. A comparative raman and CARS imaging study of colon tissue. *Journal of Biophotonics*, 2(5):303–312, 2009.
- [4] Denis Akimov, Susana Chatzipapadopoulos, Tobias Meyer, Nicolae Tarcea, Benjamin Dietzek, Michael Schmitt, and Jürgen Popp. Different contrast information obtained from CARS and nonresonant FWM images. *Journal of Raman Spectroscopy*, 40(8):941–947, 2009.
- [5] Nadine Vogler, Tobias Meyer, Denis Akimov, Ines Latka, Christoph Krafft, Niels Bendsoe, Katarina Svanberg, Benjamin Dietzek, and Jürgen Popp. Multimodal imaging to study the morphochemistry of basal cell carcinoma. *Journal of Biophotonics*, 3(10-11):728–736, 2010.
- [6] Shivangi Mishra, Tobias Meyer, Jürgen Popp, and Ranjan K. Singh. Precise

- analysis of small wavenumber shift of pyridine on dilution with  $\text{h}_2\text{o}$  and  $\text{d}_2\text{o}$  using RDS technique. *Zeitschrift für Physikalische Chemie*, 225(6-7):673–690, 2011.
- [7] Tobias Meyer, Norbert Bergner, Christiane Bielecki, Christoph Krafft, Denis Akimov, Bernd F. M. Romeike, Rupert Reichart, Rolf Kalff, Benjamin Dietzek, and Jürgen Popp. Nonlinear microscopy, infrared, and raman microspectroscopy for brain tumor analysis. *Journal of Biomedical Optics*, 16(2):021113–021113, 2011.
- [8] Martin Baumgartl, Mario Chemnitz, Cesar Jauregui, Tobias Meyer, Benjamin Dietzek, Jürgen Popp, Jens Limpert, and Andreas Tünnermann. All-fiber laser source for CARS microscopy based on fiber optical parametric frequency conversion. *Optics Express*, 20(4):4484–4493, 2012.
- [9] Martin Baumgartl, Thomas Gottschall, Javier Abreu-Afonso, Antonio Díez, Tobias Meyer, Benjamin Dietzek, Manfred Rothhardt, Jürgen Popp, Jens Limpert, and Andreas Tünnermann. Alignment-free, all-spliced fiber laser source for CARS microscopy based on four-wave-mixing. *Optics Express*, 20(19):21010–21018, 2012.
- [10] Mario Chemnitz, Martin Baumgartl, Tobias Meyer, Cesar Jauregui, Benjamin Dietzek, Jürgen Popp, Jens Limpert, and Andreas Tünnermann. Widely tuneable fiber optical parametric amplifier for coherent anti-stokes raman scattering microscopy. *Optics Express*, 20(24):26583–26595, 2012.
- [11] Anna Medyukhina, Tobias Meyer, Michael Schmitt, Bernd F. M. Romeike, Benjamin Dietzek, and Jürgen Popp. Towards automated segmentation of cells and cell nuclei in nonlinear optical microscopy. *Journal of Biophotonics*, 5(11-12):878–888, 2012.
- [12] Tobias Meyer, Norbert Bergner, Anna Medyukhina, Benjamin Dietzek, Christoph Krafft, Bernd F. M. Romeike, Rupert Reichart, Rolf Kalff, and Jürgen Popp. Interpreting CARS images of tissue within the C–H-stretching region. *Journal of Biophotonics*, 5(10):729–733, 2012.
- [13] Tobias Meyer, Orlando Guntinas-Lichius, Ferdinand von Eggeling, Günther



- Ernst, Denis Akimov, Michael Schmitt, Benjamin Dietzek, and Jürgen Popp. Multimodal nonlinear microscopic investigations on head and neck squamous cell carcinoma: Toward intraoperative imaging. *Head & Neck*, 35(9):E280-E287, 2013.
- [14] Tobias Meyer, Martin Baumgartl, Thomas Gottschall, Torbjörn Pascher, Andreas Wuttig, Christian Matthäus, Bernd F. M. Romeike, Bernhard R. Brehm, Jens Limpert, Andreas Tünnermann, Orlando Guntinas-Lichius, Benjamin Dietzek, Michael Schmitt, and Jürgen Popp. A compact microscope setup for multimodal nonlinear imaging in clinics and its application to disease diagnostics. *Analyst*, 138(14):4048-4057, 2013.
- [15] Tobias Meyer, Mario Chemnitz, Martin Baumgartl, Thomas Gottschall, Torbjörn Pascher, Christian Matthäus, Bernd F. M. Romeike, Bernhard R. Brehm, Jens Limpert, Andreas Tünnermann, Michael Schmitt, Benjamin Dietzek, and Jürgen Popp. Expanding multimodal microscopy by high spectral resolution CARS imaging for clinical disease diagnostics. *Analytical Chemistry*, 85(14):6703-6715, 2013.



# 14 | Conference Contributions

## Oral Presentations

2011

**Nonlinear microscopy, IR and Raman microspectroscopy for brain tumour analysis,**

*Tobias Meyer, Norbert Bergner, Christiane Bielecki, Christoph Krafft, Bernd F.M. Romeike, Rupert Reichart, Rolf Kalff, Benjamin Dietzek, and Jürgen Popp,*

Photonics West BIOS, San Francisco, USA, 22-27 January 2011.

**Compact setup for multimodal nonlinear microscopy in neuropathology,**

*Tobias Meyer, Benjamin Dietzek, and Jürgen Popp,*

DokDok Naumburg, Germany, 21-25 March 2011.

**Multimodal nonlinear imaging of brain tissue,**

*Tobias Meyer, Benjamin Dietzek, Norbert Bergner, Bernd F. M. Romeike, Rupert Reichart, Rolf Kalff, and Jürgen Popp,*

Seminar Abbe School of Photonics, 29 April 2011.

**Nonlinear microscopy for histopathology of brain tumors,**

*Tobias Meyer, Bernd F.M. Romeike, Rupert Reichart, Rolf Kalff, Benjamin Dietzek, and Jürgen Popp,*

3<sup>rd</sup> Postgraduate Symposium on Cancer research Dornburg, Germany, 30 April 2011.

2012

**Monitoring the morphochemistry of laryngeal carcinoma by multimodal imaging,**

*Tobias Meyer, Christoph Krafft, Orlando Guntinas-Lichius, Benjamin Dietzek, and Jürgen Popp,*

Photonics West BIOS 2012, San Francisco, USA, 21-26 January 2012.

**Alignment and maintenance free all-fiber laser sources for CARS microscopy based on frequency conversion by four-wave-mixing,**

*Martin Baumgartl, Mario Chemnitz, Tobias Meyer, Thomas Gottschall, Cesar Jauregui, Jens Limpert, and Andreas Tünnermann,*

Photonics West, San Francisco, USA, 21-26 January 2012.

**Non-invasive label free investigation and typing of head and neck cancers by multimodal nonlinear microscopy,**

*Tobias Meyer, Benjamin Dietzek, Denis Akimov, and Jürgen Popp,*

Photonics Europe, Brussels, Belgium, 16-19 April 2012.

**Fiber Optical Parametric Frequency Conversion: Alignment and Maintenance Free All-fiber Laser Concept for CARS Microscopy,**

*Martin Baumgartl, Mario Chemnitz, Cesar Jauregui, Thomas Gottschall, Tobias Meyer, Benjamin Dietzek, Jürgen Popp, Jens Limpert, and Andreas Tünnermann,*

Conference on Lasers and Electro-Optics (CLEO): Science and Innovations, San Jose, USA, 6-11 May 2012.

**All-fiber laser source for CARS-Microscopy**

*Thomas Gottschall, Javier Abreu-Afonso, Martin Baumgartl, Tobias Meyer, Benjamin Dietzek, Jürgen Popp, Jens Limpert, and Andreas Tünnermann,*  
5th EPS-QEOD EUROPHOTON 2012 "Solid State, Fibre, and Waveguide Coherent Light Sources", Stockholm, Sweden, 26-31 August 2012.

**Biomedical applications of multimodal nonlinear imaging - Towards CARS microscopy in clinics,**

*Tobias Meyer, Martin Baumgartl, Thomas Gottschall, Jens Limpert, Andreas Tünnermann, Michael Schmitt, Benjamin Dietzek, and Jürgen Popp,*  
International Conference on Raman Spectroscopy ICORS 2012, Bangalore, India, 12-17 August 2012.

**Novel instrumentation for multimodal nonlinear microscopy in clinics,**

*Tobias Meyer, Martin Baumgartl, Thomas Gottschall, Jens Limpert, Andreas Tünnermann, Christian Matthäus, Christoph Krafft, Michael Schmitt, Benjamin Dietzek, and Jürgen Popp,*  
SPEC 2012, Chiang Mai, Thailand, 11- 16 November 2012.

**2013**

**Single-beam fiber laser sources for CARS microscopy**

*Martin Baumgartl, Thomas Gottschall, Mario Chemnitz, Tobias Meyer, Javier Abreu-Afonso, Cesar Jauregui-Misas, Benjamin Dietzek, Manfred Rothhardt Jürgen Popp, Antonio Díez, Jens Limpert, and Andreas Tünnermann,*  
Photonics West, San Francisco, USA, 2-7 February 2013.

## Poster Presentations

2010

**Investigation of brain tissue by nonlinear microscopy,**

*Tobias Meyer, Norbert Bergner, Christoph Krafft, Bernd F.M. Romeike, Rupert Reichart, Rolf Kalff, Benjamin Dietzek, and Jürgen Popp,*

2nd Postgraduate Symposium on Cancer Research, Dornburg, Germany, 24 February 2010.

**Investigations on brain tissue by nonlinear microscopy,**

*Tobias Meyer, Benjamin Dietzek, Norbert Bergner, Christoph Krafft, Bernd F.M. Romeike, Rupert Reichart, Rolf Kalff, and Jürgen Popp,*

P4L Annual Meeting St. Andrews, UK, 11-12 May 2010.

**Multimodal nonlinear imaging of brain tissue on single cell level,**

*Tobias Meyer, Norbert Bergner, Christoph Krafft, Bernd F.M. Romeike, Rupert Reichart, Rolf Kalff, Benjamin Dietzek, and Jürgen Popp,*

Symposium Tumor Microenvironment, Dornburg, Germany, 18 June 2010.

**Comparative Study On The Composition Of Brain Tissue By Nonlinear Microscopy,**

*Tobias Meyer, Norbert Bergner, Benjamin Dietzek, Christoph Krafft, Denis Akimov, Bernd F.M. Romeike, Rupert Reichart, Rolf Kalff, and Jürgen Popp,*

International Conference on Raman Spectroscopy (ICORS) 2010, Boston, USA, 8-13 August 2010.

**Nonlinear Microscopy of Brain Tissue,**

*Tobias Meyer, Norbert Bergner, Benjamin Dietzek, Christoph Krafft, Denis Akimov, Bernd F.M. Romeike, Rupert Reichart, Rolf Kalff, and Jürgen Popp*

Biophotonics and Imaging Graduate Summer School, Ireland, 27 August - 2 September 2010.

2012

**Portables Mikroskop für multimodale molekulare Bildgebung in der Klinik,**

*Tobias Meyer, Benjamin Dietzek, and Jürgen Popp,*

BMBF Symposium MediWing, Nürnberg, Germany, 4-5 July 2012.

**Biomedical applications of multimodal nonlinear imaging - Towards CARS microscopy in clinics,**

*Tobias Meyer, Martin Baumgartl, Thomas Gottschall, Jens Limpert, Andreas Tünnermann, Michael Schmitt, Benjamin Dietzek, and Jürgen Popp,*

International Conference on Raman Spectroscopy ICORS 2012, Bangalore, India, 12-17 August 2012.

**Imaging of Head and Neck cancers by multimodal nonlinear microscopy,**

*Tobias Meyer, Anna Medyukhina, Christoph Krafft, Orlando Guntinas-Lichius, Michael Schmitt, Benjamin Dietzek, and Jürgen Popp,*

International Conference on Raman Spectroscopy ICORS 2012, Bangalore, India, 12-17 August 2012.

## Conference Proceedings

- [1] Nadine Vogler, Tobias Meyer, Ines Latka, Thomas Bocklitz, Christoph Krafft, Volker Deckert, Nils Bendsoe, Katharina Svanberg, Benjamin Dietzek, and Jürgen Popp. Biomedical imaging by means of linear and non-linear raman microspectroscopy. pages 77152W–77152W, April 2010.
- [2] Christoph Krafft, Benjamin Dietzek, Tobias Meyer, Norbert Bergner, Bernd F. M. Romeike, Rupert Reichart, Rolf Kalff, and Jürgen Popp. Nonlinear microscopy and infrared and raman microspectroscopy for brain tumor analysis. pages 790319–790319, February 2011.
- [3] Tobias Meyer, Benjamin Dietzek, Christoph Krafft, Bernd F. M. Romeike, Rupert Reichart, Rolf Kalff, and Jürgen Popp. Nonlinear optical imaging: toward chemical imaging during neurosurgery. pages 78833W–78833W, February 2011.
- [4] Martin Baumgartl, Mario Chemnitz, Cesar Jauregui, Tobias Meyer, Benjamin Dietzek, Jürgen Popp, Jens Limpert, and Andreas Tünnermann. Alignment and maintenance free all-fiber laser source for CARS microscopy based on frequency conversion by four-wave-mixing. pages 82470F–82470F, February 2012.
- [5] Tobias Meyer, Christoph Krafft, Orlando Guntinas-Lichius, Ferdinand von Eegeling, Günther Ernst, Benjamin Dietzek, and Jürgen Popp. Monitoring the morphochemistry of laryngeal carcinoma by multimodal imaging. pages 82200R–82200R, February 2012.
- [6] Tobias Meyer, Nadine Vogler, Benjamin Dietzek, Denis Akimov, Johanna Inhestern, Orlando Guntinas-Lichius, and Jürgen Popp. Non-invasive label-free investigation and typing of head and neck cancers by multimodal nonlinear microscopy. pages 84270Z–84270Z, June 2012.
- [7] Riccardo Cicchi, Christian Matthäus, Tobias Meyer, Annika Lattermann, Benjamin Dietzek, Bernhard R. Brehm, Jürgen Popp, and Francesco S. Pavone. Characterization of atherosclerotic arterial tissue using multimodal non-linear optical microscopy. pages 87970D–87970D, June 2013.



# 15 | Selbständigkeitserklärung

Ich erkläre,

dass mir die geltende Promotionsordnung der Fakultät bekannt ist;

dass ich die Dissertation selbst angefertigt und alle von mir benutzten Hilfsmittel, persönlichen Mitteilungen und Quellen in meiner Arbeit angegeben habe;

dass mich folgende Personen bei der Auswahl und Auswertung des Materials sowie bei der Herstellung des Manuskripts unterstützt haben:

dass die Hilfe eines Promotionsberaters nicht in Anspruch genommen wurde und das Dritte weder unmittelbar noch mittelbar geldwerte Leistungen von mir für Arbeiten erhalten haben, die im Zusammenhang mit dem Inhalt der vorgelegten Dissertation stehen;

dass ich die Dissertation noch nicht als Prüfungsarbeit für eine staatliche oder andere wissenschaftliche Prüfung eingereicht habe;

dass ich nicht die gleiche, in wesentlichen Teilen ähnliche oder eine andere Abhandlung bei einer anderen Hochschule als Dissertation eingereicht habe.

Jena,

Tobias Meyer



## 16 | Danksagung

Zum Abschluss möchte ich mich bei allen bedanken, die zum erfolgreichen Abschluss dieser Arbeit ihren Anteil beigetragen haben, und der bisher noch nicht gebührend gewürdigt wurde.

Ich danke insbesondere dem Team der Werkstatt, die geduldig immer wieder neue Löcher in diverse Teile bohrten, Gewinde schnitten, mal ganz schnell eine Kleinigkeit ändern mussten, damit ein Experiment noch weitergehen konnte.

Ganz besonders danke ich Ralph Stöpel, der die Hauptlast zu tragen hatte, da er alle mechanischen Sonderanfertigungen für die beiden Eigenbau-Laserscanning-Mikroskope erledigt hat und geduldig auch noch die zehnte Modifikation vorgenommen hat, wenn ich mich vermessen hatte, etwas vergessen hatte zu bedenken oder ähnliches.

In diesem Zusammenhang bedanke ich mich bei Daniel und Michael Fritzsche, die mich bei der Konstruktion der Mikroskope tatkräftig unterstützt haben, solange sie es bei mir ausgehalten haben.

Ein besonders großes Dankeschön gebührt Torbjörn Pascher, der die Elektronik und die Software des Mikroskops in Rekordzeit entwickelt hat und meinen oftmals etwas konfusen Vorstellungen und Wünschen angepasst hat, so dass sich das Ergebnis sehen lassen kann. Ohne Torbjörn hätte ich das nicht geschafft.

Genauso wichtig wie die richtigen Geräte sind interessante Proben zum Untersuchen. Christiane Bielecki danke ich für das Präparieren der Proben vom Kleinhirn. Für die Aufarbeitung der humanen Hirn- und Arteriosklerose-Proben und geduldige Diskussion der Ergebnisse bedanke ich mich ganz herzlich bei PD Dr. Bernd F.M. Romeike. Für die Bereitstellung von HNO-Gewebeproben möchte ich Prof. Orlan-

do Guntinas-Lichius danken, besonders auch für die Beantwortung von Fragen in Rekordzeit. Für die Aufarbeitung der Ergebnisse der HE-Färbungen danke ich Dr. Günther Ernst und Prof. Ferdinand von Eggeling.

Ein großer Dank an die Laserphysiker vom Institut für Angewandte Physik unter der Leitung von Prof. Andreas Tünnermann. Die Arbeitsgruppe von Prof. Jens Limpert, insbesondere Martin Baumgartl, Thomas Gottschall und Mario Chemnitz haben tolle Faserlasersysteme gebaut, passgenau zum Mikroskop oder besser gesagt beides entwickelte sich parallel und zusammenpassend.

Ich bedanke mich bei der gesamten AG-Dietzek und AG-CARS, für die letzten knapp 4 Jahre, die ihr mich ertragen musstet. Letztlich konnte doch jeder Streit um Messzeit ohne Blutvergießen geregelt werden, trotz der Haltung auf engstem Raum, die ja bekanntlich das Aggressionspotential erhöht. Zumindest gilt das für Legehennen, aber, wie mir auch im Rahmen dieser Arbeit bewusst geworden ist, kann man ja Tiermodelle nicht immer auf den Menschen verallgemeinern. Ich möchte mich bei meinen Büromitbewohnern bedanken für die ruhige und produktive Atmosphäre bedanken und Hilfe bei der Fehlersuche im Manuskript.

Ich danke v.a. Prof. Popp dafür, dass ich dieses interessante Thema in seiner Arbeitsgruppe mit der denkbar besten Ausstattung 4 Jahre bearbeiten konnte, für die vielen Möglichkeiten der Weiterbildung, die vielen internationalen Konferenzen und nicht zu vergessen Skiseminare. Prof. Michael Schmitt und Prof. Benjamin Dietzek danke ich für die exzellente Betreuung. Denis danke ich für alles, was ich mir im Labor von ihm abschauen durfte.

Und natürlich danke ich meiner Familie für alles. Und ganz besonders danke ich Linda für soviel, dass ich hier keinen Platz zum Aufschreiben habe.

Die der vorliegenden Arbeit zu Grunde liegenden Experimente wurden am Institut für photonische Technologien e.V. durchgeführt. Vielen Dank an alle Kollegen.

